Spin transfer in a magnetic insulator

Nicolas Thiery

Communauté
UNIVERSITÉ Grenoble Alpes

THÈSE

Pour obtenir le grade de

DOCTEUR DE LA COMMUNAUTE UNIVERSITE GRENOBLE ALPES

Spécialité : **Physique de la Matière Condensée et du Rayonnement**

Arrêté ministériel : 25 mai 2016

Présentée par

Nicolas THIERY

Thèse dirigée par **Olivier Klein, CEA Grenoble, Spintec**
et codirigée par **Laurent VILA, CEA Grenoble, Spintec**

préparée au sein du **Laboratoire Spintronique et Technologie des Composants**
dans **l'École Doctorale de Physique**

Transfert de spin dans un isolant magnétique

Thèse soutenue publiquement le **« 28 novembre 2019 »**,
devant le jury composé de :

Madame Catherine GOURDON
Directrice de Recherche, Institut des nanosciences de Paris, CNRS, Rapporteur
Monsieur Sebastian T.B. GOENNENWEIN
Professeur, Université technique de Dresde, Rapporteur
Monsieur Chrisitan H. BACK
Professor, Université technique de Munich, Président du jury
Monsieur Vittorio BASSO
Chargé de recherche, Institut national de recherche de métrologie de Turin, Examinateur
Monsieur Laurent RANNO
Maître de conférences, Université Grenoble Alpes, CNRS institut Néel, Examinateur

Résumé en français

La génération et détection de purs courants de spin dans des isolants magnétiques sont au cœur de la spintronique des isolants. Ce nouveau concept émergent permet un transport à longue distance d'une information, dites de spin, grâce à l'absence d'électrons de conduction qui favorisent la propagation. Un courant de spin peut alors être induit à travers le réseau de spin via une "onde de spin", connue aussi sous le nom de "magnons", ayant des fréquences caractéristiques allant du GHz jusque au THz avec des longueurs d'onde associée entre le μm et le nm. La spintronique des isolants moderne se focalise principalement sur le grenat de fer d'yttrium (YIG), un isolant ferrimagnétique, possédant le plus faible amortissement magnétique connu. Mon travail de thèse a consisté à étudier le transport d'onde de spin dans des films de YIG ultra-minces (quelques nm) et de hautes qualités, en exploitant l'interaction spin orbite dans les métaux et les propriétés d'interfaces pour convertir un courant de charge en ondes de spin. Par l'injection d'une forte densité de courant dans un nanofil de platine (Pt) déposé directement sur le film magnétique, un pure courant magnonique peut être induit/détecté dans le YIG par l'effet direct/inverse Hall de spin dans le Pt. La principale contribution de mon travail a consisté d'étudier cette conversion à des fortes énergies. J'ai notamment démontré expérimentalement, que la conductance de spin dans ce système présente divers régimes impliquant un changement drastique de la densité d'état des magnons. A travers différentes méthodes de mesure comme le transport de spin local et non-local, la diffusion Brillouin et des mesures de magnetoresistance, je fournis une analyse complète des différents phénomènes entourant le transfert de spin dans des films ultra-minces de YIG. Mes résultats expérimentaux apportent une contribution dans l'exploration de phénomènes collectifs nouveaux tels que la formation de condensats de Bose-Einstein à température ambiante.

Resume

The generation and detection of pure spin currents circulating in magnetic insulator materials are at the heart of insulating spintronics. It have proven its worth by enabling transport of spin information across large distances, much further than in metals, thanks to the absence of decay mechanism through the delocalized electrons. Spin currents here propagate over localized magnetic moments via spin-waves (SW), or their quanta the magnons, with characteristic frequencies ranging from GHz to THz and associated wavelengths from μm to nm. Recently, considerable attention in the field of insulating spintronics has been given Yttrium Iron garnets (YIG), which is a ferrimagnetic insulator with the lowest known amount of magnetic damping. My thesis work focuses on spin waves transport in high-quality ultra-thin films exploiting spin-orbit tools to interconvert the spin signal into an electrical signal. By injecting a high current density in Pt electrodes deposited few microns apart on top of a YIG film, a pure magnon current propagating in the YIG can be induced/detected via the direct/inverse spin Hall effect. The main contribution of my work is a thorough investigation of the spin transfer at large energies. We have found that the spin conductance in this system can cross several regimes that involve a strong change in the magnon distribution. Throughout various techniques such as local and non-local transport as a function of various parameters (current, field, temperature), Brillouin light scattering spectroscopy, and magnetoresistance measurements, we provide a complete analysis of the different phenomena surrounding the spin transport at large energy in thin YIG films and we will show that our experimental findings can be explained classically and do not support yet the emergence of the new collective quantum behaviors, such as Bose-Einstein condensation at room temperature.

Remerciements

Cette grande aventure qu'a été ma thèse n'aurait bien sur pas été possible sans le soutien précieux de toutes les personnes qui m'ont accompagné durant ces trois années.
Afin de commencer en bonne et due forme, je remercie chaleureusement les membres de mon jury : Catherine GOURDON, Sebastian GOENNENWEIN, Christian BACK, Vittorio BASSO et Laurent RANNO d'avoir lu et étudié mes travaux de recherche. Vos remarques et discussions ont contribué à améliorer la qualité de ce manuscrit et de ma thèse dans sa globalité.
C'est avec une grande sincérité et beaucoup d'émotions que je remercie mes directeurs de thèse Olivier KLEIN et Laurent VILA pour m'avoir guidé et grandement soutenu pendant ces trois ans. Olivier pour ta sympathie, ton soutien, ton enthousiasme sans faille ainsi que ta grande, que dis-je, de ton immense connaisance du YIG ont été les clefs qui font que j'écris ces mots aujourd'hui en tant que docteur ! Laurent un immense merci à toi pour ta bonne humeur naturelle, tes conseils et encouragements, particulièrement dans les moments difficiles et de doute, et qui m'ont énormément aidé au quotidien. Je n'ai bien sur pas besoin de vanter tes talents de litho qui ont bien fait chauffer mojito et étoffé mes habilités au bonding (plus de 200 devices mesurés ça en fait du bonding !). Je te remerice aussi de m'avoir initié au ski, ce qui fait de moi un docteur 100% Grenoblois ! Avoir été votre thésard m'a fait grandir professionnelement mais aussi personellement, et je regrette déja notre triomphant trio.
Je tiens à remercier les talentueuses personnes avec qui j'ai collaboré pour ce travail. Tout d'abord j'aimerais remercier la team Brestoise et particulièrement Jamal BEN YOUSSEF alias le "wizard" du YIG, pour avoir élaboré les fines couches de YIG "high quality", ce qui a fait l'originalité de ma thèse. Merci pour ta sympathie et ta spontanéité (je pense particulièrement au colloque Louis Néel !). Un grand merci également à Nathan BEAULIEU pour sa gentilesse et avec qui j'ai eu de fructueuses conversations sur le YIG. Je te souhaite le meilleur pour la suite de ta carrière.
Un immense merci à Vladimir NALETOV avec qui j'ai eu le plaisir de travailler durant les trois premiers mois de ma thèse. J'ai beaucoup appris durant cette période et te suis extremement reconnaisant d'avoir "customisé" et optimisé mojito pour les mesures bas bruits en pulse. Ton profesionalisme et tes qualités humaines ont largement contribué à lancer ma thèse sur les chapeaux de roues !
Un grand merci a la team CEA Saclay et notamment à Gregoire DE LOUBENS et Michel VIRET pour leur charac du YIG et de leurs expertises qui ont enormément contribué à avoir une vue d'ensemble sur mes travaux mais aussi à affiner les papiers durant les nombreux mois de bataille avec les referees.
Je souhaite également remercier la team CNRS Thalès, notamment Vincent CROS pour avoir contribué et suivi mes travaux avec intérêt, ainsi que Abdelmadjid ANANE et Lucile SOUMAH. Sans leur remarquable travail sur le BiYIG, ma thèse ne se serait pas terminée par une cerise sur le gâteau (×10 sur le signal de spin tout de même !). Et bien sur je remercie Vladislav DEMIDOV et Sergej DEMOKRITOV de Münster pour leurs mesures BLS, ce qui a donné une valeur ajoutée à mon travail.
Pour en revenir à Grenoble, je souhaite chaleureusement remercier Ariel BRENAC pour ses dépots de Si_3N_4 mais également pour son important soutien technique lorsque j'en avais besoin et toujours avec le sourire. Un immense merci à Jean François JACQUOT pour son aide précieuse apportée notamment sur les mesures de résistivités du YIG qui m'auront donné bien du fil à retordre. Ta gentilesse et tes compétences à tout épreuve

m'ont beaucoup apporté et c'était toujours un plaisir de discuter avec toi. Je dois biensur remericer l'incontournable Paul NÖEL, avec qui j'ai eu le plaisir de partager mon bureau durant ces trois années, et qui m'a aussi aidé à réaliser les mesures spin pumping. Je pense déja avec nostalgie à cette époque, tes éclats de rire dans les couloirs, tes arrivées tardives au labo (car tu étais au broadband hein ?), et les 30 s de délais à chaque fois que je te posais une question. Je te souhaite une bonne continuation pour ta carrière de chercheur (défonces tout !). Et je remercie Kyongmo AN avec qui j'ai eu le plaisir de travailler durant la dernière année de ma thèse. Merci pour ta bienveillance, sympathie, et d'avoir toujours consacré du temps pour moi (et aussi de m'avoir fait découvrir les meilleurs resto coréens de Grenoble !). Je souhaite également de la réussite à Ryuhei KOHNO qui prend la suite de mon travail.
Je tiens à remercier en particulier les personnes qui m'ont accompagné au quotien au C5. Merci à crazy Van Tuong PHAM pour tous ces moments de convivialités notamment pendant les dejeuners ou pauses café. Je repense particulièrement à cette première journée découverte du ski qui restera gravée dans ma mémoire. Merci à Marie MARMIESSE pour ta gentilesse et ta bonne humeur au quotidien, lorsque tu étais en stage et quand tu passais nous saluer au bureau. Je te souhaite bon courage pour la fin de ta thèse. Je remercie Yu FU, pour avoir apporté un rayon de soleil et de joie au labo durant ma dernière année. J'ai apprécié d'avoir été ton mentor en python et tous les moments passés ensemble. Je souhaite remercier également Sambit GHOSH, qui a apporté du dynamisme dans le petit groupe. J'ai adoré notre petite virée en Belgique et j'ai hate de réitérer l'experience ! Je remercie aussi Sara VAROTTO qui a passé un temps bien trop court à spintec mais a laissé un souvenir impérisable à tous. Finalement je tiens a remercier la machine à café de Paul qui a fait ... et bien ... le café ! Ce truc m'a été d'un immense soutien psychologique et physique, particulièrement pendant la rédaction de thèse même si cela m'a fait retomber dans mes plus vieilles habitudes d'accro à la caféine.
Big up à toutes les personnes avec qui j'ai aussi partagé mon quotidien au C5 : Jean-Phillipe, Gilles, Toshiki, Maxen, Matthieu, Céline, Tuan, Alain, Thomas, Cyrille, Lucien, Patrick ...
Un grand merci également aux personnes que j'ai cotoyé à spintec. Une petite pensée à mes acolytes Van Dai NGUYEN et Steven LEQUEUX pour toutes ces scéances de tennis le midi qui m'ont été d'un grand secours pendant la rédaction ! Je remercie entre autre : Rachelle, Céline, Léa, Sabrina, Vincent, Ursula, Mathieu, Thomas, Chandra, Gilles, Mihai, Lilliana, Lucian, Mairbek, Olivier, Daria, Isabelle, Marco, Vadym, Olga, Micheal, Daniel, Haozhe, Arnaud, Cécile, Lamprini pour ces moments de convivialité passés à spintec. Désolé si j'en oublie, je commence à me faire vieux ...
Je voudrais remercier mes amis pour m'avoir soutenu. Je pense en particulier à Maxime GAY pour toutes ces sorties ciné et ski et ces moments passés à Grenoble. Mais c'est sans oublier : Keshav, Mathieu, Olivier, Nathan, Marie, Jean-Francois, Anouck, Céline, Thomas, Connor.
Et pour finir en beauté je remercie infiniment ma famille pour leur amour et leur soutien inébranlable durant toutes ces années. Sans vous je ne serai pas arrivé là ou j'en suis !

Summuary

Introduction

Spintronics has proven its worth by causing a revolution in data storage and the advent of the big data era [1]. Spintronics uses the spin, an internal angular momentum of the electrons (or holes), for various information sensing, storage and processing. Nevertheless, the majority of spintronics devices continues to function via mobile electrons, which inherently dissipates power due to resistive losses. This is because in metallic ferromagnets, the charge current is spin polarized and a flow of angular momentum, called spin current, is joined to the charge flow. Propagating excitations of localized magnetic moments can also carry spin currents. However, in metals, spin excitations are strongly attenuate due to considerable viscous damping of magnetic excitations. Only in magnetic insulators, spin currents propagate with significantly reduced dissipation since there are no conduction electrons dissipating heat. The coined term "spin insulatronics" covers efforts to transport spin information without transport of carriers. The aim is to facilitate a revolution of information and communication technologies by controlling electric signals through the deployment of ferromagnetic insulators (FIs). For spin insulatronics to succeed, spin signals in magnetic insulators must seamlessly integrate with conventional electronics. This shall be the only way the transport and manipulation of spin information in an insulator can become feasible and useful in devices.
Spin insulatronics offers several novelties. The small energy losses in insulators enable transport of spin information across large distances (up to tens of micrometers [2, 3]), much farther than in metals. Furthermore, magnetic insulators transfer and contain data in original ways, even allowing for ballistic propagation. Since the transport is anisotropic, an external field changing the direction of the magnetic configuration controls the device as well. The reduced dissipation also facilitates quantum coherent phenomena. Magnons can condense [4] and one might achieve the state of spin superfluidity [5], an entirely new route to mediate spin information without loss. While magnonics [6], the exploration of spin waves in magnetic structures, is a part of this emerging field [7], recent developments have enabled the possibilities of controlling spin waves electrically or thermally in ferromagnetic insulator via a neighboring metal [8].

Magnetic Insulators

Ferromagnets are often electrical conductors since ferromagnetic exchange relies on electron delocalization. Conversely, magnetic insulators are usually governed by indirect antiferromagnetic super-exchange. The coupling generates either pure antiferromagnets or ferrimagnets when the magnetizations of the different sublattices do not compensate entirely. It is sometimes possible to tune (or dope) the two (or more) sublattices and adjust their magnetization from zero for antiferromagnets to rather large values of the order of $100\,\mathrm{kAm^{-1}}$. In magnetic insulators, the only way to carry a spin current is via the localized magnetic moments. The spin flow is the propagation of their local disturbance. In its simplest manifestation, the spin current propagates via spin-waves (SW), or their quanta the magnons. The characteristic frequencies range from GHz to THz and the associated wavelengths are from μm to nm [9]. A key feature of magnetic materials is that the spin-wave dispersion relation can be tuned continuously by an external magnetic field on a very wide range. Additionally, changing or controlling the material alters the magnetic anisotropy, which gives additional means for tuning the spin transport properties.

In ferrimagnets, high-frequency excitations (up to THz) exist naturally, and not only at very short wavelengths, through excitation of the magnetization between the two sublattices. Antiferromagnets are ferrimagnets with no net magnetization and associated absence of the low-energy dispersion branch. While all magnetic insulators are useful in spin insulatronics, antiferromagnetic insulators are of particularly high interest. Their THz response is a real ace card and can facilitate ultra-fast spintronics devices. They are also robust against an external magnetic field. Early theories of antiferromagnetic metals as active spintronic elements [10, 11] inspired their validation as memory devices [12, 13]. There are demonstrations that antiferromagnetic insulators are good spin conductors [3, 14, 15]. The first pieces of evidence were indirect. There is a relatively short-range spin current propagation in antiferromagnetic insulators coupled to ferromagnetic insulators. Importantly, there are more recent reports of a truly long-range spin transport in an antiferromagnetic insulator [3]. Other possible materials for room-temperature operation are the archetype NiO, CoO, as well as the magnetoelectric Cr_2O_3 and $BiFeO_3$. Many insulating materials can function as spintronic elements. However, this variety is predominantly unexplored as most published reports utilize Yttrium Iron Garnet $Y_3Fe_5O_{12}$ (YIG). YIG is a ferrimagnetic insulator with the lowest known amount of spin dissipation as characterized by its exceptional small Gilbert damping constant. It is, therefore, optimal to propagate spin waves. At low energies, the excitations in YIG resemble that of a ferromagnet. The well-mastered growth of thin films, either by liquid phase epitaxy [16, 17, 18] or by pulsed laser deposition [19, 20, 21], so far prevents other materials from competing. Surprisingly, there are recent reports on spin propagation across micrometers in paramagnetic insulators with a larger spin conductivity than YIG [22]. These results challenge the conventional view of spin transport, and further elucidation of its fundamental origin should be considered.

Spin Injection and Detection in Magnetic Insulators

Insulators, in contrast to their metallic counterparts, have no (polarized) conduction electrons that can inject, detect or transport spin angular momentum. The absence of this simple link between charge and spin requires other couplings to the magnetic system. Spin insulatronics aims to deliver, control and eventually measure electric signals associated with spins in insulators. FIG.1 provides a summary of the five interconversion processes that one could use in insulators to inter-convert the spin information with another signal type: inductive, magneto-optical, magneto-elastic, magneto-electric, and spin-transfer processes. All of them have been envisioned, but so far, in spin insulatronics, most reported measurements have used electric current-driven spin current injection and detection. Before focusing on the latter, we present alternative means, including strain, light, electric and magnetic fields.

The classical way to excite and detect spin waves is inductive coupling. However, this approach has shortcomings when applied to the microscopic scale exploited by spin. The spatial resolution of the nano-patterning technology exploited to fabricate the microwave antenna limits the smallest wavelength that can be excited and detected [23]. In practice, the resolution limit is in the sub-micron range. Therefore, the inductive scheme only addresses spin-waves with energies that are orders of magnitude below thermal magnons. More importantly, the coupling is a volumetric effect. The wavelength mismatch between the microwaves and spin waves makes the process inherently inefficient to detect spin-waves in thin films [24], implying either poor sensitivity or inability to induce large power excitation.

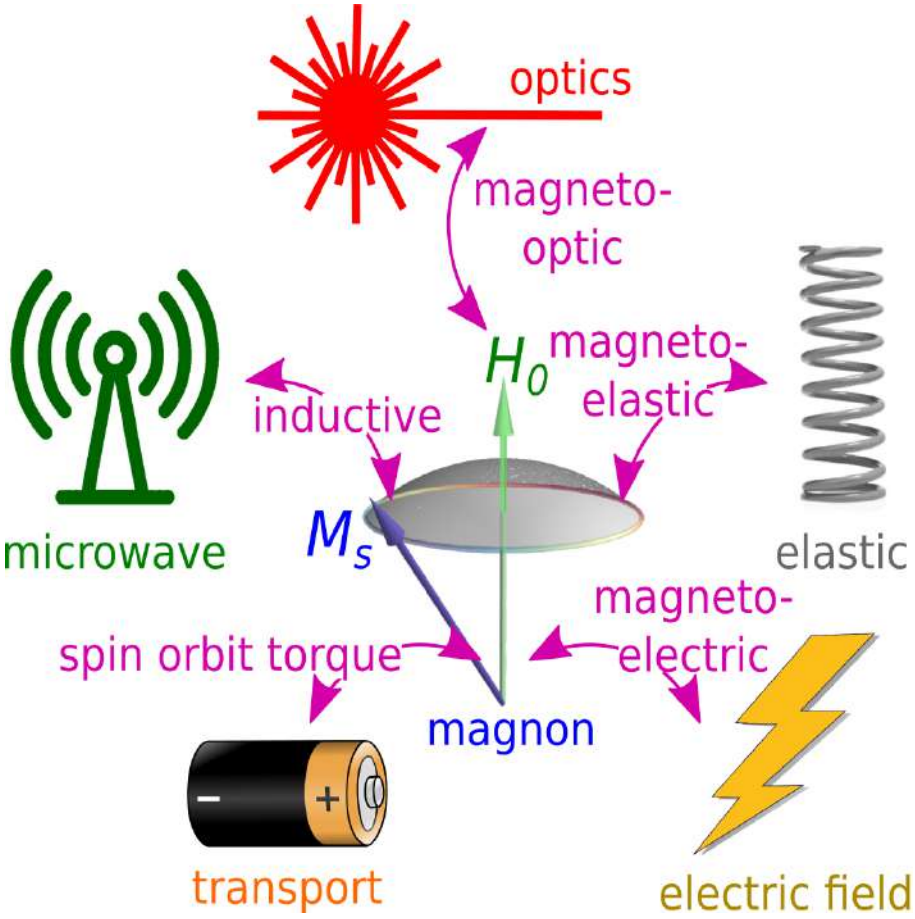

Figure 1: *There are different ways to control the spin in magnetic materials. Inductive coupling with microwaves, elastic vibrations, optical irradiations, and electric field causing a torques on the magnetic moments exerted by the spin-orbit-torque effect.*

Applying strain is a gripping handle for controlling magnetic excitations. Magnetostriction is very common in magnetic materials [25]. In antiferromagnets, a strain can also couple to the Neel vector through the linear magnetoelastic coupling [26, 27]. The ability to trigger collective excitations using magneto-elastic coupling [28] and the interconversion into elastic waves [29] through interdigitated piezo-electric transducers is an alternative way to detect angular momentum [30, 31]. There are also demonstrations of spin pumping in YIG using acoustic waves providing an electrically tuneable source of spin current [32], albeit at rather low frequencies (MHz). The use of magnon polaron processes [33] enables the investigations of high-frequency spin transport in ferromagnetic materials. Moreover, the development of high-frequency coherent shear acoustic waves [34] has opened opportunities for coupling magnons in antiferromagnets with acoustic phonons [35, 36].
The issue of weak coupling to the magnetic information is the soft spot of magneto-optical techniques [37, 38]. Nevertheless, there was a recent demonstration of the hybridization of whispering gallery optical modes with walker spin-wave modes propagating at the equator of a YIG sphere [39]. The development of ultra-fast light sources has enabled triggering and detecting magnetic excitations in ferromagnets in the time domain. This control is achieved using ultra-fast femtosecond lasers [40] in a pump-probe fashion, through different interactions. Ultra-fast shock wave generation [41, 42] can generate magnons, either directly inside the material of interest or help with a thin layer of transducer material [43]. It is also important to mention the injection of spin currents by ultra-fast demagnetization

[44] or the even more direct inverse Faraday effect [45, 46, 47]. Another photo-induced mechanism is the ultra-fast change of anisotropy used for triggering spin waves in NiO [48, 49], as well as the direct torque induced by the magnetic component of THz monocycle pulses [50]. Noticeably, many of the pump-probe studies are on bulk insulators because optimal dynamical properties require the low damping obtained when electrical currents cannot flow, and signals from the magnetic excitations often require a significant sample volume. Thus, measurements carried out in thin films in the framework of spintronics and magnonics remain scarce. Moreover, precise control of the spin wave emission using these techniques is currently lacking.

In materials where magnetic and electric order are intrinsically coupled, pure electric fields can enable the electric control of their magnetic properties. Such magneto-electric phenomena have been at the center stage since the turn of the century [51]. These 'multiferroic' compounds have rich physics and are potentially appealing for applications, especially when they are ferromagnetic and ferroelectric [52]. A significant magneto-electric coupling between the two order parameters allows for magnetic manipulation of the ferroelectricity or, conversely, electrical control of the magnetic order parameter [53, 54]. A common of expressing this coupling is by introducing terms in the free energy coupling the polarization and the magnetization. There can be linear or quadratic couplings [55]. Surprisingly, the dynamical properties of the magneto-electric coupling and its utilization in the design of magnonic structures are underexplored. Conceptually, it has been shown that magnons in magnetoelectrics can be hybrid entities because of their coupling to the electric order [56, 57]. In principle, one can envision that electric fields can launch the resulting 'electromagnons' to generate and control magnonic transport at the micron scale, a feature not yet demonstrated. In any case, the magnetoelectric effect could be very useful in the field of spin insulatronics, particularly to address and control antiferromagnets for which magnetic fields are inoperable.

Recently it has been shown that spin transfer and spin-orbit effects allow injecting an external spin current through the interface from an adjacent non-magnetic layer [58]. This method provides direct electric control of spin transport and has overcome many limitations of earlier established routes. Electric currents passing through conductors can generate pure spin signals. In metals with a significant spin-orbit interaction like Pt and W, the spin Hall effect converts a charge current into a transverse spin current [59]. The generated spin current is :

$$\boldsymbol{j}_{ij}^{(s)} = \theta_{\mathrm{SHE}} \boldsymbol{\varepsilon}_{ijk} \boldsymbol{j}_{k}^{(c)} \tag{1}$$

where θ_{SHE} is the spin Hall angle, and ε_{ijk} is the Levi-Civita tensor. The charge current $\boldsymbol{j}_{k}^{(c)}$ is the component that flows along the k direction. The spin current $\boldsymbol{j}_{ij}^{(s)}$ flows along the j direction and is polarized along the i direction. It is the generated transverse spin current that we, in turn, can inject into magnetic insulators. Detection of spin currents is feasible as well. There is a reciprocal effect to the spin Hall effect where a spin current can cause a secondary transverse charge current via the inverse spin Hall effect. In this, so-called inverse spin Hall effect, the generated charge current is proportional to the primary spin current :

$$\boldsymbol{j}_{i}^{(c)} = \theta_{\mathrm{SHE}} \boldsymbol{\varepsilon}_{ijk} \boldsymbol{j}_{jk}^{(s)} \tag{2}$$

Rasbha coupled interfaces [60] or topological insulators like Bi_2Se_3 also facilitate an analogous spin-charge coupling [61]. A spin Hall magnetoresistance, the dependence of the resistance in metals on the magnetic configuration of adjacent insulators, can probe the ferromagnetic order [62, 63]. Spin angular momentum can flow from metals to magnetic insulators or in the opposite direction via the exchange coupling at the metal-insulator

interfaces. At these connections, the energy depends on the relative orientation of the localized and the itinerant spins. A disturbance in either of the spin subsystems can, therefore, propagate from metals into insulators and vice versa. In the metal, spin-polarized transport or spin-orbit coupling together with charge transport can cause the spin imbalance, resulting in a spin-transfer torque and spin-orbit torque, respectively. In the spin-transfer torques in ferromagnets, a spin accumulation, resulting, for instance, from the spin Hall effect, is transferred as a torque on the magnetization :

$$\boldsymbol{\tau} = \boldsymbol{a} \cdot \boldsymbol{m} \times (\boldsymbol{m} \times \Delta\boldsymbol{\mu}) \tag{3}$$

Where $\boldsymbol{a}$ is a measure of the efficiency, m is a unit vector along the magnetization direction, and $\Delta\boldsymbol{\mu}$ is the electrochemical potential resulting from the out of equilibrium spin imbalance. The reciprocal effect also exists. A dynamical magnet pumps spin currents to adjacent conductors :

$$j_{iz}^{(s)} = \boldsymbol{b} \cdot \boldsymbol{m} \times \frac{\delta \boldsymbol{m}}{\delta t} \tag{4}$$

While spin-transfer torque is the reciprocal effect, in insulators, it has turned out easier to measure the former effect. In ferromagnets, a broad range of experiments on a variety of systems have unambiguously established spin-pumping [64, 65, 66, 67, 68, 69, 70, 71, 72]. Until now, there are no direct demonstrations of spin-pumping from antiferromagnet insulators (due to their very high resonant frequencies). Theoretically, spin-pumping is predicted to be as strong from ferromagnetic insulators [73] as from ferromagnetic metals [74, 75, 76]. This essential mechanism should, therefore, be robust.
Spin-transfer and spin-orbit torques provide new avenues to alter the magnon energy distribution in insulators [77, 78, 79]. However, the generation of magnons in these ways lacks frequency selectivity, and, therefore, can lead to excitations in a broad frequency range [80, 81]. This lack of discernment poses a challenge in identifying the spin-wave modes that are propagating the spin information. Although the selection rules of spin transfer effects seem insensitive to the spatial pattern, the spin transfer efficiency increases with decreasing magnon frequency [82]. The energy transfer relies on a stimulated emission process [83, 84]. By favoring the spin wave eigenmodes with the most substantial fluctuations, spin-transfer targets preferentially the modes with the lowest damping rates, the lowest energy eigenmodes since the relaxation rate is proportional to energy [81, 85]. The situation is different for spin-waves excited by thermal heating, where the excitations predominantly consist of thermal magnons, whose number overwhelmingly exceeds the number of other modes at a finite temperature [86, 87]. Additional opportunities arise from the improved efficiency of the spin transfer process. Insulating magnetic materials are particularly promising since they have exceptional low damping. Indeed, the relevant threshold quantity is the amount of external spin density injected relative to the linewidth. Using spin transfer on insulators gives a unique opportunity to probe non-equilibrium states, where new collective quantum states are expected to emerge, such as Bose-Einstein condensation at room temperature [88, 89]. It is important to recall that nonlinear processes are responsible for energy-dependent magnon-magnon interactions, which leads to threshold effects such as spin-wave instabilities [90]. It is possible to describe such effects as turbulences, most well-known as the mechanism behind the saturation of the Kittel mode or the rapid decay of coherent spin waves into incoherent motions [91]. As a consequence, they alter the energy distribution of magnons inside the magnetic body. These processes should conserve both energy and angular momentum. Thus, a critical parameter that controls magnon-magnon interactions is confinement. By lifting the degeneracy between modes through finite size effects, it is possible to limit the possibility of finding quasi-degenerate modes (i.e., within the linewidth) available at the

first harmonics, which substantially increases the nonlinear threshold values. In closed geometries (e.g., nano-pillars), when confinement lifts the degeneracy between the spin-wave modes, spin-transfer processes generate large coherent GHz-frequency magnon dynamics. There, a single mode tends to dominate the dynamics beyond the damping compensation threshold current. This selection enables controlling the amplitude. The demonstrations of current-induced torques affecting the magnons in Yttrium iron garnet [80, 85, 92, 93] use this feature.

Spin Transport and Manipulation in Magnetic Insulators

Transport of spin information is possible in many materials including metals [94], semiconductors [95] and 2D materials such as graphene [96]. In these materials, the conduction electrons mediate the spin flow. However, disturbances of localized spins can also propagate and carry spin information. Remarkably, it is possible to transport spin angular momentum over distances as large as 40 micrometers in Yttrium iron garnet [2] and as far as 80 micrometers in hematite [3]. The magnon diffusion length is around ten micrometers at room temperature in YIG [2, 97].
The incoherent magnon transport in insulating materials such as YIG is dominated by thermal magnons whose number overwhelmingly exceeds the number of other modes at finite temperature. This is demonstrated in the Spin Seebeck effect [98], where a transverse voltage in a Pt electrode fabricated on a YIG layer develops as a result of thermally induced magnon spin transport. This process can also be reversed [2, 99] and can be used for electrically driven magnon spin injection. In the so called non-local geometry, a charge current through the Pt injector strip generates an electron spin accumulation at the Pt|YIG interface via the spin Hall effect. Exchange processes across the interface result in a magnon spin accumulation and a non-zero magnon chemical potential. This drives magnon diffusion at the detector electrode, the resulting non-zero magnon chemical potential drives an electron spin current in the Pt and converted into an electrical voltage via the inverse spin Hall effect. By varying the spacing between the injector and detector electrodes a typical magnon spin relaxation length of 10 micrometers at room temperature could be determined [2]. This was confirmed by simultaneously measuring the effects of electrical as well as thermal magnon injection. The spin Seebeck effect under the injector electrode gave rise to the latter effect. This effect has also been used to control damping [100] and even to generate auto-oscillations of magnetization [101]. This and consecutive experiments [102] confirmed that in addition to driving a magnon spin current by a temperature gradient, the magnon chemical potential plays a crucial role in driving magnon currents in magnetic insulators. The universality of this non-local technique has been shown recently for the study of thermal magnon transport in the most ubiquitous antiferromagnet α Fe_2O_3, where magnon spin relaxation lengths of typical 10 micrometers were observed at temperatures of 200 K [3]. Magnon modes with frequency of tens of GHz, or as large as 0.5 THz can carry spin information over micrometers. Importantly, this result demonstrates the suitability of antiferromagnets to replace currently used components. These developments open the door towards exploring a wider class of materials with a richer physics. The non-local geometry was also used to demonstrate that the anomalous spin Hall effect and its inverse in conventional ferromagnets such as Py can be used as efficient spin injectors and detectors in YIG and other non-magnetic materials. The efficiencies are comparable to that of heavy metal Pt. An advantage is that a magnetic field controls the polarisation direction of the perpendicularly injected spins [103].

The pioneering report of Kajiwara et al [8] addressed, for the first time, experimental

proof of excitation and detection of propagative spin waves in YIG film interconverted by the SHE. This opened the possibility of an all-electrical manipulation of magnon in an insulator base ferrimagnet above a threshold current injection. At that time, the reported propagation length of the spin waves exceeded mm distance which triggered a large renewed interest into YIG. The experiments which were operated in a quite thick film (1.3 μm) could not be reproduced. Subsequently came the work of Cornelissen et al [2], where spin angular momentum transport over tens nm/μm distances in thick YIG was reported and was confirmed by Goennenwein et al [104]. The thermal nature of the traveling spin was clearly identified by studying the decay of the spin signal with the distance between the two spin Hall probes. This thermal spin waves transport was characterized by a linear voltage drop with the current. The smaller thickness (200 nm) of the magnetic film and the low current regime could only produce thermal spin waves [105]. An important breakthrough in the field of insulatorics was the fabrication of high quality low damping epitaxial YIG ultra-thin film by liquid phase epitaxy [20]. It was demonstrated [106] that, in these thin films, full compensation of the magnetic damping can be reached through the action of the spin-orbit torque in an adjacent metal layer. It enables the excitation of low-energy spin waves and thus coherent information [92].
This thesis work focuses on spin waves manipulation in ultra-thin YIG films through non-local measurement. In this manuscript, I will provide experimental measurement on the nature/characteristic of excited magnons for large applied torque and investigation of the spin transfer mechanisms at high energy/temperature in magnetic insulator and try to solve the controversy of Kajiwara [8] and Cornelissen [2] experiments.

This manuscript is organized into six chapters :

Chapter 1 sets the basis of the theoretical concepts on magnetization dynamics and properties of spin waves in thin films. The fundamental aspects of spin current will be presented and a phenomenological picture of the spin Hall effect, spin Hall magnetoresistance and spin Seebeck effect will be provided. It will help to set up a bridge between spin current and spin wave which is the main framework of magnonic spintronics.

Chapter 2 will be dedicated to the magnetic characterization of ultra-thin LPE YIG films and a large presentation of non-local measurements. After presenting the static and dynamics properties of those films, we will focus on the non-local measurement of propagating spin waves and will lay the basis of the measurement. Finally, we will present results on the investigation of YIG|Pt interface subject to a local heating by Joule effect and will cover the main mechanisms of the spin transfer.

Chapter 3 focus on the spurious electrical properties of LPE YIG films, which should be viewed as large gap semiconductors at high temperature. We will emphasize the impact of this characteristic on the non-local spin transport and provide a simple method to subtract the contribution of electrical leakage in YIG. Out-of-plane measurements in non-local geometry at high temperatures will be presented and we will show that the signal observed in this geometry is compatible with a thermal Hall effect.

Chapter 4 describes the main result of the non-local measurements in the strongly out of equilibrium regime. Especially we observe a shift from linear to non-linear spin conductance around a crossover threshold current and we will try to prove the origin of those signals. We will also investigate the magnon transport in perpendicular magnetic anisotropy (PMA) Bi-doped YIG thin film made by pulsed laser deposition. The spatial spectroscopy of the excited spin waves will be studied and comparison with the analytical model will be given. We will show PMA magnetic insulators are particularly interest-

ing for long distance magnon transport because of the compensation of self-localization effect, preventing large magnon diffusion length in in-plane anisotropy magnetic insulator.

Chapter 5 will cover the spin transport at low temperature and we will attempt to provide the main ingredients governing the observed features in the strong out-of-equilibrium regime. The purpose of this chapter is to observe the behavior when the spurious electronic conduction is frozen out and deduce the role of the temperature in the non-local magnon transport.

Chapter 6 is a comparative study on the same device of the local and non-local transport properties before and after putting an Al cap layer on the top of the injector/detector. The purpose of the Al cap layer is to change the amplitude of the thermal gradient while keeping all the other parameters identical. This allows separating effects that should be ascribed to the current density to effects that should be ascribed to thermal gradients. We see that this capping as an influence on the non-local signal and can also shift the spin signal drop. Besides we observed that the Al capping can dramatically change the temperature profile in the YIG film and thus can tune the spatial distribution of thermal magnon in YIG. An analytical model will be provided to explain the experimental results.

Thereafter, a conclusion and perspectives of this work will be given.

Chapter 1

Fundamental concepts

In this chapter, we will focus on the theoretical background necessary to understand the content of this thesis. We will first focus on how localized magnetic moments can transport spin information through spin waves. We will characterize spin waves specific propagation properties through their dispersion relation, which is sensitive to the orientation of the wavevector compared to the magnetization direction well as the boundary conditions. We will be interested in particular to the propagation of spin waves in thin films inside the so called magneto-exchange regime. We will briefly mention the non-linear regime, which is reached at large excitation energy.
We will also develop in general the problematic of spin transport in metal, spin conversion at magnetic insulator/spin-orbit metal interfaces and the effect of a spin polarized current on the magnetization dynamics toward the concept of spin superfluity. Via several phenomena such as the spin Hall effect, spin pumping and the spin Hall magnetoresistance, we give a complete description of the tools box that has been used to induce, modulate and detect spin waves in ferrimagnetic insulator through the interconversion with an electrical current flowing in an adjacent metallic layer.

1.1 Magnetization dynamics

1.1.1 Fundamental magnetic interaction

Elementary magnetic moment μ_m can be defined as intrinsic angular momentum of electrons coupled to a nonzero spin and is at the origin of magnetic properties. Ferromagnetic materials are composed of many atoms that possess magnetic moments. Below critical temperature known as the Curie temperature T_c, spin are coupled via exchange and tends to align with each other resulting in a net non-zero total magnetic moment leading to a spontaneous magnetization M(μ_m per unit volume). Magnetic order in such materials are ruled by self-energies. In the following we will be interested in the dynamical behavior of magnetic thin film that have been grown along the [111] direction (see FIG.2).

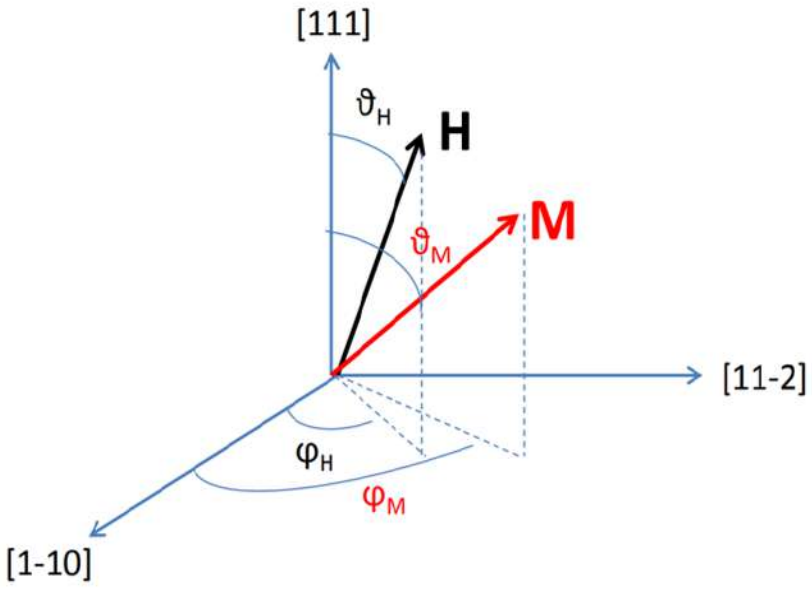

Figure 2: *Representation of the magnetization* $\boldsymbol{M}$ *inside the magnetic films grown along the [111] direction, and internal field* H *in a spherical coordinate system define by* ϑ_{H_0},φ_{H_0} *and* ϑ_M,φ_M.

To describe how these interactions affect the resulting magnetization M, we define the coordinate system presented in FIG.2. The applied field $\boldsymbol{H_0}$ is described with the general spherical coordinates ϑ_{H_0},φ_{H_0} and the equilibrium position of the magnetization M is represented with the angle ϑ_M,φ_M. The total energies can be composed of different terms [107, 9]:

- **Exchange energy:**
  If we consider a two electrons system, due to the Pauli exclusion principle, the mean energy of the electrostatic interaction of the system will depend on the orientation of the spins. It means that the total energy of the spin system will vary depending on the parallel or anti-parallel alignment of the spins. The difference in energy between these two configurations is called the exchange energy and is the main contribution of magnetic ordering.
  According to the Heisenberg model, the Hamiltonian of the exchange interaction

generalized for an n-electrons system can be written in the form :

$$\mathcal{H}_{\text{ex}} = -\frac{2}{\hbar^2}\sum_{i\neq j}^{n} J_{i,j}^{\text{ex}}\mathbf{S}_i \cdot \mathbf{S}_j \tag{1.1}$$

where $J_{i,j}^{\text{ex}}>0$ is the exchange constant between the i$^{\text{th}}$ and j$^{\text{th}}$ spins. A positive $J_{i,j}^{\text{ex}}$ means that the exchange energy favors a parallel alignment of the neighbor spins which is the primary cause of the ferromagnetism.
The energy of this short distance interaction can be calculated over the nearest neighbors magnetic atoms. In the semi-classical model the exchange energy is express as :

$$F_{\text{ex}} = -2\sum_{i>j} J_{i,j}^{\text{ex}}\mathbf{S}\cos\vartheta_{i,j} \tag{1.2}$$

with $\theta_{i,j}$ been the angle between the magnetic moment of the spin $\mathbf{S}_i$ and $\mathbf{S}_j$. Through a Taylor series expansion, the above equation can be written as :

$$F_{\text{ex}} = \frac{A_{\text{ex}}}{M_s^2} V\,(\nabla \cdot \boldsymbol{M})^2 \tag{1.3}$$

where A_{ex} is the exchange constant (material depend), M_s is the saturation magnetization and V the volume. The exchange energy is minimized when the neighbor magnetic moments are aligned.

- **Demagnetizing field:**
  If we consider a magnetic object, the internal field H in the media can be different from the applied filed H_0. Due to surface charges, a demagnetized field $\mathcal{H}_d = -N_i M$ $(i = x, y, z)$ is produced with a direction opposite to the internal magnetization with N_i the demagnetize factor. This interaction tens to reduce the total magnetic moment in magnetic materials. In thin film the demagnetization factor can be expressed as $N_x = N_y = 0$ and $N_z = 4\pi$. The demagnetization energy in this case can thus be written:

$$F_d = -2\pi M_z^2 \sin^2\vartheta_M \tag{1.4}$$

- **Zeeman energy:**
  When an electron is subject to an external magnetic field H_0, the energy of the electron is split into sub-energy levels due to the intrinsic magnetic moment. This phenomena is called the Zeeman splitting. The Zeeman interaction can be characterized by the following Hamiltonian :

$$\mathcal{H}_z = -\mu_0 \boldsymbol{M} \cdot \boldsymbol{H_0} \tag{1.5}$$

  Thus the energy of the magnetic body associated with the Zeeman interaction can be express as :

$$F_z = -M_s H_0[\sin\vartheta_{H_0}\sin\vartheta_M\cos(\varphi_{H_0}-\varphi_M) + \cos\vartheta_{H_0}\cos\vartheta_M] \tag{1.6}$$

- **Magnetocrystalline anisotropy:**
  Intrinsically, crystal possesses an easy and hard magnetic axis. The magnetocrystalline anisotropy describes the tendency of the magnetization to align with the

easy crystallographic direction. If one want to magnetize a magnetic crystal along it hard axis, an energy F_{anis} has to be overcome. In the case of uniaxial and cubic anisotropy, this energy can be written as :

$$E_{\text{anis}} = K_U \sin^2 \vartheta_M + K_1[\frac{1}{3}\cos^4 \vartheta_M + \frac{1}{4}\sin^4 \vartheta_M - \frac{\sqrt{2}}{3}\sin^3 \vartheta_M \cos \vartheta_M \sin 3\varphi_M] \quad (1.7)$$

with K_U the uniaxial perpendicular anisotropy constant and K_1 first-order cubic anisotropy constant.

The total energy $\boldsymbol{F}$ is the results from the combination of magnetic interactions such as :

$$\boldsymbol{F} = \boldsymbol{F}_{\text{ex}} + \boldsymbol{F}_{\text{d}} + \boldsymbol{F}_{\text{z}} + \boldsymbol{F}_{\text{anis}} \quad (1.8)$$

the equilibrium orientation of the magnetization vector can be found by minimizing the energy :

$$\boldsymbol{F}_\vartheta = \frac{\partial \boldsymbol{F}}{\partial \vartheta} = 0 \qquad \boldsymbol{F}_\varphi = \frac{\partial \boldsymbol{F}}{\partial \varphi} = 0 \quad (1.9)$$

1.1.2 Landau-Lifshitz-Gilbert equation

When an external bias magnetic field is applied to a magnetic material, magnetic moments μ_m will feel an effective field $\boldsymbol{H}_{\text{eff}}$ that can be define as:

$$\boldsymbol{H}_{\text{eff}} = -\frac{\partial \boldsymbol{F}}{\partial M} \quad (1.10)$$

Inner to the kinetic motion of the magnetic moments, $\boldsymbol{\mu}_m$ will not align directly along the magnetic field but will instead experience a torque :

$$\boldsymbol{\tau} = \boldsymbol{\mu}_m \times \boldsymbol{H}_{\text{eff}} \quad (1.11)$$

However, we can express the magnetic moment $\boldsymbol{\mu}_m$ in terms of angular momentum $\boldsymbol{J}$:

$$\boldsymbol{\mu}_m = -\frac{g\mu_B}{\hbar}\boldsymbol{J} = -\gamma \boldsymbol{J} \quad (1.12)$$

where g $\simeq$ 2 is the Landé factor, μ_B the Bohr magneton whereas γ referred to the gyromagnetic ratio. Knowing that $\boldsymbol{\tau}$=d$\boldsymbol{J}$/dt, we can express :

$$\frac{d\mathbf{J}}{dt} = -\frac{1}{\gamma}\frac{d\boldsymbol{\mu}_m}{dt} = \boldsymbol{\mu}_m \times \boldsymbol{H}_{\text{eff}} \quad (1.13)$$

Considering whole magnetic volume V_f, we can replace the atomic magnetic moment by the macroscopic magnetization $\boldsymbol{M}$ resulting :

$$\frac{d\boldsymbol{M}}{dt} = -\gamma \boldsymbol{M} \times \boldsymbol{H}_{\text{eff}} \quad (1.14)$$

This expression is known as the Landau-Lifshitz equation (LL) and describes the precessional motion of the magnetization (also referred as the Larmor precision) around effective

magnetic field. However, the Landau-Lifshitz description implies a non-dissipative motion of the magnetization and thus a perpetual precession. Nonetheless, LL equation fails in describing the magnetization dynamic in real systems because of the magnetization motion is always influence by magnetic losses. Due to non-conservative coupling, the magnetization will always tend to be parallelly aligned with the effective magnetic field. In order to simulate real systems, Gilbert introduced a phenomenological damping term to the Landau-Lifshitz equation that acts locally on the magnetization [108]:

$$\frac{d\boldsymbol{M}}{dt} = -\gamma \boldsymbol{M} \times \boldsymbol{H}_{\text{eff}} + \alpha \frac{\boldsymbol{M}}{M_s} \times \frac{d\boldsymbol{M}}{dt} \tag{1.15}$$

where α>0 stands for the dimensionless Gilbert magnetic damping parameter and is analog to viscous damping. The equation (1.15) known as the Landau-Lifshitz-Gilbert equation (LLG) describe the magnetization relaxation in a spiral motion within a time scale in the order of $1/\alpha\gamma H_{\text{eff}}$.

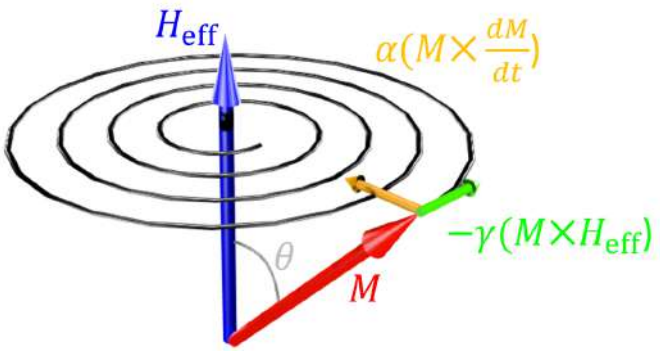

Figure 3: *Schematic representation of the magnetization relaxation around an effective field $\boldsymbol{H}_{eff}$ described by the LLG equation. The precessional motion is provided by the torque $-\gamma \boldsymbol{M} \times \boldsymbol{H}_{eff}$ while the Gilbert damping term $\alpha \times \frac{d\boldsymbol{M}}{dt}$ forces the magnetization to align along the effective field. The θ angle between the effective magnetic field and the magnetization is referred to the precession cone angle.*

Note that the constant of the motion, $\boldsymbol{M}$, is the saturation magnetization measured at the temperature of the experiment and counts the number of thermals magnons. Being a constant of the motion, it assumes that the excitation of Kittel mode is decoupled from the thermal bath.

1.1.3 Ferromagnetic resonance

Resonance is a phenomenon describing the property of a physical system to accumulate energy. Close to the natural "resonance frequency", the system will oscillate with an amplitude larger than the out of resonance frequency condition.
Suppose that a magnetic system is subject to an external source of electromagnetic waves with a defined frequency. The whole spin system can enter in resonance when the Fermi golden rule is satisfied, also called the Larmor condition. The magnetic resonance phenomena is a large topic, going from Nuclear Magnetic Resonance (NMR) to the Electron Paramagnetic Resonance (EPR) [109]. Those resonance results from the absorption of a resonant photon by the spin system which can flip individual spin. In the case of a

ferromagnetic material, the exchange coupling prevents the electromagnetic wave to flip the spin system. Instead, if the micro-wave field $\boldsymbol{h}$ is oriented perpendicularly to the effective field $\boldsymbol{H}_{\text{eff}}$, it produces a torque that acts on the magnetization dynamics. If this additional motion matches with the natural Larmor precession in term of amplitude and frequency, the system becomes resonant and lead to a steady state of the magnetization motion monitored by the external microwave field and counteract the natural damping torque. This leads to high absorption of microwave energy into the magnetic system at the resonance condition of the ferromagnet. This effect is referred to the Ferromagnetic Resonance (FMR).

Magnetic susceptibility:

To describe the response of the magnetic system to the applied microwave field, we consider a magnetic object with an initial magnetization $\boldsymbol{M_0}$ and effective field $\boldsymbol{H_0}$ under microwave field $\boldsymbol{h}$. The total effective magnetic field and the magnetization in that case will express as the sums :

$$H_{\text{tot}} = H_{\text{eff}} + h(r,t) \qquad M_{\text{tot}} = M_0 + m(r,t) \tag{1.16}$$

were $h(r,t)$ and $m(r,t)$ are the dynamic component resulting from the microwave field. We assume that the microwave field is relatively small compared to the effective field :

$$h(r,t) \ll H_{\text{eff}} \qquad m(r,t) \ll M_0 \tag{1.17}$$

By inserting (1.16) to the LLG equation, in the first approximation we obtain :

$$\frac{d\,\boldsymbol{m}(r,t)}{dt} + \gamma\,\boldsymbol{m}(r,t) \times \boldsymbol{H}_{\text{eff}} = -\gamma\,\boldsymbol{M_0} \times \boldsymbol{h}(r,t) + \alpha\frac{\boldsymbol{M}}{M_s} \times \frac{d\,\boldsymbol{m}(r,t)}{dt} \tag{1.18}$$

This equation leads to the expression of the magnetic response under a microwave field. We solve this equation by introducing the $\boldsymbol{h}$ and $\boldsymbol{m}$ component in the frequency domain :

$$h(r,t) \Rightarrow h(k,w)e^{i(\mathbf{k}.\mathbf{r}-wt)} \qquad m(r,t) \Rightarrow m(k,w)e^{i(\mathbf{k}.\mathbf{r}-wt)} \tag{1.19}$$

Thus the equilibrium response of the magnetic system to the perturbation $\boldsymbol{h}$ can be expressed as :

$$m(k,w) = \overleftrightarrow{\chi} h(k,w) \tag{1.20}$$

were the high-frequency magnetic susceptibility tensor $\overleftrightarrow{\chi}$ is called the Polder tensor is:

$$\overleftrightarrow{\chi} = \begin{pmatrix} \chi & i\,\chi_a & 0 \\ -i\,\chi_a & \chi & 0 \\ 0 & 0 & \chi_{||} \end{pmatrix} \tag{1.21}$$

Kittel law:

For the particular case of k, the electromagnetic power absorbed by the ferromagnetic volume V_f can be expressed as a function of the imaginary part of the Polder tensor χ'' :

$$P_\mathrm{abs} = \int_{V_\mathrm{f}} \frac{\partial M_0}{\partial t} \cdot h dV = w\chi'' h^2 \tag{1.22}$$

with :

$$\chi''(\omega) = \frac{\alpha\gamma M_s \omega_H/2}{(\alpha\omega)^2 + (\omega - \omega_H)^2} \tag{1.23}$$

while $\omega_H = \gamma H_\mathrm{eff}$.
Equation (1.22) and (1.23) implies that the absorption power of the electromagnetic waves is maximum when $\omega = \omega_H$, resulting in ferromagnetic resonance condition. Absorption close to the ferromagnetic resonance is described with a Lorentzian shape $1/(1+x^2)$ and can be seen in FIG.4. The amplitude of this Lorentzian, for parallel alignment of magnetization $\boldsymbol{M}$ and field $\boldsymbol{H}$ in a perpendicular orientation, is inversely proportional to the Gilbert damping α while the full width half maximum is equal to $\Delta H = 2\alpha\omega/\gamma$.

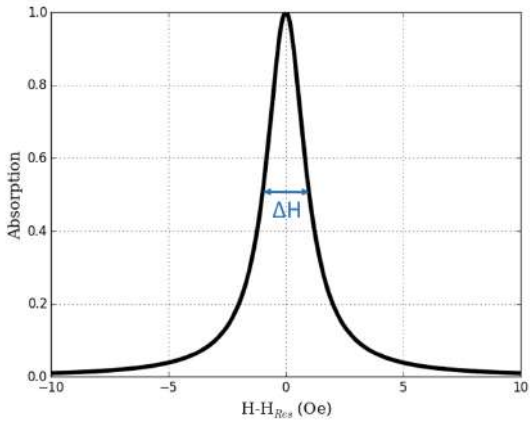

Figure 4: *Plot of the Lorentzian shape, while sweeping field* $\boldsymbol{H}$ *for a fixed* ω.

In order to deduce correctly the ferromagnetic resonance conditions, it is necessary to take into account the difference between the effective field H_eff and external field H_0. For instance in a soft magnetic material like Yttrium Iron garnet, the anisotropy need to be considered. The determination of the ferromagnetic resonance conditions can be calculated according to the Smit and Beljers equation:

$$(\frac{\omega}{\gamma})^2 = \frac{1}{M_s \sin^2\vartheta_M}\left[\frac{\partial^2 F}{\partial\vartheta_M^2}\frac{\partial^2 F}{\partial\varphi_M^2} - (\frac{\partial^2 F}{\partial\vartheta_M \partial\varphi_M})^2\right] \tag{1.24}$$

which is the generalized form of what is called the Kittel law.

1.1.4 Spin waves

Up to now, we only considered a local and coherent precession of the magnetization also qualified as the FMR mode. This consideration supposed that the magnetization is uniform and homogeneously distributed throughout the whole magnetic volume. However,

in a case of a non-uniform dynamic, the spin system can precess at the same frequency but not in phase. Such disturbance of the magnetic system is mentioned as a spin wave or as its quanta: magnon. This quasi-particles can couple with external excitation under specific conditions and even interact with other excited modes that will contribute to the magnetic relaxation process.
In this section, we will determine general dispersion relation for spin-waves, in the approximation of thin films, by considering first the dipolar interactions between the spins and then the exchange interaction.

Magnetostatic spin waves

In the magnetostatic approximation electrics and magnetic variables are static and thus are considered free from each other. This is viable only if the wave vector $\boldsymbol{k}$ of the spin wave is much smaller than the light wave vector $\boldsymbol{k_0}$ and particularly true if the size of the sample is large ($>$ mm). This approximation is described by Maxwell equations :

$$\vec{\nabla} \times \boldsymbol{H} = 0 \tag{1.25}$$

$$\vec{\nabla} \times \boldsymbol{B} = 0 \tag{1.26}$$

with $\boldsymbol{B} = (1 + \overleftrightarrow{\chi})\boldsymbol{H}$ been the magnetic flux density. If we consider a large magnetic volume, the contribution of the dipolar field is higher than the exchange ($k < 2\pi/\lambda_{\text{ex}}$). The effective field can thus be express in term of magnetostatic potential $\boldsymbol{\phi}$:

$$\boldsymbol{H} = -\nabla\boldsymbol{\phi} \tag{1.27}$$

Introducing equation (1.27) into (1.26), we obtain the generalized Walker's equation [110]:

$$\nabla[(1 + \overleftrightarrow{\chi}) \cdot \nabla\boldsymbol{\phi}] = 0 \tag{1.28}$$

Walker's equation describes magnetostatic spin waves in a uniform dipolar field. The solution of this equation will depend on the relative orientation between the wave vector $\boldsymbol{k}$ and the magnetization $\boldsymbol{M}$.

Forward Volume Magnetostatic Spin Wave (FVMSW) :

In a case of a magnetic field $\boldsymbol{M}$ oriented perpendicularly to the film plane and wave vector $\boldsymbol{k}$, the dispersion relation can be approximated by :

$$\omega = \sqrt{\omega_H(\omega_H + \omega_M(1 - \frac{1 - e^{(-kd)}}{kd}))} \tag{1.29}$$

with $\omega_M = \gamma M$ and d the film thickness. Known as the Forward Volume Magnetostatic Spin waves (FVMSW), the resonance frequency increase with the wave vector $\boldsymbol{k}$ (forward character) and converge toward $\omega = \sqrt{\omega_H(\omega_H + \omega_M)}$, with a slope that is mainly determined by the thickness of the sample. One of the main features of FVMSW is that it dispersion is independent of its direction of propagation as long as $\boldsymbol{M}$ and $\boldsymbol{k}$ remain perpendicular because the wave propagates always along the bias field.

Magnetostatic Surface Spin Wave (MSSW) :

In a configuration where the magnetic field is along the sample plane and perpendicular to the wave vector $\boldsymbol{k}$, the dispersion relation takes the form :

$$\omega = \sqrt{(\omega_H + \omega_M/2)^2 - (\omega_M/2)^2 e^{(-2kd)}} \tag{1.30}$$

Also know as the Damon-Eshbach mode [111], Magnetostatic Surface spin Wave (MSSW) is located at one surface of the film and is distributed exponentially along the film thickness. This mode is particularly interesting for the field of magnonic because the surface in which the spin waves propagate can be changed by reversing either polarity of magnetic field or direction of propagation.

Backward Volume Magnetostatic Spin Wave (BVMSW):

Finally, if the magnetic field is oriented in the plane of the magnetic media and parallel to the wave vector $\boldsymbol{k}$, the dispersion relation is:

$$\omega = \sqrt{\omega_H(\omega_H + \omega_M \frac{1 - e^{(-kd)}}{kd})} \tag{1.31}$$

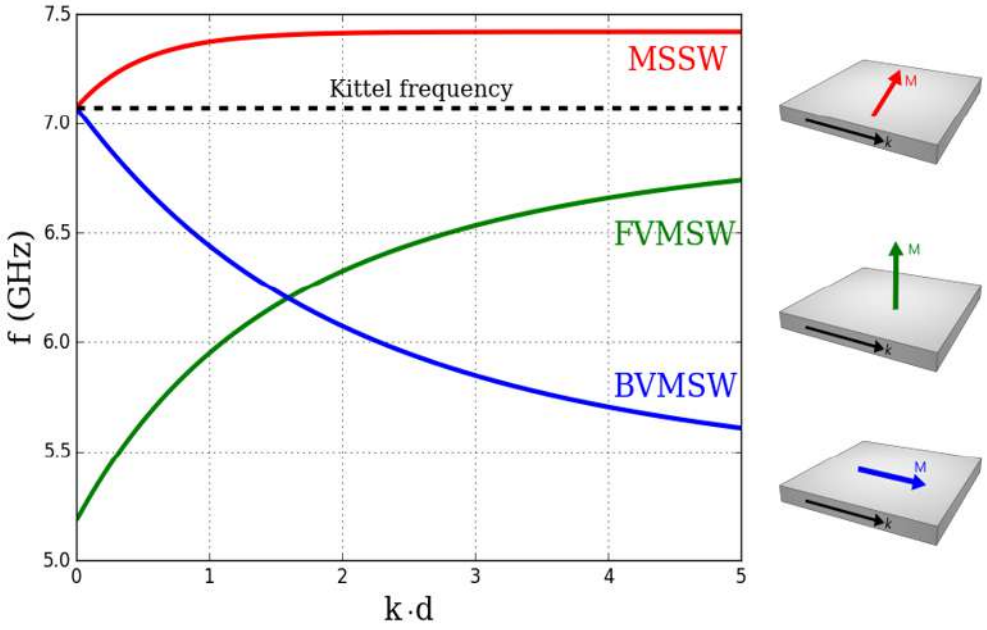

Figure 5: *Dispersion relations of MSSW (red curve), FVMSW (green curve) and BVMSW (blue curve) for $H_0 = 1850\,G$, $M_0 = 1600\,G$ and d=1 μm. The spin wave dispersion relation depend on the relative orientation between the wave vector k and the magnetization. The frequency at $k = 0$ (Kittel frequency) corresponds to a uniform precession.*

The so called Backward Volume Magnetostatic Spin Wave (BVMSW) is a volume

mode, meaning that the amplitude of the magnetization precession is distributed in the thickness of the film in contrast to the case $\boldsymbol{M} \perp \boldsymbol{k}$ where the spin wave is localized near the surface. The exponential component comes from self-depolarization effect in a thin film [112]. For small wave vector $\boldsymbol{k}$, the group velocity of this mode became negative and opposite to its phase velocity. This implies that the group and the phase velocity of the spin waves are counter-acting each other and give rise to a negative slope in the dispersion relation. This regime is of particular interest in this thesis since we need to align the magnetization along the $\boldsymbol{k}$ direction in-plane.

1.1.5 Exchange regime

If the wave vector $\boldsymbol{k}$ become higher that the ratio $2\pi/\lambda_{\text{ex}}$ the exchange interaction is dominant over the dipolar coupling. The dispersion relation in this regime can be expressed has [113]:

$$\omega = \sqrt{(\omega_H + \eta k^2)(\omega_H + \eta k^2 + \omega_M \sin^2 \theta_k)} \tag{1.32}$$

with $\eta = 2A\gamma/M_s$ been the exchange constant and $\omega_H = \gamma(H_{\text{ext}} - 4\pi N_z M_s)$, $\omega_M = \gamma 4\pi M_s$. This relation implies a parabolic curvature of the dispersion relation that results in an enhancement of mode's energy in higher $\boldsymbol{k}$ region. In this regime, due to the short wavelength, we consider the spin waves to propagate in an infinite medium without any limit condition to the magnetic volume V_{f}.

1.1.6 Dipolar-exchange regime

For thin magnetic films, size effects and exchange have to be simultaneously introduced. In Kalinikos and Slavin work [112], such a regime is mentioned as the dipolar-exchange regime. Their main contribution was to have worked out depolarization effects in thin films. This regime is relatively important to understand spin dynamics in thin film because it ensures the transition between the magnetostatic regime and the pure exchange regime and introduces the notion of degenerate magnon band.

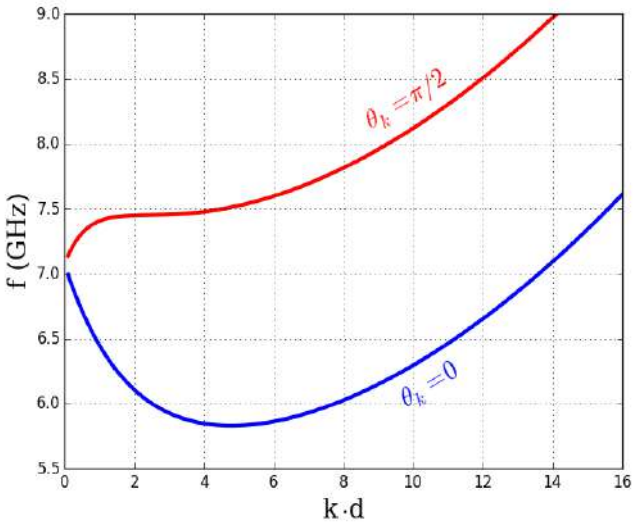

Figure 6: *Dispersion relations of spin waves in the dipolar-exchange regime for $\theta_k = 0$ and $\theta_k = \pi/2$ (in-plane) for a magnetic film with thickness $d = 20\,nm$.*

Taking account the considerations mentioned above, the dispersion relation in the dipolar exchange regime can be written as [114]:

$$\omega = \sqrt{(\omega_H + \eta k^2 + \omega_M(1 - N_z)N_k)(\omega_H + \eta k^2 + \omega_M(1 - N_k)\sin^2\theta_k)} \tag{1.33}$$

with $N_k = (1-e^{-kd})/kd$ and $\theta_{\boldsymbol{k}}$ the angle between the wave vector $\boldsymbol{k}$ and the magnetization. Dispersion relation in the dipolar-exchange regime for an in-plane magnetization thin film is displayed in FIG.6. For large wave vector $\boldsymbol{k}$, the frequency evolves as a parabole and highlights the domination of exchange interaction. However, for short wave vector $\boldsymbol{k}$ range, the dispersion relation presents a particular curvature. This directly implies that magnons can have a similar wave vector $\boldsymbol{k}$ with different direction and magnitude but with similar energies (frequencies). This phenomenon is called a degenerate magnon band, and allows energy transfer between two degenerate magnons via a scattering process [115, 116]. If the magnetization is perpendicular to the film plane, the dispersion relation is no longer dependent on the in-plane orientation of the wave vector, and thus the dispersion relation tends to pure magnetostatic waves.

1.2 Non-linear regime

Until now, it was implicitly assumed that low power was used to probe the system. At large power, the magnetic system deviates into a non-linear regime. This is coming from the fact that the internal field, which depends on the static component of the magnetization because of dipolar effect, may vary with power (see eq (1.4)). The static component is just the component of the magnetization projected on the equilibrium axis. Clearly, this value decreases as the cone angle increases. As a rule of thumb, non-linearities start to become important when the change of internal field is of the order of the linewidth. It thus occurs quite prematurely in low damping materials.

1.2.1 Magnetic relaxation mechanisms

Many mechanisms are responsible for the magnetic relaxation and result from the coupling between the spin system and its environment. In magnetic insulators, the absence of conduction electron prevent the large contribution of the magnon-electron scattering in the relaxation and is one of the main reason of the low magnetic loss of YIG. Apart from the electronic coupling, the spin waves can couple to the thermal bath (intrinsic damping) through phonon. These processes result in an energy transfer of the uniform and nonuniform spin waves modes to the lattice by creating a phonon. This phenomenon is often induced via magnetic impurities or lattice mismatch (extrinsic damping). On the other hand, magnon-magnon interactions can largely affect the magnetic relaxation. In that matter, we can mention the Kasuya-Le Craw mechanism, where a three magnon scattering cushions the coherent mode through phonons or thermal magnons [117]. Other mechanisms like two or four-magnons scattering couple the uniform mode with degenerate magnon. This is particularly true for in-plane magnetized thin magnetic film because of the magnon manifold which provides a degenerate magnons band. This relaxation mediates an energy redistribution of the FMR mode toward other spin wave modes. This mechanism will be relatively important to understand the spin waves transport in YIG at high energy.

1.2.2 Foldover

The first non-linear effect is the so-called foldover effect. This is a very generic feature of any non-linear system. Providing enough radio frequency field to a uniform precession mode make the magnetization $\boldsymbol{M}$ tilted such that a cone angle θ is open between $\boldsymbol{M}$ and the effective field. The higher external perturbation is, the cone angle becomes more pronounced. Although for large processional angle the longitudinal component of the magnetization M_z decreases as (1-cos θ) for the Kittel mode which induce a variation of the demagnetization field and thus shift the resonance frequency. For a uniform mode, the resonance frequency can be express as a function of the cone angle :

$$\omega_{\text{res}} = \gamma(H - 4\pi M) + 2\pi\gamma M\theta^2 \tag{1.34}$$

were θ is the precession angle of the magnetization. Thus the resonance frequency is power dependant introducing an asymmetry of the lineshape away from Lorentzian shape. When the distortion exceeds the linewidth, hysteretic behavior kicks in.

1.2.3 Sulh threshold

The second effect is the so-called Suhl threshold. They are in principle several Suhl thresholds classified in increasing order of non-linearities. This can be seen as a power expansion of the internal field in terms of magnon's energy. The first is the confluence of three magnons: two magnons of energy $\omega/2$ merge in one magnon at ω. This effect is also called subsidiary absorption. It also corresponds to the known case of parametric excitation. This process depends critically on the ellipticity of the magnetic precession. The next leading term if the four-magnons process. It consists of the confluence of two magnons at energy degenerate with the Kittel frequency and merging to create two new particles of same energy and opposite k-vector. This process is called the four-magnons process and it is responsible for the premature saturation of the main resonance. Those instabilities can be driven by large radiofrequency field h_{rf}. According to the Anderson and Suhl theory [90], the critical threshold field resulting in instability can be written as:

$$h_{\text{crit}} = \Delta H \sqrt{\frac{1.54\Delta H_k}{4\pi M_s}} \tag{1.35}$$

where ΔH is the half power linewidth of $\boldsymbol{k}$ =0 mode, ΔH_k the spin waves linewidth of wave vector $\boldsymbol{k}$ and $4\pi M_s$ the saturation magnetization.
These non-linear phenomena typically prevent an external source to drive the magnetization to large cone angles in extended films.

1.3 Spin transfers at insulating ferromagnet/normal-metal interfaces

1.3.1 Spin current

The spin can be pictured as an intrinsic form of angular momentum and was originally deduce from the Stern-Gerlach experiment [118], where it as been found that the orbital angular momenta have a quantum nature. In a general manner, the transfer of angular

momentum in a magnetic material is called a spin current. If one considers the electron charge degree of freedom $q = -e$ and the spin degree of freedom $s = -\hbar/2$, the electric charge current density can be written as a sum of spin "up" and spin "down" that originates from the two states of the electron spin. Within these two current model introduced by Mott, the current density can be express as :

$$j_q = (j_{q\uparrow} + j_{q\downarrow}) \tag{1.36}$$

with $j_{q\uparrow} = qn_{\uparrow}\mathrm{v}_{\uparrow}$ and $j_{q\downarrow} = qn_{\downarrow}\mathrm{v}_{\downarrow}$ been the spin up (down) current density according to the number $n_{\uparrow}$ ($n_{\downarrow}$) and their velocity $\mathrm{v}_{\uparrow}$ ($\mathrm{v}_{\downarrow}$) flowing through a unit surface.
We can associate to a charge current density a spin current density that is given by difference between the two spin channels :

$$j_s = \frac{\hbar}{2q}(j_{q\uparrow} - j_{q\downarrow}) \tag{1.37}$$

These considerations reflect the nature of j_q that can be considered as a flow of charge carrier and j_s as a flow of angular momentum.
From Ohm's law, the electrical current density can be written as :

$$j_{q\uparrow} = \sigma_{\uparrow}\Delta(\frac{\mu_{\uparrow}}{q}) \qquad j_{q\downarrow} = \sigma_{\downarrow}\Delta(\frac{\mu_{\downarrow}}{q}) \tag{1.38}$$

with $\sigma_{\uparrow\downarrow}$ the spin dependent electrical conductivity and $\mu_{\uparrow\downarrow}$ the electrochemical potential associate to the spin. From these relations, it becomes clear that an imbalance between $\sigma_{\uparrow}$ and $\sigma_{\downarrow}$ or $\mu_{\uparrow}$ and $\mu_{\downarrow}$ will give rise to a net spin current. According to (1.36) and (1.37), we distinguish several scenarios.

Pure charge current

When the flow of spin down is equal to the flow of spin down, it corresponds to a net flow of charge current without any transport of angular momentum. We can define it as *pure charge current*. This is generally the case for paramagnetic metal in the absence of spin-orbit coupling.

Spin-polarized current

In transition ferromagnetic metals such as Ni, Co, Fe and their alloys, the electronic state density energy is influenced by the *s-d* transition probabilities. This induces a splitting of the electronic band into a spin up and spin down subbands at the Fermi level. This splitting induces an imbalance of spin up and spin down and thus a spin dependent conductivity $\sigma_{\uparrow\downarrow}$ (see FIG.7). The difference in conductivity between the two spin channels is expressed by the Einstein formula [119] :

$$\sigma_{\uparrow\downarrow} = e^2 D_{\uparrow\downarrow} n_{\uparrow\downarrow}(E_{\mathrm{f}}) \tag{1.39}$$

with $D_{\uparrow\downarrow}$ the electron diffusion constant that depends on the mobility of the up/down spin. A current that possesses a conductivity that depends on the spin state is referred as a *spin polarized current* and is commonly the case in ferromagnetic conductors.

Pure spin current

If we assume that the spin conductivity from both spin up and down channels are equal, there should have the same spin current density. However, in the case of non-equilibrium electrochemical potential, up and down spin current can flow in opposite direction $j_{q\uparrow} = -j_{q\downarrow}$. It results in a net transport of angular momentum that is not follow up by a charge current. We qualify this flow of angular momentum by a *pure spin current*.

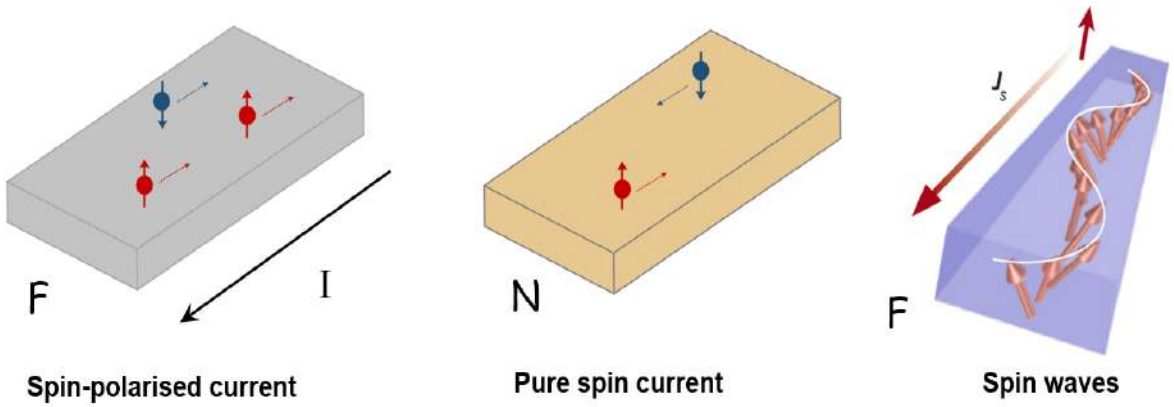

Figure 7: *Schematic picture of a spin-polarized current in a ferromagnet, pure spin current in a strong spin-orbit normal metal, and spin waves in insulating ferromagnet (taken from [8]).*

Magnonic current

Due to the absence of conduction electrons, the angular momentum in magnetic insulators is carried through spin waves, and do not suffer from any electron-magnon scattering. This manuscript focuses mainly on angular momentum transport that is carried through spin waves in magnetic insulators.

1.3.2 Spin transport and spin diffusion

Spin diffusion length

In the following, we introduce the fundamental mechanisms surrounding the spin transport in various materials. Magneto-transport in electronic systems is described through the spin diffusion length λ_{sd}, in which the spin will "flip" it state within a certain characteristic distance. We consider a conduction electron moving at Fermi velocity v_F. Electron will experience multiple collision during its travel that will lead in a "random" change of direction described as Brownian motion. Thus the mean free path λ_e which is the distance traveled by the electron between two collisions can be express by $\lambda_e = \mathrm{v}_F \tau_e$, where τ_e is the characteristic time of a collision event. However during this process, the spin of that one electron is not indefinitely conserved due to the spin-orbit interaction. We can attribute a spin-flip distance λ_{sf}, which is the distance between two "flip" event and is described by a spin-flip time τ_{sf} where $\lambda_{\mathrm{sf}} = \mathrm{v}_F \tau_{\mathrm{sf}} = N\lambda_e$ (N been the average number of collisions that the electron experience between two flip events). The spin diffusion length can then

be written as:

$$l_{\mathrm{sf}} = \lambda_e \sqrt{\frac{N}{3}} \tag{1.40}$$

Taking account of the relation cited above we can develop this expression in :

$$l_{\mathrm{sf}} = \sqrt{\frac{\lambda_{\mathrm{sf}}\lambda_e}{3}} = \mathrm{v}_F \sqrt{\frac{\tau_{\mathrm{sf}}\tau_e}{3}} \tag{1.41}$$

Finally, we simplify this expression by introducing the electron diffusion constant D :

$$l_{\mathrm{sf}} = \sqrt{D\tau_{\mathrm{sf}}} \tag{1.42}$$

where $D = \mathrm{v}_F^2\tau_e/3$. We note that these characteristics are spin-dependent as well, which means that the diffusion is specific to both spin population.

Spin accumulation

An excess of one spin population over another is called a spin accumulation. In two channel model, this accumulation is defined as the difference between local electrochemical potential of the spin up and down :

$$\Delta\mu = \mu_\uparrow - \mu_\downarrow \tag{1.43}$$

This quantity is defined by a vector pointing in the polarization direction of the accumulate spin.
The spin accumulation in the system will then relax through a spin diffusion mechanism that will tend to locally equilibrate the spin populations. The spin current density of the two spin population can be written as :

$$j_\uparrow = \frac{\sigma_\uparrow}{e}\frac{\partial\mu_\uparrow(x)}{\partial x} \qquad j_\downarrow = \frac{\sigma_\downarrow}{e}\frac{\partial\mu_\downarrow(x)}{\partial x} \tag{1.44}$$

where $\sigma_{\uparrow(\downarrow)} = (n_{\uparrow(\downarrow)}e^2\tau_{e\uparrow(\downarrow)})/\mathrm{m}_e$ is the electrical conductivity of each spin channel, with $n_{\uparrow(\downarrow)}$ the number of electrons, $\tau_{e\uparrow(\downarrow)}$ the relaxation time of up and down electrons and m_e the electron mass. The spin current flow can thus be express as :

$$j_s = j_\uparrow - j_\downarrow \tag{1.45}$$

According to the Valet Fert model [120], the spin-diffusion equation is:

$$\frac{\partial^2\Delta\mu(x)}{\partial^2 x} = \frac{\Delta\mu(x)}{l_{\mathrm{sf}}^2} \tag{1.46}$$

The one-dimensional solution of the diffusion equation takes the form:

$$\mu(x) = Ae^{-x/l_{\mathrm{sf}}} + Be^{x/l_{\mathrm{sf}}} \tag{1.47}$$

where the coefficient A and B depend on the boundary conditions. This solution can be used to calculate the spin accumulation at the vicinity of ferromagnet and normal metal

interface. In a case of a spin transparent interface, the electrochemical potential $\mu_\uparrow$ and $\mu_\downarrow$ are continued at the interface which implies $A = B$. In reality, the interfacial spin resistance does not allow a perfect flow of spin current such that only a part of the spin is able to cross the interface. This phenomenon is translated by the concept of spin mixing conductance.

1.3.3 Generation of pure spin current in NM/FMI interface

1.3.3.1 Spin Hall effect

The Hall effect, discovered in 1879, describes the generation of a transverse electric field when a charge current flow in a conductor is subject to an out of plane magnetic field. This phenomenon originates from the Lorentz force which drives the motion of electrons on the sides of the material resulting in an asymmetric distribution of charges density. The magnitude of this effect is directly proportional to the intensity of the magnetic field. In conventional ferromagnet, an additional contribution to the normal Hall effect proportional to the magnetization must be included: the anomalous Hall effect (AHE),

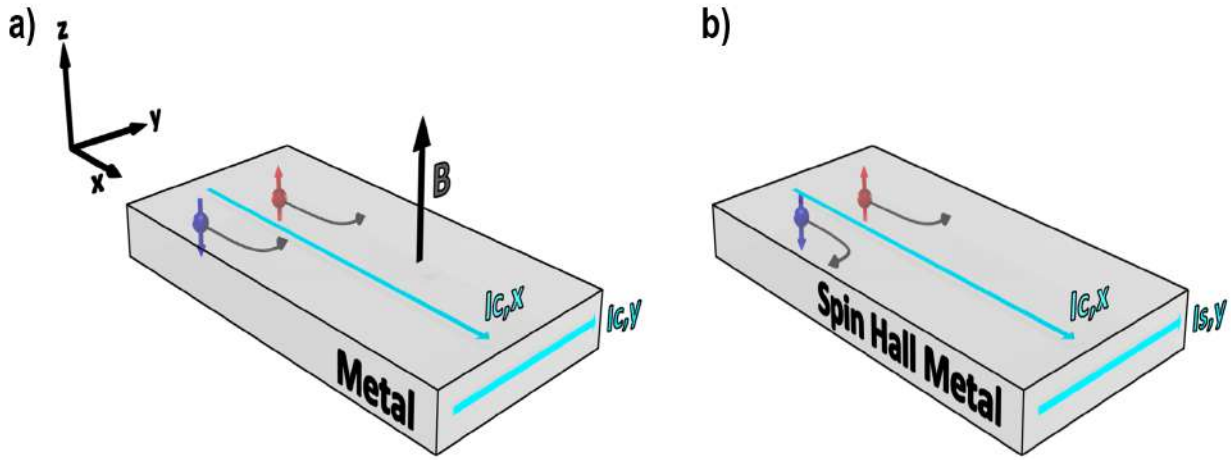

Figure 8: *a) Ordinary Hall effect. Applying an out-of-plane external magnetic field B to a metal induces a deflection of conduction electron on the border and produced a longitudinal charge current Ic,y and thus an electric field. b) Principal of the Spin Hall effect. A charge current applied in a Spin Hall metal induce a transverse spin polarized current Is,y and lead to a spin accumulation* $\Delta\mu$.

sometimes mentioned as the extraordinary Hall effect and originate from the spin-orbit interaction. The AHE results from the intrinsic Berry curvature of the band structure and extrinsic scattering process due to impurities/defects. If the number of spin up and spin down at the Fermi level are unbalance in a ferromagnet, the AHE leads to a spin polarized current that is perpendicular to the direction of the charge carrier even in absence of external magnetic field. In paramagnetic conductors, the spin up and spin down populations are equal and no AHE is induced. But if the coupling between the spin and the orbital momentum of the electron is sufficiently strong, the electron will preferably scatter in a trajectory whose angular momentum is oriented parallel or antiparallel to its spin. The spin up and down will then accumulate on the opposite side of the paramagnet giving rise to a spin current that is transverse to the charge current flow. This phenomenon

is called the spin Hall effect (SHE). This was predicted in 1971 by Dyakonov and Perel [121] and experimentally observed by Kato et al in 2004. The phenomenon is independent of the applied magnetic field just like the AHE. Two main scenarios are supporting the spin Hall effect :

- **Intrinsic SHE**: the intrinsic part of the SHE arise from the topological spin-splitted band structure of the material in the presence of strong spin orbit-coupling. We can attribute this contribution to the Berry curvature acting as an effective magnetic field which is significantly strong in broken inversion symmetry system. This contribution is the dominant mechanism behind the spin Hall properties of paramagnetic metals such as Ta or Pt which have strongly spin-orbit-coupled bands. This interaction also describes quite reliably the magnitude and the sign of the SHE.

- **Extrinsic SHE**: the extrinsic contribution of the SHE originate from the scattering of conduction electron with impurities. This was originally proposed to explained the origin of the AHE in ferromagnets, but this effect has been observed in non-magnetic materials as well. We can distinguish two scattering mechanisms.

  - **Skew scattering**: it addresses the collision of charge carriers with spin-dependent impurities due to the spin-orbit coupling. Depending on the direction of the spherical impurities potential, the electrons will get deflected asymmetrically (by an θ angle) according to the spin orientation. This will split the spin population yielding to a transverse spin Hall current.

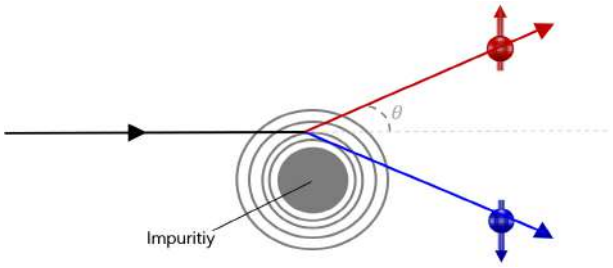

Figure 9: *Illustration of the skew scattering mechanism after collision with impurity. The up (red arrow) and down (blue arrow) spins are perpendicular to the dash grey line.*

  - **Side jump**: this mechanism has been introduced by Berger in 1970. It suggests that the unpolarized electron's charge will experience after scattering a spin-dependent displacement transverse to its initial direction due to the spin-orbit interaction. This result in a spin-dependent lateral displacement and thus a finite spin Hall conductivity.

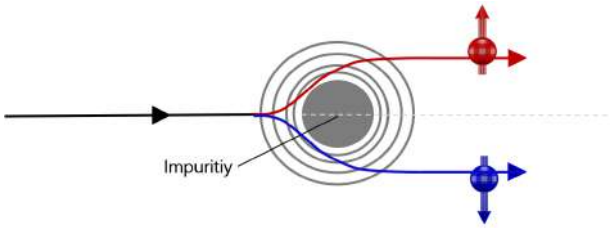

Figure 10: *Illustration of the side jump mechanism.*

By associating all of these contributions, we can express the spin Hall resistivity ρ_{SHE} in terms of electrical resistivity ρ :

$$\rho_{\mathrm{SHE}} = a_{\mathrm{intri}}\rho^2 + b_{\mathrm{skew}}\rho + c_{\mathrm{side}}\rho^2 \tag{1.48}$$

were a_{intri}, b_{skew} and c_{side} are parameters describing the intrinsic and extrinsic mechanism at the origin of the spin Hall effect. These parameters will vary by the influence of the impurities potential and the band structure of the spin-orbit material.
Those mechanisms enable a direct interconversion between a charge current j_c and a spin current j_s in SOC material. The transverse spin current generated by the SHE can be introduce by :

$$\boldsymbol{j}_s = \theta_{\mathrm{SHE}}(\frac{\hbar}{2e})(\boldsymbol{s} \times \boldsymbol{j}_c) \tag{1.49}$$

where s denotes the spin-polarized vector and θ_{SHE} the dimensionless conversion rate of the spin to charge conversion often mentioned as the *spin Hall angle*, ratio of the transverse to longitudinal resistivities.
If we consider the other way around, owing to the Onsager reciprocity, a spin current j_s flowing in a SOC metal will generate a transverse charge current j_c. The mechanism responsible for this conversion is similar to the SHE and has been naturally named inverse spin Hall effect (ISHE) :

$$\boldsymbol{j}_c = \theta_{\mathrm{SHE}}(\frac{\hbar}{2e})(\boldsymbol{s} \times \boldsymbol{j}_s) \tag{1.50}$$

The efficiency of the spin-to-charge conversion translated by θ_{SHE} varies from different material and depends on the spin-orbit strength. Platinum is the archetype metal for the spin Hall effect. It can be found in the literature [16, 66, 122, 123] a broad estimation of the spin Hall angle $\theta_{\mathrm{SHE}}^{\mathrm{Pt}} = 0.01\text{-}0.2$ but the value $\theta_{\mathrm{SHE}}^{\mathrm{Pt}} l_{\mathrm{sf}}$ seems to be largely accepted [124]. In this manuscript, Pt we will be used as a spin to charge converter to induce/detect spin wave in a ferromagnetic insulator.

1.3.3.2 Spin pumping

Up to now, we only considered the properties of a spin current flowing into a normal metal. In this section, we will mainly focus on the magnetization dynamics of a ferromagnet (FM) close to a normal metal (NM). Through the concept introduced in the previous section, we will show that a transfer of angular momentum at the NM/FM is possible and can mediate spin wave dynamics. Particularly, this interplay is very interesting to excite/detect spin waves and control them via a self assisted amplification.

Spin pumping refers to the generation of a spin current in an adjacent metallic layer that is mediate by magnetization precession in a ferromagnet through the interface. It was theoretically developed by Tserkovnyak et al [76, 75, 125] and first observed by Saitoh et al [126]. Generally, the magnetization dynamic is driven by a microwave-field where the spin angular momentum is dissipating toward the lattice by magnetic loss (Gilbert damping). If we consider a ferromagnet (FM) sandwiched by two normal metals (NM), a flow of angular momentum provided by the precessing magnetization can escape from the ferromagnet toward the metal through the interface resulting in a net flow of spin current in the metal. The spin current $\boldsymbol{I}_s^{\mathrm{pump}}$ that is driven from the magnetization precession of the ferromagnet to one of the normal metal can be calculated following an adiabatic approximation :

$$\boldsymbol{I}_s^{\mathrm{pump}} = \frac{\hbar}{4\pi}(A_r \boldsymbol{m} \times \frac{d\,\boldsymbol{m}}{dt} - A_i \frac{d\,\boldsymbol{m}}{dt}) \tag{1.51}$$

where $\boldsymbol{m} = \boldsymbol{M}/M_s$ while A_r and A_i are the interface parameters described as:

$$A_r = \frac{1}{2}\sum_{\mathrm{mn}}[|r^{\uparrow}_{\mathrm{mn}} - r^{\downarrow}_{\mathrm{mn}}|^2 + |t^{\uparrow}_{\mathrm{mn}} - t^{\downarrow}_{\mathrm{mn}}|^2] \tag{1.52}$$

$$A_i = \mathrm{Im}(\sum_{\mathrm{mn}}[r^{\uparrow}_{\mathrm{mn}}(r^{\downarrow}_{\mathrm{mn}})^* + t^{\uparrow}_{\mathrm{mn}}(t^{\downarrow}_{\mathrm{mn}})^*]) \tag{1.53}$$

$r^{\uparrow}$ and $r^{\downarrow}$ are the reflection coefficient for up and down electron's spin while $t^{\uparrow}$ and $t^{\downarrow}$ are the transmission coefficient across the FM. Index m and n are labeled as the transverse modes at the Fermi energy in the adjacent metal layer. Equation (1.52) and (1.53) can be summarize in :

$$A_r + \mathrm{i}A_i = \sum_{\mathrm{mn}}(\delta_{\mathrm{nm}} - r^{\downarrow}_{\mathrm{mn}}(r^{\uparrow}_{\mathrm{mn}})^*) - \sum_{\mathrm{mn}} t^{\uparrow}_{\mathrm{mn}}(t^{\downarrow}_{\mathrm{mn}})^* = G^{\uparrow\downarrow} - T^{\uparrow\downarrow} \tag{1.54}$$

where $G^{\uparrow\downarrow}$ is the spin mixing conductance and $T^{\uparrow\downarrow}$ the total transmission coefficient. During one revolution, the angular momentum sink into the normal metal is proportional to A_r in the direction of the applied field.
In this work, we will assume that the ferromagnetic layer is thicker than the coherence length $\lambda_c = \pi/(k_{\uparrow} - k_{\downarrow})$ where $k_{\uparrow}$ and $k_{\downarrow}$ are spin up and down Fermi wave vector. For a single NM/FM interface, the total transmission coefficient $T^{\uparrow\downarrow}$ vanish and the imaginary part A_i =Im($G^{\uparrow\downarrow}$) is usually small such that only real part of the spin mixing conductance remains. Thus we can actualize equation (1.51) in :

$$I_s^{\mathrm{pump}} = \frac{\hbar}{4\pi} G_{\uparrow\downarrow}\boldsymbol{m} \times \frac{d\,\boldsymbol{m}}{dt} \tag{1.55}$$

Loss of spin momenta from the ferromagnet into the normal metal via spin pumping process will result in an additional damping term $\Delta\alpha$ in the LLG equation (1.15). Therefore, the damping in NM/FM structures can be considered as an effective damping $\alpha_{\mathrm{eff}} = \alpha + \Delta\alpha$. According to the spin angular momentum conservation principle the pumped spin current can be written as :

$$\frac{d\,\boldsymbol{S}}{dt} = -\boldsymbol{I}_s^{\mathrm{pump}} \tag{1.56}$$

$\boldsymbol{S}$ been the total spin in the ferromagnet which is related to the total magnetic moment $\boldsymbol{M} = \boldsymbol{m}M_s = \gamma\boldsymbol{S}$ with $\gamma = g\mu_B/\hbar$. Hence :

$$\frac{d\,\boldsymbol{m}}{dt} = -\frac{g\mu_{\mathrm{B}}}{\hbar M_s}\frac{d\,\boldsymbol{S}}{dt} = \frac{g\mu_B}{\hbar M_s}\boldsymbol{I}_s^{\mathrm{pump}} \tag{1.57}$$

Combining equation (1.55) and (1.57) yields:

$$\frac{d\,\boldsymbol{m}}{dt} = \Delta\alpha(\boldsymbol{m} \times \frac{d\,\boldsymbol{m}}{dt}) \tag{1.58}$$

where $\Delta\alpha$ is the additional damping term due to the spin pumping process and can be written as :

$$\Delta\alpha = \frac{g\mu_B g_{\uparrow\downarrow}}{4\pi M_s d_{\mathrm{FM}}} \tag{1.59}$$

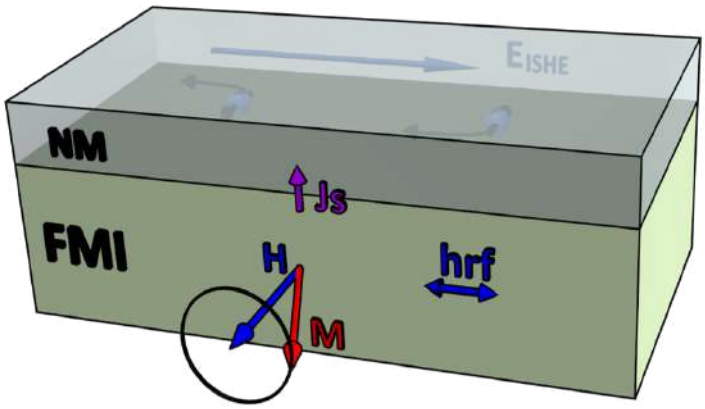

Figure 11: *Schematic of the spin pumping phenomena at the interface between a ferromagnetic insulator (FMI) and normal metal (NM).*

where d_{FM} is the thickness of the ferromagnetic film and $G_{\uparrow\downarrow} = g_{\uparrow\downarrow}/d_{\mathrm{FM}}$. From this expression we can deduce that the magnetization dynamic of thin ferromagnet will be govern by the spin pumping process due to the spin dissipation channel introduce via the NM/FM interface. Following a phenomenological approach, we can express the DC component of the spin pumping current density in the normal metal [127] :

$$j_s^{\mathrm{eff}} = \mathrm{f}\int_0^{1/\mathrm{f}} \frac{\hbar}{4\pi} g_{\uparrow\downarrow} \frac{1}{M_s^2} [\boldsymbol{M}(t) \times \frac{d\,\boldsymbol{M}(t)}{dt}]_z dt \tag{1.60}$$

with f the frequency of the magnetization precession and z the axis oriented parallel to the magnetization precession axis. Under ferromagnetic resonance condition, the flow of angular momentum in the normal metal produced by the external radiofrequency field h_{rf} can be estimated by :

$$j_s^{\mathrm{eff}} = \frac{2e}{\hbar} \frac{g_{\uparrow\downarrow}\gamma^2\hbar h_{\mathrm{rf}}^2}{8\pi\alpha_{\mathrm{eff}}^2} \frac{4\pi M_s\gamma + \sqrt{(4\pi M_s\gamma)^2 + 4\omega^2}}{(4\pi M_s\gamma)^2 + 4\omega^2} \tag{1.61}$$

$\omega = 2\pi\mathrm{f}$ been the microwave pulsation and reflecting the precession cone angle of the magnetization.
As already mentioned in the section 1.3.3.1, a spin current flowing in a spin-orbit NM can be converted into a charge current by ISHE. This interplay is generally an efficient way to investigate the spin conversion because it is sensitive to the NM/FM interface and the magnetization dynamic (directly related to the Gilbert damping). At ferromagnetic resonance conditions, ISHE current associated with the spin pumping can be translated with the following relation:

$$I_c = W\lambda_{\mathrm{sd}}^{\mathrm{NM}}\theta_{\mathrm{SHE}} \tanh(t_{\mathrm{NM}}/2\lambda_{\mathrm{sd}}^{\mathrm{NM}}) j_s^{\mathrm{eff}}. \tag{1.62}$$

where W is the section area, t_{NM} and $\lambda_{\mathrm{sd}}^{\mathrm{NM}}$ being the thickness and spin diffusion length of NM.

1.3.4 Interconversion between a spin current and a magnon current

As described in the previous section, we have seen that a flow of angular momentum in a ferromagnet can be generated at the FM/NM interface and be converted in a charge current via ISHE. This mechanism holds for insulating ferromagnet as well. A spin current flowing in NM can also lead to a net magnon current propagating in the ferromagnet. In this section, we introduce the fundamental physics behind the interconversion between an electronic current and a magnon spin current in the framework of Zhang et al [128, 99].

We assume that, at the interface between a ferromagnetic insulator (FI) and a spin-orbit normal-metal (NM), the conduction electron in the NM are reflected at the junction of FI/NM due to the large energy gap at the Fermi energy of the FI. This scattering lead to spin-flip processes at the interface where the electron reverses its spin from down to up or up to down. In a non-equilibrium state where the effective temperature and chemical potential of FI and NM are different, one of the spin-flip processes is dominating. This lead to a magnon excitation by transfer of angular momentum so that a net spin current flows across the FI/NM interface. The interconversion between electrons and magnon can be described by the s-d exchange interaction between the local moments and conduction electrons at the junction:

$$H_{\mathrm{sd}} = \frac{J_{\mathrm{sd}}}{N_a} \sum_{n=1}^{N_i} \int d^3 r \mathbf{S}_n . \psi_\sigma^\dagger(\mathbf{r}_n) \widehat{\sigma}_\sigma \psi_\sigma(\mathbf{r}_n) \tag{1.63}$$

where $\mathbf{S}_n$ are local moments with a position $\mathbf{r}_n$ at the interface, $\psi_\sigma^\dagger(\mathbf{r}_n)$ and $\psi_\sigma(\mathbf{r}_n)$ are the annihilation and creation operator of the incident electron in the NM with a spin σ at position $\mathbf{r}_n$, $\widehat{\sigma}$ been the Pauli spin operator, N_a the number of lattice sites in NM and N_i is the number of local moments that interact with conduction electrons at the interface. By using the Fourier transformation we can write: $\psi_\sigma(\mathbf{r}) = \sum_k c_\sigma(\boldsymbol{k}) e^{i\boldsymbol{k}.\mathbf{r}}$ and $\mathbf{S}_n = N_S^{-1/2} \sum_q S_q e^{i\mathbf{q}.\mathbf{r}}$ where $c_{\boldsymbol{k}\sigma}$ is the annihilation operator of an incident electron with a momentum $\boldsymbol{k}$ and a spin σ, N_S been the number of localized moments in FI. Thus the equation (1.63) can be written as:

$$H_{\mathrm{sd}} = J_{\mathrm{eff}} \sum_{k,k',q} [S_q^- c_{k'\uparrow}^\dagger c_{k\downarrow} + S_q^+ c_{k'\downarrow}^\dagger c_{k\uparrow} + S_q^z (c_{k'\uparrow}^\dagger c_{k\downarrow} - c_{k'\downarrow}^\dagger c_{k\uparrow})] \rho_{q-k'+k} \tag{1.64}$$

where $J_{\mathrm{eff}} = J_{\mathrm{sd}}/(N_a N_S^{1/2})$, $S_q^\pm = S_q^x \pm i S_q^y$ and $\rho_{q-k'+k} = \sum_{n=1}^{N_i} e^{i(p-k'+k).r_n}$. The net spin current at the FI/NM interface can be calculated from the equation : $J_{\mathrm{FI/NM}}^s = (\hbar/2)(d/dt)(\langle N_e^\uparrow \rangle - \langle N_e^\downarrow \rangle)$, where $N_e^\sigma = \sum_k c_{k\sigma}^\dagger c_{k\sigma}$ is the number operator of electrons with spin σ. Using the second-order perturbation the spin current $J_{\mathrm{FI/NM}}^s$ across the interface can be express as:

$$J_{\mathrm{NM/FI}}^s = \frac{1}{\hbar} N_I J_{\mathrm{eff}}^2 \int_{-\infty}^{+\infty} dt [e^{i\delta_\mu t/\hbar} \langle S_{-q}^-(t) S_q^+(0) \rangle \langle \sigma_q^+(t) \sigma_{-q}^-(0) \rangle - e^{-i\Delta\mu t/\hbar} \langle S_q^+(t) S_{-q}^-(0) \rangle \langle \sigma_{-q}^+(t) \sigma_q^-(0) \rangle] \tag{1.65}$$

where $\langle S^-_{-q}(t)S^+_q(0)\rangle$ and $\langle \sigma^+_q(t)\sigma^-_{-q}(0)\rangle$ are the spin correlation functions for local moments and conduction electrons, when $\sigma^+_p = \sum_k c_{k\uparrow}c_{k+p\downarrow}$ and $\sigma^-_p = \sum_k c_{k\downarrow}c_{k+p\uparrow}$. Note that this spin-flip scattering event of an NM electron at the FI/NM interface produces a spin accumulation $\Delta\mu = \mu_\uparrow - \mu_\downarrow$, which appears as the time dependent phase vector in equation (1.65). From the fluctuation-dissipation theorem, the correlation functions can be expressed in terms of imaginary parts of the dynamical spin susceptibilities of the FM. The spin current at the interface can thus be expressed as :

$$J^s_{\mathrm{NM/FI}} = \frac{2\hbar}{\pi} N_I J^2_{\mathrm{eff}} \sum_{p,q} \int_{-\infty}^{+\infty} d\omega e^{-iwt}[n(w, T_m) - n(w + \Delta\mu/\hbar, T_e)] \times \mathrm{Im}_{\chi^{+-}_{\mathrm{FI}}}(q,\omega)\mathrm{Im}_{\chi^{+-}_{\mathrm{NM}}}(p, \omega + \Delta\mu/\hbar) \tag{1.66}$$

where T_m is the magnon temperature in FI and T_e is the conduction-electron temperature in NM. The conduction electrons quickly equilibrate with the lattice, so that T_e is equal to the lattice temperature (phonon) T_p. By using $\chi^{+-}_{\mathrm{FI}}(q,\omega) = 2\langle S_Z\rangle/(\hbar\omega - \hbar\omega_q + i\delta)$ for the localized moments without damping, where $\hbar\omega_q$ is the magnon excitation energy, and $\chi^{+-}_{\mathrm{NM}}(p,\omega) = \sum_k [f(\xi_k) - f(\xi_{k+p})]/(\hbar\omega - \xi_k + \xi_{k+p} + i\delta)$ for the conduction electrons, where $f(\xi_k)$ is one-electron energy measured from the Fermi level, the interfacial spin current becomes :

$$J^s_{\mathrm{NM/FI}} = 4\pi A_J \frac{\langle S_Z\rangle}{a^2}\frac{J_{sd}}{\epsilon_F}^2 \frac{1}{N_S} \times \sum_q (\hbar\omega_q + \Delta\mu)[\coth(\frac{\hbar\omega_q + \Delta\mu}{2k_B T_e}) - \coth(\frac{\hbar\omega_q}{2k_B T_m})] \tag{1.67}$$

Thus the condition resulting in $J^s_{\mathrm{NM/FI}} = 0$ correspond to an equilibrium condition of $T_m = T_e$ and $\Delta\mu = \mu_\uparrow - \mu_\downarrow = 0$.

To quantify how the spin accumulation in the FI/NM interface is converted into a magnon spin current and how the spin current depends on the magnon energy, we consider a simple model where magnon have a parabolic dispersion with no excitation gap as $\hbar\omega_q = A_{\mathrm{ex}}k^2$. With a first order development in respect to $\Delta\mu$ and the temperature difference T_m-T_e, the equation (1.67) become :

$$J^s_{\mathrm{NM/FI}} \approx -\frac{\hbar}{2e}\frac{G^{(\Delta\mu)}_{\uparrow\downarrow}}{2eA_J}\Delta\mu(0) - \frac{\hbar}{2e}\frac{G^{(T)}_{\uparrow\downarrow}}{2eA_J}k_B(T_m - T_e) \tag{1.68}$$

where the $\Delta\mu$ and T component of the interfacial spin conductance normalized to the quantity $(2e^2/\hbar)A_J$ can be express as :

$$g^{(\Delta\mu)}_{\uparrow\downarrow} = \frac{G^{(\Delta\mu)}_{\uparrow\downarrow}}{(2e^2/h)A_J} \approx 8\pi(6/\pi)^{1/3}\frac{\langle S_Z\rangle}{a^2}(\frac{J_{\mathrm{sd}}}{\epsilon_F})^2(\frac{k_B T_m}{A_{\mathrm{ex}}}) \tag{1.69}$$

$$g^{(T)}_{\uparrow\downarrow} = \frac{G^{(T)}_{\uparrow\downarrow}}{(2e^2/h)A_J} \approx 16\pi^2\frac{\langle S_Z\rangle}{a^2}(\frac{J_{\mathrm{sd}}}{\epsilon_F})^2 \tag{1.70}$$

The sum of those two components corresponds to the total spin mixing conductance. Taking the approximation where spin current is continuous at the interface, one obtains the spin accumulation and spin current using equation (1.47) in the NM layer thickness of d_{NM}

$$\Delta\mu(x) = 2e\rho_N l_{\mathrm{sf}} j^s_{\mathrm{NM/FI}}\frac{\cosh[(x - d_N/l_{\mathrm{sf}})]}{\sinh(d_N/l_{\mathrm{sf}})}) \tag{1.71}$$

$$j^s_{\rm NM}(x) = -j^s_{\rm NM/FI}\frac{\sinh[(x-d_N)/l_{\rm sf}]}{\sinh(d_N/l_{\rm sf})} \tag{1.72}$$

the interface spin current is thus:

$$j^s_{\rm NM/FI} = -\frac{1}{4\pi}g^{(T)}_{\uparrow\downarrow}\frac{k_B(T_m - T_e)}{1 + (g^{(\Delta\mu)}_{\uparrow\downarrow}/g^s_{\rm NM})\coth(d_N/l_{\rm sf})} \tag{1.73}$$

where $g^s_{\rm NM} = (h/2e^2)/(\rho_{\rm NM}l_{\rm sf})$ is the spin conductance of the NM electrode.
Thus in a non-equilibrium state, a magnon current j_m may flow according to the phenomenological equation :

$$j_m = -D_m\Delta\delta n_m + L_m(-\nabla T) \tag{1.74}$$

where D_m is the diffusion constant of magnons. The first term is the contribution of non-equilibrium magnon accumulation δn_m, and the second is the contribution driven by the temperature gradient. Since individual magnons carry a spin angular momentum -$\hbar$, the magnon spin current is $j^s_m = -\hbar j_m$. The magnon accumulation can be written as:

$$\delta n_m = n_m - \bar{n_m} \tag{1.75}$$

where $n_m = (\hbar\gamma)^{-1}(M_s - M_z) = \sum_q\langle b^\dagger_q b_q\rangle$ is the magnon population in a non-equilibrium state, $b^\dagger_q(b_q)$ is the magnon creation/annihilation operator, while $\langle b^\dagger_q b_q\rangle$ is the distribution of magnon with energy $\hbar\omega_q$ and a Bose distribution function with magnon temperature T_m. Local equilibrium magnon population is described by $\bar{n_m}$ with the lattice temperature (phonon) T_p equal to the applied temperature. The magnon distribution functions can be expanded with respect to $\hbar\omega_q/k_BT_\zeta$, yielding :

$$\delta n_m \approx (6/\pi)^{1/3}\frac{k_B}{2\pi A_{\rm ex}a_S}(T_m - T_p) \tag{1.76}$$

This relation describes that the temperature difference (the deviation of magnon temperature from the lattice temperature) is responsible for the magnon accumulation.
If we assume the continuity equation for magnons, $\nabla.j_m = -\delta n_m/\tau_m$, where τ_m is the magnon relaxation time, and using the magnon-diffusion equation we can write :

$$\nabla^2\delta n_m(z) = \frac{1}{\lambda^2_m}\nabla_m\delta n_m(z) \tag{1.77}$$

where $\lambda_m = \sqrt{D_m\tau_m}$ is the magnon-diffusion length. Using the boundary condition $j_m = 0$ at the sample ends of z = $\pm L/2$, the magnon spin current ($j^s_m = -\hbar j_m$) and the magnon accumulation become :

$$j^s_m(z) = -\hbar[1 - \frac{\cosh(z/\lambda_m)}{\cosh(L/2\lambda_m)}]L_m(-\nabla T) \tag{1.78}$$

$$\delta n_m(z) = \frac{\lambda_m}{D_m}[\frac{\sinh(z/\lambda_m)}{\cosh(L/2\lambda_m)}]L_m(-\nabla T) \tag{1.79}$$

When a temperature difference ΔT is applied between the end of the sample in a FI of length w the temperature gradient is given by $\nabla T = \Delta/w$. So the non-equilibrium magnon temperature varies along the temperature gradient as :

$$T_m - T_p = -\eta_m \frac{\lambda_m}{w}[\frac{\sinh(z/\lambda_m)}{\cosh(w/2\lambda_m)}]\nabla T \tag{1.80}$$

where $\eta_m = 2\pi(6/\pi)^{1/3}(L_m A_{\rm ex} a_S/k_B D_m)$.
This analysis can also be used to describe the conversion of a magnon current to a spin current at FI/NM interface using relation (1.73). The electric field produced by ISHE in the NM layer due to the magnon current in FI is given by the relation $E_{\rm ISHE} = \theta_{\rm SHE}\,\rho_N(2e/\hbar)\langle j_N^s(z)\rangle$, so that a voltage of $V_{\rm ISHE}$ reads :

$$V_{\rm ISHE} = L_N E_{\rm ISHE} \tag{1.81}$$

$$V_{\rm ISHE} = -\theta_{\rm SHE}(\frac{L_N}{d_N})\frac{(g_{\uparrow\downarrow}^{(T)}/g_N^s)\tanh(d_N/2l_{\rm sf})}{1+(g_{\uparrow\downarrow}^{(\mu)}/g_N^s)\coth(d_N/2l_{\rm sf})}\frac{k_B}{e}(T_m - T_e) \tag{1.82}$$

where L_N is the length of Pt. This allows deducing a non-equilibrium difference of about $3{\times}10^{-4}K$ for a $V_{\rm ISHE}$ =1.5 μV in YIG/Pt device ($\theta_{\rm SHE}$ ≈0.05) and $g_{\uparrow\downarrow}^{(T)}/g_N^s = g_{\uparrow\downarrow}^{(\mu)}/g_N^s$ =0.01(J_{sd}/ϵ_F ≈1).

1.3.5 Spin-orbit torque

In 1996, Slonczewski and Berger predicted that a spin polarized current flowing across a NM/FM interface can influence the magnetization dynamic by mean of spin-orbit torque (SOT). It was originally introduced in FM/NM/FM system and opened up the road of spin-transfer oscillators and new magnetic memory where the magnetic orientation of the reference layer can be controlled electrically.
However, it has been demonstrated [8] that such interplay does not only rely on the conduction electron of ferromagnet and can be performed in NM/FMI systems. The spin-polarized electrons are scattered at the insulating interface, but in a situation where the spin of the electrons in NM are transverse to the magnetization and angular momentum is transferred from NM to the FMI through SOT. The SOT can act on the FMI magnetization dynamic via a torque taking the form :

$$\tau_{\rm SOT} = -\frac{\gamma J_s}{M_s t_{\rm FM}}\boldsymbol{M}\times(\boldsymbol{M}\times\boldsymbol{s}) \tag{1.83}$$

with J_s being the spin current density at the NM/FM interface, $d_{\rm FM}$ the thickness of the FM and $\boldsymbol{s}$ the spin orientation. From this equation, the torque resulting from the SOT is always perpendicular to the magnetization direction. Introducing this torque to the LLG equation (1.15), we obtain :

$$\frac{d\boldsymbol{M}}{dt} = -\gamma\boldsymbol{M}\times\boldsymbol{H}_{\rm eff} + \alpha\boldsymbol{M}\times\frac{d\boldsymbol{M}}{dt} - \frac{\gamma J_s}{M_s t_{\rm FM}}\boldsymbol{M}\times(\boldsymbol{M}\times\boldsymbol{s}) \tag{1.84}$$

This expression implies that the SOT can be (anti)collinear to the magnetic loss depending on the direction of the spin current (see FIG.12). It means that the spin current can either

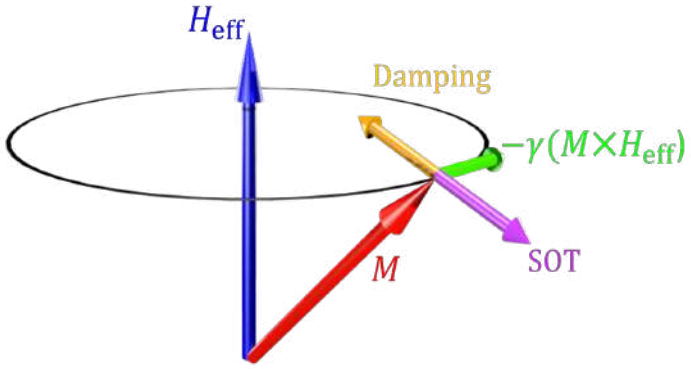

Figure 12: *Schematic illustration of the spin-orbit torque acting on the magnetization dynamic. The direction of the torque is defined by the polarity of the spin current.*

enhance or reduce the natural Gilbert damping α via SOT [129, 130, 131]. This process is often called "damping like torque".
We have already seen that a slight perturbation of the magnetic state can result in a net cone angle, where magnetization will tend to recover its equilibrium position to minimize its energy. Such dynamic will lead to a spiral precession of the magnetization around effective field. However, the situation is dramatically changed in presence of SOT. For the right polarity of applied magnetic field and current, the torque resulting from the SOT can counteract the magnetic relaxation and even fully compensate the natural Gilbert damping. If we consider NM/FMI system, the relaxation rate at the interface can be expressed using equation (1.59) :

$$\frac{1}{\tau} = (\alpha + \frac{\gamma\hbar}{4\pi M_s d_{\mathrm{FM}}} g_{\uparrow\downarrow}) \frac{\partial\omega}{\partial H} \frac{\omega}{\gamma} \tag{1.85}$$

with ω the precession pulsation of the magnetization. Thus the SOT is expected to exactly compensate the flow of spin lost by relaxation when $\tau^{-1} = \tau_{\mathrm{SOT}}$. The spin current density threshold J_s^* necessary to reach this regime can be determined using equation (1.83) and (1.85) :

$$J_s^* = -\frac{1}{\tau} \frac{d_{\mathrm{FM}} M_s}{\gamma} \tag{1.86}$$

Since the spin current at the NM/FMI interface is generated by a transverse charge current via SHE, we can define a threshold charge current [4] :

$$J_c^* = -\frac{2e}{\tau} \frac{d_{\mathrm{FM}} M_s}{\gamma \theta_{\mathrm{SHE}} \hbar} \tag{1.87}$$

By fulfilling this condition, the magnetization can be driven by the SOT into an auto-oscillation regime, where the magnetic system evolves in a steady-state precession. This new paradigm is subject to intense research activity and could lead to many applications. The figure of merit in this field rely on two main parameters: the Gilbert damping α and the ferromagnetic insulator thickness d_{FM}. At first, it came naturally to choose a material that possesses the smallest damping to minimize the threshold current necessary to trigger auto-oscillations. In that matter, Yttrium Iron Garnet (YIG) is the optimal choice. Second, the thickness of the ferromagnetic layer d_{FM} should be low, since the spin-orbit torque induced via a spin current is an interfacial effect. Nevertheless, this will

mainly depend on the quality of the film and the strength of the coupling between the normal metal and the ferromagnet which is determined by the spin mixing conductance $g_{\uparrow\downarrow}$.

1.3.6 Bose-Einstein condensation and spin superfluidity

In previous report [92, 132], the electrical control of the damping in magnetic insulators has been realized in confined geometry (nano-disk). The nanometric dimension of the pillar allows to lift the degeneracy between spin wave modes through finite size effects [4] which prevent the occurrence of the magnon-magnon scattering at the origin of saturation effects such as the Sulh threshold. Thus only one spin wave mode is driven out-of-equilibrium by the spin transfer torque. The situation is fundamentally different in an extended thin film because several spin wave modes are degenerate in energy within the linewidth. This triggers all the phenomena of energy redistribution within the magnon manifold. Multiple spin waves modes contribute to the total linewidth and can interact with each other. One important open question is whether, such geometry is suitable to trigger condensate. Indeed magnons are recalled as Bosonic quasi-particle that follow, in a quasi-equilibrium state, Bose-Einstein distribution n_m :

$$n_m[\beta(\epsilon-\mu_m)] = \frac{1}{(\mathrm{e}^{\beta(\epsilon-\mu_m)}-1)} \tag{1.88}$$

where $\beta(x) = x/k_B T_m$, ϵ is the magnon energy, μ_m is the magnon chemical potential and T_m the magnon temperature. Traditionally, in magnetic insulators, the utilization of spin phenomena is via semi-classical spin waves [6]. If one assume a quadratic dispersion relation of spin waves $\hbar\omega = J_s k^2$, where J_s is the spin stiffness that take the form $J_s = \hbar\omega_M \lambda_{\mathrm{ex}}^2$, the magnon density of state can be expressed as:

$$D(\epsilon) = \sqrt{\epsilon}/4\pi^2 J_s^{3/2} \tag{1.89}$$

This shows that the majority of the magnons present in the system are mostly located at thermal energy. The only interest in the low energy part of the spectrum is because it is there that the fluctuations are the largest. One important question is how this energy distribution affects macroscopic quantities. In this manuscript we will be interested in the characteristic propagation length of the spin information $\bar{\lambda}$. Already if one uses the grand partition theorem to predict the value of this quantity the result follows a complex expression:

$$\bar{\lambda} = \int \partial\epsilon D(\epsilon)\lambda_\epsilon n_m[\beta(\epsilon-\mu_m)] \tag{1.90}$$

where λ_ϵ is the classic magnon propagation length. An algebraic expression of λ_ϵ can be proposed using the spin wave dispersion relation (dependent of the relaxation rate). FIG.13 shows the variation in energy of the spin wave as a function of the amplitude of the wavevector k as well as its orientation compared to the magnetization. As one can see the behavior is not trivial. Magnons become localized around $k \approx 10^4 \mathrm{cm}^{-1}$ due to the vanishing group velocity for backward volume wave. Concerning the average $\bar{\lambda}$, the result needs also to incorporate the magnon density $D(\epsilon)$ and the Bose-Einstein distribution $n_m[\beta(\epsilon-\mu_m)]$. Thus we can expect different propagation lengths from low to high energy spin waves. At large energy, in the order of $k_B T$ (large wavevector k), the transport is carried through *thermal* magnons ($k > 10^4$, THz). On the other hand, at low energy, the transport is mediated by spin waves which as small wavevector k. For the purpose of this manuscript, such spin waves will be called *subthermal* magnons ($k << 10^4$, GHz).

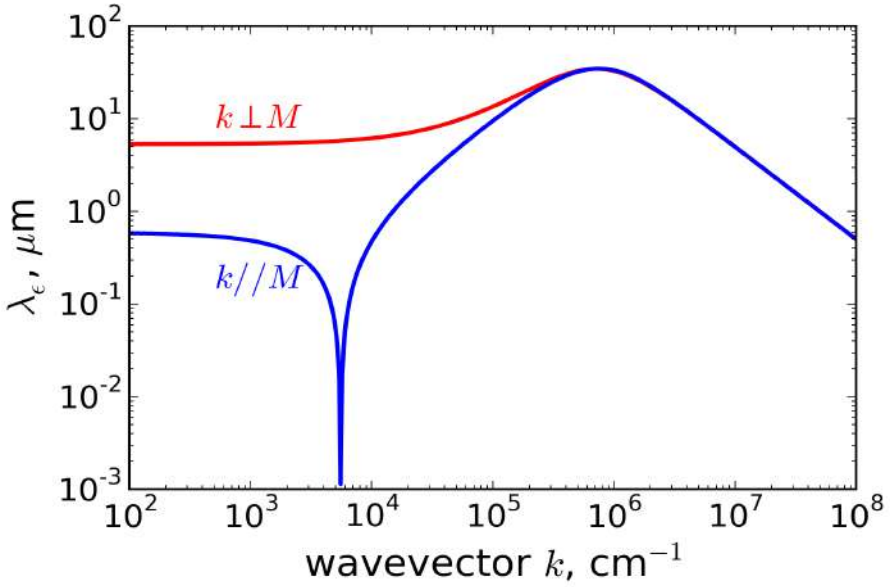

Figure 13: *Characteristic magnon propagation length in a Bose-Einstein distribution calculated as a function of the wavevector k using equation.*(1.90)*. The blue line correspond to wavevector k parallel to the magnetization while the red line is for a wavevector k that is perpendicular to the magnetization.*

At a sufficient density, magnon can condense into a single Bose quantum state [133] and has been our deep motivation for working in extended films. In ferromagnets, magnon Bose-Einstein condensation manifests itself by a phase-coherent precession of the magnetization. Let us consider a ferromagnet where the magnetization is homogeneous in the ground state and the lowest energy excitations are also homogeneous. Semi classically, a unit vector along the magnetization represents the magnetic state. At equilibrium, it points along an axis that we take to be the longitudinal z direction. Condensation is represented by a small deviation of magnetization in the transverse directions:

$$m_+ = m_x + i\ m_y = a\ exp(i\omega t + \varphi) \tag{1.91}$$

where the real number a is an amplitude, ω is the ferromagnetic resonance precession frequency, and φ is the phase of the condensate. The reduction of the unit vector of the magnetization along the longitudinal direction $\delta m_z = a^2/2$ is proportional to the number of magnons. The manifestation of condensation is that the magnon population is larger at the energy minimum of the magnon bands as described by the Bose-Einstein distribution or, at high temperatures, than the Rayleigh-Jeans distribution [134]. In thin ferromagnetic films, the dipole-dipole interaction dramatically changes the magnon dispersion. When the ground magnetization state is in-plane, the dispersion is anisotropic, and the energy minimum is at a finite wave-vector. The condensed magnons will then be around this energy minimum. Importantly, there have been observations of spectroscopically generated magnon condensates in a thin film of ferrimagnetic insulator at room temperatures [135]. These are also reports as spin superfluidity [136, 137]. Crucial for spin insulatronics, there is a hypothesis that we can electrically control magnon condensation via spin-transfer and spin-pumping in ferromagnets [88, 89]. These measurements and theoretical suggestions imply that it may become feasible to demonstrate coherent quantum phenomena that utilize magnons. Eventually, it might become possible to use these aspects in devices without the need for complicated cooling devices. Superfluidity is a dissipationless flow governed

by the gradient of the condensate phase. In the absence of spin-relaxation, there is an analogy between the spin dynamics in planar magnetic systems and the hydrodynamic behavior of ideal liquids [5]. There are subsequent extensions of these concepts dubbed spin superfluidity [138, 139]. When magnons condense, the phase of the order parameter equals the phase of the corresponding semiclassical precession angle. The spin current is proportional to the spatial variations of the precession angle φ.

$$j_s = A\nabla\varphi \tag{1.92}$$

where A is a constant related to the spin-stiffness. Electrical injection of superfluid transport is possible via spin-transfer and spin-pumping [140]. In other words, the bulk superfluid spin-current is supplemented with boundary conditions for the injection and detection of the spin currents. These boundary conditions depend on the contacts via the transverse (or "mixing") conductance. The physics is similar to the case of the conductance of normal metal-superconductor-normal metal systems that also depends on the contact interfaces between the normal metals and the superconductors. However, there are differences between the case of spin superfluidity and dissipationless charge transport. Even though there are no free carriers in insulators, spins, nevertheless, interact with lattice vibrations that cause dissipation. As a result, in a simple one-dimensional geometry, in a metal-magnetic insulator-metal system, the ratio between the emitted spin current and the spin accumulation bias becomes

$$\frac{j_s}{\mu_s} = \frac{1}{4\pi}\frac{g_L g_R}{g_L + g_R + g_\alpha^{'}} \tag{1.93}$$

where g_L is the transverse "mixing" conductance of the left metal-magnetic insulator contact, g_R is the transverse "mixing" conductance of the right magnetic insulator-metal contact, and g_α includes the effects of magnetization dissipation via Gilbert damping. When there is no magnetization dissipation, g_α vanishes. In this case, the total resistance of the device is a sum of the resistances of the left and right metal-magnetic insulators contacts. This result implies that there is no resistance in the bulk of the magnetic insulators, spin transport is dissipationless therein. g_α is proportional to the Gilbert damping coefficient and the length of the device, i.e., the total amount of dissipation versus the injection and detection efficiencies. A signature of spin supercurrent is, therefore, that it decays algebraically as a function of the length of the magnetic insulator [140]. This contrasts the expectations of diffusive spin transport via magnons that decay exponentially when the system exceeds the spin relaxation length [2, 97]. However, in ferromagnets, the simple picture above is incomplete. The ubiquitous dipole-dipole interaction dramatically affects spin transport and reduces the range to a few hundred nanometers even in ferromagnetic films as thin as five nanometers [141, 142]. So far, electrical control of magnon condensation and spin superfluidity has not yet been realized experimentally.

1.3.7 Spin Hall magnetoresistance

In a normal metal with strong spin-orbit coupling (NM), we can distinguish the ordinary Hall effect (OHE) from the Spin Hall effect (SHE). In a single band model, charge carriers flowing along the x-axis in a magnetic metal subject to an external magnetic field along the z-axis will experience a Lorentz force that generates a transverse charge current due to the OHE. In an open circuit condition, charge carriers cannot escape and accumulate on the border of the material. This result in a Hall electric field E_{Hall} along the y-axis and thus a net voltage. From this observation, we tend to think that the longitudinal resistance R_{long} is not affected by the OHE. But one as to take into account the boundary

conditions where E_{Hall} =0. This forces the system to increase the applied longitudinal voltage V_{long} to compensate the generation of the transverse current density $J_{c,y}$ such that longitudinal current $I_{c,x}$ remains constant. Thus the longitudinal resistance $R_{\text{long}} = V_{\text{long}}/I_{c,x}$ depends on the orientation and amplitude of the applied magnetic field. SHE describes the generation of a transverse spin current J_s induced by a charge current J_c.

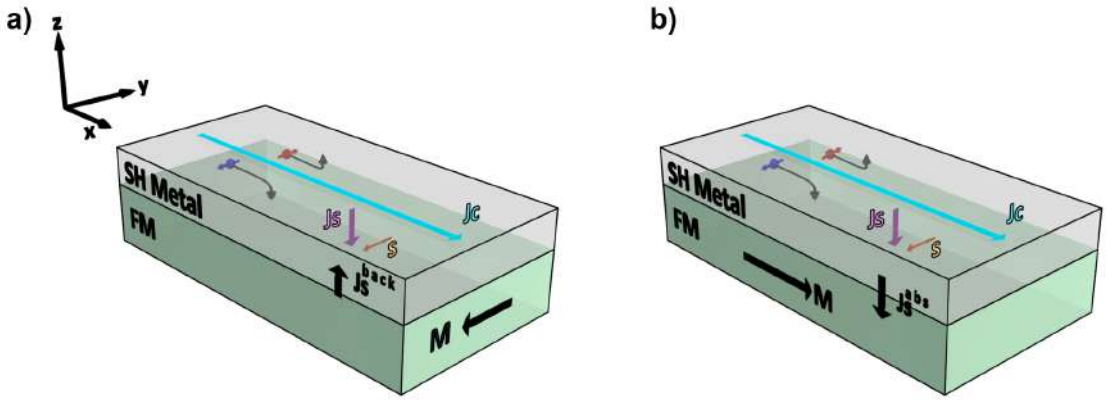

Figure 14: *a) and b) Illustration of the Spin Hall magnetoresistance effect at NM/FM interface for a magnetization* $\boldsymbol{M}$ *colinear (a) and perpendicular (b) to the spin accumulation polarization* $\boldsymbol{s}$.

According to equation (1.49), the spin current J_s flowing along the z-axis implies a spin polarization along the y-axis. If we now consider an NM/FMI interface, the spin current polarized perpendicularly to the interface normal will accumulate at the interface leading to a spin accumulation $\Delta\mu$. Just as the OHE, for a short-circuited boundary ($\Delta\mu$ = 0) the source current has to compensate the transverse component by increasing the longitudinal resistance. The switching between the open and closed boundary condition can be realized if the NM/FMI interface is strongly exchanged coupled. Thus one can change the longitudinal resistance in the NM via the magnetization orientation in the FMI. This effect is called Spin Hall Magnetoresistance (SMR). It has been experimentally observed for the first time by Nakayama et al [143] and theoretically developed by Chen et al [144].
For a better understanding of the effect, we consider a charge current density J_c, x flowing along the x-axis as scheme in FIG.14. The spin current J_s, z induce by SHE is parallel to the interface normal with spin orientation aligned along the y-axis. The spin current at the NM/FM is composed of two quantities, the spin Hall current and the spin diffusion current :

$$J_{s,\text{SHE}} = -\theta_{\text{SHE}} E/\rho \tag{1.94}$$

$$J_{s,\text{diff}} = -\frac{\sigma}{2e}\frac{\partial \Delta\mu}{\partial z} \tag{1.95}$$

where ρ=σ^{-1} is the intrinsic resistivity and E the electric field produced by the injected charge current. The spin accumulation at the interface can be calculated using equation (1.47), taking into account that the spin current is continuous at the interfaces and vanish in air [144] as boundary conditions. At the NM/FM interface, the spin accumulation is governed by the spin mixing conductance through $G_r\, \boldsymbol{m} \times (\boldsymbol{m} \times \boldsymbol{\mu})$. As mentioned previously, the imaginary part of the spin mixing conductance G_i can be disregarded in ferrimagnetic insulators like YIG. It results from these conditions, that the spin current at the interface is ruled from the torque exerted by the spin accumulation. If the spin

polarization $\boldsymbol{s}$ is not colinear to the magnetization orientation $\boldsymbol{M}$ of the FM, a spin-transfer occurs from NM to FM via the torque and result in net absorption of the spin current at the interface (through a spin-flip scattering). However, in a case where the spin accumulation $\boldsymbol{s}$ is colinear to the magnetization $\boldsymbol{M}$, the spin current doesn't fulfill the condition to be absorbed and is rather reflected at the interface. Finally when $\boldsymbol{M}$ is aligned along the interface normal, the spin current is absorbed because the spin accumulation $\boldsymbol{s}$ and magnetization $\boldsymbol{M}$ are again not colinear. From this simple picture, we can predict a low resistivity state of the NM when $\boldsymbol{M}||\boldsymbol{s}$ due to the action of the ISHE caused by the reflected spin current. If spin current is absorbed in the interface by the condition $\boldsymbol{M}\perp\boldsymbol{s}$, it results a high resistivity state in the normal metal. Those observation implies : $\mathrm{R}_{\boldsymbol{M}\perp\boldsymbol{s}}>\mathrm{R}_{\boldsymbol{M}||\boldsymbol{s}}$. We can thus describe the SMR effect via the longitudinal ρ_{long} resistivity of the NM that depend on the magnetization orientation of the FM :

$$\rho_{\mathrm{long}} = \rho + \Delta\rho_0 + \Delta\rho_1 m_y^2 \tag{1.96}$$

where $\Delta\rho_0$ the change of resistivity due to the spin-orbit interaction (for small NM thickness) and $\Delta\rho_1$ the change of resistivity due to the finite angle between spin accumulation polarization at the interface and magnetization in YIG. The parameters m_y is the projections of the magnetization orientation along the unit vector $\boldsymbol{y}$ as scheme in FIG.14. To characterize the magnitude of the SMR, we can express the change of resistivity following the description giving in [144]:

$$\frac{\Delta\rho_0}{\rho} = -\frac{\theta_{\mathrm{SHE}}^2\, 2l_{\mathrm{sf}}}{d_{\mathrm{NM}}}\tanh(\frac{d_{\mathrm{NM}}}{2l_{\mathrm{sf}}}) \tag{1.97}$$

$$\frac{\Delta\rho_1}{\rho} = \frac{\theta_{\mathrm{SHE}}^2\, l_{\mathrm{sf}}}{d_{\mathrm{NM}}}\frac{2\, l_{\mathrm{sf}} G_r \tanh^2(\frac{d_{\mathrm{NM}}}{2l_{\mathrm{sf}}})}{\sigma + 2\, l_{\mathrm{sf}} G_r \coth(\frac{d_{\mathrm{NM}}}{l_{\mathrm{sf}}})} \tag{1.98}$$

with d_{NM} the thickness of the NM and l_{sf} the spin diffusion length in the NM. By introducing the total NM resistivity $\rho_{\mathrm{NM}} = \rho + \Delta\rho_0$, the change of resistivity relative to the magnetization orientation in FM can be expressed as :

$$\frac{\Delta\rho_1}{\rho_{\mathrm{NM}}} = \theta_{\mathrm{SHE}}^2\frac{(\frac{2l_{\mathrm{sf}}^2\rho}{t_{\mathrm{NM}}})\, G_r \tanh^2(\frac{t_{\mathrm{NM}}}{2l_{\mathrm{sf}}})}{1 + 2\lambda_{\mathrm{NM}}\rho_{\mathrm{NM}} G_r \coth(\frac{t_{\mathrm{NM}}}{l_{\mathrm{sf}}})} \tag{1.99}$$

The magnitude of SMR can be well described by the quantity $|\Delta\rho_1/\rho_{\mathrm{NM}}|$. From equation (1.99) we can see that the dimensionless SHMR ratio is mostly determined by θ_{SHE}^2. Taking account of the spin Hall angle of the Pt θ_{SHE} =0.05 we can expect an SMR ratio in between 10^{-5} and 10^{-4}. The spread variation of the SMR ratio found in the literature can be attributed to the combine variation of θ_{SHE}^2, ρ_{NM} , G_r and mainly depend on the fabrication process.
However in conducting FM, the contribution of the anisotropic magnetoresistance (AMR) has to be taking into account and follow :

$$\rho_{\mathrm{long}} = \rho_{\mathrm{NM}} + \Delta\rho m_x^2 \tag{1.100}$$

If the magnetization of the FM is magnetized in the plane of the film, the AMR follow the same behavior as the SMR and it is not possible to disentangle the respective contribution of these two effects. To identify the SMR, one has to study the change of resistivity of NM

for an out of plane magnetization and take properly into account the spin anomalous Hall effect contributions. Indeed the SMR vanished when the magnetization is rotated along the plane defined by $\boldsymbol{x}$ and $\boldsymbol{z}$ while AMR vanish if the magnetization rotates on the $\boldsymbol{y}$ and $\boldsymbol{z}$ plane. To estimate the SMR, an angle depend magnetoresistance experiment along all plane define by the ($\boldsymbol{x}$,$\boldsymbol{y}$,$\boldsymbol{z}$) orientations is necessary to eliminate possible contamination. Here we note that in FMI/NM, the contribution of the AMR is expected to be null. But since magnetic proximity effect [145, 146] can appear in a few atomic layers of NM, an angular dependent measurement is highly preferable.

1.3.8 Spin Seebeck

The Seebeck effect is a thermoelectric phenomenon first observed by Alessandro Volta in 1794 but so called over the Thomas Johann Seebeck experiments in 1821. It describes the generation of a charge current when a conductor is subject to a temperature gradient. The difference in energy levels of electrons in both hot and cold sides of the conductor produces an electronic flow and thus a net voltage. The ratio of this conversion is determined by the Seebeck coefficient which is material dependent (refer to the Peltier and Thomson coefficient).
In a ferromagnetic material, the spin Seebeck effect (SSE) known as the spin counterpart of the Seebeck effect can occur. This implies that a temperature difference in magnetic order system induces a spin voltage across the ferromagnet. It has been demonstrated that the contribution of conduction electron to the SSE is relatively small since such effect can be observed in magnetic insulators [147]. It differs from the spin dependent Seebeck effect in which two defined spin channels with different Seebeck coefficient induce a spin imbalance. For the purpose of this manuscript, we consider a non-magnetic metal with a temperature T_N attached to a ferromagnetic insulator with a temperature T_F that interact through the interface via the exchange coupling. Thus a simple picture of the SSE can be drawn considering a thermal excitation of localized spin in the ferromagnetic materials flowing into the NM which generates a spin current due to the imbalance of pumped and backflow spin current:

$$I_s = I_s^{\text{pumped}} - I_s^{\text{back}} \tag{1.101}$$

Where I_s^{pumped} can be understood as the spin current drag into the NM by the thermal noise in the FM, while I_s^{back} denotes the spin current reflected into the FM from the thermal noise in NM.
The SSE can be found in two different configurations of temperature gradient and magnetic field which are known as longitudinal and transverse configuration (see FIG.15). Transverse spin Seebeck effect (TSSE) corresponds to the geometry where the spin current is perpendicular to the temperature gradient. The keys element to understand TSSE is the concept of phonon drag. If the phonon population deviates from thermal stability, non-equilibrium phonons in the NM can interact with the magnon in the FMI. Thus the magnon deviates from there equilibrium distribution and will relax by injecting a spin current into the NM via the interface. This interplay between phonon, magnon and spin density is called acoustic spin pumping. Through a perturbation theory [86] it has been found that the injected spin current vanishes for a local equilibrium condition of the magnons and phonons ($T_N = T_F$). Now if we consider the phonon-drag, any temperature difference across the ferromagnet will be felt by the phonons due to the phonon-phonon interaction but not by the magnons. This lead to a non-equilibrium propagation of the phonon and the production of a spin current by the phonon-drag process.
By contrast, if the spin current generated by the phonon-drag is parallel to the tempera-

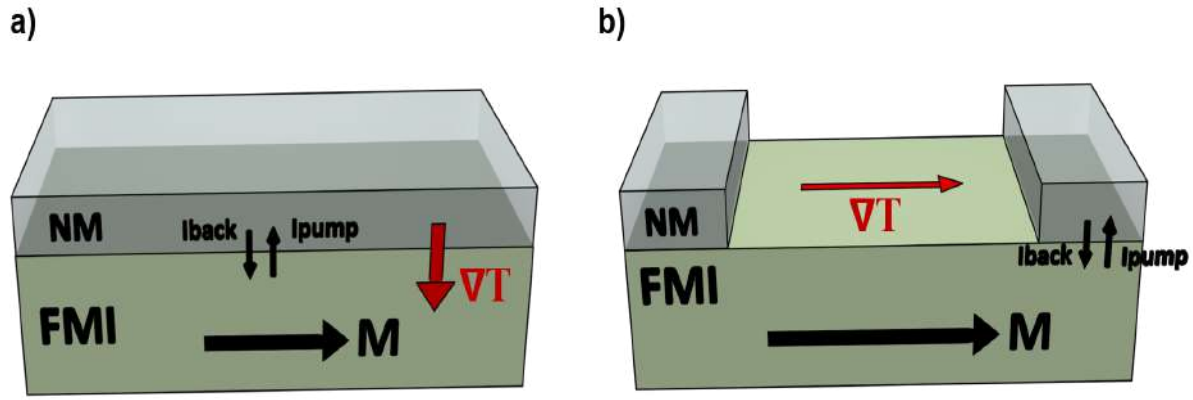

Figure 15: *a) Schematic of the longitudinal spin Seebeck geometry. In this configuration, the thermally injected spin current is parallel to the temperature gradient. b) Transverse spin Seebeck configuration, where the thermally injected spin current is perpendicular to the temperature gradient. In any spin Seebeck experiment, the thermally injected spin current, defined as the sum of the pumped and backflow spin current, is being probed in the NM by mean of inverse spin Hall effect.*

ture gradient, we are in a Longitudinal spin Seebeck (LSSE) geometry. In linear response theory, it can be understood as an imbalance between the thermal noise of the conduction electron spin in NM and the thermal noise of the magnon in the FM. Since the thermal noise is directly related to the effective temperature, the LSSE can be attributed to the difference between the effective temperature of conduction electron spin T_e in NM and the effective temperature of the magnon T_m in the FM.
One of the most important features of the LSSE is that the sign of the injected spin current is opposite to the spin current in the TSSE geometry. This observation can be supported by the following consideration: the heat flow in NM/FM system is mainly carried by the phonons (which is also true for magnetic insulator), and the electron-phonon interaction in NM is much stronger than the magnon-phonon interaction in FMI. From those assumptions, it can be understood that for LSSE, the conduction electrons in NM which are directly in contact with the phonon bath heat up much faster than the magnon in FMI. Thus a spin current is flowing from the thermal noise in NM into the FMI and is much greater than the spin current pumped from FMI to NM. Although in the TSSE configuration, conduction electrons are too far away from the heat bath. In this situation, the effective temperature of the conduction electron in NM is much lower than the magnon effective temperature in the FM. This difference is at the origin of the sign change. These effects will be an important source of spin current in the following experimental part and care will be taken to identify thermal spin signal.

Chapter 2

Characterization of YIG films and YIG|Pt nanostructures for spin transport

---

While in the case of metals, many phenomena could contribute to the spin conduction, the situation simplifies greatly in the case of magnetic insulator, where the only channel in principle allowed to transmit the spin information is spin waves. Furthermore, the physics at stake is more interesting when non-linear phenomena kick in. For that purpose, we have seen in the last chapter that it is interesting to use low damping materials since this lowers the threshold for the onset of these new phenomena. In my thesis, I have chosen to concentrate exclusively on the spin transmission properties of pure and *Bi*-doped YIG films.

This chapter is dedicated to a broad characterization of YIG ultra-thin films for ultimately studying spin waves transport. After a brief explanation of the fabrication of ultra-fine YIG films made by liquid phase epitaxy, we will detail their main static and dynamical properties. The thickness dependence of magnetic damping in YIG from 16 to 200 nm will be addressed.

We will then develop in detail the non-local magnons transport experiment in YIG which is performed via angular moment transfer at a YIG|Pt interface, allowing the excitation and detection of magnons. Through various control experiments, we provide the main ingredient necessary to induce propagative spin waves in YIG through a static excitation. Moreover, particular attention will be given to the efficiency of the spin transfer at the YIG|Pt interface. In this chapter, we will investigate mostly the low current regime. The high power behavior and non-linear effects will be discussed in Chapter 4.

2.1 YIG ultra-thin films

In the field of magnonic spintronics, high-quality magnetic films are crucial [148, 7, 105]. Among them, Yttrium Iron Garnet ($Y_3Fe_5O_{12}$, YIG) is of particular interest, mainly because of its low magnetic damping. This makes YIG an optimal choice for magnonic base devices that could operate in a wide range of frequency (from GHz to THz). As already mentioned in section 1.2.1 the relaxation in YIG come from three mechanisms. First, a charge transfer between the Fe^{2+} and Fe^{3+} ions can be mediated by impurities (through exchange coupling). This effect can be minimized in YIG by growing the crystal with ultra-pure material composition. The second mechanism is linked to the spin-orbit coupling, which is relatively small in YIG and would result in a magnon-phonon coupling that contributes to the linewidth. Finally, the influence of the dipole-dipole interaction between thin magnetic film and the paramagnetic substrate dominates the relaxation even at room temperature [4].
To implement spintronics tools for processing spin wave information, the thickness of the magnetic films has to be in the order of nanometer range which was many years ago considered to exceed the ability of fabrication methods. This challenge has been overcome by the growth of thin YIG film through sputtering [149, 150] or pulse laser deposition [20, 151, 152, 21]. However, recent work [17] have proven that the growth of high quality (small damping, low impurity level) YIG film with a thickness in the nanoscale ($< 100\,\text{nm}$) can also be achieved by liquid phase epitaxy. This opened up the route toward the manipulation of spin waves via spin-orbit torques.

2.1.1 Liquid phase epitaxy ultra-thin Yttrium Iron Garnet (YIG) films

Liquid phase epitaxy (LPE) is a growth technique that is an extension of the flux method [153]. It allows the deposition of thin single crystalline film from its liquid phase on a crystalline film. LPE garnet films are usually grown onto a (111) Gadolinium Gallium Garnet (GGG) substrate, which provides the necessary lattice matching to achieve epitaxial growth. The deposition is performed in a platinum crucible which is placed in a furnace (see Fig 16).

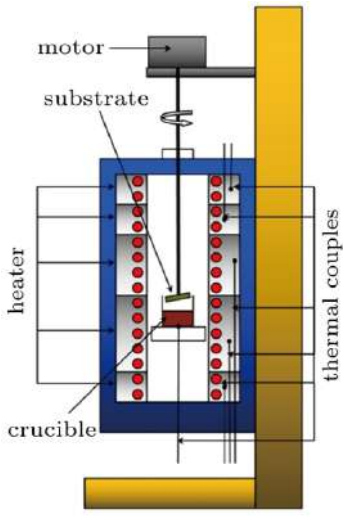

Figure 16: *Schematic of the LPE growth setup taken from [154].*

The substrate is attached to an upper motor to ensure rotation during the kinetic growth and is placed in the solvent mixture contained in the crucible. The initial temperature of the furnace is set 100 °C above the undercooling temperature where the growth rate is zero and stir for a few hours to melt the flux. The composition of the mixture is made of rare earth oxides like Fe_2O_3 and $YFeO_3$, melt in a PbO-PbF_2 and B_2O_3 mixture to increase the solubility.
The garnet film growth is then realized by dipping and rotating the GGG substrate onto the melt solution to obtain a uniform film thickness. Optimization of the growth process parameters is achieved by studying the dependencies of the depositing conditions on the structural, morphological, and magnetic properties. The key to very good growth is to keep the solution perfectly homogeneous and the growth rate very slow.

2.1.2 Magnetic characterizations of YIG ultra-thin film

The YIG films used in this thesis work have been provided by the group of J. Ben Youssef in Laboratoire de Magnétisme de Bretagne at Univeristé de Bretagne.

Ferromagnetic resonance measurements

The magnetic relaxation of those films has been determined by studying there dynamic properties via ferromagnetic resonance (FMR) in a broadband setup. These characterizations have been performed by G.de Loubens in CEA-Saclay.
FIG.17 display the FMR response of a 17 nm YIG film at a frequency of 10 GHz for an out of plane magnetization. From a Lorentzian fit, we can extract a small linewidth ΔH=2.83 Oe inherent from the low magnetic damping of YIG. FIG.18 presents the extracted FMR linewidth for different excitation frequencies allows getting more depth about the dynamics properties of YIG films. In FIG.18.a, the frequency dependence linewidth has been fitted with the Gilbert formula which predicts a linear evolution of the linewidth with frequency.

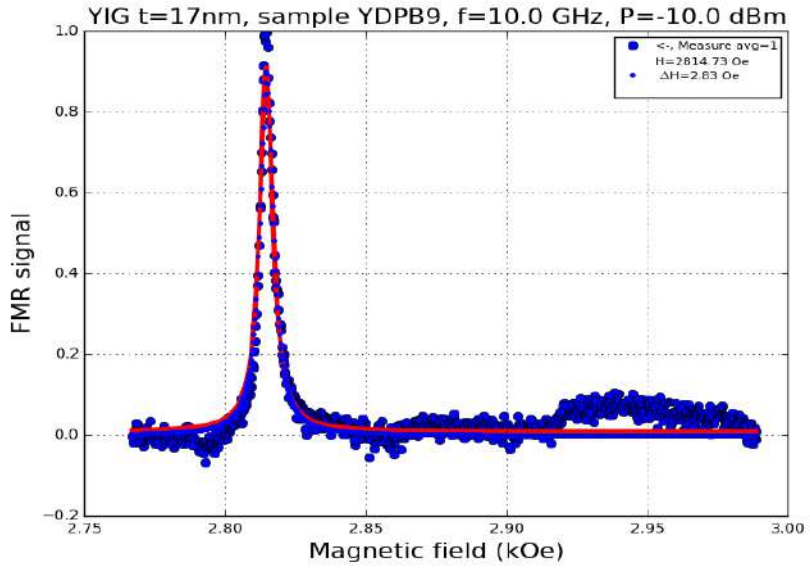

Figure 17: *FMR spectra of a 17 nm YIG film with an excitation frequency of 10 GHz and power of -10 dBm.*

The finite ordinate intercept can be attributed to the inhomogeneous contribution of the linewidth. The spectra acquired in the normal orientation excludes any contribution due to the two-magnon scattering. We can already see that the slope of those fit, directly linked to the Gilbert damping parameter α has a net dependence with the thickness of the YIG film.

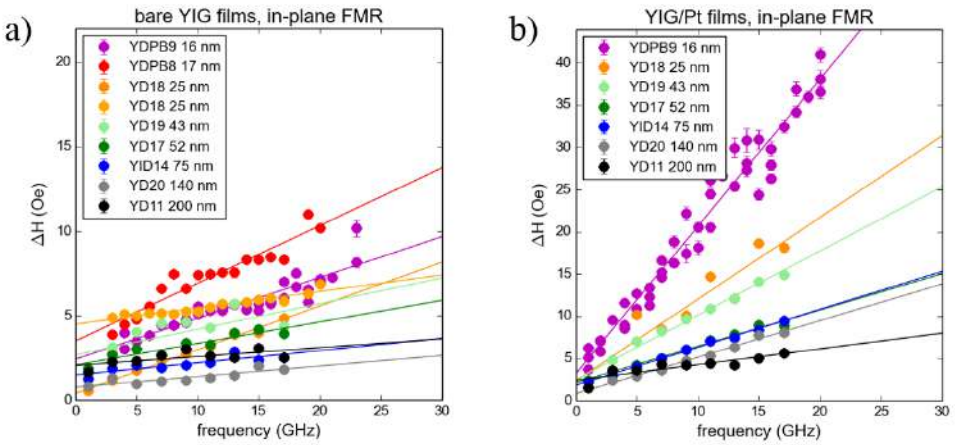

Figure 18: *FMR linewidth ΔH extracted from Lorentzian fit as a function of the microwave frequency and for different thickness of YIG film and an in-plane magnetization. a) Full width half maximum for pure YIG film while b) present the measure of FMR linewidth from the same YIG film covered by a 7 nm Pt layer.*

We present in FIG.18.b the FMR result measured on the same films when a Pt overlayer of thickness 7 nm is deposited on the top surface. In all cases, we observe an enhancement of the damping by at least a factor of 3, and the value of the enhancement is more pronounced for the thinner films. This unambiguously shows that in these films the dominant decay mechanism is the escaping of angular momentum through the YIG|Pt interface and its absorption by the Pt. The variation of the damping α with the thickness is shown in FIG.19.

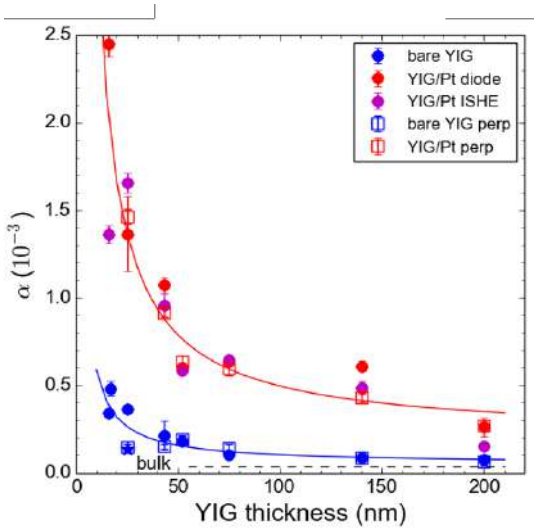

Figure 19: *Gilbert damping of pure YIG film (blue) and YIG|Pt (red) measured from FMR as a function of the YIG thickness.*

The striking feature of those LPE YIG thin films is the increase of the Gilbert damping for thinner film. Moreover, this dependency seems to vary inversely proportional to the film thickness (blue dot). Considering that the inhomogenous broadening and Larmor precession are rather independent of the thickness, we cannot exclude at this point an additional contribution due to a surface damping mechanism (YIG|GGG interface).

SQUID measurements

Static magnetic characteristic of YIG film have been measured in a Quantum Design MPMS 5XL SQUID Magnetometer.
In FIG.20.a we have plotted the hysteresis loop of YIG|GGG sample at 150K. The raw data sketch as red dots displays a linear evolution with the applied magnetic field above 5 G while in the low field range (<5 G), the hysteresis behavior can be observed. The linear slope can be attributed to the paramagnetic nature of the GGG substrate. To separate the linear contribution from the hysteresis loop, we have systematically calculated the linear slop (via linear regression) at high field. The hysteresis loop is disentangled by subtracting the linear behavior for the raw data and is shown as black dots. To get more insight about the paramagnetic contribution of the substrate, we have plotted the magnetization as a function of the temperature and for an applied field of 10 G in FIG.20.b. We can observe that the linear contribution evolved inversely proportional to the temperature.

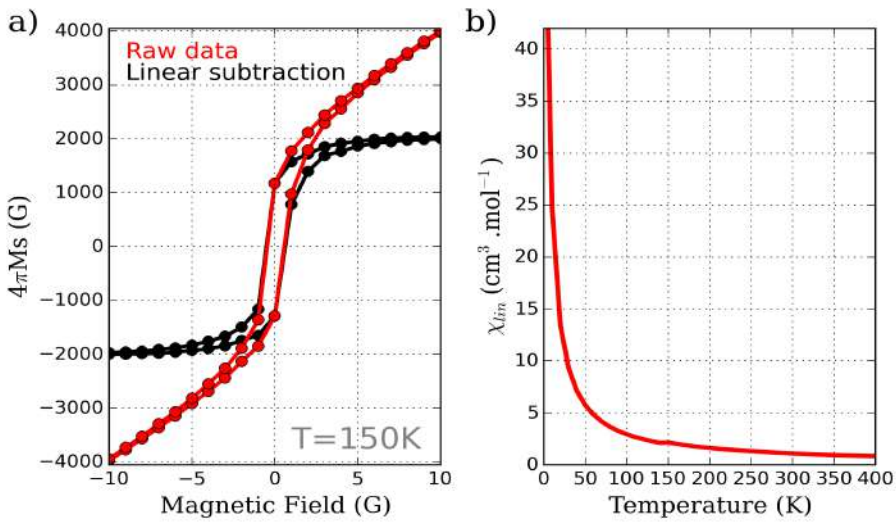

Figure 20: *a) Hysteresis loop of 18 nm YIG|GGG sample a 150K. The red dots are the raw data while the black dots present the hysteresis loop of pure YIG film after subtraction of the linear behavior. b) Temperature dependence of the paramagnetic contribution of GGG. We have make sure that the $1/\chi$ temperature dependence is solely linear (not shown).*

Indeed from Curie's law, the magnetization of paramagnetic material is expected to take the form :

$$M = \chi H = \frac{C}{T} H \tag{2.1}$$

where χ is the volume magnetic susceptibility and C the Curie constant. From equation (2.1) we can extract the material dependent parameter C =20.3 cm^3.K.mol^{-1}.

The magnetization saturation $4\pi Ms$ of the YIG film as a function of the temperature is display in FIG.21.

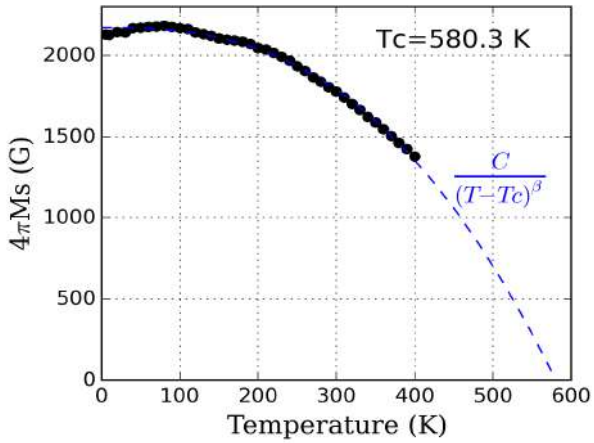

Figure 21: *Saturation magnetization of the 18nm YIG film as a function of the temperature. The blue dash line is a fit of the Curie's law which allow us to deduce a Curie temperature of 580K, and a critical exponent β=2.63*

Inner to the uncompensated ferrimagnetic nature of the YIG [148], we expect the magnetization to evolve as :

$$M = \frac{C}{(T - T_c)^{\beta}} H \tag{2.2}$$

where C is the Curie constant, Tc the Curie temperature and β the critical exponent. From a fit of the equation (2.2), we extrapolate a Curie temperature T_c =580.3 K and critical exponent of β=2.6 which is close to the value found in the literature [148, 155, 156]. The saturation magnetization at room temperature estimated from SQUID measurements is about 1780 G which is consistent with the FMR measurement.

The physical properties of the LPE YIG films used in this thesis for spin transport experiments are summarized in the table below:

Sample	t_{YIG} (nm)	t_{Pt} (nm)	α_{YIG}	$\alpha_{\mathrm{YIG\|Pt}}$	$4\pi M_{\mathrm{s}}$(kG)	T_{c} (K)
YDPB8	18	10	4.4×10^{-4}	2.4×10^{-3}	1.78	580.3
YDPB9	19	7	3.2×10^{-4}	1.35×10^{-3}	1.67	-
YDPB10	56	7	2.0×10^{-4}	0.6×10^{-3}	1.65	-

Table 2.1: *Summary of the physical properties of the LPE YIG thin films and Pt used in this thesis.*

2.2 Transport in YIG|Pt nanostructures

In section 1.3, we developed the concept of charge current-induced spin dynamics at NM/FMI interfaces. This interplay allows one to inject and detect propagative spin

waves in YIG via the flow of electron in a spin-orbit metal.
Such perspective has been considered theoretically in the work of Zhang et al [99, 128] in a Pt|YIG|Pt trilayer where a spin current is produced by the Pt|YIG bottom layer and detect in the YIG|Pt upper layer. Experimental proof of spin wave propagation up to 100 nm in a sandwich configuration is addressed in work [157, 158]. However, the experiment requires the growth of the YIG film directly on a Pt substrate. This fabrication method suffers from a dramatic increase of the magnetic damping of the YIG due to the large lattice mismatch between YIG and Pt. This geometry is thus not preferable for manipulating propagative spin waves since it will reduce the magnon propagation length.

2.2.1 Lateral geometry

Optimal geometry for spin wave transport in YIG is to spread the metallic probes laterally. In the spirit of lateral spin valves, this consists of two narrow Pt stripes deposited on the top of the YIG film as displayed in FIG.22.a. This geometry is highly optimal for studying magnon transport in YIG for two reasons: first, we can benefit from the small damping of YIG grown on GGG substrate. Second, it makes the possibility of fabricating multiples devices on the same YIG sample with various distances between the two Pt contacts allowing to probe the transport properties of magnon in YIG more reliably.

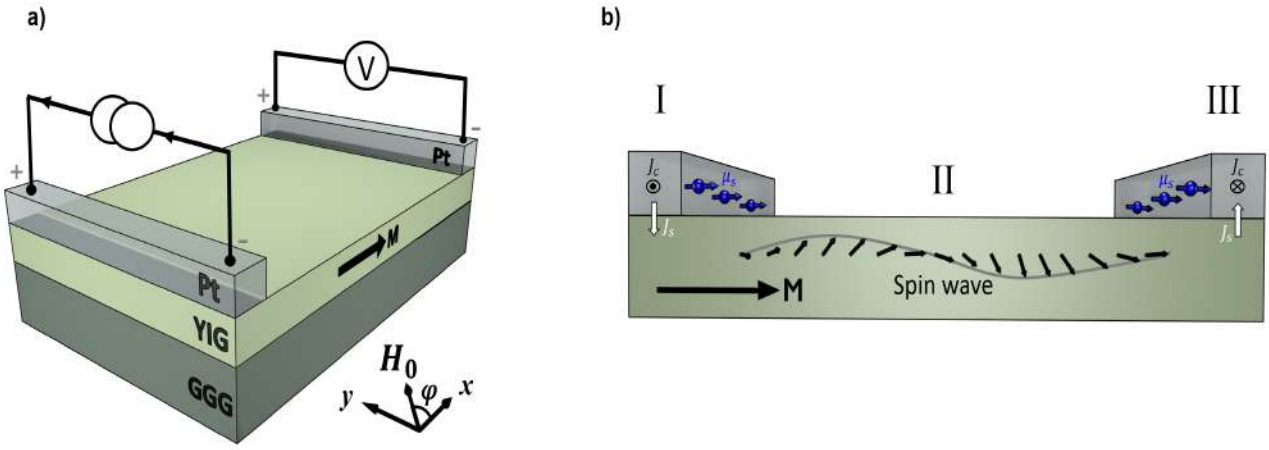

Figure 22: *a) Schematic of the lateral geometry for non-local spin waves transport in Pt|YIG|GGG heterostructures. b) Side view of the non-local spin waves transport. Sending a charge current into the left side Pt will produce a spin accumulation $\Delta\mu$ at the Pt|YIG interface and induce an excess of magnons if the magnetization $\boldsymbol{M}$ is colinear to the spin accumulation polarization. According to the low magnetic damping of YIG, the spin wave will propagate over μm distances. When the propagative spin wave reached the right Pt strip, the angular momentum is pumped into the Pt layer due to the spin pumping process. The net spin current flow into the Pt is then reconverted back into a measurable current via ISHE.*

The physical mechanism of non-local spin waves transport can be summarized as follows (see FIG.22.b) :

I: A charge current $\boldsymbol{J}_c$ is induced in the left Pt strip which generate a spin current $\boldsymbol{J}_s$ by SHE. This spin current will generates a steady state spin accumulation $\Delta\mu$ at

the Pt|YIG interface with a spin polarization s. If the YIG magnetization $\boldsymbol{M}$ is colinear to s, the spin accumulation can be transferred to the underneath YIG by spin-flip scattering process (section 1.3.4) and result in a broad excitation of the magnon spectrum. Through this static method, several magnon branches are produced within a frequency range from GHz to THz in contrast to the inductive method [159, 160, 161, 162] in which the wavelength of the excited wave is selected.

II: Each magnon mode n produced at the Pt|YIG interface will propagate in the YIG film according to the magnon propagation length L_m^n.

III: Propagating magnons will reach the right Pt strip and accumulate at the YIG|Pt interface. This will generate a spin current $\boldsymbol{J}_\mathrm{s}$ via the spin pumping process which will be converted back the spin current $\boldsymbol{J}_\mathrm{s}$ into a charge current $\boldsymbol{J}_\mathrm{c}$ and thus a measurable voltage.

2.2.2 Pulse Delta method

An essential element of our studies on YIG|Pt devices has been the use of a pulse method to measure the non-local voltage, as it allows a significant reduction of Joule heating when a large electrical current is injected in the Pt wires. For our setup, the current pulses are generated by a 6221 Keithley Current Sources and the induced voltage pulses are measured synchronously by a 2182A Keithley Nanovoltmeter. We use the so-called delta-mode, where the induced voltage is calculated through a 3-point-average reading, taking into account also the induced voltage before and after the pulse (when I=0). In the Keithleys, the clock is set by the power line cycle (PLC), which has a period of 20ms. We chose the width of the pulse duration to be 10 ms and the interval between pulses to be 100 ms (5 PLC), which corresponds to a 10% duty cycle. We have checked that no significant additional heating is generated by the cumulative reading of the voltage with these cycles. The analysis of the pulse current injection in our devices is also reported in *Physical Review B* [163]. Temperature sensing is provided by the change of relative resistance of the Pt wire during the pulse. In FIG.23.c, we have plotted $T_\mathrm{Pt} = \kappa_\mathrm{Pt}\ (R_I - R_0)/R_0$ as a function of the current I, where R_I and R_0 =1.3 kΩ are respectively the electric resistance of Pt in the presence and absence of large heating current, and the coefficient $\kappa_\mathrm{Pt} = 254$ K is specific to Pt at R_0. We observe that the pulse method allows keeping the absolute temperature of YIG below 355 K (YIG saturation magnetization decreases by about 4G/°C) at the maximum current amplitude of 2.5 mA ($12 \times 10^{11}\mathrm{A/m^2}$). Reduction of the duty cycle to 1% shows no significant temperature deviations with the 10% setting when one monitors the variation of the Pt relative resistance as a function of current. To avoid any transient regime, a 100 μs delay is applied on the detector voltmeter in order to wait for the stabilization of the voltage before triggering the reading of the nanovoltmeter. For each bias, the non-local voltage is calculated from the average of 100 pulses, to obtain a ten-fold enhancement of the signal to noise ratio.
We characterized the transient regime associated with the use of current pulses to make sure that it doesn't alter the determination of the non-local voltage. First, we shall concentrate on the time evolution of the saturation magnetization underneath the injector, when a pulse of electrical current is injected in the Pt wire. These measurements are inferred from time resolved μ-BLS spectroscopy (see Appendix A). To achieve this, we use a current pulse generator that produces 250 ns wide current burst, synchronized with the μ-BLS setup. We use this to register the spectrum at different delays. One can extract the variation of saturation magnetization produced by Joule heating, ΔM_s, from the shift in the position of the main peak in the μ-BLS spectrum using the Kittel's formula and by assuming that this maximum corresponds to the FMR frequency. The result is

shown in FIG.23.a and b for both positive and negative current pulses while the applied magnetic is set at H_0 =1 kOe perpendicularly to the Pt strip (along y). The temporal evolution shows a characteristic rise time of about 200 ns at $I = +2$ mA. It is interesting to note that the variation of the saturation magnetization caused by the current in the Pt stripe, shows the same sign for both polarities of the current. The possible explanation is that the efficiency of SOT reduces with increasing frequency of magnons because of the increase of their relaxation frequency, while the effects of the Joule heating on the magnon population are expected to be frequency-independent. Because of the large phase volume of high-frequency magnons, the total magnon population is then strongly affected by the Joule heating, which counteracts the magnon "cooling" effect of SOT. This conclusion is further supported by the slow temporal variation of M_s at $I < 0$ (FIG.23.a), which can be associated with the slow temperature rise due to the Joule heating. By comparing the data for I >0 and I <0 in FIG.23a, one can conclude that, in spite of the large contribution of the heating effects, at least 60% of the detected signal at $I = +2$ mA is due to the magnons excited by SOT. This significant contribution, enabling reliable characterization of the effects of SOT, originates from the small width of the current pulses preventing significant increase in the temperature of YIG. With these settings, the noise floor obtained is around the 5 nV range for a measurement period of about 10 s.

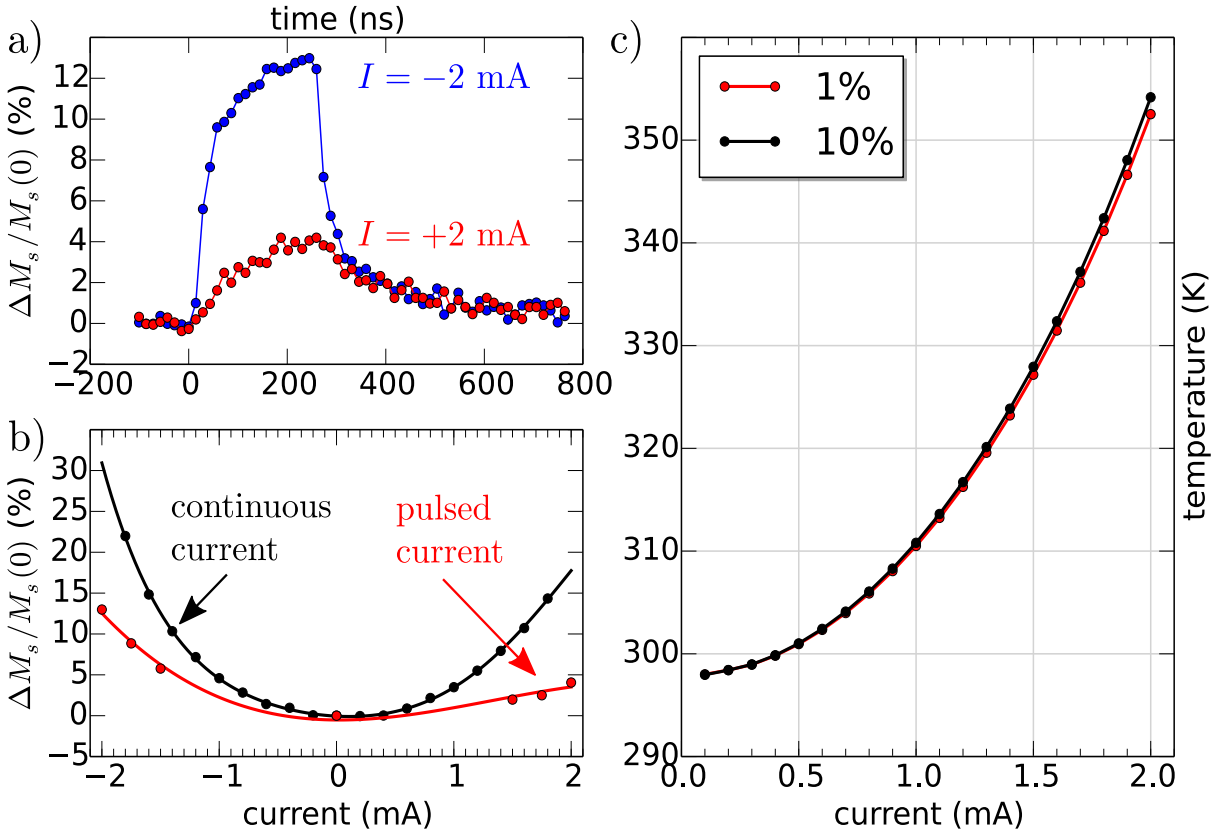

Figure 23: *a) Temporal evolution of the relative reduction of the saturation magnetization, $\Delta M_s(I)$ / $M_s(0)$, during a current pulse for the two different polarities. b) Current dependence of the maximum obtained in the pulsed- and continuous-current regimes. The data were recorded by placing the probing spot onto the Pt injector stripe. The solid curves are guides for the eye. c) Variation of the effective temperature of the Pt wire as a function of the duty cycle using the pulse method.*

2.2.3 Symmetry and sign considerations

In non-local devices, the electrical current flowing in the metallic wire can affect the magnon population inside the magnetic insulator in two ways. Spin transfer is the first mechanism. Spin-polarized currents generated inside the metallic wire due to spin-orbit effects transfer to the adjacent magnetic insulator layer and produce a torque on the magnetization. Joule heating is the second possibility. The Ohmic dissipation in the metallic wire locally increases the magnetic layer temperature, which is in thermal contact, and correspondingly, the number of thermal magnons (the saturation magnetization in YIG decreases at a rate of about 4G/°C at room temperature).
To separate these two contributions, we rely on the symmetry of the signal with respect to the current or field polarity. We first concentrate on the current symmetries. In the case of spin-orbit torques, the electron trajectory inside the normal metal is deflected towards the interface depending on the spin polarization of the electron.

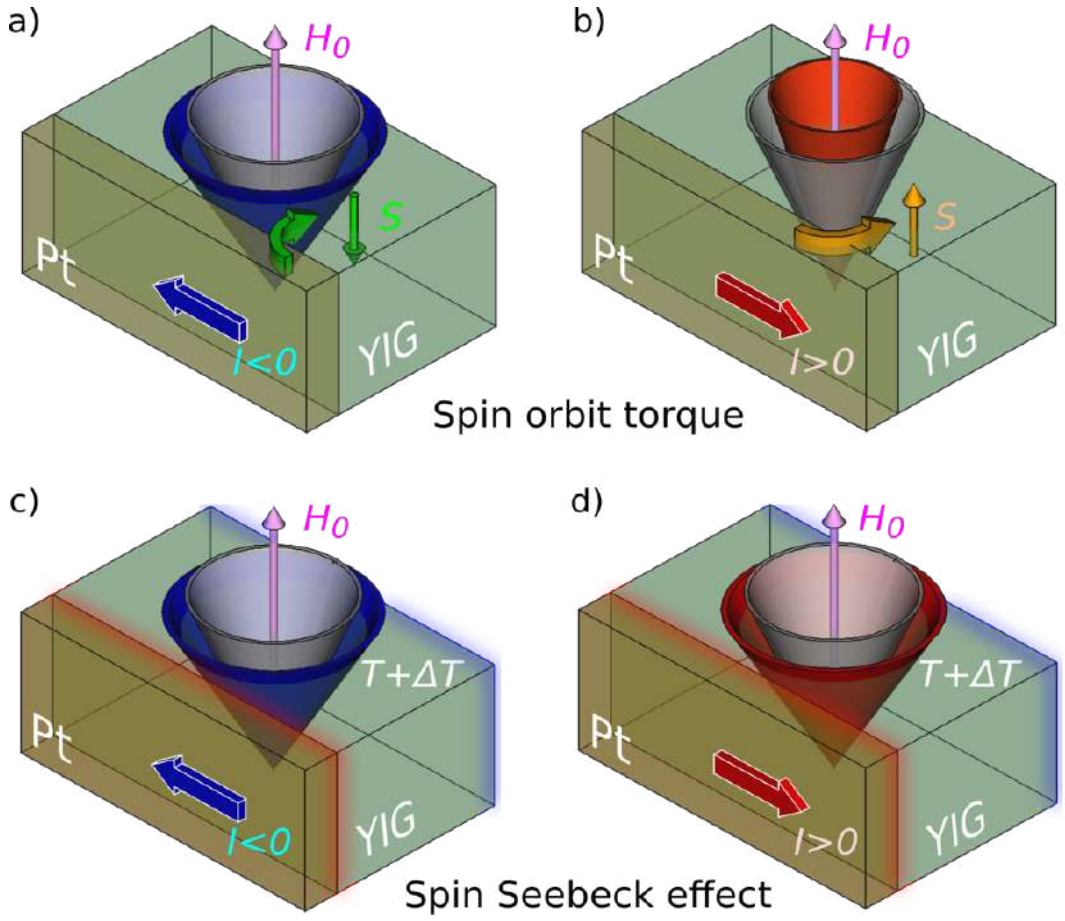

Figure 24: *Schematic illustration of spin-transfer processes between a magnetic insulator and an adjacent metallic layer where an electrical current circulates. The first row shows the principle of SOT, where the electron trajectory inside the normal metal is deflected towards the interface depending on the spin polarization of the electron. The second row shows the principle of SSE, where temperature rises associated with Joule heating change the distribution of thermal magnons. Changes in the amplitude of magnon mode is illustrated as a variation of its cone angle from nominal occupation shown in grey (thermal population at device temperature).*

As seen from the comparison of the current dependences of M_s obtained in the pulsed-

and continuous-current regimes (FIG.23.b), utilization of short pulses results in a strong increase of the asymmetry of the measured dependences reflecting the antisymmetric contribution of SOT. As a precaution, the 20 first pulses are disregarded from the statistics to ensure that a steady state regime has been reached. In this condition, the deviation of the individual pulse appears to follow a normal distribution around the average, for all pulse amplitude. For metals like Pt, where the spin Hall angle θ_{SHE} is positive, the deflection follows the right-hand side rule as shown schematically in FIG.24.a) and b) for both positive and negative currents. The result is an inversion of the polarity of the outward spin current when the electrical current direction is inverted. The net effect is an opposite change in the magnon population. The nominal occupation (thermal population at device temperature) of a particular mode is depicted as a gray cone in FIG.24. If the spin is injected parallel to the magnetization direction, it will decrease the cone angle (magnons annihilation, FIG.24.b), while if the spin direction is opposite to the magnetization direction, this will increase the cone angle (magnon creation, FIG.24.a). Thus, an important signature of SOT is that the signal is odd with respect to the current polarity. In contrast, a change of the magnons population produced by thermal effects is even in current, since the origin is Joule heating which is proportional to I^2. This distinction between even and odd symmetries with respect to the current polarity translates in a signal appearing in different harmonics when performing lock-in measurements [2]. In the case of SOT, odd in current, the signal is captured by the 1st harmonics, while in the case of SSE, even in current, the signal is captured by the 2nd harmonics. There is a direct correspondence between these symmetries concerning current direction and symmetries related to the magnetization direction.

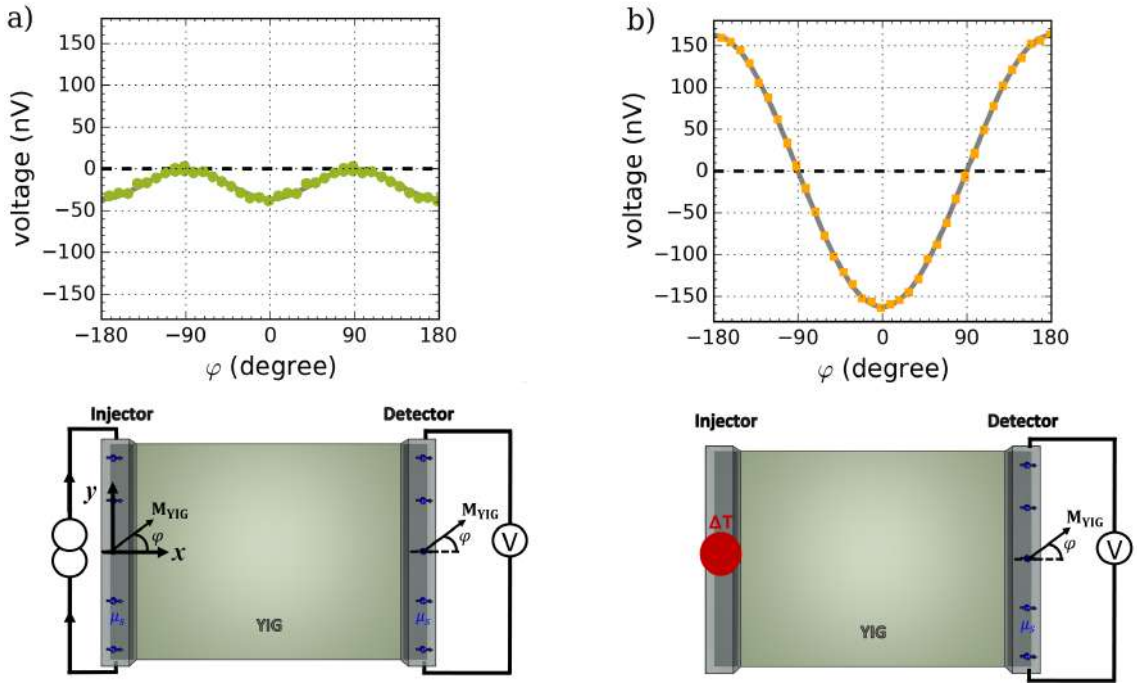

Figure 25: *a) and b) present the angular dependence of the Σ_φ and Δ_φ signal calculated from equations* (2.3) *and* (2.4) *for an injected current I=+1.5 mA and applied field of $H_0 = \pm 2kOe$ (the grey lines are $\cos(\varphi)$ and $\cos^2(\varphi)$. c) Schematic of injection and detection of magnon in YIG by SOT. d) Schematic of detection of spin Seebeck signal induced by temperature gradient generate via Joule heating.*

The magnetization is, in the case of YIG, set by the external magnetic field orientation.

However, we also need to take into account that the signal inverts its polarity when the magnetization reverses underneath the detector. Thus, the net effect is that the SOT signal is even, while the SSE signal becomes odd with respect to field polarity. If one performs an azimuthal angular dependence, the even signal follows a $\cos^2$-behavior, while the odd signal follows a cos-behavior. A simple picture of these phenomena can be seen in FIG.25. A charge current J_c flowing into the injector strip can generate a spin current inducing a spin accumulation $\Delta\mu$ at the Pt|YIG interface which is polarized along the x-axis (FIG.25a). Non-equilibrium magnons are generated in YIG by spin-orbit torque (SOT) when the magnetization of YIG is colinear to the spin accumulation which gives rise to a $\cos\varphi$ dependency of the injected magnon density. Then magnons diffuse in the YIG film. When it reaches the detector, propagative magnon density is pumped by the interface leading to a spin accumulation that also has a $\cos\varphi$ dependence. The total magnon signal is driven through the injector and detector interface lead to a $\cos^2\varphi$ dependence. Since the torque is exerted on the transverse magnetization (the oscillating part of the magnetization), the effect is maximum when the saturation magnetization is parallel to the injected spin direction, or in other words perpendicular to the current flow in the Pt, as first demonstrated in ref.[2]. However, the current in the injector strip also induces a Joule heating that produces a net temperature gradient along the Pt|YIG volume (FIG.25b). Via this heating, magnons are thermally excited by spin Seebeck effect (SSE) and diffuse in YIG as well. The thermally excited magnons are probed by the detector strip in the same way as for electrically excited spin waves but display a $\cos\varphi$ dependence [164, 98]. These thermal effects must be disentangled from pure spin effects. To separate the pure spin contribution, Cornelissen et al.[2] have proposed to consider solely the anisotropic part of the transport as one varies the orientation of the magnetization in-plane. Among these anisotropic contributions, as emphasized above, one should thoroughly distinguish the ones that are even with respect to the magnetic field or current polarity from the ones that are odd. In ref.[2], the authors, using the 1st and 2nd harmonic output of a lock-in, have relied on the current symmetry to extract the SOT and SSE. This can also be achieved by performing a pulse measurement and detect the voltage obtained with the two possible polarities of the externally applied magnetic field. Thus we construct the two following signals :

$$\Sigma_\varphi = \frac{(V_\varphi - V_{\hat{y}})}{2} + \frac{(V_{\overline{\varphi}} - V_{\hat{y}})}{2} \tag{2.3}$$

$$\Delta_\varphi = \frac{(V_\varphi - V_{\hat{y}})}{2} - \frac{(V_{\overline{\varphi}} - V_{\hat{y}})}{2} \tag{2.4}$$

where $\overline{\varphi} = \varphi + 180°$. The result is summarized in FIG.25.a and b. It is important to notice that the part that is even with respect to the magnetic field polarity (Σ) is odd with respect to the current polarity, while the part that is odd with respect to the magnetic field polarity (Δ) is even with respect to the current polarity. These are exactly the expected symmetries of SOT and spin Seebeck effects.

2.2.4 Local measurement

The features of these non-local voltages also appear in the local voltage. This can be viewed as a self-detection of the ISHE voltage on the injector side. In the case of the Σ-signal, the produced effect is the so-called spin Hall magnetoresistance [16, 62]. As explained previously, the signal is maximum when the magnetization is perpendicular to the flow of current inside the Pt and minimum when the magnetization is parallel to the flow of current. Experimentally, however, this formulation seems at a first glance

counter-intuitive since the total resistance appears to drop when the magnetization is perpendicular to the flow of current. This is because the drop in the voltage produced by SOT is negative for positive current (and reciprocally) and thus appears as a negative resistance effect. This drop is a direct consequence of the Hall origin of the Σ-signal that increases along the current direction for ISHE.
In the same way, a local-SSE signal [165] should appear on the device in continuity with the non-local Δ-signal mentioned previously. This local Δ-signal is negative in continuity with the sign of Δ observed for very small gaps, and means that the vertical thermal gradient is negative i.e. that the YIG|Pt interface is hotter than the YIG|GGG interface. The current dependence of this local-SSE should be quadratic (as I^2, Joule heating) in current. Note that this behavior has the same signature as the uniaxial magnetoresistance [166]. In this respect, a resistance that is linear in current and changes sign when the current is inverted is equivalent to a voltage that varies quadratically with I, which is usually interpreted as a Joule heating signature.

2.2.5 Angular and current dependence of the non-local signal

For the sake of demonstration, we have performed a non-local measurement in an 18 nm YIG thin film (YDPB8). In FIG.26 we present the non-local signal $V_{\varphi|I}$ as function φ which is defined as the angle between the applied magnetic field H_0 and the x-axis

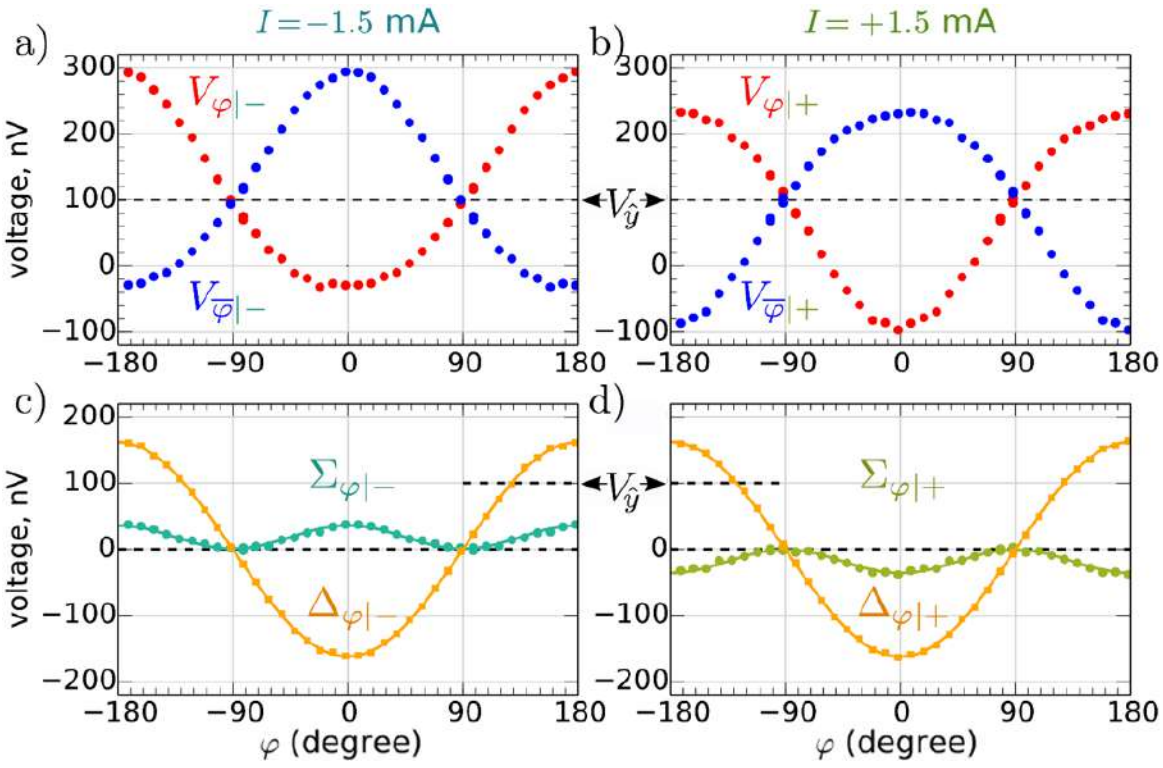

Figure 26: *Angular dependence of the non-local voltages $V_{\pm|\mp}$ measured while inverting the polarity (φ along x, $\bar{\varphi}$ along -x) of the applied field $H_0 = \pm 2kOe$ (red/blue) respectively for a) negative and b) positive current pulses $I = \mp 1.5mA$. The measured signal can be decomposed c) and d) in three components: Σ (green): the signal sum, Δ (orange): the signal difference and $V_{\hat{y}}$: the offset; respectively even/odd, odd/even in field/current, and an angle independent contribution (dashed).*

This is a crucial step since it allows us to define the exact nature of each component gather in $V_{\varphi|I}$. It is particularly interesting to measure the non-local voltage when the field H_0 is (anti)colinear to the y-axis ($\varphi = +90°$) since it switches off the spin sensibility ($M \cdot s = 0$). In such a situation, we expect no contribution to the spin transport to the $V_{\varphi|I}$ signal. For each value of φ, 4 measurements $V_{\varphi|I}$ are performed corresponding to the 4 combinations of the polarities of $H_0|I$. FIG.26.a and FIG.26.b displays the raw data obtained respectively for negative and positive current pulses ($I = |1.5|$ mA) and $H_0 = \pm 2$ kOe (much higher than the Oersted field at this current $H_{\text{Oes}} < 50$ Oe). Clearly, the non-local voltage oscillates around an offset $V_{\hat{y}}$, defined as the voltage measured at $\varphi = \pm\ 90°$. One contribution of this offset can be ascribed to thermoelectric effects at the two Pt|Al contacts of the detector circuit, which are sensitive to any temperature gradient along the y-direction inherently produced by any resistance asymmetry along the Pt wire, which imbalances Joule heating. We have sorted the SOT and SSE according to eq 2.3 and 2.4 by creating Σ_φ, the even part of $V_{\varphi|I}$ with respect to the direction of the applied magnetic field (green) and Δ_φ the odd part with respect to the direction of the applied magnetic field (orange). This separation is exposed in their angular dependences, which follow two different behaviors, one in $\cos^2\varphi$, the other one in $\cos\varphi$, respectively. The solid lines in FIG.26.c and 26.d are fits by these two functions. These angular dependences originate from the nature of the excitation of Σ_φ and Δ_φ respectively as explained above. Hereafter, we shall use the fit of the whole angular dependence as a means to extract precisely the amplitude of Σ_0 and Δ_0 at φ =0°.
FIG.27 shows their evolution as a function of the current I. One observes that $\Sigma_{0|I}$ is odd in current, while $\Delta_{0|I}$ is even in current, which are both the expected symmetry of SOT and spin Seebeck effects with respect to current polarity. Importantly, this odd/even correspondence between the symmetries of $\Sigma_{0|I}$ and $\Delta_{0|I}$ extends (within our measurement accuracy) on the whole current range. While $\Delta_{0|I}$ approximately follows the parabolic increase of the Pt temperature (cf. FIG.23.c), as expected for thermal effects, the interesting novel feature is the fact that $\Sigma_{0|I}$ deviates from a purely linear transport behavior at large I. This nonlinear regime is reached for a crossover current density of $J_c = 6.0{\times}10^{11}\text{A/m}^2$ and translates a shift of the magnon transport regime. For the rest of this chapter, we will study the physical origin of the total spin signal, and more particularly we will focus on the spin-transfer at the interface. The origin of this non-linear Σ signal will be uncovered in more detail in chapter 4.

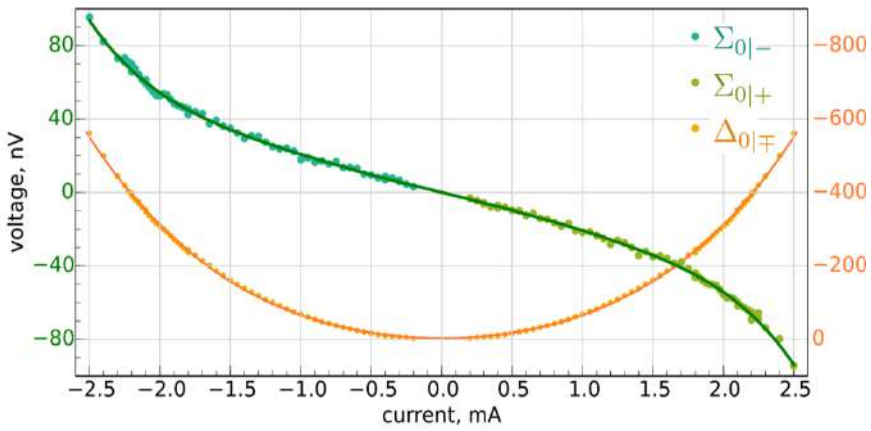

Figure 27: *Current dependence of the amplitude* Σ *and* Δ *at* $\varphi = 0$.

2.2.6 Control experiment: YIG|Ti interface

To further evidence the nature of Σ and Δ spin signals, we have performed a control experiment by using a YIG|Ti interface. Ti is a light transition metal that posses a small atomic number Z =22. This material presents quite low electrical and thermal conductivity but is strongly corrosion resistant and possess a paramagnetic order. From the literature [167], it is generally found that the strength of the spin-orbit coupling (SOC) scale as a Z^4. It has been experimentally shown via spin pumping [168, 169] that the conversion at the YIG|Ti interface is rather low. The spin Hall angle $\theta_{\mathrm{SHE}}^{\mathrm{Ti}}$ of the Ti has been estimated in the order of $4{\times}10^{-4}$ which is much smaller than any reported Pt spin Hall angle. Since the spin Hall angle θ_{SHE} in Ti is very small, we do not expect any conversion from charge to spin current in Ti neither a spin sensibility at the YIG|Ti interface.

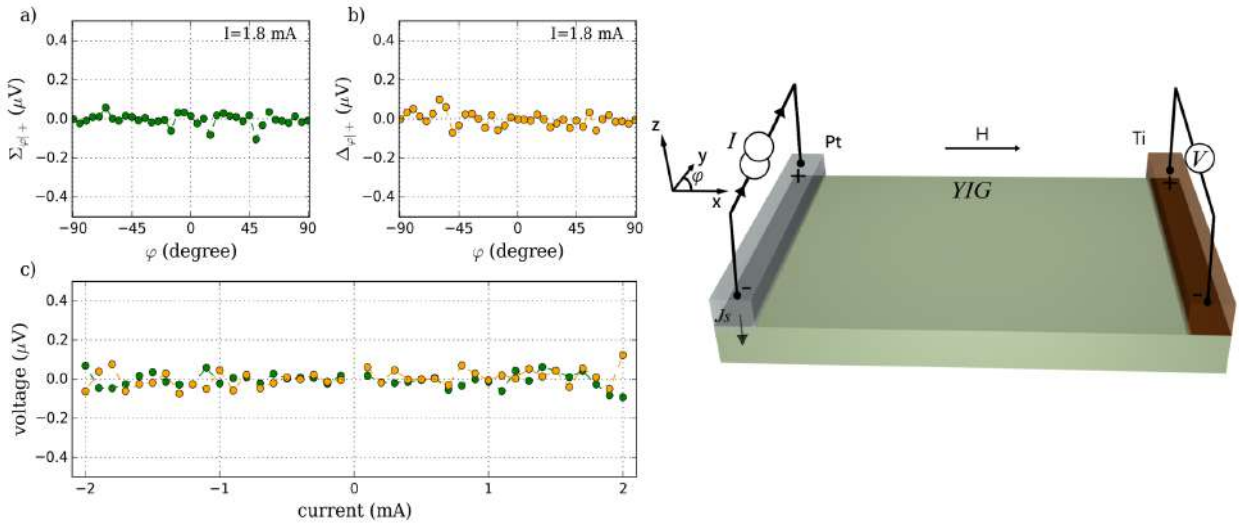

Figure 28: *Non-local spin transport experiment for a YIG|Pt(7 nm) injector and YIG|Ti(15 nm) detector separated by a distance of 200 nm. Angular dependence of Σ,Δ signal are presented in a) and b). Non-magnetic offset signal measured at φ=90° is systematically subtracted. It results that no angular dependence is detected through YIG|Ti interface. Panel c) displays Σ,Δ spin signal (at φ=0°) measured in the YIG/Ti interface as a function of the current injected in the YIG|Pt interface.*

Non-local spin transport experiment using a YIG|Ti interface can be seen in FIG.28. Here a large current density is injected into a Pt strip giving rise to a net spin wave density in YIG via the YIG|Pt interface. A Ti electrode as been deposited 200 nm away from the Pt strip and will play the role of the detector. FIG.28.a and b present the angular dependence of the voltage drop in the Ti strip while a current of I =1.8 mA is applied to the Pt strip. Like every Σ signal presented in this thesis, we have analytically subtracted the non-magnetic offset signal present at φ =90 °. We do not observe any angular dependence in the Σ and Δ signal from low to high current (see FIG.28.c). At this current density, previous measurements have shown that indeed a large spin wave density is flowing into the YIG and will inevitably cross the YIG|Ti interface. From this measurement, we can confirm that Ti has a small spin Hall angle. Using the same device, we have performed a non-local experiment where we have switched the Ti strip as an injector and the Pt strip as a detector. The result of the non-local experiment in this configuration is displayed in FIG.29. We observe a cos(φ) like angular dependence in the Δ signal that increases quadratically with the applied current in Ti strip which is this

signature of the spin Seebeck effect. This is not surprising since the Ti strip resistance was high (ρ_{Ti} =123 $\mu\Omega$.cm), resulting in a strong thermal gradient in the Ti by Joule heating. This confirms even more the thermal nature of Δ signal and the role of the Pt detector in that matter. No angular dependent is observed in the Σ signal as it can be seen in FIG.29.a.

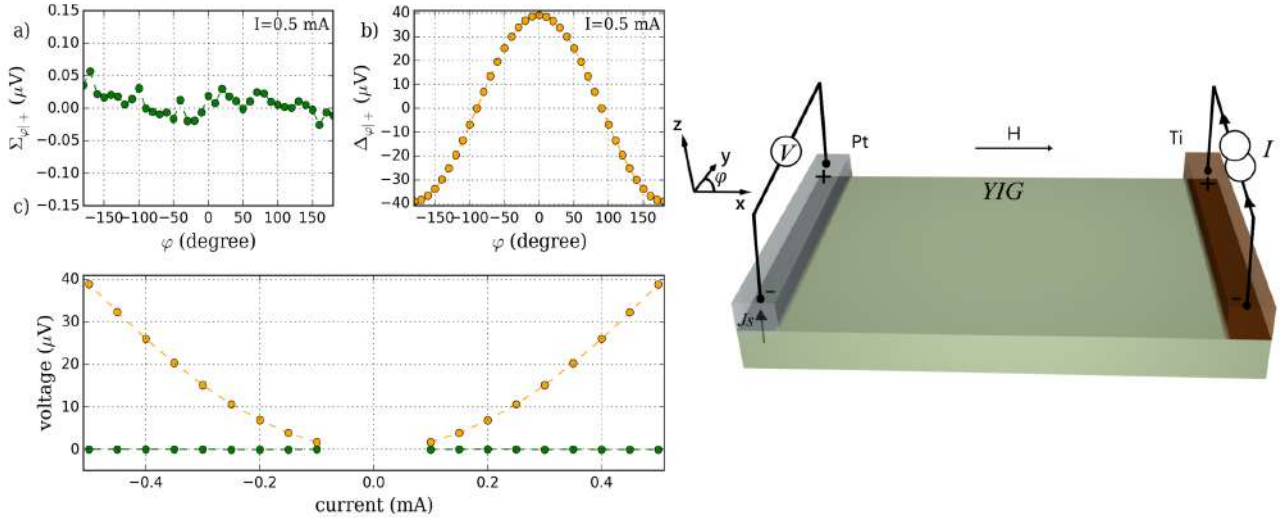

Figure 29: *Non-local spin transport experiment for a YIG|Ti(15 nm) injector and YIG|Pt(7 nm) detector separated by a distance of 200 nm. Angular dependence of* Σ,Δ *signal are presented in a) and b). We observe a strong angular dependence in the* Δ *signal due to the spin Seebeck effect while a small signal is detected in* Σ*. Black line in a) and b) panels are cos(*φ*)sin(*φ*) and cos(*φ*) fits. Panel c) display* Σ,Δ *spin signal (at* φ*=0°) measured in the YIG|Pt interface as a function of the current injected in the YIG|Ti interface.*

The absence of any Σ signal for small and large driven current is the direct prove the spin waves excitation is mediated through the spin accumulation at the interface. This can be explained by the small spin Hall angle of Ti which is in agreement with the literature.
These observations show that spin-orbit coupling is an essential ingredient for exciting and detecting spin waves in YIG.

2.3 Enhancement of YIG|Pt interfacial spin transmission via a local heating by Joule effect

Now that we have demonstrated the important role of the Pt layer to realize the spin to charge interconversion, careful engineering of the YIG|Pt interface has to be established. For future magnonics based electronics, it is crucial to realize devices that can reliably interconvert a charge current into a spin wave. The ratio of the conversion from spin to charge (or charge to spin) in the Pt is given by the spin Hall angle θ_{SHE}. In the last years, considerable attention has been given to SHE in Pt mainly for its large spin Hall angle θ_{SHE}. On the other hand, the transfer of angular momentum is carried out via the interface. A spin transparent YIG|Pt interface is then highly needed. The figure of merit in that matter stands for the spin mixing conductance $g_{\uparrow\downarrow}$, which quantitatively translates the efficiency of the spin transfer at the interface.

It is known that $g_{\uparrow\downarrow}$ is very sensitive to the chemical and structural condition of the YIG|Pt interface and can be tuned via various treatments of the YIG surface. In several reports, it has been shown that an *in-situ* O^+/Ar^+ etching [69, 170, 171] before the Pt deposition, can remove organic matter in the YIG surface in a reliable way. It results in a higher spin transparent interface as shown by the spin pumping signal which highlights an enhancement of $g_{\uparrow\downarrow}$. Annealing of the garnet crystal has also been realized in the temperature range of 500 - 1100 °C to treat lattice defects, most likely due to the formation of PbO provided by the solvent mixture [172, 173]. This also helps in evaporating any water film on the YIG surface if the Pt layer is deposited *ex-situ*. Interface treatment of the YIG with "piranha" etch, a mix of H_2SO_4 and H_2O_2 solvent, has also proven its efficiency. In ref [174], it has been demonstrated that the chemical content of YIG surface is mostly composed of C and O. The carbon contamination can be more or less removed via etching or annealing, but the best results are found in the combination of the "piranha" technique with annealing [174] or O^+/Ar^+ [170] treatment because it can remove carbide interfacial layer and sulfur elements. The surface engineering of the YIG has also an impact on the structural quality of the deposited Pt layer. Indeed if C content at the interface of the YIG is not removed, a part of the carbon can diffuse into the Pt layer [174]. This phenomenon is found to have a clear impact on the Pt conductivity, because of the formation of grain boundaries [175] which can be removed by annealing. Nevertheless, these treatments have been performed on μm thick YIG sample and cannot be realized if the thickness of the film is about a few nm because it can alter the YIG layer.
In the following, we propose to explore the spin transmission in the case of Pt deposited on top of YIG by e-beam evaporation. We will show that passing a large current inside the Pt provides a kind of annealing which enhances the spin conductivity through the interface. This trick allows investigating on the same system the consequence of enhanced spin conductivity on the crossover currents reported before. We shall show that a better spin transmission can be realized without enhancement of the spin transparency $g_{\uparrow\downarrow}$.

2.3.1 Spin Hall magnetoresistance

The sample used in this study is a YIG film with a thickness of 56 nm that has been grown by liquid phase epitaxy on a 500 μm $Gd_3Ga_5O_{12}$ (GGG) substrate [16, 176]. After evaporated a 7 nm thick Pt layer onto the YIG film, we patterned 300 nm wide and 3.0 μm long Pt strips via e-beam lithography which are connected to a Ti|Au (5 nm/50 nm) layer for electrical measurements (see fabrication method in Appendix B). The sample is then mounted into a rotative insert, that is electrically contacted to the device with wire bonding, and placed in an electro-magnet. All magneto-transport experiment has been performed at room temperature for an applied in-plane magnetic field of $H_0 = \pm 2$ kOe to saturate the YIG film.
Tuning of the YIG|Pt spin conversion through local heating by Joule effect has been investigated via spin Hall magnetoresistance (SMR) measurements. The SMR measurement is performed by injecting a pulse current into the Pt structure via a 6221 Keithley that is synchronized to a 2182A Keithley Nanovoltmeter to measure the magnetoresistive response (see FIG.30). FIG.31.a presents the magnetoresistive signal measured for a driven current of I =100 μA when an in-plane magnetic field is rotating around the φ angle. The magnetoresistance represented by blue dots has been recorded directly after the nanofabrication process. This signal reaches an absolute when the magnetization is parallel to the spin polarization while the angular dependence magnetoresistance follow a $\cos^2(\varphi)$ behavior which is in good agreement with the theoretical prediction of the SMR [144]. To disentangle any parasitic contribution of the anisotropic magnetoresistance (AMR) [16],

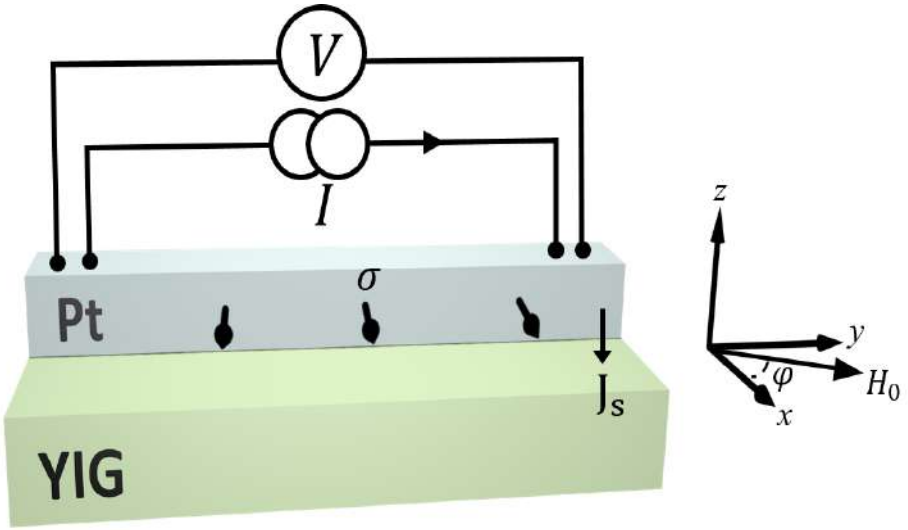

Figure 30: *Sketch of the YIG|Pt structure for SMR measurement. The Pt electrode deposited on the YIG film is electrically contacted to measure magetoresistive behavior of YIG|Pt structure when an in-plane magnetic field H_0 is rotating around the z-axis.*

we have inspected the magnetoresistive behavior at all polar angle φ, β and γ as can be seen in FIG.32. We observe a net dependence of the Pt resistance as we rotate the magnetic field H_0 around the φ and β angle while no change is measured when we rotate H_0 along the Pt wire (γ polar angle). If the AMR would have provided an additional magnetoresistive signal, we would have seen its signature by varying the γ angle. Thus we assert that the behavior observed in FIG.31.a highlights a pure spin Hall magnetoresistive signal. The SMR ratio has been calculated as SMR $= \Delta R(H)/R_0$ where R_0 =2.6 kΩ is the resistance value of the Pt strip at room temperature when no external field is applied. From a $\cos^2(\varphi)$ fit we extracted the maximum SMR magnitude $(\Delta R(\mathrm{H})/R_0)_{\max} \approx 2.9 \times 10^{-5}$. One should note that one can describe the SMR as a self SOT transport, where the effect is minimum when $H//y$ and maximum when $H//x$. Because the induced voltage by SOT subtracts to the Ohmic loss, it appears as a drop of the resistance. Thus plotted in absolute value (ie. adding Ohmic loss) appears as the signal is minimum when $H//x$.

Instead of chemically cleaning our YIG thin film with etching [170, 174], which might dramatically alter the film thickness for such thin films, we locally annealed the YIG|Pt interface by applying a large current density in the Pt layer. FIG.31.b shows the evolution of the Pt resistance when a large current density is applied. This behavior follows a quadratic dependence as the current density is increased due to Joule heating. The temperature induced in the structure has been estimated by measuring the change of Pt resistance via $\Delta T = \zeta_{\mathrm{Pt}}(R_I - R_0)/R_0$, were $\zeta_{\mathrm{Pt}} = 478$ K is a proportional factor (R_0 dependent). Around the maximum applied current, the local temperature reaches an amplitude of 550 K. Note that the current density is not high enough to reach the electromigration breakdown that would result in an increase of Pt resistivity [177]. As the amplitude of the pulse current is slowly ramped down, the resistivity of the Pt remains nearly unchanged and we systematically observe a 1% drop after $J = 12 \times 10^{11}\mathrm{A/m}^2$ (insert of FIG.31.b). After applying a current density of $12 \times 10^{11}\mathrm{A/m}^2$ (equivalent to heating the sample at 550 K) within a 10 ms pulse for 60 minutes, we have measured

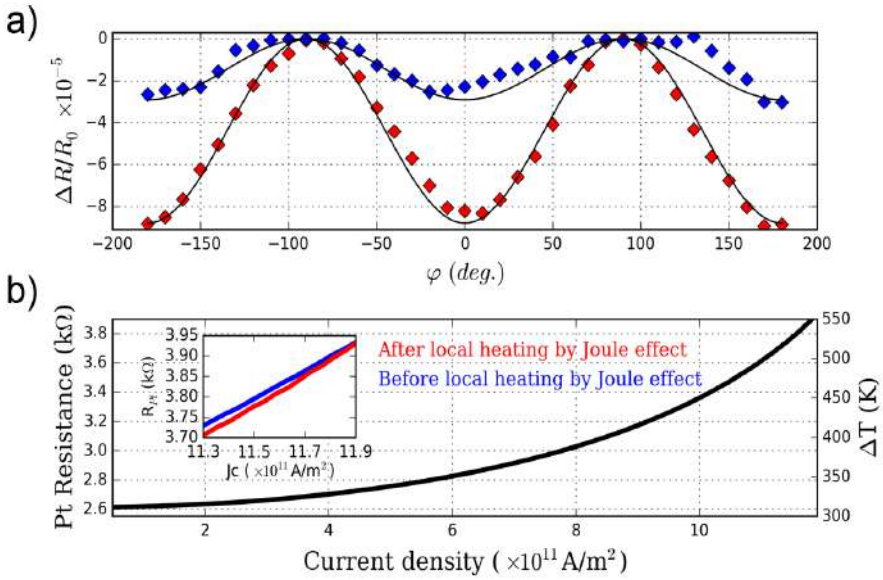

Figure 31: *a) In-plane angular dependent SMR for an applied magnetic H_0=2 kOe, before (blue dots) and after (red dots) local heating by Joule effect. b) Evolution of the Pt resistance as a function of the injected current density. The temperature generated by Joule heating has been estimated using $\Delta T = \zeta_{Pt}(R_I - R_0)/R_0$. The insert shows the small change of the Pt resistivity after annealing.*

again the angular dependent SMR in the same conditions and can be seen as red dots in FIG.31.a. We observe a SMR ratio that reaches now a maximum of $(\Delta R(H)/R_0)_{\max} \approx 8.9 \times 10^{-5}$ which is irreversibly 3 times larger than the value without annealing. To get more insight into the quality of the interface we have quantitatively studied the SMR before and after heating locally by Joule effect. From the SMR theory [144, 62] the dependence of the Pt resistance on the magnetization direction can be express as:

$$R_{\mathrm{Pt}} = R_0 - \Delta R(H)\, m_x^2 \tag{2.5}$$

Where m_x is the magnetization component along the x-direction. Using the analytical expression presented in section 1.3.7, the maximum magnitude of the SMR ratio can be described as :

$$\mathrm{SMR} = \left(\frac{\Delta R(H)}{R_0}\right)_{\max} = \theta_{\mathrm{SHE}}^2 \frac{\frac{2\, l_{\mathrm{sf}}^2 \rho}{t_{\mathrm{NM}}} G_{\uparrow\downarrow} \tanh^2\left(\frac{t_{\mathrm{NM}}}{2\, l_{\mathrm{sf}}}\right)}{1 + 2\, l_{\mathrm{sf}} \rho G_{\uparrow\downarrow} \coth\left(\frac{t_{\mathrm{NM}}}{l_{\mathrm{sf}}}\right)} \tag{2.6}$$

where $\rho = 19.5\, \mu\Omega$.cm is the resistivity, t_{NM} the thickness and λ_{sf} the spin diffusion length of the Pt layer while $G_{\uparrow\downarrow}$ is the spin mixing conductance ($g_{\uparrow\downarrow} = \frac{h}{e^2}\, G_{\uparrow\downarrow}$) of the YIG|Pt interface. Let's now discuss the potential origin of the enhancement of the SMR observed in FIG.31.a. The SMR ratio can change via various parameters. It cannot be attributed to a variation of Pt resistivity since the resistivity after local heating by Joule effect does not change more than 1 %. But heating locally by Joule effect could possibly change the quality of the Pt layer that might increase either the spin hall angle θ_{SHE} or spin diffusion length λ_{sf}. However, the θ_{SHE} is expected to be linear with the resistivity for an intrinsic origin [178] whereas the length $l_{\mathrm{sf}}\, \theta_{\mathrm{SHE}}$ is supposed to be a constant [179]. Since the local heating by Joule effect improves slightly the conduction of the Pt strip, the surge of the SMR signal is not consistent with a rise of θ_{SHE} and will be considered as a conserved

quantity throughout the whole annealing process. Thus we assume no change in the intrinsic and extrinsic spin Hall effect and only the spin conductivity of the interface is impacted by the local heating and is found to increase by a factor of 3 via local annealing. According to Eq. 2 the SMR ratio is in the same order of magnitude than the $g_{\uparrow\downarrow}$ reported after Ar^+-ion milling process [171] and "piranha" etch [170, 174]. Nevertheless, we would like to emphasize that this treatment only affects the YIG|Pt interface while the roughness of the YIG film remains unchanged contrary to etching process that alter or degrade the surface, which might be an issue in regards to ultra-thin film of YIG. We also note that we attempted to perform a similar experiment but for global annealing of the sample in oven. However, we didn't observe any change in the SMR ratio. Only a variation of total resistivity of the device has been probed due to a deterioration of Au|Ti contacts.

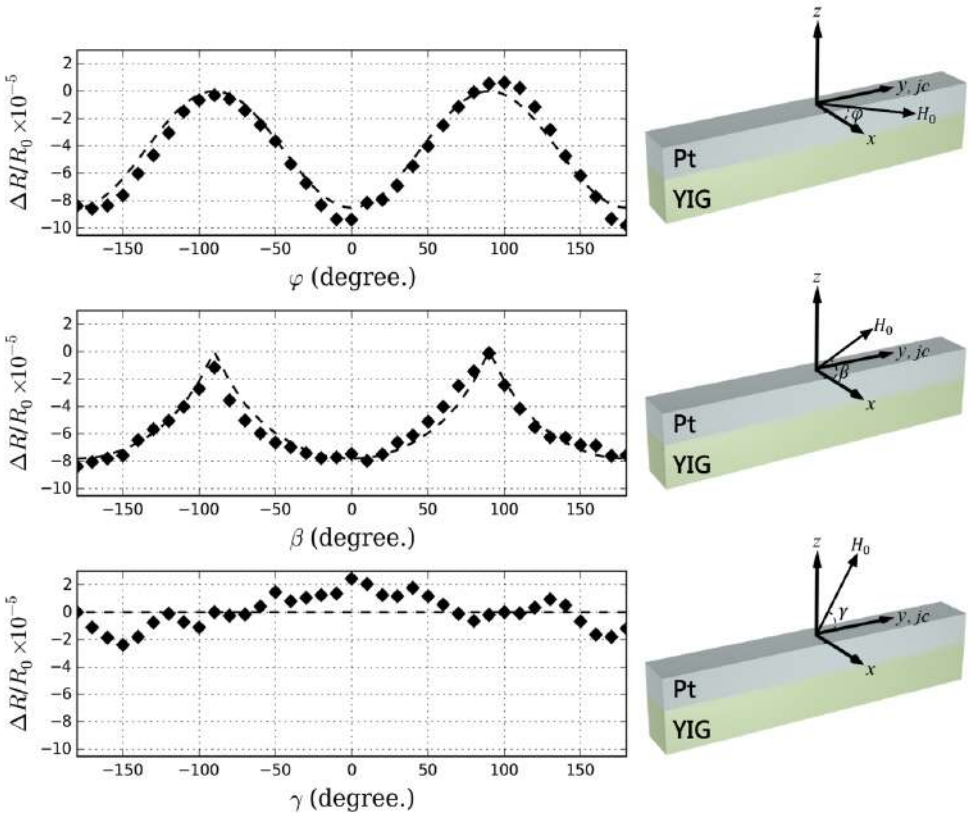

Figure 32: *a) Angular dependent SMR signal after local heating by Joule effect measured when a magnetic field H_0 with an amplitude of 2 kOe is apply along the φ, β and γ angle. The dashed lines are fit from equation 2.5. The different shape of the angular dependence with the β angle is due to the demagnetized field which tens to misaligned the equilibrium position of the YIG magnetization with the external field.*

2.3.2 Spin pumping

Next we have studied the spin transmission of our YIG|Pt interface by mean of spin pumping (SP). We have placed a sample taken from the same batch in a microwave resonant cavity where the rf magnetic field is uniform. As display in FIG.33.a, the experiment is performed by applying an rf magnetic field h_{rf} along the local Pt strip that is fixed at the frequency of 9.65 GHz. In the meantime, a static external magnetic field is sweeped perpendicularly to the Pt strip (along x). At the ferromagnetic resonance conditions, a part

of the angular momentum in YIG relax into the Pt due to the spin pumping process [125]. Unlike SMR, which translates the reflection of the spin current at the YIG|Pt interface in Pt, spin pumping highlights directly the spin transmission from YIG to Pt through the interface. The resulting spin current crossing the interface is then converted into a net voltage in the Pt via ISHE which is probe via a nanovoltmeter. The spin pumping signal for different annealing time is presented in FIG.33.a. The maximum microwave power is fixed at 5 mW to prevent non-linear effects that appear at large applied power and would result in a hysteretic shift of the FMR frequency [180, 181]. First, we focus on the spin pumping spectra of the YIG|Pt interface before local heating by Joule effect plotted as blue in FIG.33.a. The probed charge current I_c divided by h_{rf}^2 is directly calculated from the voltage drop V_{ISHE} in the Pt as the dc field is swept by $I_c = (V_{\mathrm{ISHE}}/R_{\mathrm{Pt}})/h_{\mathrm{rf}}^2$. Note that we present the result in current instead of voltage which allows taking account of the slight drop of Pt resistivity observed in FIG.31.b.

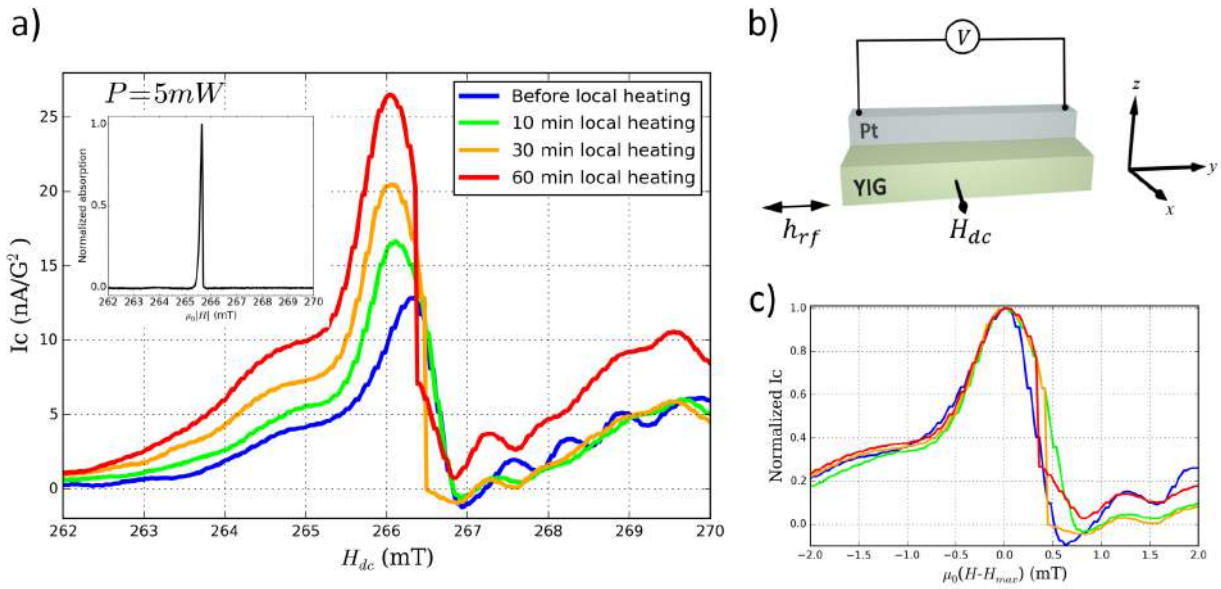

Figure 33: *a) Spin pumping spectra at different annealing step. The annealing is realized by injecting a current density $J = 12 \times 10^{11} A/m^2$ in the Pt for various time. The FWHM of the YIG|Pt nanostructure lies around 100 Oe. The insert presents the FMR of the YIG film which is measured simultaneously. The full width at half maximum of the whole film lies around 1 Oe. b) Scheme of the spin pumping setup. An rf magnetic field h_{rf} is applied along the y-axis while an external dc magnetic field H_{dc} is set along the x-axis. Close to the YIG ferromagnetic resonance, angular momentum flows through the YIG|Pt interface and is recovered as a charge current in the Pt via ISHE. c) Normalized spin pumping spectra at different annealing step. It can be seen that the full width at half maximum which is proportional to the YIG|Pt damping is not changed after local heating by Joule effect.*

A peak of SP signal is observed when the YIG|Pt is brought close to the ferromagnetic resonance. The sign of the SP spectra is negative when H_{dc} is applied along the x-axis and positive when H_{dc} is anti-colinear to the x-axis which is in agreement with the geometry of SHE and is consistent with the sign of the spin Hall angle θ_{SHE} in the Pt [182]. The shape of the spectra does not follow a simple Lorentzian and is ascribed to multiple resonances due to inhomogeneities in the YIG. The main peak of the SP spectra can

be directly linked to the main FMR mode when the YIG|Pt is brought to resonance condition. The maximum amplitude of the SP spectra is linear with the microwave power below 5 mW. We have taken this maximum as a reference to estimate the efficiency of spin transmission at the interface. After characterizing the pristine YIG|Pt interface, we performed a local heating by Joule effect by applying a current density in the Pt strip of $J = 12 \times 10^{11}\mathrm{A/m^2}$. We can see the result of the local heating by Joule effect to the SP spectra after setting 10 ms pulse current with a 10 % duty cycle in the Pt strip for 10, 30 and 60 min respectively. It can be seen in FIG.31.a, that the electrical annealing time has a drastic impact on the SP spectra. Eventually, the amplitude of the pic reaches saturation after 60 min of annealing. We were able to reproduce those behaviors quite systematically over different Pt strips deposited on this sample for identical annealing temperature and time. The spin transmission observed from the SP is enhanced with a ratio of 2.7 by local heating by Joule effect which is close to the ratio found through SMR experiments.
The most interesting feature of this experiment lies in the full width at half maximum (FWHM) of the main peak. As the amplitude of the peak becomes larger with the annealing time, it seems at first sight that the FWHM remains constant over the whole annealing process (see FIG.31.c) which is a quite surprising result. Indeed, the FWHM of the FMR pic is proportional to the YIG|Pt extra-damping $\Delta\alpha$ which is described in equation (1.59). From this expression, we expect that an enhancement of the spin mixing conductance would imply a drastic change of $\Delta\alpha$ resulting in a much larger FWHM which is not observed here. Therefore the enhancement of the reflection and the transmission of the spin signal at the interface can not be fully understood in the usual spin pumping FMR framework. This result suggests that the local heating by Joule effect improves the spin conductivity at the interface but the relaxation mechanism seen from FIG.31.a is governed by the spin waves modes excited asides from Pt which have a much larger linewidth compare to the width of the strips. The higher FHMW measured in the SP signal compare to that of YIG volume through FMR could be due to inhomogeneities of the surrounding YIG or a strain provided by the Pt layer.

2.3.3 Non-local measurement

To study more in depth the impact of the local heating by Joule effect to the non-local spin transport signal. In a sample taken from the same batch, we have placed a second Pt electrode (with same dimensions) located 2 μm away from the first Pt strip (see FIG.34). In the previous section, we have seen that in ultra-thin YIG film, injecting a crossover current density in the order of $J_c = 6.0 \times 10^{11}\mathrm{A/m^2}$ is sufficient to excite spin transport in the non-linear regime. This phenomenon is characterized by non-linear spin conduction as a function of the applied current. However, the excitation of spin waves is strongly related to the non-equilibrium spin accumulation at the YIG|Pt surface and is thus sensitive to the interface. The non-local spin transport has been probed by applying a pulse current in the injector (Pt left) while simultaneously measuring the non-local voltage on the detector (Pt right). The magnons excited either electrically (SOT) or thermally through the spin Seebeck effect [147, 98], are converted into a signal that is maximum when the in-plane magnetic field is oriented along the x-axis due to the SHE geometry. To separate these two contributions, the measurement is performed for the two polarities of the current and the applied magnetic field. Through symmetry consideration, we have extracted the Σ and Δ signal and making sure to subtract a background voltage measured when the magnetic field is applied along the y-axis. Note that the offset voltage is not affected by the local heating by Joule effect.
Let's first consider the pristine state where both interfaces of YIG|Pt are as grown. This

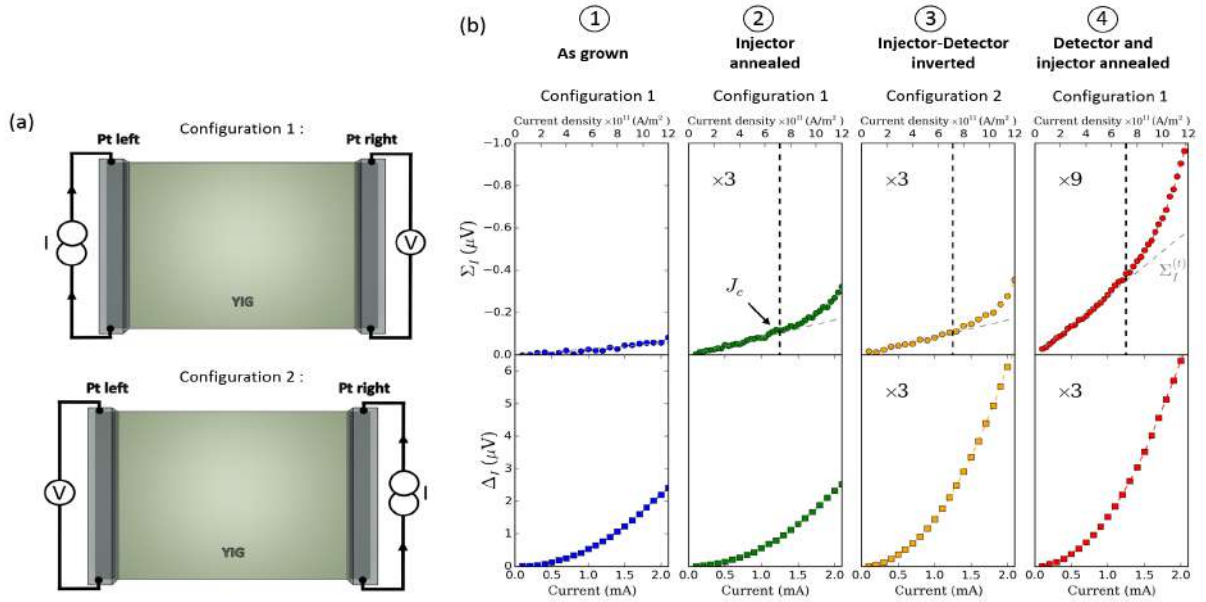

Figure 34: *a) Scheme of the non-local magnon transport measurement. Applying a charge current in a first Pt strip leads to a non-equilibrium magnon accumulation at the interface via SHE that (in the right configuration of the external field) leads to a broad excitation of propagative spin waves. The transport of magnon in YIG is probed via a second Pt strip that converts the magnon density into a measurable voltage by ISHE. b) Panel of the non-local Σ_I and Δ_I signals for different local heating steps. Panels ① present non-local spin signal measured directly after the nanofabrication, taken as a reference signal. ② show the change of Σ_I② after annealing the spin injection strip. Non-linear spin conductance is observed for a crossover current $J_c = 7.0 \times 10^{11} A/m^2$. In panels ③, we have inverted the role of the injector and detector strip such that only the detector strip is annealed. An improvement of Δ_I③ signal is observed while Σ signal and crossover current for exciting non-linearities is found to be unchanged. In the last panels ④, both injector and detector strips are annealed and we can see that a local heating by Joule effect can enhance again the Σ signal without affecting the crossover.*

measurement would be recalled as our reference. In FIG.34.b panel ①, we have displayed the reference non-local Σ_I① and Δ_I① signal, where both injector and detector have not been treated, for an external field align along the x-axis and as a function of the applied current. It can be seen that Δ_I① has a quadratic rise due to its thermal origin while the Σ_I① evolve close to the noise level making any non-linear deviation hard to detect. At the end of the scan, we keep the current density at value $J = 12 \times 10^{11} \mathrm{A/m^2}$ (550 K) for a duration $t = 60$ min, and we observe an increase of the spin signal. We call this new state the case ②, where the injector has been treated but not the detector. We observe that the Σ_I② signal is now 3 times larger. It indicates that the number of magnons excited in YIG is enhanced due to the higher spin transmission at the injector which is recovered by the untreated Pt detector. Quite remarkably, after local heating by Joule effect, we were able to easily reveal the non-linear spin conductance. This magnon population is solely excited via the torque exerted at the injector interface. We also note that the thermal spin signal Δ_I② remains unchanged. This result is not surprising, because the spin conversion of the SSE signal occurs only at the detector strip (which has not been treated) whereas the injector strip only plays the role of the heater. To investigate the role of the interface to the non-local spin signal, we have permuted the current injection

and voltage leads such as propagative magnon are excited on an untreated interface and probed in a treated interface. We call this configuration the case ③, where the detector has been treated but not the injector. As expected, the Δ_I③ is enhanced by a factor 3 due to the higher spin conversion at the probing interface. We do not observe a significant change in the amplitude of the Σ_I③ because this signal highlight the convolution of the spin conversion at both injector and detector interface. Although, the more surprising fact, is that the crossover current density J_c necessary to reach the non-linear regime is found to be unchanged independently if the YIG|Pt interface has been treated or not. This result is not straightforward, because an increase of the spin transparency at the interface should lead to a decrease in the crossover current J_c.
Finally, we have measured the non-local signal in the case where both injector and detector are treated via local heating by Joule effect and is recalled as the case ④. It can be seen that Σ_I④ is 9 times larger than the reference. It implies that injection and detection of magnon through YIG/Pt interface is 3 times more effective. To be more consistent, we have evaluated the voltage produced by the SSE on YIG|Pt structure by using :

$$V_{\mathrm{SSE}} = L_N\, \varepsilon . \frac{G_{\uparrow\downarrow}(1-\mathrm{sech}(t_{\mathrm{NM}}/l_{\mathrm{sf}}))\coth(t_{\mathrm{NM}}/l_{\mathrm{sf}})}{\sigma + l_{\mathrm{sf}}\, G_{\uparrow\downarrow}\coth(t_{\mathrm{NM}}/l_{\mathrm{sf}})} \tag{2.7}$$

$$\varepsilon = \frac{\theta_{\mathrm{SHE}} S_{\mathrm{SSE}} \nabla T l_{\mathrm{sf}}}{t_{\mathrm{NM}}} \tag{2.8}$$

where ∇T is the z component of the temperature gradient at the detector strip, S_{SSE} is the spin Seebeck coefficient of the YIG|Pt [183] and L_N the length of the Pt wire. One would see from equation (2.7) and (2.8), that the SSE signal varies on the first order as $\theta_{\mathrm{SHE}}\,\lambda_{\mathrm{sf}}\,G_{\uparrow\downarrow}$ while the SMR has a $\theta^2_{\mathrm{SHE}}\,\lambda^2_{\mathrm{sf}}\,G_{\uparrow\downarrow}$ dependence. If the local heating by Joule effect would have changed either the θ_{SHE} or the λ_{sf} we would have seen a change of the SMR ratio larger than the increase of the SSE which is not observed here. Moreover, as shown by SP and non-local measurement, the enhancement of the spin signal transmitted via the interface doesn't scale with $g_{\uparrow\downarrow}$ either.

2.3.4 Discussion

Across four different techniques, we evaluated the spin conversion at the YIG|Pt interface subject to a local heating by Joule effect. Spin Hall magnetoresistance and transverse spin Seebeck measurement that highlight respectively the spin reflectivity [144] and spin transmitivity [98] at the interface have shown a net improvement of the spin conversion at the interface. Nonetheless, spin pumping and non-local magnon transport which corroborates to emission and absorption of spin current by the interface allowed us to probe more in depth the impact of a local heating by Joule effect to the dynamic of the system [16, 176, 184]. This two experiments have proven that the increases of the emitted and absorbed spin signal is not followed by an increase of additional damping provided by the interface. Thus a higher spin signal cannot be explained by an improvement of the spin mixing conductance and is in discordance with the spin pumping theory [125].
However, a possible origin of this phenomenon can be understood by a change of the surface geometry via a better wettability of the Pt after local heating by Joule effect as sketched in FIG.35. Because the temperature induced by local heating by Joule effect does not exceed 550 K, it is highly probable that the chemical and structural quality of the YIG surface is not affected by the local heating [154]. Thus we expect the local heating by Joule effect to affect only the Pt strip [185] and could result in a larger recovery of the

surfaces contacts δL. This will improve the number of spin transmission channels at the interface which posses similar spin mixing conductance $g_{\uparrow\downarrow}$. Through this mechanism the emission, reflection or absorption of the spin current are enhanced because of the higher number of spin channels available at the interface. In the theory, the qualitative estimation of charge current in NM induce by ISHE is mediate through the electric field E_{ISHE} which take into consideration the geometry of the interface (refer to equations (1.62), (1.81), (1.94), (2.7)). This formulation implies that the generated electric field by ISHE is homogeneous along the strip which might not be a universal assumption. Following this principle, the voltage produced by ISHE in the Pt can be expressed as:

$$V_{\mathrm{ISHE}} = \sum_{\mathrm{surface}} \delta L \,.\, E_{\mathrm{ISHE}} = \Delta L \,.\, E_{\mathrm{ISHE}} \tag{2.9}$$

where ΔL is the active Pt length. Concerning the dynamic, the YIG|Pt interface is weakly exchanged coupled such that relaxation in YIG dominates other the relaxation in YIG|Pt. Because the coupling is expected to be the same at each activated spin transmission channel, the energy necessary to reach non-linearities do not differ from one channel to another. Thus a more active surface can tune the excited/detected magnon population in YIG via the interface, but local heating by Joule effect should not affect the crossover current J_c in this scheme. The spin memory loss [124] mechanism is not compatible with our observations, because it implies evidence of a loss of angular momentum that is not captured by V_{ISHE}. We would also like to point out that this effect may be a persistent issue affecting only the deposition technique by e-beam evaporation which is a soft deposition technique. The fact that the enhancement ratio of the spin transmission at the YIG|Pt interface is systematically found in the range 2-4 indicates that the low recovery of the Pt onto the surface could be due to a wetting issue linked to geometrical aspects, probably because of the lithography process.

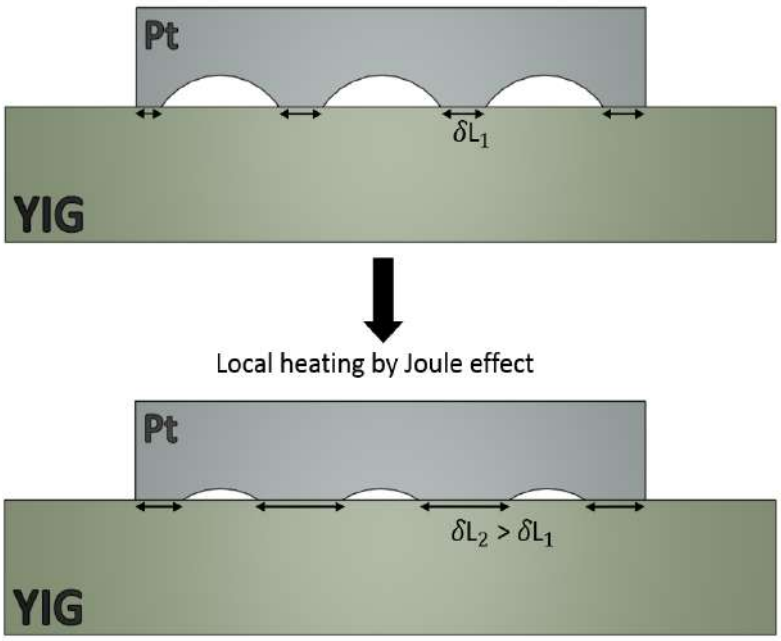

Figure 35: *Schematic of YIG|Pt surface covering with local heating by Joule effect due to better wettability of the Pt layer. This assumption involved a higher total active area that is represented as the sum of every contact surface δL.*

We would otherwise expect a much random distribution of the contact surface that would result in a higher fluctuation of the enhancement ratio.

2.4 Conclusion

In this chapter, we have characterized ultra-thick (16-200 nm) LPE YIG film for spin transport purposes. The FMR measurements have confirmed the good crystalline and magnetic properties of those thin films. This asserts the viability of those films for long distance spin transport. By varying the thickness of those films, we have seen an enhancement of the magnetic damping which seems to evolve inversely proportional to the thickness of the YIG layer as expected.
The concept of non-local measurement in YIG|Pt nano-structures has been presented. The main features of our measurement lie in the low thickness of our film which allows dynamic control of YIG damping combined with a pulse current injection that reduces considerably the temperature gradient due to Joule heating. We have demonstrated that the sign and current/field symmetry of the non-local spin signal is in agreement with the theoretical predictions. We have shown that the interface between YIG and a spin-orbit metal is necessary to either induce or detect propagative spin waves in YIG by SOT. Finally, we have demonstrated through spin Hall magnetoresistance, spin pumping and non-local magnon transport, that a local heating by Joule effect can lead to an improvement of the spin current probe at the YIG|Pt interface. Whereas those three methods lie quantitative comparable results, the measurements suggest that an enhancement of spin signal does not systematically involve an increase of the extra-damping. This can be accomplished by a higher covering of the contact surface by electrical annealing that tunes the density of spin transmission channels available at the interface. Our observations suggest that one has to be careful in analyzing the spin conversion at FM|NM interfaces since the spin mixing conductance $g_{\uparrow\downarrow}$ suppose a perfectly covered interface. This result can also explain the broad difference of $g_{\uparrow\downarrow}$, θ_{SHE} and l_{sf} that can be found in the literature [124, 16, 66, 122, 123] which is evaluated from various methods and deposition techniques.

Chapter 3

Electrical properties of epitaxial yttrium iron garnet ultra-thin films at high temperatures

---

This manuscript concentrates on the magnon transport properties of YIG in a strong out-of-equilibrium regime where large spin currents are induced in the YIG either by spin transfer torque [186, 187] or by temperature gradients [101, 188]. When performed at room temperature, this involves heating the YIG material well above 300 K. One concern is the issue of whether YIG could become an electrical conductor at high temperatures. Indeed, it is known [189, 190, 191, 192, 193] that the electrical resistivity of doped YIG could decrease by several orders of magnitude with increasing temperature due to the presence of impurities. In the case of ultra-thin films defects could come from the growth method or from interfaces and potentially lead to a spurious charge conduction channel when heated well above 300 K. To clarify this point, we propose to investigate the evolution of the electrical properties of single crystalline Yttrium Iron Garnet ultra-thin films in the temperature range [300,400] K. In a first time, we will investigate the behavior of the resistivity of the YIG thin film subject to high temperature. The thickness dependence of electrical conduction of YIG thin films will be realized. We also characterized our YIG via Hall measurements in order to uncover the origin of the conduction in YIG.
Next we will mainly focus on the impact of possible leakage current in YIG onto the non-local magnon transport measurements. The orientation of the in-plane magnetic field will be fixed (anti)colinearly to the Pt strip in order to switch-off any spin sensitivity at YIG/Pt interface according to the spin Hall geometry. Finally, we will address the case of nonlocal measurements when the external magnetic field is set out of the YIG plane. We will show that in this configuration a signal can still be detected but of thermal origin.

3.1 Electrical properties of bare YIG thin films

We will first focus on the electrical properties of YIG film before addressing the consequences of high temperatures on nonlocal measurement. These result have already been published in *Physical Review B* [163]. Therefore the following can be consider as an enlarged version of this publication.

3.1.1 Electrical conduction in YIG thin films mediated by impurities

Before describing the experimental procedure, we would like to recall that YIG is a ferrimagnet, which has an uncompensated magnetic moment on the Fe^{3+} ions, found on the octahedral and tetrahedral coordinate sites, both coupled by super-exchange. Studies on Ca and Si-doped YIG [189] have established that Fe^{2+} and Fe^{4+} ions are formed if tetravalent or respectively divalent impurities are added to the YIG, which could then lead to electrical conduction via the charge transfer mechanism, respectively of p-type and of n-type. In that case, the doped YIG behaves as a large gap semiconductor with a charge conductivity following an activation mechanism. At the present stage, different studies disagree about the microscopic mechanism at play for the electronic conduction inside doped YIG, whether it follows a localized hopping model, through small polaron conduction [192] or rather a band model, through large polaron conduction [189]. It is also known that the value of the magnetic damping coefficient of YIG is very sensitive to the doping level. This is because the charge transfer between the mixed valence iron ions is associated with a potent magnetic relaxation process, known as the valence exchange relaxation [194]. So far this mechanism activated by impurities, appears in the form of a large enhancement of the magnetic damping, usually around liquid nitrogen temperature, where the fluctuation rate of the charge transfer matches the Larmor frequency. This effect is usually minimized by growing YIG crystals from ultra-pure materials. Quite remarkably YIG can usually be synthesized in large volume in the form of a single crystal with almost no atomic disorder. It has been reported that the resistivity of bulk ultra-pure YIG can be as large as $10^{12}\ \Omega \cdot \mathrm{cm}$ at room temperature.
Recent interests in spin-transfer effects in YIG have required an effort to develop high-quality YIG material in the form of ultra-thin (below 20 nm) films (thickness should be compared here relatively to the YIG unit cell, which is 1.238 nm). This is because spin-transfer is an interfacial phenomenon and consequently its efficiency increases with decreasing thickness of the magnetic layer and reducing its volume. Three growth techniques have so far allowed producing good quality ultra-thin YIG films: sputtering [195, 196, 197]; pulsed laser deposition [20, 19, 21, 198]; and liquid phase epitaxy (LPE) [187, 17, 16]. For all these three growth processes, the quality of the YIG films deteriorates as the film thickness decreases [20, 17]. This deterioration is an inherent consequence of an increasing surface to volume ratio, which substantially enhances the possibilities for defects and impurities to be introduced into the YIG, through the two surfaces (contamination,intermixing of the species at the surface or unrelaxed strains in the film thickness), which leads to lower saturation magnetization and an out-of-plane anisotropy often accompanied by an increase in the coercive field.
So far, the highest thin film quality (the smallest combination of low magnetic damping parameter, low inhomogeneous broadening, and film thickness below 20 nm) have been reported for films grown by the LPE technique, an extension of the flux method. The main problem is the difficulty in developing a recipe leading to LPE YIG films homogeneous in both thickness and composition. Indeed, for very thin layers, the role of the transition layer is essential (chemical composition) and requires a control of the chemical

elements composing it. Indeed, the influence of this transition layer on the different contributions to the line width is important. The YIG films, that we have developed from LPE growth technique, have the following characteristics: perfect epitaxy (difference of matching parameter with the substrate is null), saturation magnetization almost equal to that of the bulk ($4\pi M_s$ of our 19 nm YIG films is about 1.7 kG), very low magnetic relaxation (damping coefficient less than or equal than 3.2×10^{-4}), no planar anisotropy and very weak coercive field (H_c <3 Oe), very low roughness (3 Å_{rms}).

3.1.2 Van der Pauw and Hall characterization

In the following, we will concentrate on the electronic properties of LPE grown YIG thin films of thickness t_{YIG}=19 nm. The dynamical characteristics of these films are summarized in 2.1. A 1×1mm^2 square slab of YIG is extracted from the batch and connected along the 4 corners using Al wire bonding. The measurements are performed inside a home-made cryostat regulated in temperature by a flow of Helium gas. To characterize the slab we use the van der Pauw four probes method [199], which is typically used to measure the sheet resistance of homogeneous semiconductor films. It allows eliminating measurement errors associated with the exact shape of the sample and contact resistance. The four points are arranged in a clockwise order around the positive field normal shown schematically inside FIG.36.a. Because of YIG high impedance, we use a Keithley 2636B source-measurement unit in order to draw very little current (sub-nA range) inside the film. In our analysis, the GGG substrate will be considered as a good insulator (resistivity $>10^{15}\Omega\cdot$cm) and its electrical conductivity can be ignored [200].

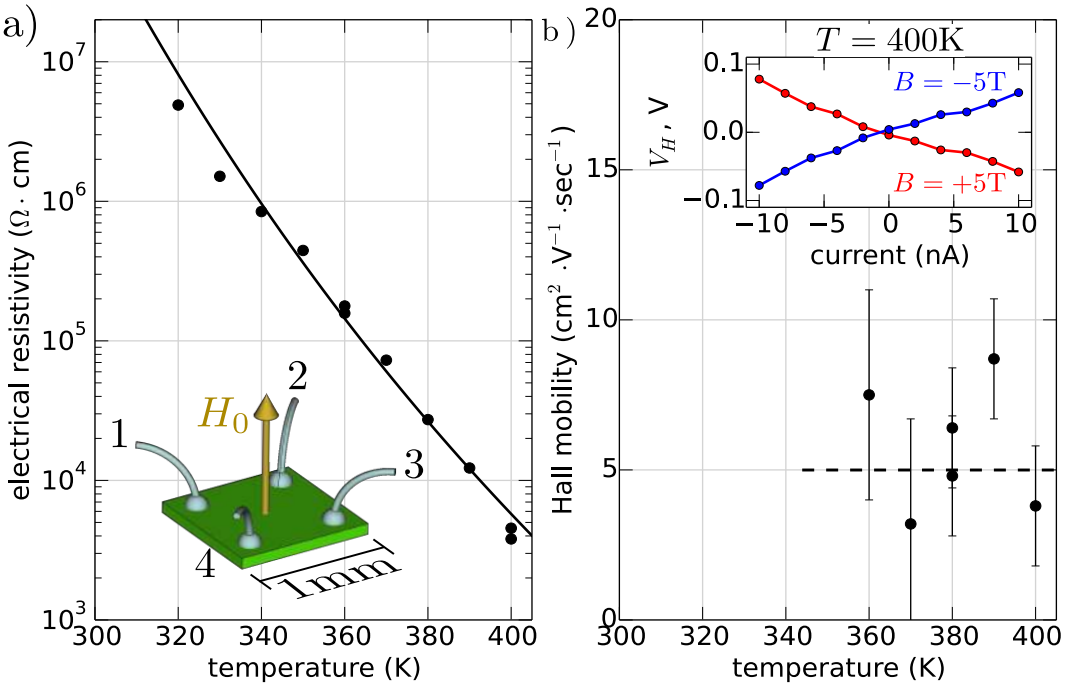

Figure 36: *Temperature dependence of a) the electrical resistivity and b) Hall mobility of 19 nm thick YIG films grown by LPE determined by a Van der Pauw four-point probe technique (see inset). The solid line in a) is a fit with an activated behavior* $\exp[E_g/(2k_B T)]$, *where* $E_g \approx 2\,eV$. *The inset in b) shows the Hall voltage drop* $V_{i+1,i+3}$ *when the current is injected between* $I_{i,i+2}$ *where* i *is the contact number modulo 4.*

Our measurements are performed at high temperatures in the range [300-400] K and for different magnetic fields in the range [0-5] T applied normally to the sample surface. The temperature range explored is still well below the Curie temperature of YIG, which is T_C =580 K. The contacts are placed exactly on the sample corners. We first extract the sheet resistance R_s, which consists of measuring all possible combinations of the cross-resistance between opposite edges. From the van der Pauw expression, one can extract R_s, whose minimum lays in a couple of GΩ range at the highest temperature. From the sheet resistance, we compute the resistivity $\rho = R_s t_{\mathrm{YIG}}$. FIG.36 shows the resistivity as a function of temperature. The first remarkable feature is that the resistivity of YIG at 400 K drops to about $5{\times}10^3\,\Omega\cdot$cm. Plotting the data on a semi-logarithmic scale helps to show that the resistivity decay follows an exponential behavior. Fitting a linear slope through the data plotted as a function of $1/T$ (in FIG.36 the data are shown as a function of T), we infer band-gap energy of about $E_g \approx$2 eV, which is about 1 eV lower than the expected band-gap of pure YIG in bulk form.
Next, we characterize the Hall conductance of our sample. For this, we now circulate the electrical current along the diagonal $I_{i,i+2}$ and measure the voltage drop along the diagonal contacts $V_{i+1,i+3}$. Here i is the contact number modulo 4, where the subscript notation is ordered according to the connections to the high/low binding posts of the current source and voltmeter. The inset of FIG.36.b shows the voltage drop measured at 400 K in the presence of a normal magnetic field of 5 T. To eliminate the resistivity offset, we have worked out the difference of the voltages for positive and negative magnetic fields. In our measurement geometry, the polarity of the Hall voltage is opposite to the magnetic field direction. It implies that the YIG behaves as a p-type conductor. Quantitatively the full variation of the Hall voltage is about 0.12 V at 10 nA when the field is changed by $H_0 = \pm 5$ T at 400 K, where the YIG resistivity is $\rho = 5{\times}10^3\,\Omega\cdot$cm. This corresponds to carrier mobility for the holes of about $\mu_H \approx 5 \pm 3\,\mathrm{cm}^2/V\cdot$ sec. We have repeated the measurement for other temperatures. The measurement at lower temperatures is difficult for two reasons. The first one is the limited voltage range of the sourcemeter, which decreases the upper current limit that could be injected in the YIG. Another consequence of the large resistivity is the associated increase of the time constant for charging effects. This increases substantially the dwell time necessary before taking a measurement. Because of these difficulties, we have limited the measurement range to 40 K below the maximum temperature.

3.1.3 Polaron conduction

The concept of a polaron was first introduced by Landau in 1933 [201] to explain the motion of an electron in a dielectric crystal. Charge carriers located in an ionic crystal will tend to slightly attract nearby positive ions whereas the negative ions will be slightly pushed away such that the carriers will always be surrounded by a phonon cloud [202, 203]. Due to this interplay, the ions will either adjust their position or balance the interaction with the charge carrier in order to hold there regular placement. This results in a local polarization causing the charge carrier to move its equilibrium position via correction of its effective mass. The charge carrier and phonon cloud took together can be considered as a quasiparticle recall as polaron. Due to the ionic displacement, the charge carrier within the polaron is confined in a defined potential which extends in a defined volume. The nature of the charge carrier can be disregarded since the description of an electron polaron is analogous to the hole polaron.
If the electron or hole is confined in a self-induced atomic displacement field within a radius that does not exceed one unit cell, the system can be regarded as a small polaron. The electrical conductivity through small polaron is characterized by a *hopping* transport

[204]. At a sufficiently high temperature, the interaction of the charge carrier and the lattice vibration induce a hopping transition of the charge from its initial site toward a neighboring site. It suggests that the charge undergo the old potential well via a multiphonon process of the lattice relaxation which annihilates small polarons states. The atoms (ions) will thus adiabatically follow the displacement of the charge by creating a potential well at the new position of the charge and recreate the small polaron state [205]. The mobility of small polarons is therefore thermally activated and follow an Arrhenius-type behavior [204, 206, 207, 208]:

$$\mu_{\text{Hall}}^{\text{SP}} \propto T^{-1/2} \exp(-\frac{W_H}{3k_B T}) \tag{3.1}$$

where W_H is the hopping activation energy. The small polaron hopping model does not support very well the results shown in FIG.36 for several reasons. First, despite the large error bars of our measurement displayed in FIG.36.b, the experimental results suggests that the temperature dependence of the mobility is small [209] indicating that most of the change in the resistivity comes from a variation of the electronic density and not of the scattering time. Second, the bandgap of our film estimated in FIG.36.a in the order of $E_g \approx 2\,\text{eV}$, is much larger than $k_B T$ which is insufficient to reach thermal activation of charge carriers. And finally, the hole mobility gathered through Hall measurement $\mu_H \approx 5 \pm 3\,\text{cm}^2/(\text{V}\cdot\text{sec})$ is expected to be very large for a small polaron conduction (in the hopping region the upper limit of the mobility can be estimated to $\mu_H << 0.1 \pm 3\,\text{cm}^2/\text{V}\cdot\text{sec}$).
However, if the polaron radius is much larger than the lattice constant, such a system is recalled as a large polaron (or Fröhlich polaron). This effect appears when the charge carriers are polarized via longitudinal optical (LO) phonons. In that case, the effective mass of the polaron became larger than the mass of the associated electron. The lattice disorder is then dragged by the electron resulting in large inertia. The conduction of large polarons can therefore be considered as a *band-like* transport. Owing to the large polarons coupling, the mobility is expected to be inversely proportional to the number of LO phonons in the crystal [205]:

$$\mu^{\text{LP}} \propto \exp(\frac{\hbar\omega_{\text{LO}}}{k_B T}) \tag{3.2}$$

its mobility is thus nearly temperature independent at high temperatures. Such behavior is compatible with what has been found previously in Ca doped YIG (p-type) [189, 210] and the above observation which is used as a signature that charge carriers are provided by large polarons [189]. This picture is even more supported by the estimated mobility in FIG.36.b than fulfill the condition $\mu_H > 1.0 \pm 3\,\text{cm}^2/\text{V}\cdot\text{sec}$ in respect to the band scheme.

3.1.4 Thickness dependence

Even though the above study highlights a clear enhancement of electrical conduction in YIG at high temperature, it does not conclude if this electrical conduction occurs in the bulk or if this is a surface effect. This important question shall be determined by monitoring the change in the electrical properties as a function of the YIG thickness.
Such experiments have been performed for YIG films with thicknesses of 56, 92 and 200 nm respectively. Those samples originate from the same preparation procedure. Therefore there physical and magnetic properties are comparable to the values measured in FIG.18 and FIG.19. Using the Van der Pauw method, we have measured the electrical conductivity of those film in the temperature range of [320-400 K]. The result of this measurement

is presented in FIG.37. The electrical resistivity of the 19 nm film shown in FIG.36.a has been implemented in the plot as well for the sake of comparison. The temperature dependence of the YIG resistivity has been fitted with an active behavior to extract the effective bandgap as a function of the YIG thickness. From this, it results that all LPE YIG thin films present an electrical conductivity which seems to be independent of the thickness. The extracted bandgap of those films fluctuated around the value $E_g \approx 1.78\,\text{eV}$. This observation tends to attribute this conductivity to a bulk doping.
Nevertheless during the last step of the fabrication process of the Pt nanostructures for nonlocal measurements, we systematically encapsulated our structures with a protective layer of Si_3N_4 to reduce the risk of alteration overtime.

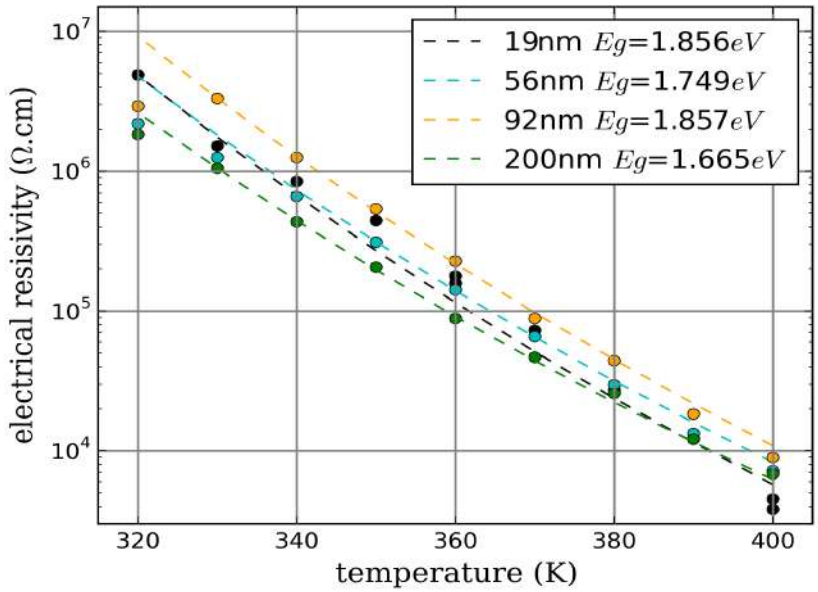

Figure 37: *Temperature dependence of the YIG resistivity measured by Van der Pauw technique for different YIG thicknesses prepared in similar conditions. The solid lines are* $\exp[E_g/(2k_B T)]$ *fits which allow extracting the bandgap. We can see in the upper legend that the effective bandgap is rather independent of the YIG thickness.*

To account for the YIG|Si_3N_4 interface into the electrical properties at high temperature, we have deposited on the same samples a 20 nm Si_3N_4 layer and measured again the electrical conductivity with temperature. The Si_3N_4 here will be taken as a good insulator and we do not expect any conduction in the bulk. In FIG.38, we can see that the extract band gap is reduced from 1.75 eV to 1.3 eV when the Si_3N_4 layer is deposited on the YIG surface. Moreover, this reduction of the effective bandgap appears to be less affected as the YIG thickness is increased as it can be seen in the FIG.38 inset. This observation point out an additional conductivity channel provided either in Si_3N_4 or either at the YIG|Si_3N_4 interface which is more dominant for thinner YIG.

From those observations, it is clear than thin LPE YIG films are extrinsically doped. It is most probable that the origin of the *p*-type conduction observed on pure YIG films is coming from the PbO,B_2O_3 flux incorporated during the LPE growth. Divalent Pb^{2+} ions can therefore enter the garnet either on the tetrahedral or octahedral site [200, 211] and act as acceptors providing the electrical conduction. On the other side, several studies [212, 189, 200] have shown that *n*-type conduction in YIG can be obtained when Si enters the garnet lattice. Through substitution of the Fe^{3+} in the tetrahedral site by Si^{4+} ions,

the concentration of donor can exceed the concentration of acceptor. In our cases, we do not exclude that the Si_3N_4 layer could provide Si^{3+} through interfacial intermixing. Unfortunately, Hall measurement on Si_3N_4 capped YIG sample could not be realized. This would have been interesting to see if the drop of resistivity can be associated to a Si^{3+} doping that could possibly result in a shift from p to n type doping for thinner films.

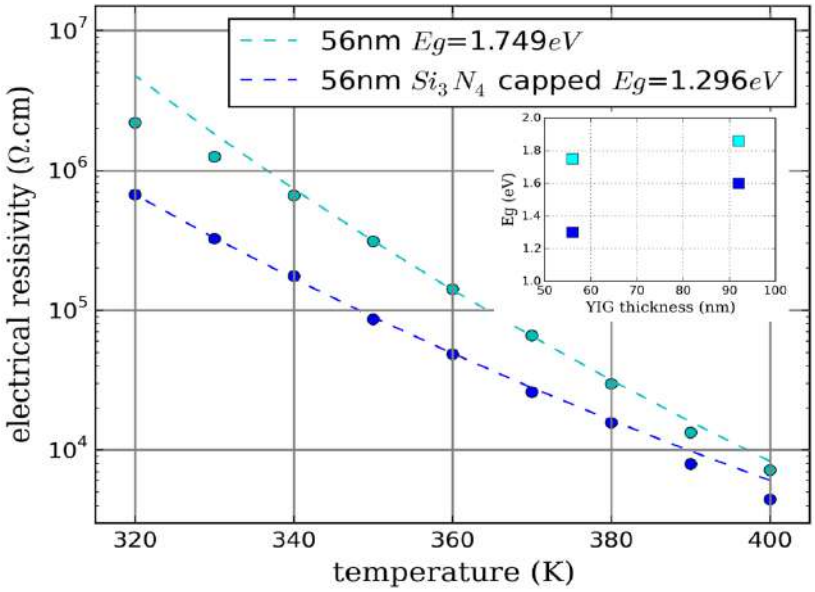

Figure 38: *Temperature dependence of the YIG resistivity measured by Van der Pauw technique for a 56 nm tick YIG with (blue) and without (lightblue) Si_3N_4 capping. The inset shows the influence of the Si_3N_4 to the extracted effective bandgap for 56 and 92 nm thick YIG films.*

However it is also known that the YIG presents intrinsic doping through oxygen vacancies [210]. It has been shown than the resistivity of Mg-doped YIG can change from n to p-type conduction by varying the oxygen pressure or the growth temperature. It reaches a maximum when the concentration of acceptor balance the concentration of donor in the film. The total electrical properties of YIG is thus expected to be the concentration difference between the Pb^{2+} and the donor (Si^{3+} and doubly ionized oxygen vacancies) [200]. Again it is not excluded that the Si_3N_4 could also significantly affect the oxygen vacancies concentration near the interface.

3.2 Leakage current in YIG: in-plane magnetization

Next, we investigate the implications of these electrical properties for non-local spin transport experiments [97] performed at room temperature and in air, where one monitors the transport properties between two parallel Pt wires (colored in red in FIG.39.a) deposited on top of YIG. More precisely, one measures the voltage along one wire (the detector) as a current flows through the other wire (the injector). FIG.39.a shows a microscopy image of the electrode patterned on top of the YIG. For the sake of clarity, we define a Cartesian frame where the $\hat{y}$-direction is set parallel to the wire and the $\hat{z}$-direction represents the out-of-plane orientation. For the lateral device series used herein, the Pt wires are 7 nm thick, 300 nm wide, and 30 μm long. Since different Pt wires (thickness and length) have been deposited between different samples [187], comparison of the results should

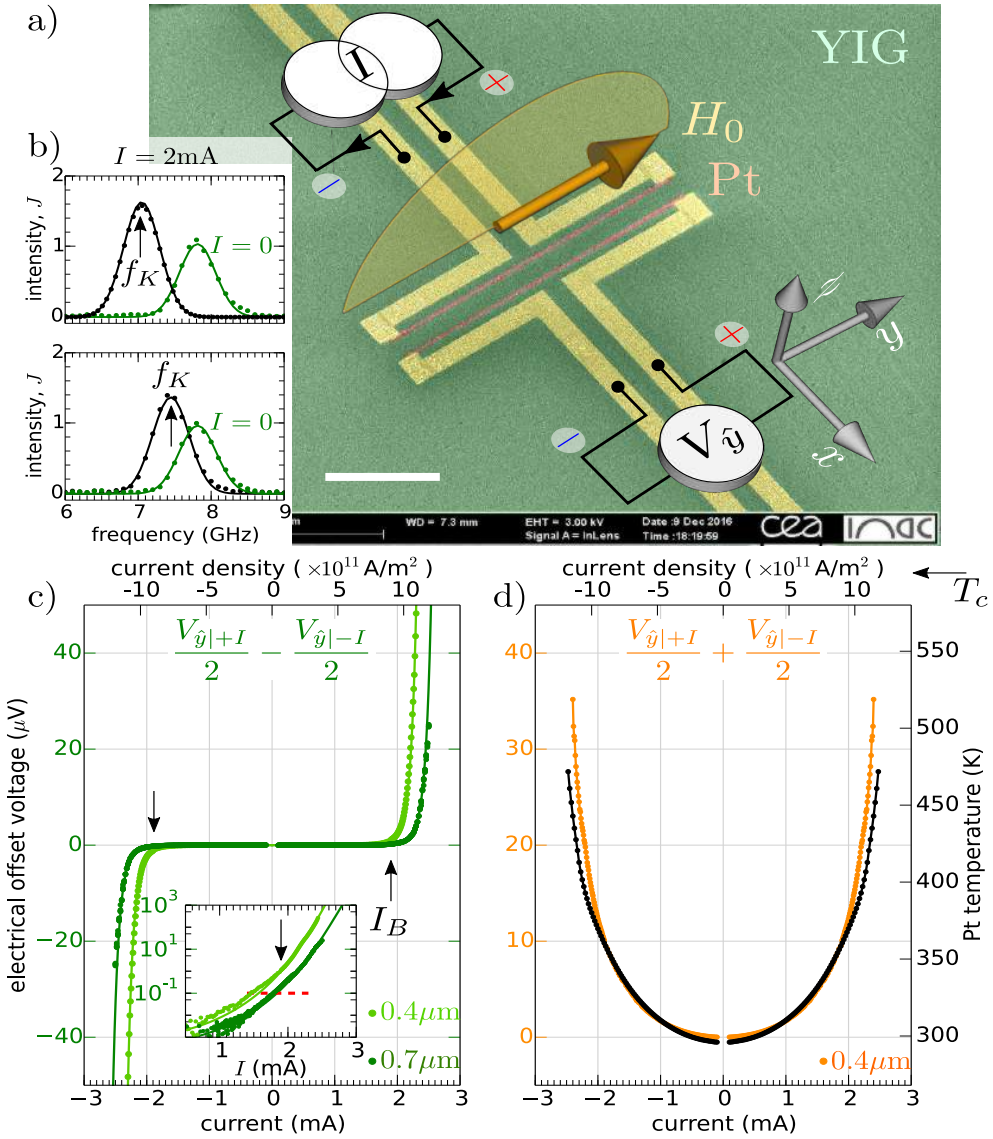

Figure 39: *Current dependence of the electrical offset voltage $V_{\hat{y}}$ in non-local transport devices performed at room temperature. The YIG magnetization is set along the y-direction by an external in-plane magnetic field biased at $H_0 = 2$ kOe. One monitors here the voltage along one wire as a current flows through a second wire separated by a variable gap (0.4 μm or 0.7μm). Panel a) is a microscopy image showing two Pt stripes aligned along the y-direction (red) (the scale bar is 10 μm). The polarity of the current source and voltmeter are specified. Panel b) is direct monitoring through microfocus Brillouin light scattering of the value of YIG saturation magnetization (temperature sensitive) underneath the Pt injector (i) and the Pt detector (d) here separated by a gap of 0.7μm (solid lines are Gaussian fits). The maximum of the curve indicates the position of the Kittel frequency (see arrows). Shifts produced by Joule heating at $I = 2$ mA (black) are shown relative to the results at $I = 0$ (green). Panels c) and d) show the current variation of the offset voltage, here decomposed in two contributions: c) $(V_{\hat{y}|+I} - V_{\hat{y}|-I})/2$, odd in current (green), and d) $(V_{\hat{y},+I} + V_{\hat{y},-I})/2$, even in current (orange). The black curve in d) shows the increase of relative resistance of the Pt used as a temperature sensor. The results in c) are shown for 2 different gap separation between the Pt wires. The solid line in b) is a fit with an exponential increase $\exp[-E_g/(2k_B T)]$, where $E_g \approx 2$ eV. The inset is a zoom of the data shown on a semi-logarithmic scale. The arrow at I_B=2 mA indicates the threshold current above which the Ohmic losses start to reach 100 nV.*

be done by juxtaposing data obtained with identical current densities (provided in the upper scale). The total resistance of the Pt wire at room temperature is R_0=3.9 kΩ, corresponding to a Pt resistivity of 27.3 $\mu\Omega$.cm. The analysis below will concentrate on two devices, with two Pt wires separated by a gap of either 0.7 μm or of 0.4 μm respectively. We emphasize that these measurements have been performed on several other devices patterned on two different LPE YIG film batches of about similar thickness (YDPB8 and YDPB9). In the following, we shall explicitly clarify the effects, that are generic to the YIG films.

In the measurements, the current is injected in the device only during 10 ms pulses long repeated every 100 ms. The increase of resistance R_I of the Pt wire is monitored during the pulse sequence. The result is shown in FIG.39.d (in black dots), where we have plotted $\kappa_{\rm Pt}(R_I - R_0)/R_0$ as a function of the current I, with the coefficient $\kappa_{\rm Pt} = 254$ K specific to Pt. For information purposes, we have also marked on the plot the position of the Curie temperature T_C. We have performed on the device with a gap of d=0.7 μm, microfocus Brillouin light scattering (μ-BLS) in the GHz energy range. The spectral distribution of light intensity measured either by focusing the light beam under the injector (i) or detector (d) Pt wire is shown in FIG.39.b. The μ-BLS spectrum is first measured at $I = \pm 0$ mA for calibration purposes. The spectral distribution is then measured at $I = \pm 2$ mA (*i.e.* 9.5×10^{11} A/m^2) while the field is set to $H_0 = +2$ kOe along the $\hat{y}$-direction. The spectrum shifts to lower frequencies, due to a reduction of the saturation magnetization M_s caused by the increase of T. Since the frequency of the maximum in the spectrum (arrows in FIG.39b) coincides with the FMR frequency, we can calculate M_s from the experimental data by using the Kittel formula. The quantity $\Delta M_s = M_s(0) - M_s(I)$, where $M_s(0)$ is the effective magnetization at $I = 0$, characterizes the total number of magnons created due to the current flowing in Pt. Comparing these values at the (i) and (d) position allows to estimate the decrease of saturation magnetization under the injector (-290 G) and the detector (-110 G). If one uses the fact that YIG magnetization decreases by 4G/°C in this temperature range, we find that at I=2 mA the temperature of the YIG underneath the injector has increased by +73°C, while the temperature of the YIG underneath the detector has increased by +27°C. This result thus suggests that the local YIG temperature is identical to that of the Pt (*i.e.* negligible Kapitza resistance).

One can then use these findings to estimate the temperature effects on the electrical properties. At I=2 mA, which corresponds to a current density of about 10^{12}A/m^2 in the Pt injector wire, the temperature of the Pt increases to about 370 K during the pulse. At this temperature, the YIG resistivity drops into the sub-10^5 $\Omega\cdot$cm range according to FIG.36.a, which corresponds to a sheet resistance of about 50 GΩ. Considering now the lateral aspect ratio of the device, this amounts to an electrical resistance of YIG of the order of the GΩ between the two wires. The leakage current inside the Pt detector wire, whose impedance is about 6 orders of magnitude smaller than that of YIG, starts thus to reach the nA range. This start to be comparable to the contributions with the effects stemming from spin currents flowing from injector to detector, either due to temperature gradients or magnon emission, propagation and transduced into an electrical current in Pt by the inverse spin Hall effects (ISHE) [16, 124].

To reveal this effect in our lateral device, we propose to measure the non-local voltage with the magnetization set precisely parallel to the Pt wire ($\hat{y}$-direction). This configuration switches off completely any sensitivity to spin conduction. To align the magnetization with the wire we used an external in-plane magnetic field of 2 kOe as shown in FIG.39. The induced offset voltage is decomposed into two contributions: b) one $(V_{\hat{y}|+I} - V_{\hat{y}|-I})/2$, which is odd in current (green) and the other c) $(V_{\hat{y}|+I} + V_{\hat{y}|-I})/2$, which is even in current (orange).

We first concentrate on the odd contribution of the offset shown in green in FIG.39.c. The result is shown for two different non-local devices, where the two Pt wires are sep-

arated by two different gaps respectively 0.4 μm and 0.7 μm. On a linear voltage scale set to the μV range, we observe that the odd offset increases abruptly above I_B =2 mA on the 0.7 μm device (corresponding to a YIG temperature of 370 K). This abrupt rise is shifted to lower current, when the gap is reduced and it actually follows approximately an exponential growth as shown in the inset using a semi-logarithmic scale. The solid line in FIG.39.c is a fit with an exponential increase $\exp[-E_g/(2k_B T)]$, where the temperature T is extracted from the Pt resistance (cf. black dots in FIG.39.d). From the fit, we extract the local band-gap $E_g \approx$2 eV, which is the same as that inferred from the resistivity. The shift of the curve as a function of the gap is consistent with a decrease of the temperature of the detector as the wire is moved away from the injector. One can actually roughly evaluate from this shift the temperature difference in the x-direction between the two devices, found to be about +20°C at I_B when the wires are shifted by 0.3 μm (the difference between the 2 gaps) along the x-axis. We can evaluate quantitatively the expected signal from current leakage through the YIG. At I =2.2 mA, when the temperature of the YIG reaches $T \approx 390$ K, the YIG resistivity drops to about $10^4\ \Omega\cdot$cm. Considering the equivalent circuit, this will produce a potential difference of 50 μV on the detector circuit, which is consistent with the observed signal amplitude. This sustains the interpretation that the odd offset voltage in our non-local device is purely produced by the decrease of the YIG electrical resistivity. Note that this offset voltage drops very quickly with decreasing current pulse amplitude. As shown in the inset of FIG.39c, it decreases by an order of magnitude, when I=2.0 mA (corresponding to a YIG temperature of $T \approx 370$ K). At this level, the offset starts to become of the same order of magnitude as the spin signal in these devices. We have thus indicated by an arrow in FIG.39c, I_B=2 mA (*i.e.* current densities of approximately 10^{12} A·m^2), the threshold current at which the electrical leakage starts to become important in the spin transport experiments, here reaching the 100 nV range. It is also important to note at this stage that, within our convention of biasing, the high/low binding posts of the current source and voltmeter are in the same direction (cf.+ and − polarities in FIG.39.a), the sign of $(V_{\hat{y}|+I} - V_{\hat{y}|-I})/2$ is positive for positive current and negative for negative current. This is opposite to the sign of the spin conductance, Σ, reported on these systems [2]. The sign of the "odd in I"-component of the non-local voltage is actually a signature that, in one case, the voltage drop is produced by electronic transport (Ohmic losses) and in the other case, it is produced by spin transport. While in both scenarios the induced electrical current flows in the same direction in the two parallel Pt wires, for Ohmic loss, the YIG acts as an electronic load and the potential drops along the current direction, *i.e.* $(V_{\hat{y}|+I} - V_{\hat{y}|-I}) \cdot I > 0$ as shown in FIG.39.c, in contrast, for ISHE, the YIG acts as a spin source for the detector and the potential increases along the current direction, *i.e.* $(\Sigma \cdot I) < 0$ (note that this effect is independent of the sign of the spin Hall angle).

We then move to the even contribution of the offset shown in orange in FIG.39.d. One observes that this contribution always follows the Joule heating of the Pt wire, so it is linked to the induced thermal gradient. We believe that it should be ascribed to thermoelectric effects produced by temperature gradients along the y-direction. This gradient is produced by inherent small resistance asymmetries along the Pt wire length, which results in one end of the Pt wire heating slightly more than the opposite end. This produces a small temperature difference at the two Pt|Al contacts of the detector circuit (indicated by the + and − polarities binding posts in FIG.39.a). Considering the electrical Seebeck coefficient of Pt|Al, of 3.5μV/°C, the offset measured at I =2 mA, corresponds to a temperature difference of less than 3 °C between the top and bottom contact electrodes, while the wire is being heated by almost 70 °C. These asymmetries in the temperature difference are expected to vary from one device to the other and this is precisely what is observed: the ratio between the even contribution of the offset and the temperature increase of the Pt wire fluctuates and even changes sign randomly between different lateral devices.

3.3 Righi-Leduc effect: out-of-plane magnetization

Although the electrical offset voltage produced by Ohmic losses and thermoelectric effects is independent of the external magnetic field direction when the latter is rotated in-plane, it is in principle sensitive to the out-of-plane component through the Hall effect. Transverse transport properties in YIG are currently attracting a lot of interest and several recent papers address the issue of transverse magnon transport effects in magnetic materials, such as the magnon Hall effect [213] or the magnon planar Hall effect [214]. The sensitivity to magnon effects can be eliminated from the measurements by keeping the magnetization vector in the yz-plane containing the interface normal and the length of the Pt stripe as this configuration selects only the transverse transport properties carried by the electrical charge. To extract the Hall voltage, we shall only consider $\Delta_{\hat{z}}$, defined as the difference between the measured voltage for two opposite polarities of the external magnetic field $\pm H_0$, $\Delta_{\hat{z}} = (V_{+\hat{z}} - V_{-\hat{z}})/2$. This signal would be also sensitive to the spin Seebeck effects if the YIG magnetization had a non-vanishing projection along the x-axis [187]. The inset of FIG.40b shows the angular dependence as a function of the polar angle, θ, being defined in FIG.40a. In all the devices, we observe that the θ-dependence of the $\Delta_{\hat{z}}$-signal is: maximum when the field is applied along the z-direction; odd in magnetic field; and negative when $\theta = +\pi/2$. Moreover, $\Delta_{\hat{z}}$ increases with both increasing current density and increasing external magnetic field. It is worth to note at this point that the offset voltage produced by the perpendicular magnetic field is about two orders of magnitude smaller than that of the in-plane direction. The observed quadratic dependence with I in FIG.40b suggests that this signal should be associated with Joule heating and thus to particle flux induced by thermal gradients. The observed linear dependence with H_0 in FIG.40c suggests that this signal should be associated to a normal Hall effect and not to an anomalous Hall effect linked to M_s. Indeed a fit of the high field data leads to a straight line that intercepts the origin, while the anomalous Hall effect would have lead to a finite intercept. One also observes in FIG.40c a departure from this linear behavior below the saturation field ($\sim 4\pi M_s$). This is because, below saturation, a component of the magnetization could point in the x-direction, hereby switching on the sensitivity to the spin Seebeck effect, which is a stronger positive signal in these devices. To check this we have repeated the measurement by tilting the applied magnetic field by 10° away from the normal and in the y-direction (θ =80°). This ensures that there is no net component along x, while retaining almost the same strength along z. The result is shown using light blue dots in FIG.40b. The fact that the observed linear behavior extends almost up to origin confirms that the origin of the rise in $\Delta_{\hat{z}}$ is indeed associated with the normal Hall effect.

Next, we discuss more in detail the potential origin of the $\Delta_{\hat{z}}$-signal. First, as noted in the previous paragraph, the source is the incoming flux of charge carriers produced by a thermal gradient. This gradient is mainly in the x-direction, through the potent Joule heating of the injector. There is in principle an electrical voltage produced in the y-direction associated with this incoming flux through the electrical Nernst effect. Our device geometry effectively shunts both contacts with a relatively low impedance Pt wire, acting as a voltage divider, which reduces drastically any sensitivity to the Nernst effect. One should mention at this point the recently reported spin Nernst effect [215]. But this signal should be maximum when the magnetization is parallel to the y-direction, while the signal that we discuss here is maximum when the magnetization is parallel to the z-direction. We propose here a different scenario to explain our data. Since our measurement of the even offset in FIG.39d seems to indicate that the two thermocouples provided by the Pt|Al contacts at both ends of the detector Pt wire are sensitive to temperature difference along the y-direction, the Hall offset signal measured in FIG.40 can thus be due to a thermal gradient in the y-direction (Righi-Leduc effects: a transverse thermal

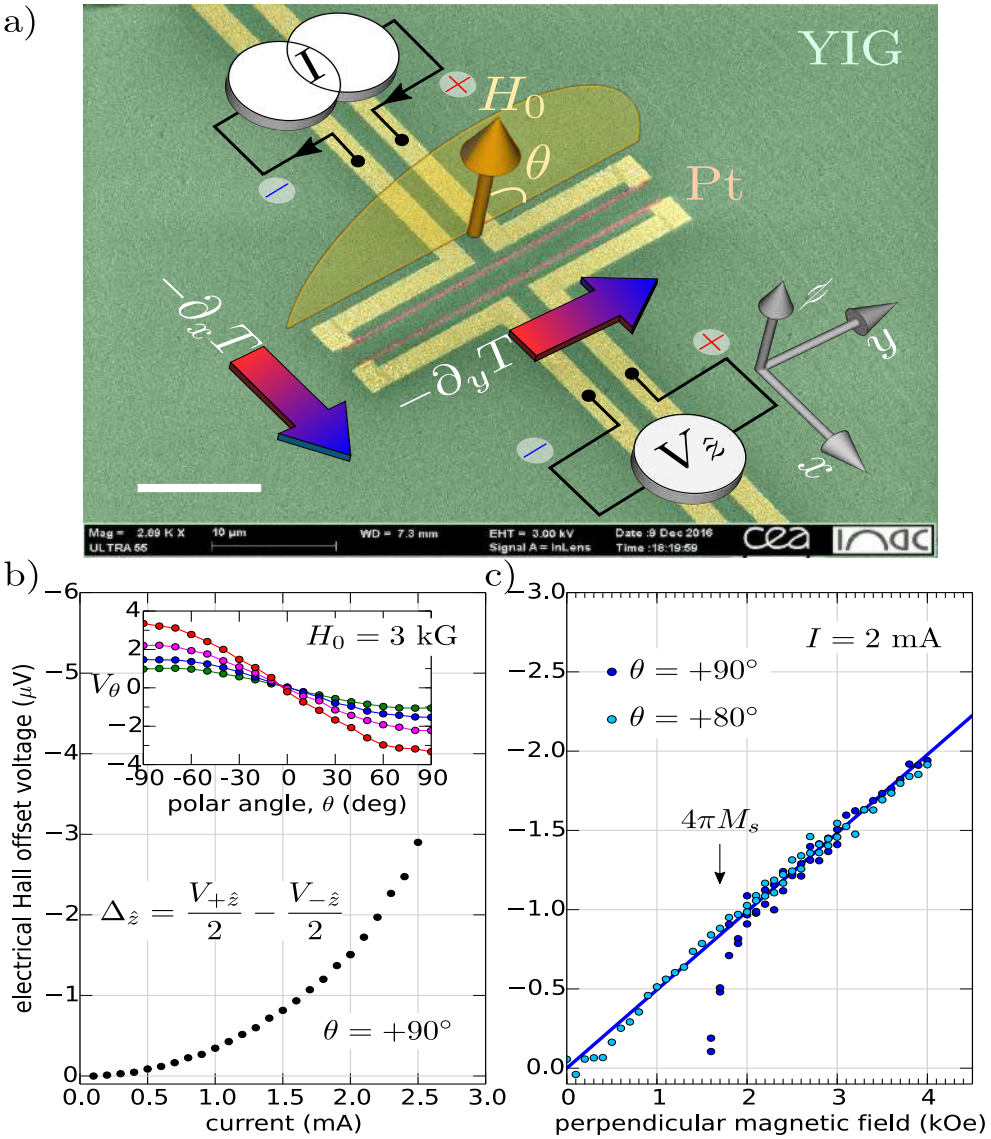

Figure 40: *a) Schematic of the Righi-Leduc effect produced on a p-type conductor magnetized out-of-plane. The large in-plane temperature gradient $\partial_x T$ produced by Joule heating creates a temperature gradient $\partial_y T$ along the wire when the sample is subject to an out-of-plane magnetic field. b) Current and c) magnetic field dependence of the Hall offset voltage $V_{\hat{z}}$ produced in the non-local transport device. Panel b) shows the variation of the $\Delta_{\hat{z}}$-signal as a function of I when $H_0 = \pm 3\,kG$. The inset of b) shows the polar angle variation, θ, for different current between [1.9-2.5] mA (step 0.2 mA). The magnetic field is rotated in the yz-plane. Panel c) shows the magnetic field dependence of $\Delta_{\hat{z}}$ measured when the polar angle reaches the normal direction ($\theta = +90°, +80°$).*

gradient whose amplitude is proportional to the out-of-plane component of the applied magnetic field [216]). Although a definite quantitative proof would require some additional measurements, in the following we shall check that this explanation is consistent with the data.

One should note that there is also a Nernst component associated with the charge transport in the presence of a perpendicular magnetic field. But because the device consists of a small wire deposited on an extended film, *i.e.* far from the edge, the Nernst component

should be completely shunted inside the YIG and this effect will be neglected in the following.
Firstly, this explanation is consistent with the I and H_0 behavior. Secondly, it also has the correct sign. Since the $\Delta_{\hat{z}}$-signal is negative for θ=+90°, this implies that $\partial_x T$ and $\partial_y T$ have the same sign when the field is positive. This is the signature of a p-type doping in agreement with FIG.36b. Concerning the amplitude of these thermal gradients, at I_B =2 mA, we shall rely on our evaluation of the temperature of the YIG underneath the injector and the detector by measuring the value of the Kittel frequency at these two positions using μ-BLS spectroscopy (cf. inset of FIG.39c). We found that at I =2 mA the temperature of the YIG increases by +73°C underneath the injector and by +27°C underneath the detector. Using the gap of 0.7 μm between the two Pt wires as the area where the thermal gradient along x occurs, we find that $\partial_x T = -65°\text{C}/\mu\text{m}$. Using a value of $\mu_H = +5\,\text{cm}^2/(\text{V}\cdot\text{sec})$ for the Hall mobility, this would produce a transverse gradient of $\partial_y T = \mu_H H_0 \partial_x T = -1\times 10^{-2}\,°\text{C}/\mu\text{m}$ in a perpendicular magnetic field of 3 kG. Recalling that the length of the Pt wires is 30 μm long, this would produce a voltage of 1 μV, using the thermoelectric coefficient of Pt|Al. So in the end, the expected signal amplitude is of the same order of magnitude as the Hall offset measured at I_B=2 mA.

3.4 Conclusion

In summary, we have shown that high-quality YIG thin films grown by LPE behave like a large gap semiconductor at high temperatures due to the presence of a small amount of impurities inside the YIG. In our case, we observe that the resistivity drops to about $5\times 10^3\ \Omega\cdot\text{cm}$ at T=400 K and can be attributed to conduction by large polarons. These results have to be taken into account for non-local transport exploring the spin conductivity, especially in cases where the YIG has a large amount of defects like in amorphous materials [186], or when improper cooling of the sintered product leads to the additional formation of Ohmic grain boundaries [217]. In non-local transport devices, these electrical properties are responsible for an offset voltage (independent of the in-plane field direction) whose amplitude, odd in current, grows exponentially with current due to Joule heating. These electrical properties also induce a sensitivity to the perpendicular component of the magnetic field through the Hall effect. In our lateral device, a thermoelectric offset voltage is produced by a temperature gradient along the wire direction proportional to the perpendicular component of the magnetic field (Righi-Leduc effect). These results also emphasize the importance of reducing drastically the Joule heating by using a pulse method, when investigating spin transport in YIG at high current density. For our devices, these electrical effects start to become significant for spin transport studies, when the YIG temperature is heated above 370 K, which corresponds in our case to injecting a current density $>1.0\times 10^{12}\ \text{A}\cdot\text{m}^2$ in the Pt (or I >2 mA for these samples). These voltages produced by Ohmic losses in the YIG can be separated from the non-local voltage produced by spin transport. Firstly, the two signals have opposite polarities. Secondly, only the latter varies with the orientation of the magnetization in-plane, as first demonstrated by the Gröningen group [97].

Chapter 4

Nonlinear spin conductance in magnetic thin films driven by large spin-orbit torque

As established in the previous section, a transfer of angular momentum in a magnetic insulator can be induced via the exchange coupling at the interface between a ferromagnetic layer and a strong spin-orbit coupling metal such as Pt. This new paradigm has been triggered thanks to the discovery of the spin Hall effect which enables the direct interconversion of charge current to a spin current and vice-versa. In the pioneer work of Kajiwara [8] and Cornelissen [2], transport of pure spin currents mediated by local magnetic moment fluctuations have been demonstrated. Such experiments have been performed in Yttrium Iron Garnet (YIG) mainly for its low magnetic damping enabling large magnon diffusion length. However, full control of the magnetic damping with spin-orbit torque exert by the charge current in Pt could not be observed at that time in extended YIG thin film having a thickness in the hundreds of nm. It turns out that two important ingredients were key to observe such effect: reducing the film thickness in the tens of nanometer thickness, as well as reducing the lateral size to avoid modes competition. Our groups highlighted in 2014, the generation of subthermal spin waves modes in micron-sized YIG discs patterned inside a 20 nm thick films via spin-orbit torque inducing auto-oscillation state [92]. This have been realized thanks to several progress in the fabrication of high-quality ultra-thin YIG films. In the following section we present experimental results of spin waves transport in ultra-thin YIG films submitted to a large spin-orbit torque.
This experiment is performed via two Pt electrodes deposited on the top of the YIG surface and separated by various distance (within μm range). This allows inducing propagative spin-wave in the YIG film by injecting a current in the first strip which is recovered at the second Pt electrode via inverse SHE. By taking advantage of the low thickness of our films, we will explore the magnon transport regime subject to a large spin-orbit torque by applying a large current density in our structure. By studying the angle and field dependence of the non-local signal probed in the detector Pt, we are able to identify the nature of the spin signal induced in YIG. These results will be further support by μ-BLS measurement which gathers directly the excited magnon density. Spatial spectroscopy of spin wave propagation in film will be covered revealing the diffusion length of the magnons probed in the different transport regimes. We will also investigate the spin waves propagation in a Bi-doped YIG which presents perpendicular magnetic anisotropy.

4.1 Current and field dependence of the non-local measurement

A series of lateral devices have been patterned on the 18 nm thick YIG film (YDPB8) grown by liquid phase epitaxy [176, 16]. In this film, we have deposited Pt wires: 10 nm thick, 300 nm wide, and 20 μm long (see fabrication method in Appendix B). The lateral device geometry is shown in FIG.41.a. A charge current I flows through a first wire as the voltage V is monitored in the second wire, separated by a gap of 1.2 μm. Here the Pt wires are connected by 50 nm thick Al electrodes colored in yellow. Thereafter, the transport studies will be performed in air and at room temperature. These results have been reported in *Physical Review B* as a rapid communication [187], and the two next sections can be considered as an enlarged version of this publication.

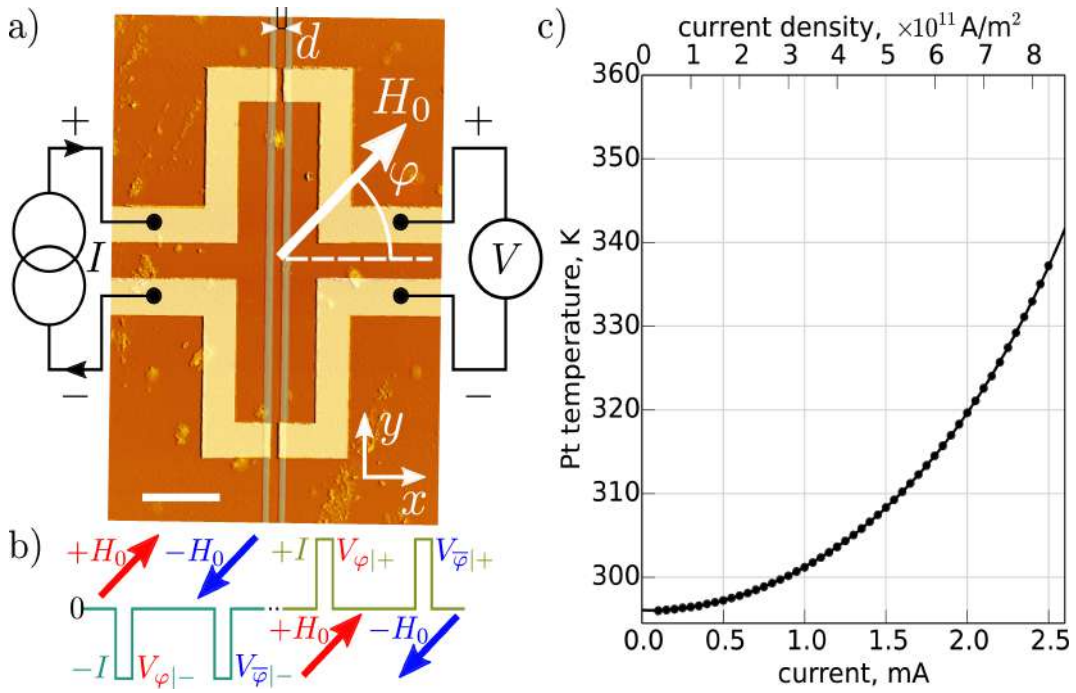

Figure 41: *a) Top view of the lateral device. Two Pt wires (grey lines) are aligned along the $\hat{y}$-direction and placed at a distance d=1.2 μm apart on top of the 18 nm thick YIG film (scale bar is 5 μm). The non-local conductance I-V (injector-detector) is measured using current pulses while rotating the magnetic field H_0 in-plane by an azimuthal angle φ. b) For each value of φ, 4 measurements of the voltage $V_{\varphi|I}$ are performed corresponding to the 4 combinations of the polarities of $H_0|I$. Panel c) shows the temperature elevation produced in the Pt injector by Joule heating while increasing the pulse amplitude I.*

The lateral device is biased by an in-plane magnetic field, H_0 =2 kG set at a variable azimuthal angle φ (or its inverse $\overline{\varphi} = \varphi + 180°$) with respect to the x-axis (see FIG.41.a). A protective layer of 20 nm of Si_3N_4 has been deposited over the top surface to prevent oxidation. The amplitude of the Oested field, at the Pt surface, can be calculated by $H_{Oe} = \mu_0 I/(2\pi R) \approx 10\,\mathrm{G.mA^{-1}}$ were R =150 nm is the radius of the Pt strip. This value is well below the applied magnetic field H_0 and it influence on the non-local measurement is thus negligible.
In FIG.42.a, we have plotted the raw data signals that have been measured according to both polarity of the current ($\pm$) and magnetic field (φ,$\bar{\varphi}$) when the H_0 is applied along

the $\hat{x}$-axis (red and blue) and the $\hat{y}$-axis. This plot highlight quite explicitly the necessity to extract the spin signal within two defined configuration of the field $(\hat{x}, \hat{y})$. The offset signal, that has been identified as a result from the electrical properties of YIG at high temperatures and Seebeck effect, accounts for almost half of the total measured signal and need to be disentangled from the spin signal by measuring the $V_{\hat{y}}|\pm$ offset signal. On the other hand, the spin signal, which is maximum when the field is applied along the $\hat{x}$-axis, majority accounts for the the spin Seebeck effect (quadratic in I). Although the SOT signature can be seen from the asymmetry between the positive and negative current. FIG.42.b shows the current dependence of $\Sigma_{0|I}$ and $\Delta_{0|I}$ signals using equations (2.3) and (2.4). Here, it is worthwhile to emphasize that, when the high/low binding posts of the current source and voltmeter are biased in the same orientation (cf. FIG.41.a), $(\Sigma_0 \cdot I)$ is negative. This is a signature that the observed non-local voltage is produced by ISHE. In the following, we shall concentrate exclusively on the nonlinear behavior of $\Sigma_{0|I}$ which measures the number of magnons created by SOT relatively to the number of magnons annihilated by SOT while being immune to the spin current generated by Joule heating.

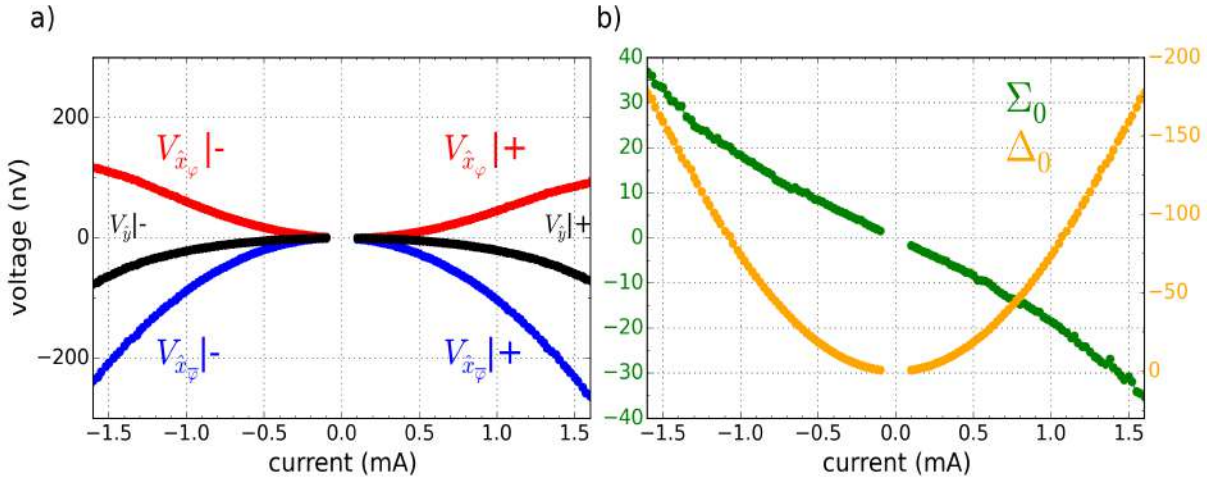

Figure 42: *a) evolution of the raw data signal with the applied current. The b) Current dependence of the amplitude* Σ *and* Δ *at* $\varphi = 0$.

Using the same color code, we have plotted in FIG.43.a both the variation of $\Sigma_{0|+}$ and $-\Sigma_{0|-}$ as a function of the current intensity. Since both quantities follow the same behavior on the whole current range, for the sake of simplicity we shall call simply $\Sigma = (\Sigma_{0|+} - \Sigma_{0|-})/2$ (dark green) their averaged. At low current, the SOT signal follows first a linear behavior $\Sigma^{(t)}/I = \partial\Sigma/\partial I|_{\mathrm{I}=0}$ which is believed to be dominated by thermal magnons transport [2] (the non-local linear resistance between the two Pt wires is $\Sigma^{(t)}/I = 0.019\,\mathrm{m}\Omega$). The rationale for that is that at low current density exactly similar decay behavior is observed in Σ and Δ [2, 218]. Since Δ is understood as being dominated by thermal magnons it is legitimate to assume that Σ is mainly transported by thermal magnons in this regime. We will show in Chapter 5 while discussing the temperature dependence that the situation is certainly fuzzier and part of the linear contribution should be associated with subthermal magnons. Quite remarkably the deviation from the linear conductance occurs very gradually and approximately follows a quadratic behavior. Such a progressive rise is very different from the sudden surge of magnons number reported before in these systems [8, 186]. We have plotted in the insert of FIG.43.a the variation of the normalized inverse spin conductance $\Sigma^{(t)}/\Sigma$ as a function

of current. The observed drop follows a parabolic behavior (cf. solid line fit). We indicate by an arrow, I_c =1.8 mA ($J_c \approx 6 \times 10^{11}$A/m^2), the current intensity necessary to change the normalized spin conductance by 25%, chosen as a landmark for the crossover from a linear spin conduction regime to a nonlinear spin conduction regime. Note that J_c is of the same order of magnitude as the threshold current for damping compensation of low energy modes observed at the same applied field (H_0 =2 kOe) in microstructures [92, 106] (a more precise comparison of the threshold values should also take into account the different thermalization of YIG underneath the Pt between systems). More insight about the nature of the magnons excited above I_c can be obtained by studying the field dependence of Σ [219]. The results are shown in FIG.43.b and 43.c for two values of the current I =0.4 and 2.5 mA, respectively below and above I_c. While in the field range explored, the signal is almost independent of H_0 when $I < I_c$, it becomes strongly field dependent when $I > I_c$. These different behaviors are consistent with assigning the spin transport to thermal magnons below I_c and mainly to subthermal magnons above I_c. In the former case, the magnons' energy is of the order of the exchange energy, while in the latter case, because of their long wavelength, their energy is of the order of the magnetostatic energy. In consequence, Σ is expected to increase with decreasing field at fixed I, because of the associated decrease of the threshold current for damping compensation. The behavior scales well with the reduced quantity I/I_c. This is shown by the solid line in FIG.43.b, which displays the expected field dependence of $1/I_c(H_0)$ [92]) where $I_c \propto (\omega_H + \omega_M/2)[\alpha + \gamma\Delta H_0/(2\omega_K)]$, with $\omega_H = \gamma H_0$ and $\omega_M = 4\pi\gamma M_s$, γ being the gyromagnetic ratio, and $\omega_K = \sqrt{\omega_H(\omega_H + \omega_M)}$ is the Kittel's law. We have used here the amount of inhomogeneous broadening, $\Delta H_0 = 1.5$ G (probably position dependent), as an adjustable parameter, while the value of the other parameters are those extracted from Table 2.1 in Chapter 2.

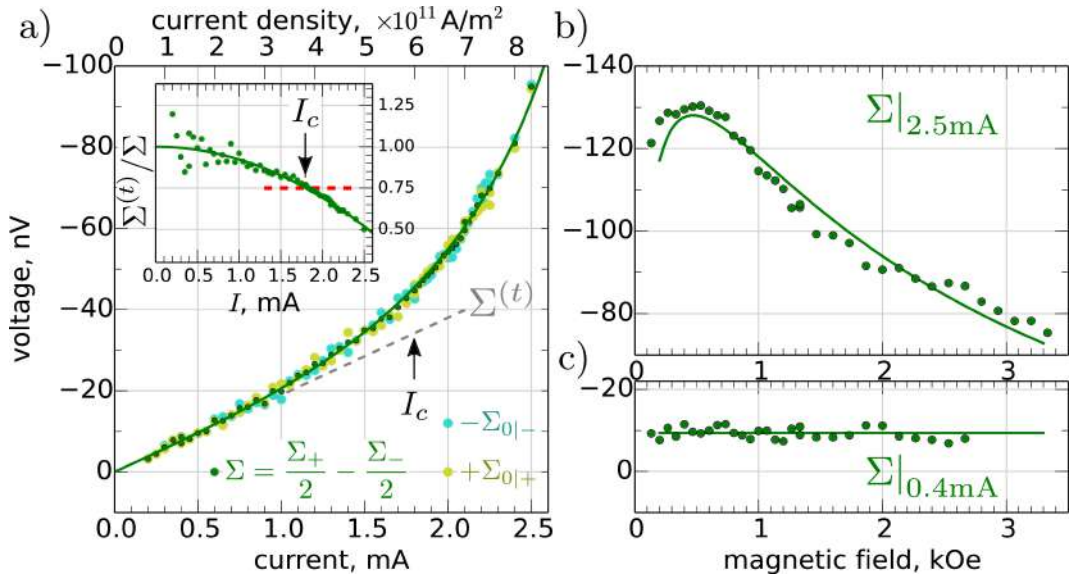

Figure 43: *a) Current dependence of the sum signal Σ averaged over the two current polarities. The dashed line, $\Sigma^{(t)}$, is a linear fit of the low current regime. The insert shows the variation of the normalized inverse spin conductance $\Sigma^{(t)}/\Sigma$ as a function of current. The solid line is a parabolic fit of its drop and the arrow indicates the current required to observe a 25% change in normalized conductance. We use it to mark the crossover from a linear to a nonlinear spin transport regime. Variation of Σ as a function of the magnetic field for two different current intensities b) above and c) below I_c.*

4.2 Non-linear regime detected by μBLS

The above interpretation has been checked by performing microfocus Brillouin light scattering (μ-BLS) in the subthermal energy range on the exact same device as the one used above. FIG.44.a and 44b show the spectral distribution of the BLS intensity J, underneath the injector while rotating the sample in-plane relative to a fixed external magnetic field biased at $H_0 = +2\,\mathrm{kOe}$. Since this produces a shift in the position of the spot along the Pt wire, the different spectra are normalized by the maximum BLS intensity measured at $I = 0$ (green) (we find that the normalized spectra are invariant with respect to a translation of the μ-BLS spot position along the wire direction). We first perform BLS spectroscopy by applying the external field parallel to the wires, *i.e.* along the $\hat{y}$-direction (or $\varphi = \pm 90°$), hereby providing a reference spectrum about the out-of-equilibrium magnons distribution produced by Joule heating. The current injected in the wire is $I = 2.5\,\mathrm{mA}$ and we use here the same pulse method. The results are shown in black in the two panels FIG.44a and 44.b for respectively positive and negative current pulses. The maximum intensity of these black curves indicates the resonance frequency of the Kittel mode, $\omega_K/(2\pi)$, at the corresponding temperature. This is because the μ-BLS response function is centered around the long wavelength magnons. Indeed, the detected signal decreases once the magnon wavelength is smaller than the spot size (approximately $0.4\,\mu\mathrm{m}$: diffraction limited). We then turn the magnetic field in the $+\hat{x}$-direction (or $\varphi = 0°$). We show in panel FIG.44.a the result for positive current pulses (red) and in panel 44.b the result for negative current pulses (blue). The shaded areas on the figures underline the differences with respect to their reference spectra.

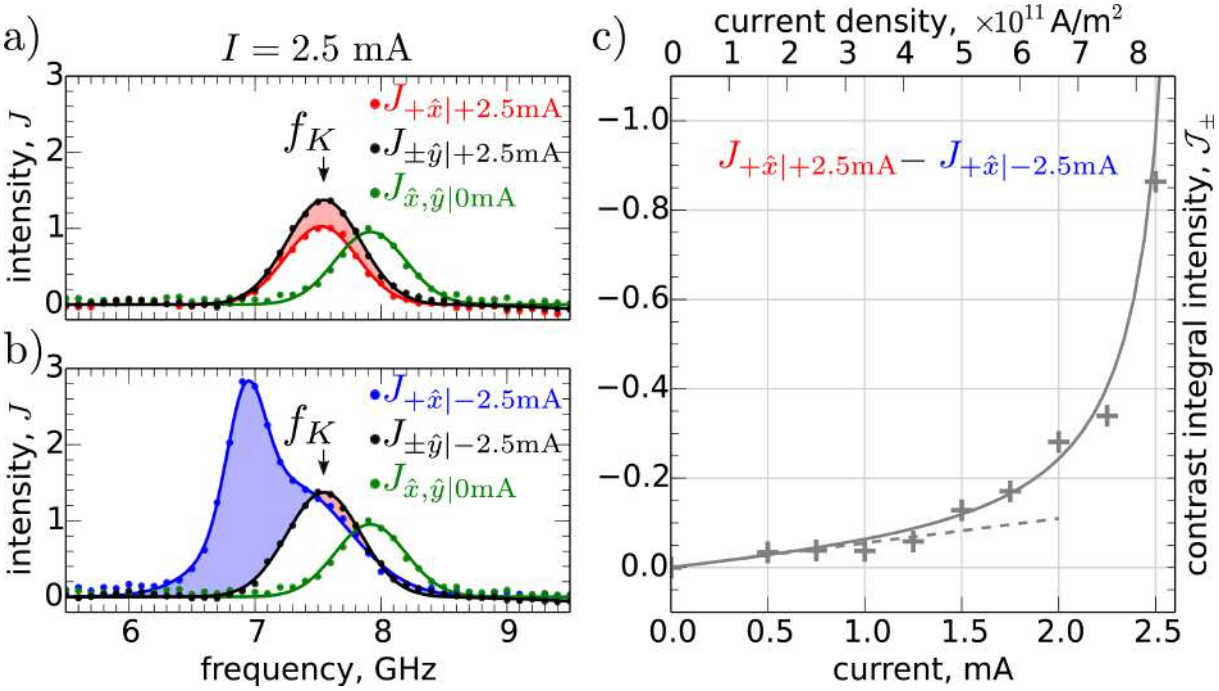

Figure 44: *Micro-BLS studies of the subthermal magnons spectrum measured directly underneath the injector at $H_0 = +2\,kOe$. Panels a) and b) show the spectral deformation at respectively $I = \pm 2.5\,mA$ when H_0 is oriented in the $+\hat{x}$-direction (azimuthal angle $\varphi = 0°$) comparatively to the $\hat{y}$-direction ($\varphi = \pm 90°$). The red/blue area shows the magnons annihilated/created by SOT. The arrows mark the Kittel frequency $f_K = \omega_K/(2\pi)$. Panel c) shows the current evolution of the integrated contrast: difference between magnons annihilated by SOT relative to the ones excited.*

We clearly observe in FIG.44.a, a decrease of the number of subthermal magnons around f_K and in FIG.44.b their enhancement 0.6 GHz below f_K. The enhancement is observed when $(I \cdot H_0)$ <0 (blue), which corresponds to the configuration where the SOT compensates the damping (cf. convention in FIG41.a). In order to isolate the contribution produced solely by SOT, we subtract the spectral contribution measured at $+I$ to the one measured at $-I$. We have plotted in FIG44.c how the spectral integration of this differential signal $\mathcal{J}_\pm = \int J_\pm d\omega$ varies as a function of the current. One observes a regime of linear rise at a small current, followed by a growth above $J_c \approx 6\times 10^{11}\mathrm{A/m^2}$ in a similar fashion as the one reported in FIG43.a. The μ-BLS experiment thus provides direct evidence that an additional spin conduction channel has indeed emerged in the GHz frequency range (subthermal) at large current when SOT is in the range to compensate the damping.
As a short summary of this first non-local experiment, we demonstrated that the regime probed at a low current density regime ($I < I_c$) is the result of thermal magnon diffusion modes within the energy range of $k_B T$ which is in good agreement with previous work [2]. The magnetization order in this region can be considered in a quasi-equilibrium state. Around the crossover current ($I = I_c$), the current density is able to create a large enough torque to compensate the lowest energy magnon mode ($\simeq$ GHz). But it also induces an enhancement of the magnetic fluctuation due to non-linear phenomena that rule the magnetization dynamic behavior at large spin-torque [4]. Increasing furthermore the fluctuations invoke a strong out-of-equilibrium magnon population. Multiples magnon generated in the process will be thermalized near the spin wave spectra bottom via magnon-magnon scattering. We believe that this non-linear spin conductance observed in the high current density regime ($I > I_c$) is due to the generation by SOT of a magnetostatic spin waves density.

4.3 Spatial spectroscopy of spin waves in LPE YIG thin film

We now move on to the YDPB9 sample (19 nm YIG) where the same experiment has been repeated at a similar bias field over different distance d between Pt strips. We might want to note that the Pt thickness in this sample has been reduced to 7 nm while the strip length has been increased up to 30 μm for two main reasons: first it helps the detection of SOT signal by increasing the nominal resistance of Pt strip R_0 and second it enables to enhance the current density applied in the Pt which increases furthermore the torque strength. These changes have a double edge effect since its logically increases the temperature gradient induced by Joule heating in the Pt.
The current dependence of Σ as a function of the distance d is presented in the FIG.45 in the range [0.2-2]μm. The non-linear regime can be observed over different samples and different devices which proved the good reproducibility of the phenomena. Furthermore, the evolution of the SOT signal with the gap d provides the characteristic propagation length of magnon modes involved in the transport. We have plotted in FIG.45.b the decay of the Σ in the two magnon transport regime (thermal/subthermal). By fitting an exponential function through the data points at small gap values, we systematically extract a characteristic thermal magnons decay length of $\mathrm{L}_{\mathrm{exp}}^{(T)} = 0.4\,\mu\mathrm{m}$.
Thermal magnon interacts through short-distance by exchange interactions. According to the Dyson theory [220], magnon-magnon scattering (most likely two-magnons scattering) is the dominant relaxation mechanism. The decay rate of thermal magnon accounting for

the exchange interaction can be calculated through the approximation [97]:

$$\Gamma_{\text{ex}} = \left[(\frac{T}{T_c})^3 \frac{k_B T}{\hbar} \right]^{-1} \tag{4.1}$$

which lies in the $0.17\,\text{ps}^{-1}$ for YIG. The characteristic length of thermal spin waves can thus be calculated using :

$$L^{(T)} = \frac{v_g}{\Gamma_{\text{ex}}} \tag{4.2}$$

where v_g is the spin wave group velocity and Γ is the decay rate. In this scheme, the spin waves spectra in the exchange regime can be expressed as:

$$\omega_T = k_B T/\hbar = \omega_M \lambda_{\text{ex}}^2 k_T^2 \tag{4.3}$$

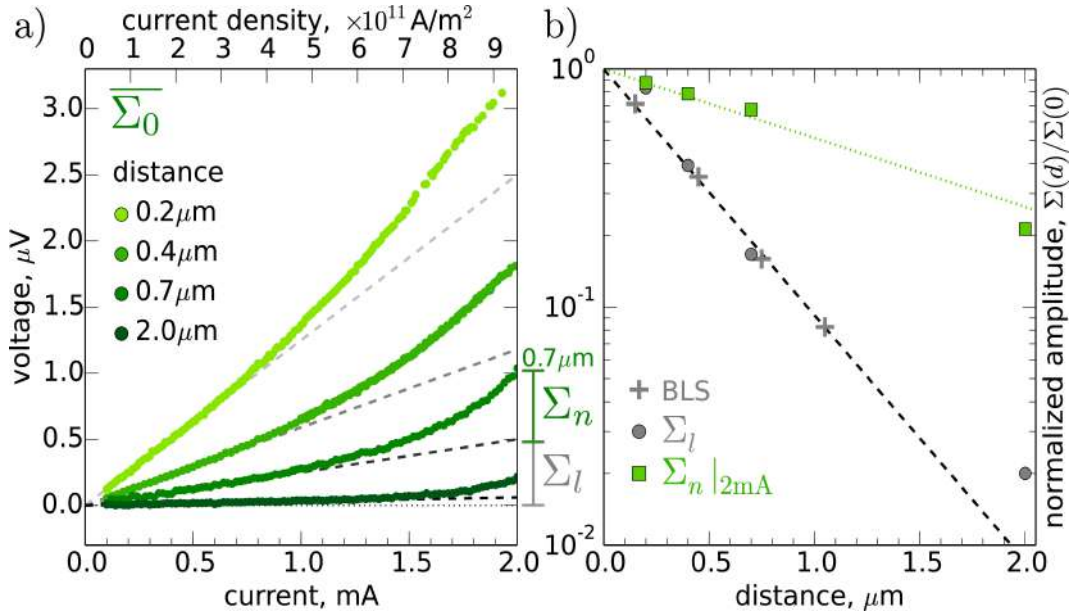

Figure 45: *a) Current dependence of* Σ *measured on 4 devices with different gap d between the two Pt wires. b) Spatial decay of* $\Sigma^{(t)}$ *(dot) and* $\Sigma^{(s)}_{I=2mA}$ *(square) and differential component of the BLS integral intensity (cross).*

where $\omega_M = 4\pi\gamma M_s = 2\pi \times 4.48\,\text{GHz}$ and $\lambda_{\text{ex}} = \sqrt{2A_{\text{ex}}/\mu_0 M_s^2} = 17\,\text{nm}$ is the exchange length (A_{ex}=$3.6\times10^{-7}\,\text{g.cm.s}^{-2}$). This lays a wavevector $k_T = \sqrt{k_B T/(\hbar\omega_M)}/\lambda_{\text{ex}}$ of about $2.25\,\text{nm}^{-1}$, (even though multiple spin waves branches may contribute to the thermal magnons transport). Then the group velocity can be written as :

$$v_g = 2\omega_M \lambda_{\text{ex}}^2 k_T = \frac{2\omega_T}{k_T} \tag{4.4}$$

Using equation (4.1) and (4.2), this given a thermal spin waves propagation length of $L^{(T)} = 6.4\,\text{nm}$ which is two or three orders of magnitude lower than our experimental value. If we assume that LLG extends up to thermal energies, the decay rate of thermal

magnon can be expressed in term of YIG damping α_{YIG} measured in the GHz range:

$$\Gamma^{(T)} = 2\alpha\omega_T \tag{4.5}$$

Combining equation (4.4) and (4.5) this gives:

$$L^{(T)}_{\mathrm{theory}} = \frac{1}{\alpha k_T} = 1.4\,\mu\mathrm{m} \tag{4.6}$$

which is surprisingly in the same order of magnitude than the length measured in our YIG film and in the literature [2, 221]. However, this picture assumes that the LLG equation remains valid up to the THz energies where M_s (i.e the number of thermal magnons) is a constant of the motion.
In the case of subthermal magnon $\Sigma^{(s)}$ (Σ_n in FIG.45), the signal is extracted by subtracting the linear part of Σ from the total Σ signal. The spatial behavior at 2 mA experimentally reveals a decay length of $L^{(s)}_{\mathrm{exp}} = 1.5\,\mu$m. It is not straightforward to estimate this length for dipolar magnons, because it strongly depends on the wavevector and anisotropy. Since the wavelength of these spin waves are much larger than the thickness of the YIG film we can make the estimation $k \to 0$. Thus the damping rate, accounting the spin waves ellipticity, is given by:

$$\Gamma^{(s)} = 2\alpha(\omega_H + \frac{\omega_M}{2}) = 3.15 \times 10^7 \mathrm{s}^{-1} \tag{4.7}$$

with $\omega_H = \gamma H_0$ =2$\pi\times$ 5.60 GHz. Concerning the used bias magnetic field, we have to note that the difference of group velocities of BVMSW and MSSW is relatively small ($\approx$ 25%). For the sake of this estimation we shall use the group velocity of the BVMSW for magnetization polarity where Σ is maximum (θ=0).The velocity can be written as:

$$v_g = \frac{\omega_H \omega_M}{4\omega_0} t_{\mathrm{YIG}} \tag{4.8}$$

where

$$\omega_0 = \sqrt{\omega_H(\omega_H + \omega_M)} = 2\pi \times 7.51\,\mathrm{GHz} \tag{4.9}$$

where ω_H is the FMR frequency and t_{YIG} =19 nm is the YIG thickness.
By using the relation (4.7) and (4.8), the decay length of magnon in the subthermal regime can be estimated at $L^{(s)}_{\mathrm{theory}}$ =3 μm which is reasonably close to the experimental value. Those results are supported by BLS measurements realized in the same sample (see FIG45.b).

t_{YIG} (nm)	α_{YIG}	$L^{(T)}_{\mathrm{theory}}$ (μm)	$L^{(T)}_{\mathrm{exp}}$ (μm)	$L^{(s)}_{\mathrm{theory}}$ (μm)	$L^{(s)}_{\mathrm{exp}}$ (μm)
19	3.2×10^{-4}	1.4	0.4	3	1.5
56	2.0×10^{-4}	2.2	0.6	10	1.3

Table 4.1: *Estimated and measured thermal and subthermal magnon propagation length for 19 nm and 56 nm thick YIG. The measured magnon propagation length is calculated through a exp(-d/L) fit from 0.2 to 2 μm distance between the two Pt electrodes.*

The slightly higher value of the theoretical estimation may be explained by the existence of a magnetically dead layer in the YIG film which effectively reduced the YIG thickness d and thus decrease the dipolar group velocity. Decay of the SOT signal with the distance between the two Pt electrode has been performed for 19 and 56 nm where the characteristic decay length of thermal and subthermal magnon have been probed within the range of 0.2-2 μm. A summary of these experiments is presented in table 4.1. In the case of 56 nm YIG sample, the decay of thermal and subthermal magnon propagation length is quite similar to the 19 nm sample. This result is not in agreement with the scaling of the spin wave velocity. Furthermore, we did not take into account the fact that the damping is reduced when the thickness of the YIG increases. This would lead to an even larger subthermal magnon propagation length.

4.4 Magnon transport in a magnetic insulator with perpendicular magnetic anisotropy : BiYIG

The key parameter for magnon transport lies in the magnetic damping parameter α which has to be as small as possible. It allows magnon to propagate over large distance (μm) in YIG. As described in Chapter 2, the exerted spin-orbit torque enable the broad excitation of spin waves in YIG through the dynamic control of YIG damping via a spin current in YIG|Pt. The ultimate goal would be to achieve Bose-Einstein condensation resulting in a spontaneous excitation of coherent magnons inside extended films in analogy to the auto-oscillation achieved in confined structures [92, 4]. We have seen in the previous section that for small driven torque, the spin information is mostly carried by thermal magnon. This type of spin wave is not compatible for information processing because it lacks phase coherence. Therefore subthermal magnon source is highly desirable, and can be achieved for large applied torque when damping compensation is expected to occur. In YIG film, this can be achieved at large applied current, after a transition from linear to non-linear magnon transport is observed and is expected to be the signature of subthermal magnon excitation.
However, it is known that near the damping compensation point, due to the reduction of M_s by the Joule heating and an increase of magnetic fluctuations, a non-linear red-shift of the magnon frequency appears at large current and causes a spatial self localization of subthermal magnons [81, 79, 93, 92]. Non-linear effects might prevent large spin waves propagation in YIG film especially if the Joule heating produced by the necessary charge current is large. Nonetheless, this problem can be overcome using a thin Bismuth-substituted YIG film with strong perpendicular magnetic anisotropy (PMA) [222]. The effect of the PMA on the Kittel frequency can be written as :

$$\omega = \gamma \sqrt{H_0(H_0 + (4\pi - N^{\mathrm{PMA}})M_s)} \tag{4.10}$$

where N^{PMA} is the demagnetization factor associated with the PMA. If the anisotropy field compensates the demagnetizing field we can express $N^{\mathrm{PMA}} = 4\pi$. It results that the frequency of subthermal magnon becomes independent of M_s and thus leads to a vanishing of the non-linear shift [223]. In the following, we propose a first study of magnon transport in a thin $Bi_1Y_2Fe_5O_{12}$ film via non-local measurement.

4.4.1 Bismuth-substituted YIG

It is well known that the substitution of Y by rare earth elements in garnet crystal grown by liquid phase epitaxy can induce large uniaxial magnetic anisotropy [224, 225]. But most substituted YIG thin films present a large enhancement of magnetic losses incompatible with magnonics spintronic.
Recently, the growth of low damping thin Bi-YIG film has been realized by pulsed laser deposition [222]. The role of Bi substitute is to induce PMA via the hybridization of the Bi^{+3} *6p* in the dodecahedral site with the Fe^{+3} *3d* at the octahedral site [226]. Due to the larger ionic radius of Bi (133 pm), a linear increase of the BiYIG lattice parameter is expected with the amount of Bi content. To account for the substitution, the $Bi_xY_{x-3}IG$ film has been grown on a substituted GGG substrate with a Bi content x =1 to avoid lattice mismatch. The fine tuning of the Bi content induces a large out of plane anisotropy field ($\approx$ 200 mT) that compensates the demagnetizing field. Through FMR measurement the magnetic damping of those film were found to be in the order of 3×10^{-4} which is relatively close to the damping of in-plane anisotropy LPE YIG film at similar thicknesses. This result makes BiYIG film a serious candidate for long range magnon transport but also for magnonic devices based on forward volume waves that require out-of-plane magnetization.

4.4.2 Spin transport in BiYIG

We have performed non-local magnon transport on a 25 nm $Bi_1Y_{2-3}IG$ thin film. On top of the magnetic film, we have patterned two Pt strips that are 30 μm long, 300 nm in length and 6 nm in thickness. There are electrically contacted with Au|Ti electrodes as it can be seen in FIG.46.a. Like the other samples, we have put a Si_3N_4 capping layer on top of the sample, to prevent oxidation. In this sample, we have deposited the Pt layer with a different technique. In contrary to the YIG/Pt device where the Pt is evaporated, the Pt in BiYIG film has been sputtered. Due to the energetic deposition of dc sputtering, it ensures good covering of the contact surface between BiYIG and Pt whereas the soft deposition of evaporated Pt can result in a poorly coupled interface and thus less spin conversion [227]. To ensure the good quality of sputtered Pt in BiYIG, we have measured the spin Hall magnetoresistance (SMR) ratio by injecting a current of 100μA in the Pt while rotating an in-plane external field of 2 kG. The angular dependence of the SMR ratio is plotted in FIG.46.b. Using equation 2.5, this gives a spin mixing conductance of the order of $g_{\uparrow\downarrow}$ =2.42×10^{-18} m^{-2}, which is much higher than the evaporated Pt (without local Joule heating) and assert a better coupling between the Pt and BiYIG at the interface.
FIG.46.c shows the non-local voltage as a function of the current for different directions of the external field H_0. When H_0 is colinear to the x-axis (red and blue dots), one can see that the non-local voltage does not change sign as the polarity of the current is reversed. This strongly indicates that the signal is dominated by thermal effects. However the asymmetry between $V_\varphi|\pm$ and $V_{\hat{\varphi}}|\pm$ in the BiYIG|Pt system is found to be large. FIG.46.c also shows that the spin conduction is larger when $H_x.I < 0$. The condition $H.I << 0$ corresponds to the case where the damping is compensated (or decreased), while $H.I > 0$ corresponds to the case where the damping is enhanced. This demonstrates that in the case of BiYIG the enhancement of the fluctuation of sub-thermal magnons is directly visible in the raw data. This is mostly because the parasite electrical conduction is strongly reduced in this case. By investigating the evolution of this offset (measured when the external field is aligned along φ =90°) with the applied current, we observed that $V_{\hat{y}}$ presents a very similar electrical behavior as in FIG.39. This electrical leakage-like property (exponential rise, dissipative energy) is reproducible among every tested devices while the Seebeck-like signal largely fluctuates in sign and amplitude due to mismatch

of Kapitza resistance of top and bottom Au|Ti|Pt contact. From this observation, we attribute the offset $V_{\hat{y}}|\pm$ to a pure parasitic signal due to the elevation of temperature via Joule heating. Even though, BiYIG seems to present similar spin transport properties than YIG samples, we can already see from FIG.46.c that the pure offset signal $V_{\hat{y}}$ contribution is less than 10% of the total signal whereas it was around 35% in YIG system. This result can be explained by various reasons. First due to the high resistance value of the Pt strip in this batch, the spin Hall angle $\theta_{\mathrm{SHE}}^{\mathrm{Pt}}$ of the Pt strip could be higher than Pt evaporated on YIG and thus a better spin to charge conversion. Second due to sputtering, the spin mixing conductance of BiYIG|Pt interface is much higher. Finally, the large enhancement of the spin signal could be the first indication of a long decay of spin waves in BiYIG and enhancement of the probed magnon density. It results in an increase of the signal to about a factor 10 compared to YIG samples. Next we investigated the angular dependence of the non-local spin signal in BiYIG|Pt.

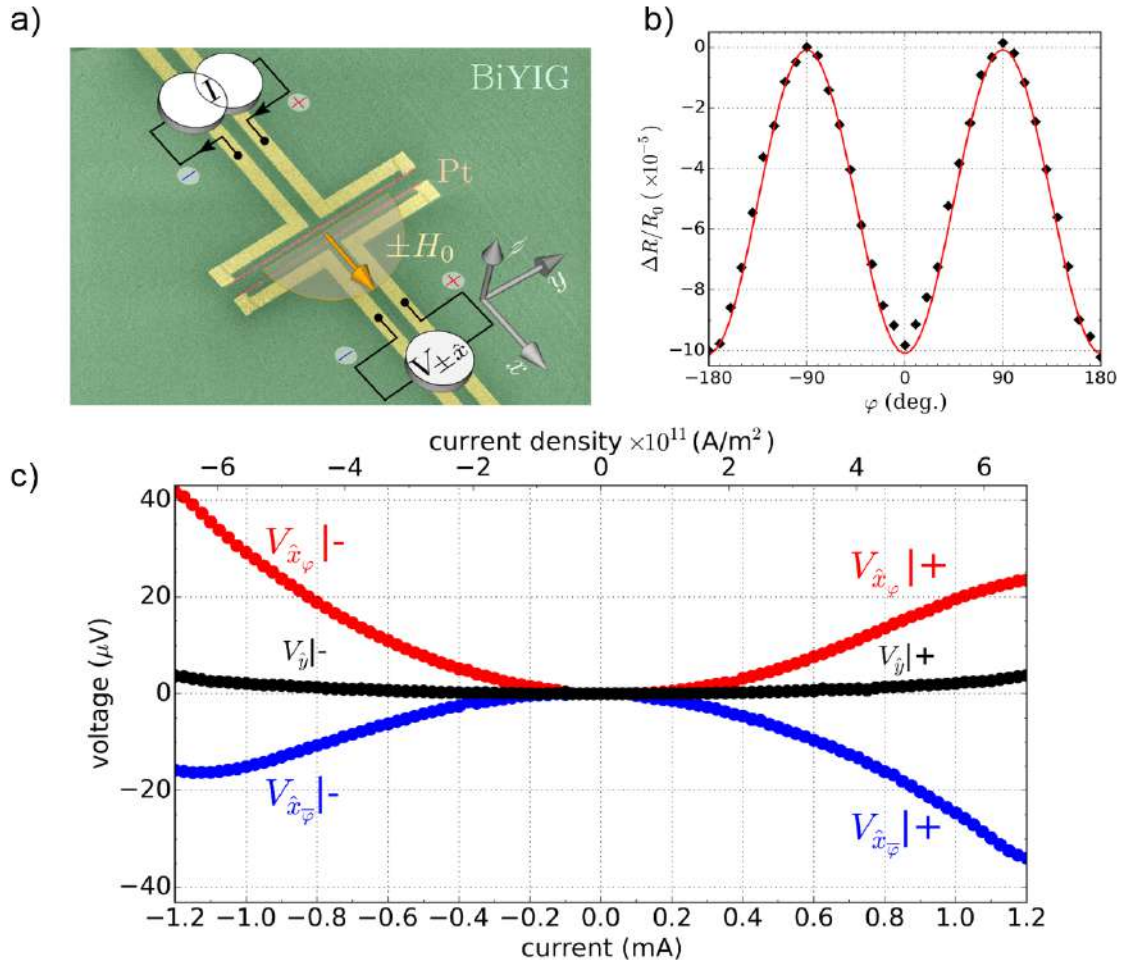

Figure 46: *a) SEM image of the BiYIG/Pt nanostructures with a sketch of the polarity of current injection and voltage detection in the Pt strips. b) Spin Hall magnetoresistance ratio (back dot) of sputtered Pt in BiYIG for an applied current of 100μA and applied field of 2 kG. The red line is a $\cos^2(\varphi)$ fit. c) Raw data of non-local experiment in BiYIG|Pt. The measured voltage is plotted as a function of the current and for an external field H_0 =2 kG apply perpendicularly to the Pt strip for both polarity of H_0 (φ along the x-axis as red dots and $\bar{\varphi} = \varphi + 180°$ along the -x-axis in blue dots). The voltage measured when the external field is applied along the y-axis is display as black dots.*

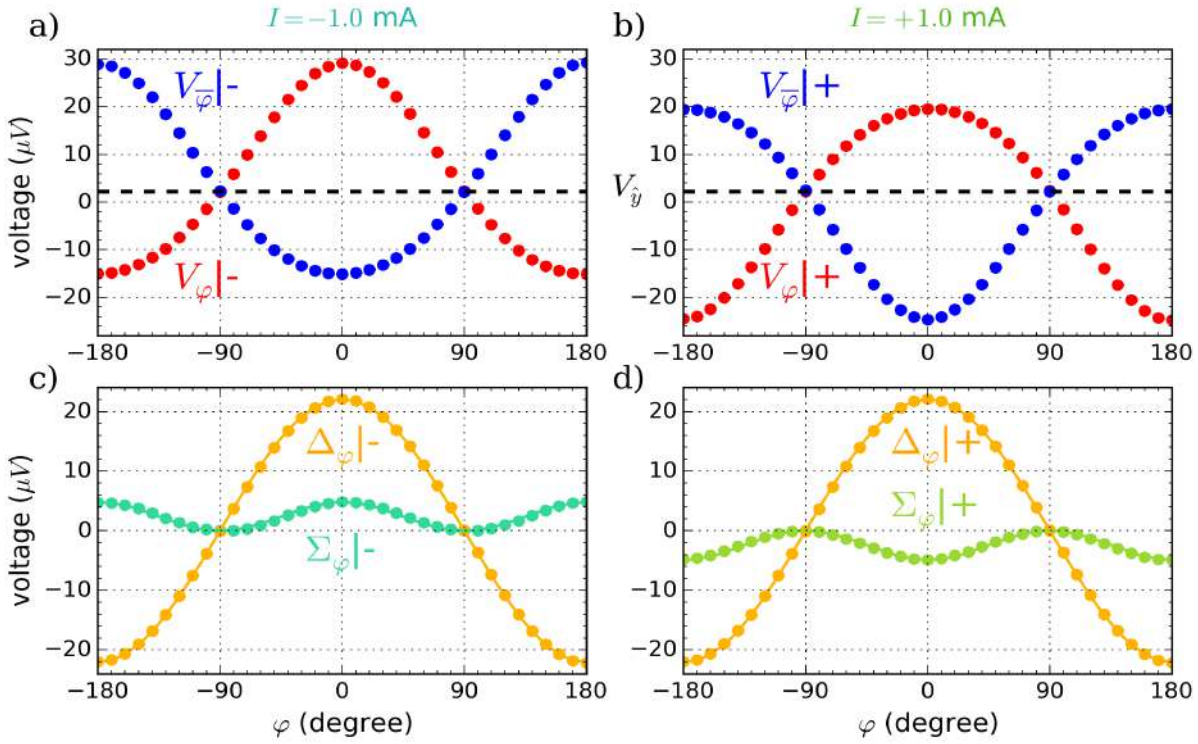

Figure 47: *Angular dependence of the non-local voltages $V_{\pm|\mp}$ measured in $Bi_1Y_2Fe_5O_{12}$ while inverting the polarity of the applied field $H_0 = \pm 2kOe$ (red/blue) for a) negative and b) positive current pulses $I = \mp 1.0mA$. The measured signal can be decomposed c) and d) in three components: Σ (green): the signal sum, Δ (orange): the signal difference and $V_{\hat{y}}$: the offset (dashed). The gap between the Pt electrode is 0.7μm*

FIG.47.a and FIG.47.b present the raw spin signal as a function of the φ angle between the x-axis and external field for an in-plane magnetic field of 2 kG. As for YIG|Pt system, we have measured the non-local spin signal for both polarity of the applied field and current which allows extracting $\Sigma_\varphi|\pm$ and $\Delta_\varphi|\pm$. The total spin signal is defined around an offset which can see as black dashed line in FIG.47.a and FIG.47.b. From the raw spin signal, we have extracted $\Sigma_\varphi|\pm$ and $\Delta_\varphi|\pm$ signals using equation 2.3 and 2.4 as seen in FIG.47.c and FIG.47.d. One can observe two different angular dependence of $\Sigma_\varphi|\pm$ and $\Delta_\varphi|\pm$ that evolve in $\cos(\varphi)^2$ and $\cos(\varphi)$ respectively. The sign of $\Delta_\varphi|\pm$ signal is independent of the current direction while $\Sigma_\varphi|\pm$ is reversed by changing the polarity of the injected current. These characteristics are in good agreement with the symmetry of non-local SOT and SSE. Note that in those devices, the Σ signal is much higher than the offset signal (one order of magnitude) and helps considerably to reduce the noise in the measurement (especially at high current).
The evolution of $\Sigma_0|\pm$ and $\Delta_0|\pm$ with the apply current are presented in FIG.48. As predicted by the angular dependence, $\Delta_0|\pm$ is even with current polarity and rises quadratically with the apply current. This behavior confirms the thermal nature of $\Delta_0|\pm$ and can fully be attributed to the spin Seebeck effect. On the other hand, $\Sigma_0|\pm$ seems to present every ingredient of SOT. Besides the sign change of $\Sigma_0|\pm$ with the current due to the SHE, magnon transport in BiYIG seems to contain linear regime at low bias current while nonlinear spin conduction is probed for large torque.
The crossover from linear to nonlinear in BiYIG can be seen in more detail in FIG.49.a. The Σ signal is the difference of $\Sigma_0|+$ and $\Sigma_0|-$ and translates the average amplitude of Σ. To be more quantitative about the shift from linear to nonlinear spin conductance, we have fitted the linear part of SOT signal $\Sigma^{(t)}$ in the low current regime as grey dash

line. In the insert we show the deviation of the normalized inverse Σ from linear spin conduction. The crossover, defined as 25% deviation, can be seen by the intersection of $\Sigma^{(t)}/\Sigma$ with the red line. We found a crossover current density on the order of $J_c \approx 6 \times 10^{11}\mathrm{A/m^2}$ which is similar to YIG|Pt system. To unambiguously disentangle the nature of the Σ signal in both low and high current regime, we have performed the field dependence of Σ below and above the crossover current J_c which can be seen in FIG.49.b. Σ signal in this plot has been sorted by current symmetry consideration in order to probe the SOT signal for both polarities of the applied magnetic field H_0. The spin signal reached a maximum value at H_0 =700 Oe when the total magnetization of YIG is fully saturated in-plane (similar for Σ and Δ). In the linear regime (I=0.4 mA) the SOT signal is found to be poorly dependent on the external field whereas in the nonlinear regime, Σ is highly tuned with H_0.

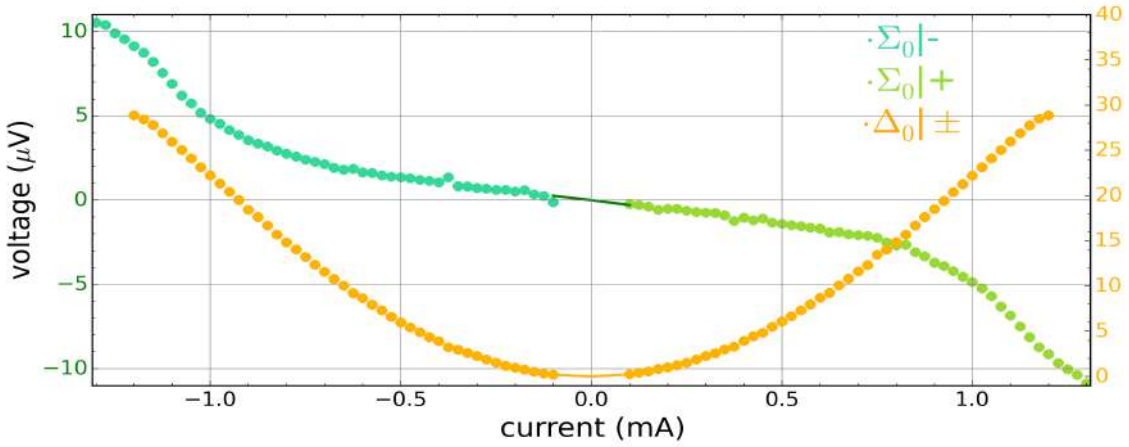

Figure 48: *Current dependence of the amplitude Σ and Δ at φ =0 in $Bi_1Y_2Fe_5O_{12}$.*

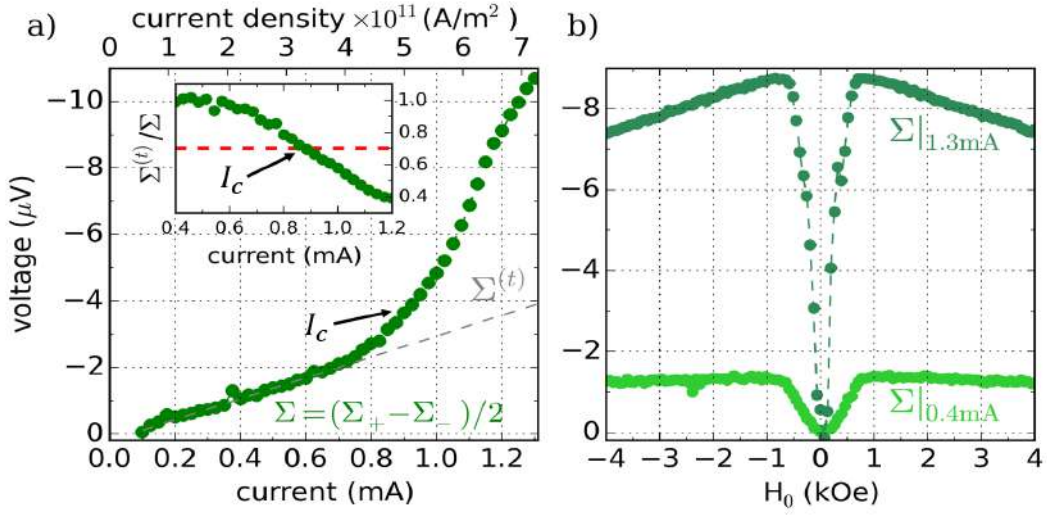

Figure 49: *a) Current dependence of the sum signal Σ in $Bi_1Y_2Fe_5O_{12}$ averaged over the two current polarities. The dashed line $\Sigma^{(t)}$, is a linear fit of the low current regime. The insert shows the variation of the normalized inverse spin conductance $\Sigma^{(t)}/\Sigma$ as a function of current. b) Variation of Σ as a function of the magnetic field for two different current intensities bellow and above I_c. Σ here as been calculated with current symmetry.*

Those characteristics are compatible with the spin signal probed in YIG/Pt system. This proves an efficient subthermal magnon excitation by SOT in BiYIG thin film. The fact that the energy necessary to reached non-linearity is almost identical than in YIG, assert the high quality of these films.

4.4.3 Spatial spectroscopy of spin waves in BiYIG thin film

Finally, we address the spatial spectroscopy of magnon in BiYIG. Using the same procedure, we have measured the non-local Σ signal for various distances between the two Pt strip which goes from 0.2 μm up to 20 μm. For each distance, we have estimated the thermal contribution $\Sigma^{(t)}$ in the SOT signal by fitting the linear spin conduction at low bias current. The subthermal magnon population is then extracted by subtracted $\Sigma^{(t)}$ from the total Σ signal. The decay of thermal $\Sigma^{(t)}$ and subthermal magnon Σ-$\Sigma^{(t)}$ can be found in FIG.50.a and FIG.50.b. The spin signal is plotted as the probed charge current by ISHE $I_{\mathrm{ISHE}} = V_{\mathrm{ISHE}}/R_{\mathrm{Pt}}$ to account for the detector Pt strip resistance value which can vary from device to device by more than 20% here. This helps to reduce the error in the extraction of magnon diffusion length. FIG.50.a shows the exponential decay of thermal magnon population I^{L}_{ISHE} for an applied current of 1.2 mA and an external field of H_0=2 kOe. For small gap [0.2-0.7] μm, we could determine thermal magnon propagation length L^T of 0.4μm through an exponential fit which is similar to the value found in YIG samples. Although, contrary to YIG samples, the spin conversion at the BiYIG|Pt is much stronger and Pt resistance much higher which allow to have much better sensitivity at large distances.

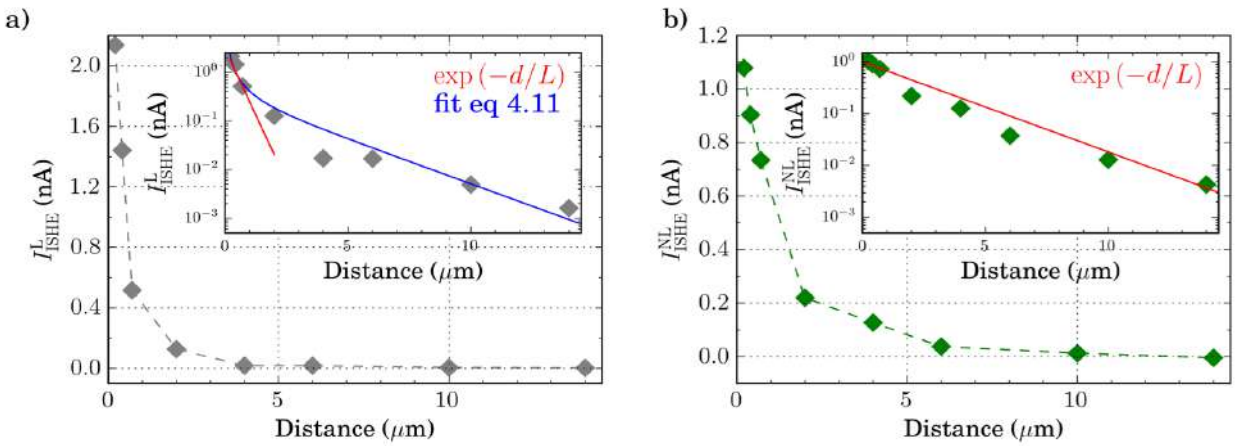

Figure 50: *a) Spatial decay of thermal magnons for an external field H_0 =2 kOe. We have plotted the charge current probed by the Pt detector when a current of I =1.2 mA is applied in the injector strip. The insert presents a log scale of the spin signal measured as a function of the distance between the injector and detector. The red lines are exp(-d/L) fit in the small distance regime with lies a propagation distance of L^T. The blue line is a fit of equation* (4.12) *which supposes that the thermal magnon transport decay within a diffusive transport in short distance and is followed by a relaxation regime at long distance. From this, we extract a thermal magnon diffusion length in the order of L^{T}_{diff} =2.7 μm. b) Spatial decay of subthermal magnon. This is estimated by subtracting the contribution of thermal magnon from the total Σ signal. From an exponential fit (red line), a subthermal magnon propagation length is extracted $L^{(s)}$ =2.5 μm.*

As can be seen in FIG.50.a, the propagation of thermal magnon at long distance (d >2.0 μm) seems to decay with much longer characteristic distance in respect to short gap (d <2.0 μm). These two transport mechanisms have been described in the work of Cornelissen et al [2] in the framework of a spin diffusion theory [97]. It implies that the thermal magnon in short distance is ruled by a diffusive transport while at large distance, magnon relaxation is dominating. These two regimes can be analytically described by a one-dimensional spin-diffusion equation that takes the form [2]:

$$\frac{\partial^2 n_m}{\partial^2 x} = \frac{n_m}{L^{(T)2}} \tag{4.11}$$

with n_m the non-equilibrium magnon population and $L^{(T)}$ the thermal magnon diffusion length. This diffusion equation takes the solution for the spin accumulation define in equation (1.47). Taking the boundary conditions that every magnon is absorbed at the interface, the decay of thermal magnon signal the distance d can be found as:

$$I^L_{\mathrm{ISHE}}(d) = (\xi / L^{(T)}_{\mathrm{diff}}) \frac{\exp(d/L^{(T)}_{\mathrm{diff}})}{1 - \exp(2d/L^{(T)}_{\mathrm{diff}})} \tag{4.12}$$

where ξ is a distance independent parameter. A fit of equation (4.12) can be seen as blue line in FIG.50.a and gives a magnon diffusion length of L^T_{diff} =2.7 μm in quantitative agreement with the reported value for thick YIG [2, 221]. On the other hand subthermal magnon population $I^{\mathrm{NL}}_{\mathrm{ISHE}}$ in FIG.50.b exhibits a defined exponential decrease with the distance that seems to be slower than for thermal magnons in the vicinity. But eventually, the two decay have the same characteristic propagation length for large gap (d>5 μm). As it can be seen in the insert, a fit can extract subthermal magnon propagation length of $L^{(s)}$ =2.5 μm. The decay length of subthermal magnon in thin BiYIG is compatible with the value found by our collaborators via BLS where a propagation length of 3.7 μm has been reported [223]. We emphasize that spin waves propagation in BiYIG is two to three times larger than in YIG film of similar thickness and damping which can be attributed to the fine tuning of the spin waves spectrum due to the PMA. This allows to extend the emission radius of spin waves by avoiding the self-localization effect due to non-linear dynamics at large apply current.

4.5 Conclusion

In this chapter, we presented spin waves transport in ultra-thin YIG films by non-local measurements. This method allows an all-electrical excitation and detection of magnon via the YIG|Pt interface. We have demonstrated, than for a small current density applied in the Pt injector, the transport probed in the Pt detector is ruled by thermal magnon belonging in to THz frequency domain. This observation is supported by the field dependence which did not show any particular evolution of the thermal magnon population with the amplitude of the external magnetic field owing to the exchange interaction (energy of the order of $k_B T$). The thermal magnon conduction has already been uncovered in several reports by studying the gap [2], temperature [104, 218], field [219] and YIG thickness [221] dependences. Nonetheless, we will see in the next chapter that the full picture of the linear regime could be in fact more complex. This magnon density excited only electrically differs from the spin current induced via temperature gradient and known as spin Seebeck effect which is also detected in our structures. We have make sure to disentangle

these two defined quantity by symmetry considerations. This assumption has been check by studying the variation of spin signal with the direction of the in-plane magnetic field. The major contribution of this work is the investigation of the spin waves transport at large applied current densities. We take advantage of the high quality and low thickness of our films to electrically control the damping in YIG via the spin-orbit torque induced by the Pt layer. Besides the wide frequency excitation of spin waves in YIG, a large current density in the Pt strip allows to supply a strong enough torque to compensate the damping of low energy magnon modes. Subthermal magnon population is detected in our system at a crossover current of $J_c \approx 6 \times 10^{11}\mathrm{A/m^2}$ which is in the same order of magnitude than the threshold observed for compensate the Kittel mode in YIG micro-discs [92]. The characteristic feature of subthermal magnon regime is a shift from linear to nonlinear spin conductance. The nature of this signal has been identified by a net dependence of the nonlinear signal with the applied magnetic field. This behavior is consistent with theory since the threshold current is expected to increase with the applied field. We believe from those observations, that the magnon population in this new spin conducting channel are long wavelength spin waves in the GHz frequency range (magnetostatic energy). Ultimate proof of a crossover from thermal to subthermal magnon regime, are the μ-BLS measurements realized on the same device. This technique is ideal to confirm our results since it enables to recover the density of state of short wave-vector magnons. From BLS intensity we saw an enhancement of the magnon density for damping compensation configuration, while a reduction of the magnon population is observed in an anti-damping like configuration. Combined with a current dependence, these measurements demonstrated that the nonlinear spin conductance observed in non-local spin transport is the hallmark of subthermal magnon transport in YIG excited by SOT. Nonetheless, this nonlinear signal does not rise exponentially has expected by the theory but follows a $\frac{I}{I_c} \cdot \frac{1}{(1-(I/I_c)^2)}$ [228] behavior instead. This indicates that this nonlinear spin conductance can be qualified as a subcritical regime. When the system is driven in a strong out of equilibrium regime via SOT, it induces magnetic fluctuation. These cause the subsystem to redistribute the magnetic energy to other magnon modes throughout nonlinear magnon scattering. This prevents the SOT to fully compensate a single magnon mode into auto-oscillation regime characterised and an exponential increase. Through a gap dependence, we have probed the magnon diffusion length in the different regimes. We observe a much higher diffusion length in the case of subthermal magnon than thermal magnon in our ultra-thin YIG films.

Finally, we have presented the first non-local magnon transport in large PMA thin magnetic insulator BiYIG. We have demonstrated that such film can be a reliable medium for subthermal magnon emission of spin waves by spin-orbit torque since it can partially overcome the self-localisation effect due to the magnon frequency red-shift. It results in an enhancement of the magnon propagation length in BiYIG compare to YIG thin film which is the reference material for manipulating spin waves. From a technological point of view, BiYIG offers interesting functionalities due to the strong PMA and is a promising material for future spin waves devices design that would require out of plane magnetization. In addition, BiYIG could also be a bridge between magnonics and photonics due to its large Faraday rotation coefficient.

Chapter 5

Spin transport at high temperature

In the last chapter, we demonstrated that subthermal magnons can be induced by SOT in the YIG|Pt system. However it is an important statement to study the reliability of this excitation and its limitations. In the following, we present the spin transport at large current density ($>10^{12}$A/m^2) and more particularly when the elevation of the Pt strip temperature induced by Joule heating is getting close to the Curie temperature of the YIG. We will first measure the influence of the onset temperature on the dynamic properties of YIG thin film and YIG|Pt system by investigating non-local magnon transport at low temperatures. Moreover, an analytic model of the subthermal magnon excited by a spin current will be given and will be compared to our experimental results to disentangle the role of the temperature. Finally, we will study the spin transport when the injector/detector Pt strip has a thinner or larger width. We will show that the temperature rise is an important matter for SOT and SSE signals in non-local experiments.

5.1 Spin signal at large current

5.1.1 Estimation of temperature

In this section, we will focus on high energy spin transport in the YDPB9 sample where the Pt dimension has been upscale to 30 μm×0.3 μm for a thickness of 7 nm. By changing these parameters, we have increased the input and output resistance of about 47% compared to the YDPB8 sample. It results that the temperature gradient induced by the application of large current in the Pt has dramatically increased compared to the YDPB8 sample and has to be recalibrated. In FIG.51.a we show the resistivity of the Pt as a function of the temperature. Since the evaporation of the Pt layer has been done within the same procedure in every LPE YIG films, this measurement has been taken as a reference to estimate the temperature in the Pt (also used for FIG.41.c). Linearly fitting this dependence allow us to extract the slope $\Delta\rho_{\mathrm{Pt}}/\Delta T$=0.038 $\mu\Omega$.cm.K^{-1}. To estimate the temperature gradient in the YDPB9 sample, we have measured the evolution of the Pt resistance as a function of the injected pulse current as shown in FIG.51.b. The resistance follows a quadratic evolution due to Joule heating ($R_{\mathrm{Pt}}I^2$). Knowing the variation of the Pt resistance with the current, we used the following relation to estimate the actual temperature in the Pt :

$$\rho(T) = \rho_0(1 + \alpha\Delta T) \tag{5.1}$$

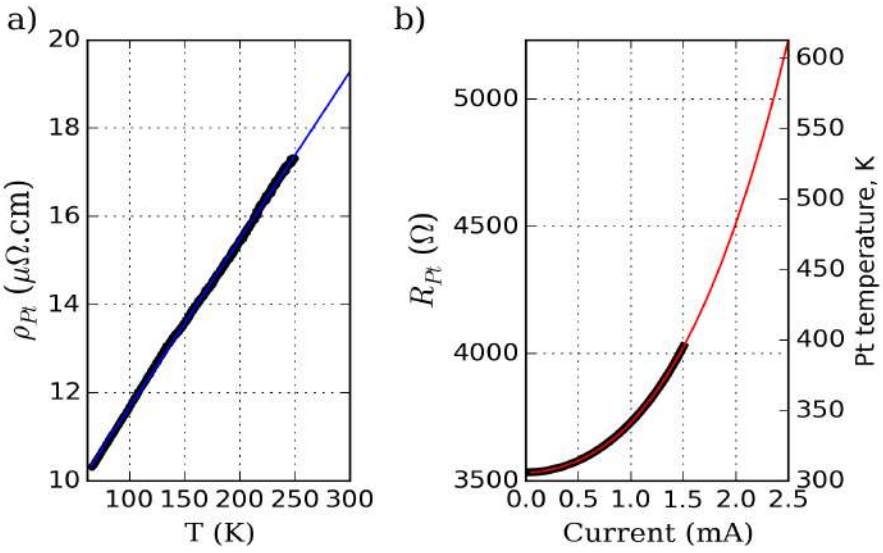

Figure 51: *a) Temperature dependence of the Pt resistivity. Through a linear fit (blue curve) we extract a slope $\Delta\rho_{Pt}/\Delta T$ =0.038 $\mu\Omega$.cm.K^{-1}. b) Evolution of the Pt resistance as a function of the pulsed current. We observe a quadratic behavior due to the Joule heating. The red curve is a polynomial fit allowing us to deduce the temperature in Pt as a function of the applied current.*

with ρ_0 being the resistivity of the Pt at room temperature and $\alpha = \Delta\rho_{\mathrm{Pt}}/(\Delta T)\rho_0$. The estimated temperature in the Pt calculated from eq (5.1) is indicated in the right abscissa of FIG.51.b. Due to the larger input resistance and higher injected current density, the temperature in the Pt is larger in the case of the YDPB9 sample.

5.1.2 Spin signal

In the following, we explore the non-local spin transport at large current density ($J_c > 8{\times}10^{11}$ A/m^2). As a matter of comparison, we have injected current in the same Pt strip as in FIG.51.b and measured the non-local spin conductance Σ in a Pt strip located 0.4 μm away from the injection. The evolution of Σ with the current can be seen in FIG.52.a. Quite unexpectedly, additional regimes appear in the SOT signal at large current density. After crossing the linear (blue area) to non-linear (green area) spin conductance regimes, the SOT signal reaches a maximum conductance for $J_c \approx 10.4 \times 10^{11}$A/m^2 and then decreases toward a zero spin conductance around 11.9×10^{11}A/m^2 (orange area). More information can be obtained from the current dependence of Δ plotted in FIG.52.b. As for Σ signal, a drop of the Δ signal can also be observed with the difference that it appears for lower current density ($\approx 8.7{\times}10^{11}$ A/m^2). Nonetheless, the Δ signal reaches a zero value and even change sign. It is important to note that the upper limit of the third regime (orange) involving a drop of spin signal to zero corresponds to a Pt temperature of T=587.5 K which is relatively close to the Curie temperature T_c of YIG. If we neglect interfacial thermal resistance of YIG|Pt, this result indicates that the magnetization of a small YIG region located underneath the Pt injector can be considered as null in this regime. Those behaviors are observed in both YIG and BiYIG thin films. The fact that the drop of the total spin signal appears close to the Curie temperature implies that the temperature is somehow involved in the appearance of a maximum spin conductance in YIG|Pt.

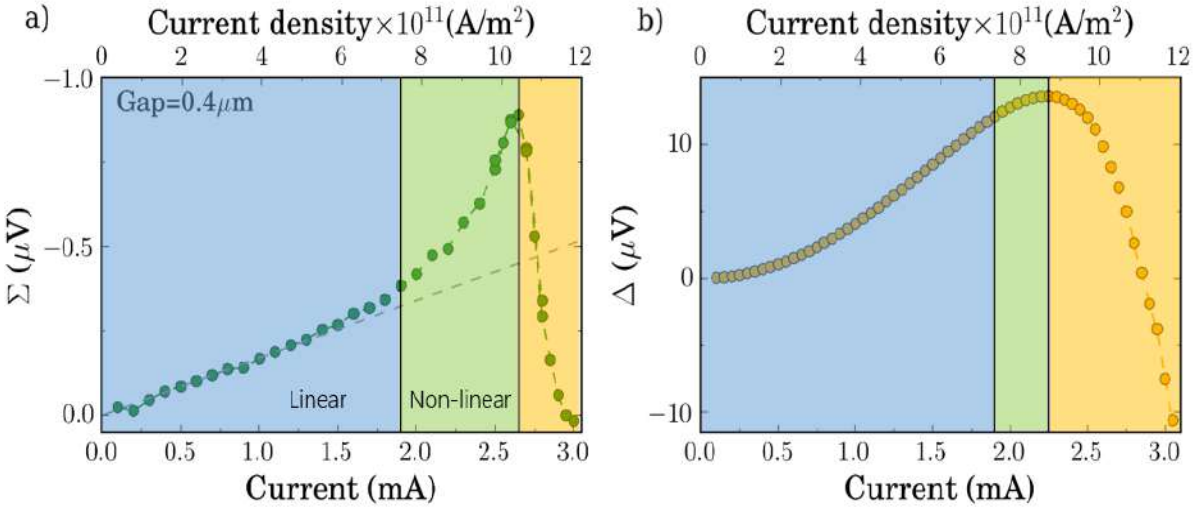

Figure 52: *a) Non-local SOT signal dependence on the amplitude of the pulse current applied at a fixed external field of H_0 =2 kG. b) Non-local SSE signal as a function of the applied pulse current. The orange area correspond to the regime where the spin signal drops.*

5.2 Low temperature measurements

In an attempt to reduce the spurious electrical contribution to the spin conductance, we have performed non-local magnon transport measurements in a low temperature environment. However, a deep understanding of such experiments might not be straightforward. It is known that the magnetic properties of bulk YIG can vary with the temperature. For instance, it has been reported that the cubic anisotropy [229] (K_1 in equation (1.7)) and

uniaxial perpendicular anisotropy [230, 231] have a net dependence with temperature. It is thus an important statement to investigate the magnetic properties of YIG thin film at low temperature and the effect of the Pt layer overlayer.

5.2.1 Temperature dependence of the magnetic properties of YIG thin film covered by Pt

The low temperature magnetic characterization as been performed on the 19 nm thick YIG film sample (YDPB9). The following section follow a work that has been published in *IEEE Magnetic letters* [18]. To investigate the anisotropy constants with the temperature, FMR measurement has been performed in a X-band cavity for rf field at the fixed frequency of 9.3 GHz. The first-order cubic anisotropy constant K_1 and uniaxial perpendicular anisotropy constant K_U were extracted by measuring the variation of the resonance field when the static magnetic field is set from the normal to the film plane [232]. The evolution of anisotropy constants of YIG thin film with the temperature can be seen in FIG.53.a and b as black dots. We observe an increase of the absolute value of K_1 as the temperature is decreased which is in really good agreement with the variation found in bulk YIG [229]. On the other hand K_U appears to be positive and increases with temperature. Two main contributions can be at the origin of $K_U(T)$. The first one can be attributed to the growth anisotropy induced by Pb impurities from the solvent [230]. The second contribution can be identified as an uniaxial stress anisotropy arising from the small lattice parameter mismatch between the GGG substrate (a_{GGG}=12.383 Å) and the YIG film (a_{YIG}=12.376 Å). By taking into account these two considerations, the calculated value for K_U with bulk parameters only covers 40% of experimental values. This difference can be ascribed to surface induced contribution to the uniaxial perpendicular anisotropy present in ultra thin films.
To probe the magnetic relaxation of YIG thin film, the full width at half maximum of the FMR spectra is extracted for an in-plane magnetization configuration. The FWHM responds linearly with the rf field frequency and the inhomogeneous contribution to the linewidth is found to be in the order of 2.44 Oe which is close to the reported value on PLD-grown YIG films of similar thickness [20]. The interesting feature of this experiment is the temperature dependence of the FWHM that has been recorded at 9.3 GHz and is shown in FIG.53.c. The spectra reveal that the FMR linewidth increases for decreasing temperatures. Such behavior has been reported on ultra thin YIG films grown either by a spin-coating method [233] or by off-axis sputtering [234]. This observation was ascribed to the slowly relaxing impurity mechanism that has already been extensively studied on bulk YIG [235, 115]. The relaxing impurity mechanism was attributed to the rare earth Fe^{2+} impurities, induced during the growth process. The additional linewidth ΔH_{SR} due to this relaxation can be described by the expression [234]:

$$\Delta H_{\mathrm{SR}} = A(T)\frac{\omega\tau}{1+(\omega\tau)^2} \tag{5.2}$$

where $A(T)$ is a frequency-independent prefactor and τ a temperature-dependent time constant. By comparing our experimental results with equation (5.2), we found that this model cannot fully reproduce our data. This suggests that other relaxation mechanisms contribute to the FMR linewidth at low temperatures. As put forward in [17], the existence of a transition layer between LPE-grown YIG films and the GGG substrate, whose thickness is estimated to be around 5 nm (nearly a third of our film thickness), could produce additional relaxation channels.

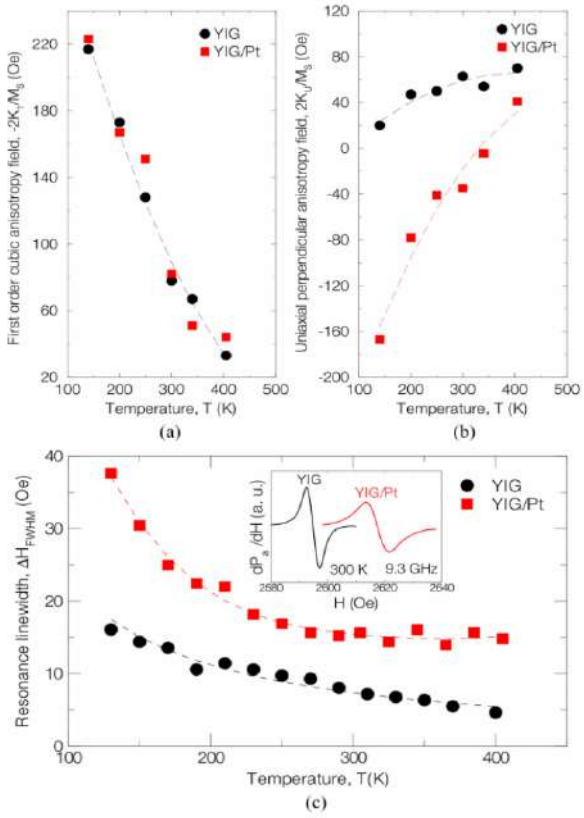

Figure 53: *Temperature dependence of a) cubic anisotropy, b) uniaxial perpendicular anisotropy and c) resonance linewidth for both the bare YIG layer (blacks dots) and the YIG layer capped with 3 nm Pt (red squares). The inset shows the FMR lines measured at 300 K on both samples. The dashed lines or arbitrary fit of the FMR linewidth with the temperature.*

We shall also expect a sizeable surface-induced contribution to the linewidth for ultra thin film.
Similar experiments have been reproduced after evaporating a Pt layer, with a thickness of 3 nm, on the top of the YIG film. Anisotropy constants and resonance linewidth of YIG|Pt system is plotted as red squares in FIG.53. Since no magnetic moment is induced in the Pt layer by proximity effect [236] (refer to section 3.3), the temperature dependence of YIG magnetization saturation $4\pi M_s$ is expected to be similar to the bare YIG film. It can be seen from FIG.53.a and b that the cubic anisotropy is unchanged owing to its bulk magnetocrystalline origin, while the temperature dependent uniaxial perpendicular anisotropy change in sign and slope. This means that an interfacial mechanism with spin-orbit origin [237] changes the surface anisotropy of YIG when putting a Pt layer on the top. Moreover, the FMR linewidth at low temperature is also enhanced in YIG|Pt. This is not surprising since the YIG|Pt interface provides an additional relaxation channel due to the spin pumping [125] (equation (1.59)). However, the increase of FWHM is not constant as function the temperature. The increment in the damping depends both on the strength of the interfacial coupling (spin mixing conductance) and the spin transport parameters in the Pt layer whereas the thickness of the latter being comparable to the spin diffusion length in Pt at room temperature. These contributions can be temperature dependent, leading to a nontrivial behavior of the enhancement of the YIG| damping at low temperature.

5.2.2 Magnon transport at low temperature

Non-local measurement

Next we measured the non-local Σ and Δ signals when the sample environment is set below room temperature. It allows us to study the temperature dependence of the thermal and subthermal magnon population in YIG and the role of the thermal gradient to the maximum and zero spin conductance regimes. To do so, the sample has been placed into a closed-cycle cryostat. Helium gas is inserted in the main chamber and is cooldown by a cold head. To fix the environment temperature, a heater is set close to the sample and is monitored via a temperature controller. The experiment is realized for two Pt strips deposited on the YDPB9 sample (19 nm). We have chosen to perform non-local measurements on a device with a 200 nm separation between the injection and the detection to probe the largest possible spin signal. We apply an in-plane magnetic field H =2 kOe to fully saturate the magnetization of YIG. The results of this experiment can be seen in the FIG.54.
First, we focus on the behavior of the Σ signal with temperature. It can be seen that the total Σ signal decreases to about 85% from 300 K to 130 K at 2.0 mA. It is not really surprising since thermal spin waves are dominating the whole magnon population.

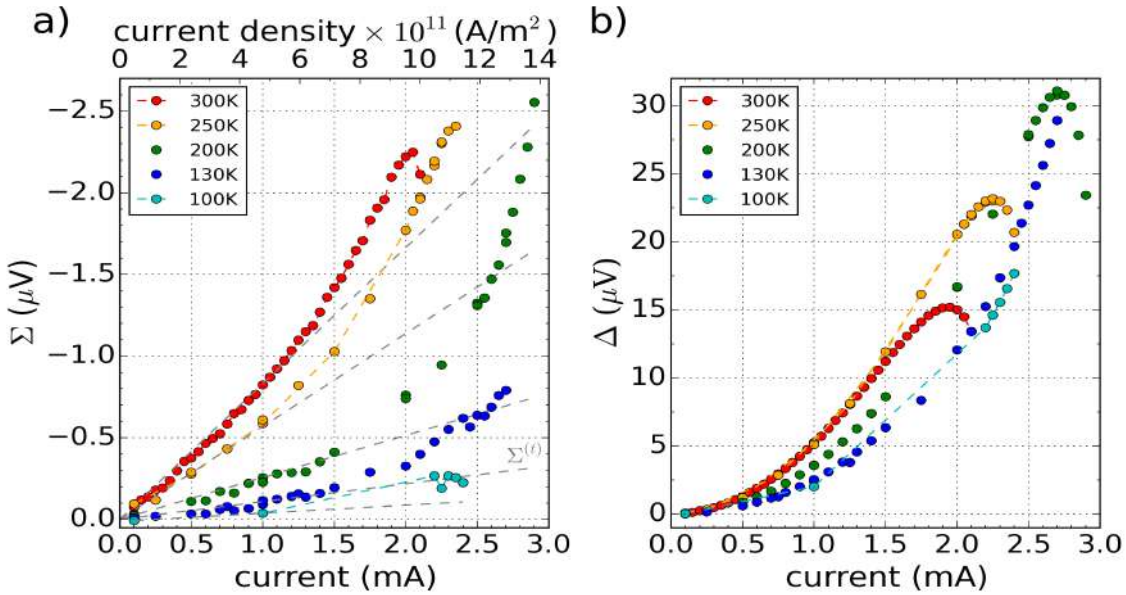

Figure 54: *a) Current dependence of the Σ signal for two Pt strips separated by a 200 nm gap at different temperatures. Thermal and subthermal magnon signals decrease at lower temperatures. b) Current dependence of the Δ signal at different temperatures. We can see that the drop of the Δ signal can be tuned with temperature.*

Nonetheless, this variation appears to decay faster than the temperature. Another interesting feature revealed by this measurement is the behavior of the large current density regime with the temperature. We can see in FIG.54.a that the turning current in which Σ suddenly drop can be modulated with temperature. It seems that this regime is pushed toward larger current by decreasing temperature (see red and orange curves). Moreover, reducing further the temperature enables to inject higher current densities inside the Pt thus reaching deeper in the non-linear regime. This is because we can put a much higher current density into the injector Pt strip without breaking it. Indeed it is known that injecting a large current density in a Pt wire can lead to a drift of Pt atoms

in the direction of the electron flow by electromigration. It potentially forms nanogaps that are enhanced by the melting produced by Joule heating [177]. This breaking point is usually reached for a defined local temperature. However reducing the temperature and thus the Pt total sheet resistance, allow us to limit the local rise of temperature in the Pt and push toward higher currents the melting effect. Next, we have studied the Δ signal as a function of the temperature, as seen in FIG.54.b. We see clearly a shift of the maximum spin conductance with temperature which again tends to put forward that the drop of the Σ and Δ signals have the same physical origin. Using FIG.51.a we can estimate the difference of maximum spin conductance point of the red, orange and green curves in terms of temperature. It turns out that the temperature shift between the turning point of red and orange curves can be estimated to 40 K and about 90 K between red and green. This shift matches pretty well with the temperature difference of the environment temperature. It implies that the drop of Δ signal is monitored by the elevation of temperature provided by the Pt injector. Since the resistivity of Pt and thus the resistance is lower with temperature, the dropping point of Δ and Σ signal appears for much higher current at low temperature. Those results have shown the important role of the temperature to the maximum spin conductance point probed at large current density.

Subthermal magnon in a subcritical regime with thermal fluctuations

To get more insight about the non-local magnon transport and the behavior of the subthermal magnon regime at low temperature, we shall give a qualitative analysis of the Σ signal. This can be formulated via the equipartition theorem for a harmonic oscillator described in [228]. It supposes that the number of subthermal magnon in a subcritical regime follows a stochastic nonlinear oscillator model under the influence of thermal fluctuations and that only one spin wave mode is driven by the SOT, which is formally true for the macrospin, but not for open system that is being handled in this experiment. Through these assumptions, the fluctuation of the number of subthermal magnon in the subcritical regime can be approximated as [132]:

$$N(I) \approx \frac{k_B T}{V} \frac{1}{1-(I/I_{\mathrm{th}})} \tag{5.3}$$

where V is the volume and I_{th} the threshold current for auto-oscillation which can be expressed as :

$$I_{\mathrm{th}} = 2\alpha\omega_{\mathrm{SW}}\eta e/\epsilon \tag{5.4}$$

with α the magnetic damping, ω_{SW} the frequency of the spin wave mode driven by the SOT assumed to be approximately the Kittel mode which stand close to the FMR gap, $\eta = VM_s/(g\mu_B)$, e the electron charge and ϵ the spin-torque efficiency. Since the Σ signal in our experiment translates the number of magnons that are enhanced by the SOT $(+I)$ compare to the number magnons annihilated by SOT $(-I)$, we can write $\Sigma(I) = N(+I) - N(-I)$. Using equation (5.3), this lies :

$$\Sigma(I) \approx \frac{2k_B T}{V} \frac{I}{I_{\mathrm{th}}} \frac{1}{1-(I/I_{\mathrm{th}})^2} \tag{5.5}$$

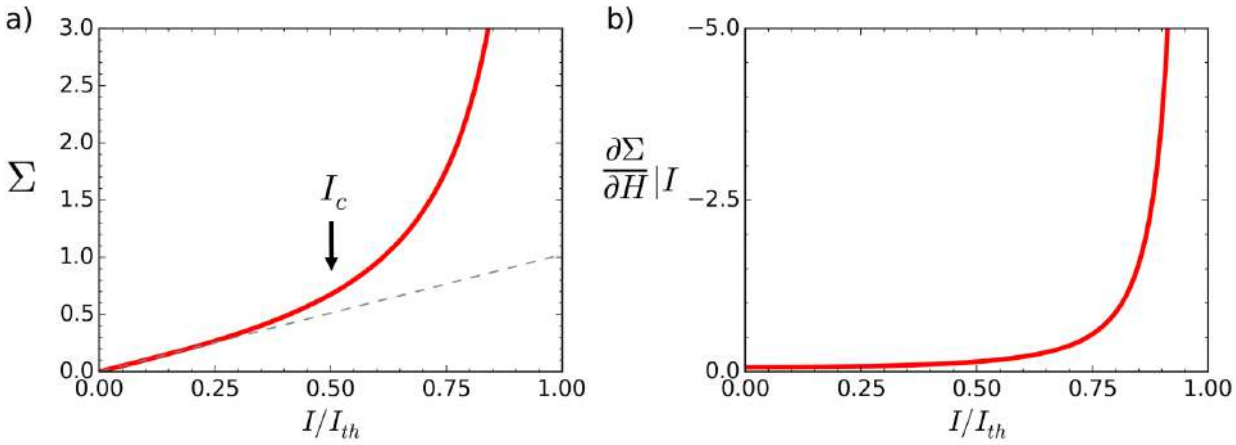

Figure 55: *a) Evolution of* Σ*, calculated from equation* (5.5)*, with the ratio* I/I_{th}*.* I_c *is the crossover current from linear to non-linear spin conductance that is defined by* $I_c = I_{th}/2$*. b) Derivative of* Σ *with the field as a function of* I/I_{th}*.*

A demonstrative plot of equation (5.5) is shown in FIG.55.a. From this simple model, we can see that subthermal magnon transport driven by spin-polarized current is actually composed of two main regimes. The first one appears when the applied current I is far from the threshold current for damping compensation I_{th} ($I << I_{\text{th}}$). In this region, the subthermal Σ can simplify as :

$$\Sigma(I)|_{I<<I_{\text{th}}} \approx \frac{k_B T}{V} \frac{I}{I_{\text{th}}} \tag{5.6}$$

which highlights a linear response of subthermal spin waves with I. When the applied current reaches half of the threshold current for auto-oscillation, which is exactly our definition of the crossover current $I_c = I_{th}/2$ from linear to non-linear spin conductance, Σ enters a second regime when the spin waves mode driven by SOT increases non-linearly with the current. The signature that the dominant transport is being carried by subthermal magnons is to look at the magnetic field dependence. Although the sensitivity of Σ to an externally applied magnetic field is a necessary signature, this might not be a sufficient condition. To convince ourself we have calculated the sensitivity of Σ to a variation of the externally applied magnetic field as a function of the criticality defined as I/I_c. This has been done by considering that the spin wave mode driven by the SOT is the FMR mode which lies $I_{\text{th}} \approx M_s\sqrt{H_0(H_0 + 4\pi M_s)}$ and allow to calculate the derivative $\partial\Sigma/\partial H$ that can be analytically expressed as:

$$\frac{\partial\Sigma}{\partial H}|_I \approx \frac{k_B T}{V} \frac{M_s(M_s - 2H_0)(I^2 + M_s^2 H_0(H_0 + M_s))}{2\sqrt{H_0(H_0 + M_s)}(I^2 - M_s^2 H_0(H_0 + M_s))^2} \tag{5.7}$$

Equation (5.7) is plotted as a function of the ratio I/I_{th} in FIG.55.b. We find that the slope of $\partial\Sigma/\partial H$ is vanishing far below I_c. The absence of field dependence behavior at low current is thus not in itself a sufficient proof to ensure that the subthermal magnons are not involved in the linear regime. However, we note that the model described through equation (5.5) captures the essential behaviors of the subthermal magnon conduction in the subcritical regime (nonlinearity with I, H_0-dependency). However this description implies that, at low bias current, linear subthermal conduction is expected and is monitored by thermal fluctuations. According to this model, the low current subthermal regime cannot be disentangled from thermal magnon conduction through a field dependence since subthermal fluctuations have a slow variation with I_{th} and thus a low sensitivity with the

external filed H_0.
To compare the model with our experimental results, we have fitted the $\Sigma(I)$ signal at different temperatures with equation (5.5) as it can be seen in FIG.56.a. The linear spin conduction regime $\Sigma^{(t)}$ is probed by fitting the low current part of Σ. Besides the fact that the model is able to reproduce quite reliably the behavior of $\Sigma(I)$, we can estimate the value of I_{th}. From these fits, we extract a threshold current that tends to decrease at low temperature experiments. This observation disagrees with equation (5.4) which predicts an increase of I_{th} as the temperature is decreased due to the rise of M_s and the enhancement of the YIG damping (or YIG|Pt damping). The dissonance of the experimental data with the model can be seen more clearly by measuring the variation of $\Sigma^{(t)}/\Sigma$ with the current and is displayed in FIG.56.b. According to [228], the auto-oscillation threshold current can be estimated when the inverse of Σ intercept the abscissa axis. It can be seen clearly that the experimental data point out to a low sensibility of I_{th} with the temperature. However, we have to take into consideration that, during a scan where the current is varied, the temperature of the YIG largely increases. This implies that the auto-oscillation threshold current is also current dependent through the decrease of M_s and might result in a distortion of $(\Sigma^{(t)}/\Sigma)(I)$ toward lower current value. The quasi-independent of $(\Sigma^{(t)}/\Sigma)(\text{I})$ with nominal temperature can be attributed to the fact that the temperature shift induced by the current is larger for lower initial temperatures. We can also mention the spin-torque efficiency that could increase at low temperature as suggested by FIG.53 and might contribute to the reduction of $(\Sigma^{(t)}/\Sigma)(I)$ with the low temperature. These findings suggest that it is not straightforward to estimate the auto-oscillation threshold current I_{th} from the nonlocal $\Sigma(I)$ because of the Joule heating that introduces a current dependence of all the threshold values.

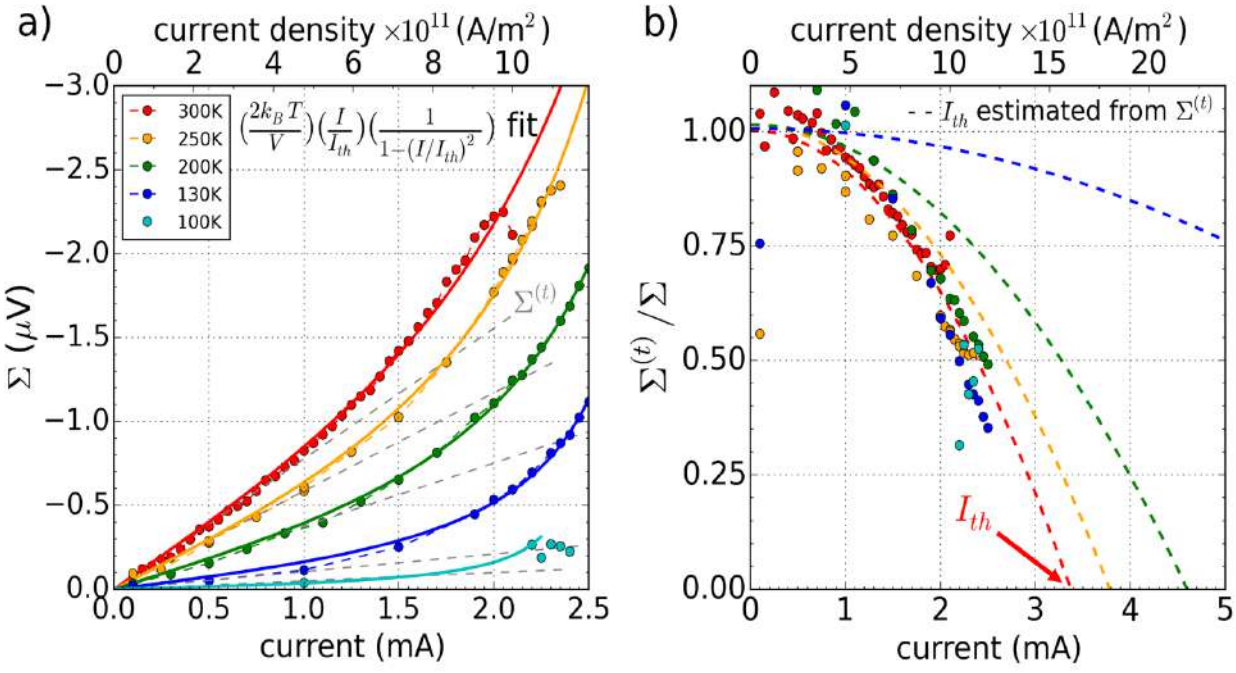

Figure 56: *Current dependence of Σ for different temperatures. The lines are fits to equation (5.5). The grey dash lines are linear fits allowing to extract the linear part of the SOT signal $\Sigma^{(t)}$. b) Variation of $\Sigma^{(t)}/\Sigma$ with the current at different temperatures. We observe a nearly independent evolution of the subcritical regime with the temperature. The dash lines are fit to equation (5.5) using a threshold current I_{th} estimated from $\Sigma^{(t)}$.*

Note that this is mostly a problem that affects the non-local devices and not nano-

pillars [92, 80], because the latter are better thermalized.
Nonetheless, a rough estimation of I_{th} can be achieved through the linear part of SOT signal $\Sigma^{(t)}$ which accounts for the subthermal fluctuation according to our model. Indeed, the subthermal fluctuations have a direct sensibility with the threshold current and can be measured in the low current regime when I_{th} is expected to be less influenced by the temperature rise in YIG. FIG.57.a shows the variation of $\Sigma(I)$ with the temperature. $\Sigma(I)$ evolution doesn't not simply rises linearly with the temperature. This can be understood by the influence of I_{th} which is sensitive to both damping α and magnetization M_s (equation (5.4)). Considering the $1/T$ character of α, the subthermal fluctuations should follow as quadratic evolution with the temperature. Via a T^2 fit displayed as grey line FIG.57.a, this is close to the behavior experimentally observed. Although we might want to note that $\Sigma^{(t)}$ also accounts for thermal magnons that should overwhelm the magnon population, especially when the applied current is far from I_{th}, and follow a linear dependence with the temperature. Since we cannot make a clear distinction between subthermal fluctuations and thermal spin waves, we will neglect the latter for the sake of a rough analysis. This contrasts with our first interpretation of the linear regime. We do not also take into account possible variations of the magnon conductivity with the temperature [218]. Using equation (5.6), we extracted the threshold current for auto-oscillation I_{th} as a function of the temperature which can be observed in FIG.57.b. As anticipated from equation (5.4), I_{th} is largely increased at low temperatures. This variation might also be enhanced by the thermal magnon that is not subtracted in our analysis. But since this population has a slower dependency with the temperature rather than subcritical fluctuations, the behavior observed in FIG.57.b, should mainly be attributed to I_{th}. In FIG.56.b, we have plotted as dash lines the expected behavior of $(\Sigma^{(t)}/\Sigma)(I)$ by fitting $\Sigma(I)$ with equation (5.5) for the threshold current calculated in FIG.57.b. These fits largely deviate from our experimental data. Indeed, the calculation supposes that the threshold I_{th} is independent of I, herein a $(\Sigma^{(t)}/\Sigma)(I)$ that is highly tuned at low temperatures. This indicates, that the nonlinear regime in our devices is triggered through the elevation temperature in the injector strip which tends to shift the subcritical regime toward lower currents values.

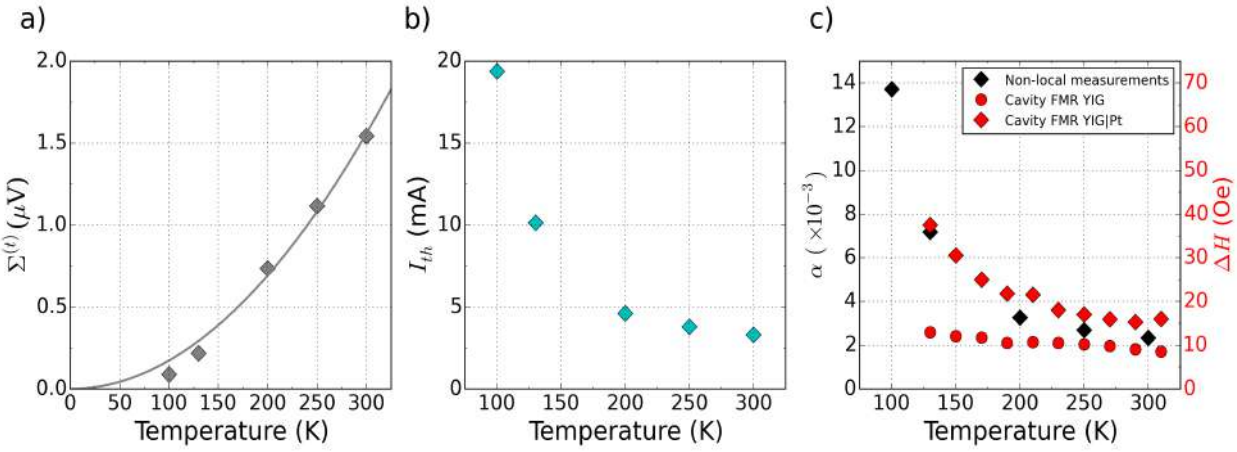

Figure 57: *a) Evolution of the thermal spin waves signal $\Sigma^{(t)}$ for an applied current of $I = 2.0\,mA$ as a function of the cryostat temperature. To extract the $\Sigma^{(t)}$ signal we have linearly fitted the Σ in the low bias current regime. The grey line is a T^2 fit. b) Temperature dependence of the inverse of the critical current I_{th} estimated from the fits of $\Sigma(I)$ signal with the model presented in equation (5.5). c) Increase of the damping α estimated from I_{th} as a function of the temperature. The red data are the broadband FMR linewidth of the YIG and YIG|PT system with T from the FIG.53.*

Finally, we have estimated the magnetic damping view from I_{th} that can be calculated from equation (5.4). This estimation takes into account that the magnetization saturation increases at low temperature which as been probed in section 2.1.2. The result of the calculation can be seen in FIG.57.c. Quite remarkably, the evolution of the damping extracted from I_{th} is close to the damping of YIG|Pt system measured via FMR in section 2.1.2 [16]. The enhancement of α with the temperature seems also to follow similar variation with the YIG|Pt FWHM as it can be seen in red diamonds in FIG.57.c. It seems that the damping calculated from non-local measurement depends on the relaxation of YIG|Pt rather than YIG (red dots). This result tends to disagree with the study in section 2.3 where the YIG damping as been put forward as the main relaxation mechanism due to the low coupling at the interface and the small width of the Pt strip (300 nm) compare to the wavelength of spin waves. However, we might also consider that, in this study, the distance between the two Pt probe was 200 nm which is lower than the strip linewidth. It implies that the surface of the traveling spin wave is mostly covered by Pt where the spin pumping mechanism dominates the relaxation. This might explain the matching of I_{th} with $\alpha_{YIG|Pt}$ in this device (the Pt strip distances use in section 2.3 were 10 times larger).

5.3 Gap dependence at high current

In FIG.58, we show the spin signal when a large current density is applied for various gaps. The Σ and Δ signals have been normalized by their maximum amplitude reached before the drop. The Pt resistance in this batch didn't vary more than 10%. Herein we can consider that the power applied to the Pt injector is similar for each devices. In FIG.58.a we can see that the maximum spin conductance of the Σ appears at a critical current density of $10.5\times\ 10^{11}\mathrm{A/m^2}$ and does not depend on the distance between to Pt electrodes. We have to remember that the spin conversion in the case of Σ occurs on both YIG|Pt interfaces. Therefore Σ translate the convolution of magnetization state of YIG beneath the two Pt strips. This would imply that the drop of Σ is a local effect that is trigger solely at the injector strip. However, we observe in FIG.58.b a net evolution of the maximum spin conductance current with the gap for the Δ signal. Moreover, the drop of Δ seems to surge for smaller current density than the Σ. This behavior can be reproduced throughout several devices and samples (YDPB9, YDPB10, BiYIG).

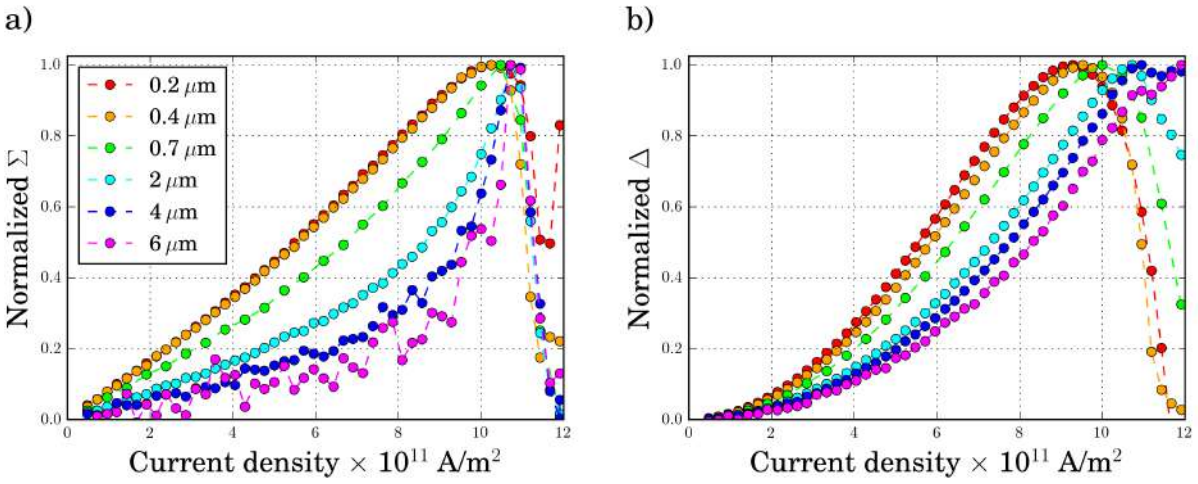

Figure 58: *a) and b) present the normalized Σ and Δ signal of 56 nm thick YIG sample (YDPB9) at large current density and for different distances between the Pt strips.*

Knowing that the spin conversion in the case of Δ appears solely at the detector, Δ contains only information on the magnetic properties of YIG under the detector. This is proof that the maximum of Δ should be attributed to a physical phenomenon occurring at the detector. Due to the different shape and critical current of the signal drop for Σ and Δ it seems that the physical mechanism involved in the drops of SOT and SSE in YIG|Pt are not totally similar.

5.4 Dependence with the width of the Platinum strip

Next we have studied the influence of the width of the Pt strip on the non-local signal for either injection or absorption of spin waves in YIG.

5.4.1 Influence of the absorber width:

First, we have investigated the evolution of the Σ signal when the width of the Pt detector w_{Pt} is tuned to 100, 300 and 1000 nm as it can be seen in FIG.59. The width of the Pt injector is kept at 300 nm which has been the nominal Pt width used in this thesis. The distance between the two Pt strips in this experiment is set to 0.4μm. To account for the change of the detector resistance with the width, we have plotted the Σ signal normalized by the resistance of the Pt probe R_{Pt} which highlights the average charge current probed at the detector by ISHE. From FIG.59.a we observe an increase of the probed spin current at the YIG|Pt interface. Note that we have make sure that the spin mixing conductance of each YIG|Pt interface was relatively similar so such a variation with the width cannot be fully regarded as a decrease of the spin resistance at the interface.

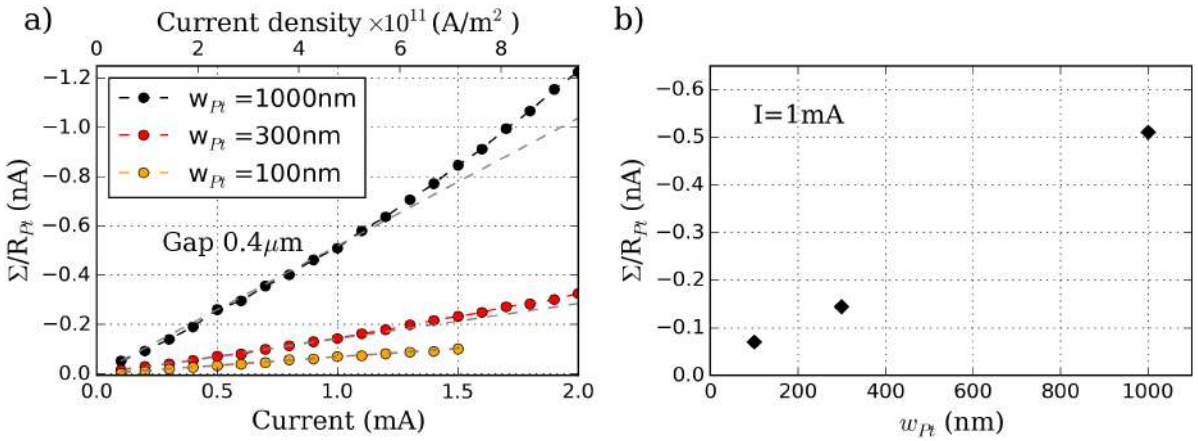

Figure 59: *a) Current dependence of the Sigma signal normalized by the resistance of the Pt detector as a function of the current and for different detector width. The distance between Pt strips is 0.4μm. b) Variation of the "even-in-field" charge current detected with the Pt width w_{Pt} when a current of 1 mA is applied to the Pt injector.*

Moreover, the crossover current for the merge of subcritical regime is found to be independent of the detector width w_{Pt}. This again confirms that this excitation appears solely at the Pt injector. To characterize the absorption of the spin current by the interface, we have plotted in FIG.59.b the detected charge current Σ/R_{Pt} at the interface for an apply current of I =1 mA as a function of the width of the detector. Interestingly the absorption seems to evolve quasi-proportionally with w_{Pt} which is quite a surprising

result. According to [238], the YIG|Pt bilayer made of a spin carrier channel (YIG) and absorption channel (Pt) could be considered as a unique channel with an effective spin diffusion length l_{eff}. This length is typically lower than the spin diffusion length in the spin carrier channel due to the contact with the absorber element of very short spin diffusion length. Owing to the diffusive character of the thermal magnon transport [97, 2, 239] the spin diffusion in our case can be substituted by the thermal magnon diffusion length which has been experimentally estimated to $L^{(t)}_{\text{exp}} = 0.4\,\mu$m. A large part of the spin current is still absorbed by the interface, at distances that are more than two times larger than the spin diffusion length. In principal the absorption is supposed to have an exponential decrease along the width of the Pt. This observation suggests that the two spin channels are in a weakly coupled regime. Absorption of angular momentum in YIG by the Pt can be considered as low due to the poor spin conductivity at the interface. Thus only a small amount of the magnon population is recover in the Pt. At some point, we should also consider that the magnon density that is not probed by the interface will also decay along the width of the platinum according to magnetic damping in YIG and should be reduced via the extra damping provided by the YIG|Pt interface. Additional measurement would be needed to determine if the spin current probed by the interface has reached saturation at w_{Pt} =1000 nm or if more magnon can be probed by increasing further the contact surface. But we would like to point out that the small mixing conductance in our YIG|Pt device should not affect much the detection of subthermal magnons, since the absorbed spin current at the interface is an average of magnon density in the whole frequency domain.
In FIG.60 we have plotted the influence of the detector width for the Δ signal. As for the SOT signal, we have normalized Δ by the detector resistance to estimate the spin current induced at the YIG|Pt interface via the spin Seebeck effect. A net increase of the thermal spin signal can be observed in FIG.60.a.

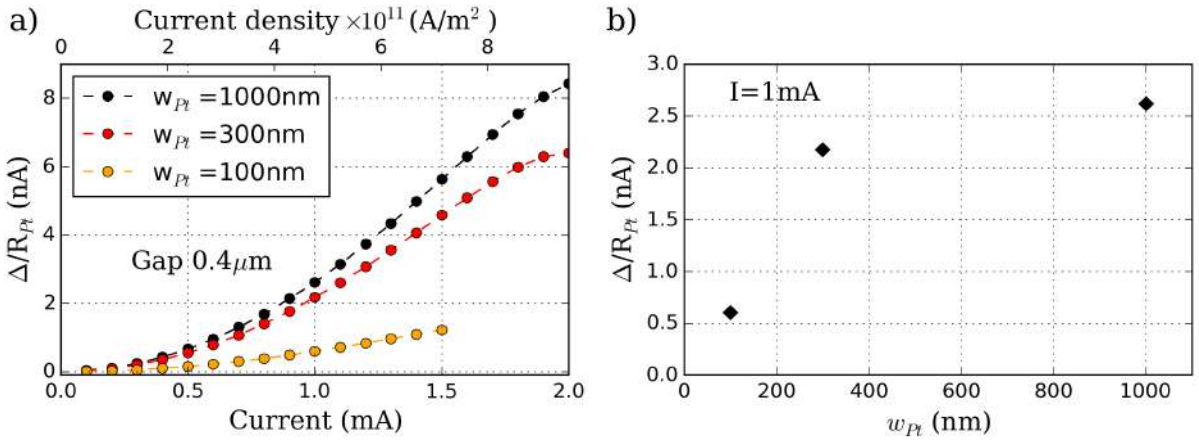

Figure 60: *a) Current dependence of the Delta signal normalized by the resistance of the Pt detector as a function of the current for different detector widths and a distance between Pt strip of 0.4 μm. b) Variation of the "odd-in-field" charge current detected with the Pt width when a current of 1 mA is applied to the Pt injector.*

However, this rise doesn't scale linearly with the w_{Pt}. Instead, the thermal spin signal appears to saturate much faster than the SOT signal as it can be seen in FIG.59.b. It indicates that besides the thermal magnon diffusion length, another characteristic length is ruling the conversion. This could be due to the decay of the temperature gradient $\partial_x T$ along the axis perpendicular to the Pt strip and has been estimated by μ-BLS to about $\partial_x T$ =-65°C.μm^{-1}. The spin accumulation due to the spin Seebeck effect could thus be

dramatically reduced by the transverse temperature profile in YIG.

5.4.2 Influence of the injector width:

Second, we have measured the non-local spin signal while the width of the injector Pt strip is varied and for a detector width fixed to the nominal value of 300 nm. The distance between the Pt strips is kept to 0.4 μm for comparison with the study on Pt absorber width. This study is very important because it allows to tune crucial parameter: the injector resistance $R_{\mathrm{Pt}} = \rho_{\mathrm{Pt}}(L_{\mathrm{Pt}}/w_{\mathrm{Pt}}\,d_{\mathrm{Pt}})$. Since the Joule heating in the Pt scale with $R_{\mathrm{Pt}}(T)I^2$, a decrease of the Pt width should considerably increase the Pt resistance and thus enhance the temperature elevation by Joule heating at a given current. Another interesting side effect of this experiment is that at similar applied current I in the Pt injector, the current density will also be different following $J_c = I/(w_{\mathrm{Pt}}\,d_{\mathrm{Pt}})$. With that, we can disentangle the role of the torque and the temperature gradient from the nonlinear spin conductance regime and the point of maximum spin conductance.
In FIG.61, we focus on the influence of the current density on the Σ and Δ signal. First of all, we observe a decrease in the amplitude with the injector width which is more than a factor of 3. Here the spin signals are not translated into a charge current since the Pt detector resistances are similar. Also, it seems clear that the excited magnon density depends on the contact surface of the Pt injector. We can understand this result in the same way as for detection. Only a part of the angular momentum is able to cross the YIG|Pt interface due to the weak coupling. By raising the contact surface, we increase the total spin current absorbed by the interface. We should also take into account that the spin transmission of the injector strip can change from device to device, but cannot fully explain the change of the amplitude of the Σ and Δ signal. We note that local Joule heating was performed on both devices before measuring the spin signal. The remarkable result is that the nonlinear spin conductance regime in the Σ signal does not rise at a fix current density as it can be seen in FIG.61.a.

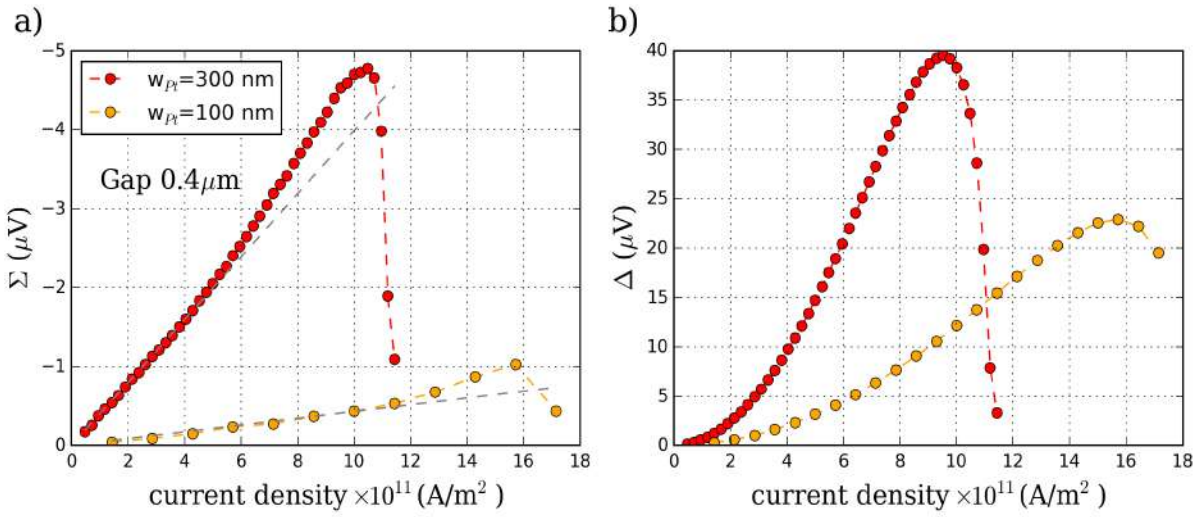

Figure 61: *a)* Σ *and b)* Δ *signal as function of the current density applied for 100 nm and 300 nm injector width and a distance of 0.4* μ*m between the injector and detector.*

We would like to note here that for a given current density in the Pt injector, the temperature gradient in the 100 nm injector is lower than in the 300 nm strip. This result in good agreement with the non-local experiment at low temperature which proves that the enhancement of the temperature gradient in the Pt injector favors the rise of the

subcritical regime due to the reduction of the threshold current I_{th} with the current I. This demonstrates that the rise of nonlinear conductance matches preferentially with the temperature rather than current density. However, these results do not disregard the role of the torque in the excitation of subthermal magnon but suggest that the temperature is a major ingredient for subthermal magnons excitation. Concerning the Δ signal in FIG.61.b, the drop of the signal does not scale with the current density as already highlighted by the low temperature experiment.
Finally, we have scaled the Σ and Δ signal with the temperature in the Pt injector. In section 2.2.6, we have shown that the thermal gradient induced by a Ti layer can induces SSE in YIG|Pt. We assume here that the gradient is proportional to the temperature of the injector. This demonstrated that the main source of the SSE signal comes from the temperature gradient. Thus the measured Δ signal has been plotted as a function of the temperature of the Pt injector in FIG.62.b. To do so, we have measured the change of resistance for different panel of Pt strip. Using the temperature coefficient of the Pt and relation 5.1, we estimated the temperature gradient in the Pt strip possessing different width. From FIG.62.b, we can clearly see that the drop of the Δ signal starts for a similar Pt injector temperature. This shows that the drop of the Δ signal is trigger by the temperature in the YIG film. From the literature, it has been experimentally established [240] that the longitudinal spin Seebeck (LSSE) in YIG|Pt is decreasing at high temperatures and even disappears at the Curie temperature. The drop of LSSE in the experiment, following the relation $V_{\text{LSSE}}/\Delta T \approx (T_c - T)^{\gamma}$, was found to decrease faster than the magnetization which proves that the decay cannot be simply explained in terms of static magnetization. From our result, we also observe a fast and non-monotonic drop of Δ when the temperature induced by Joule heating is getting close to the Curie temperature (see FIG.62.b) which doesn't seem to match with the magnetic properties of YIG at high temperature. Theoretical work [241] suggested that the deviation of experiments from the theory can be resolved by considering the ferrimagnetic nature of the YIG and taking into account the surface anisotropy of YIG|Pt [242]. In our case, we might also attribute the fast drop to a non-trivial distribution of the temperature gradient in our system due to the non-local geometry.

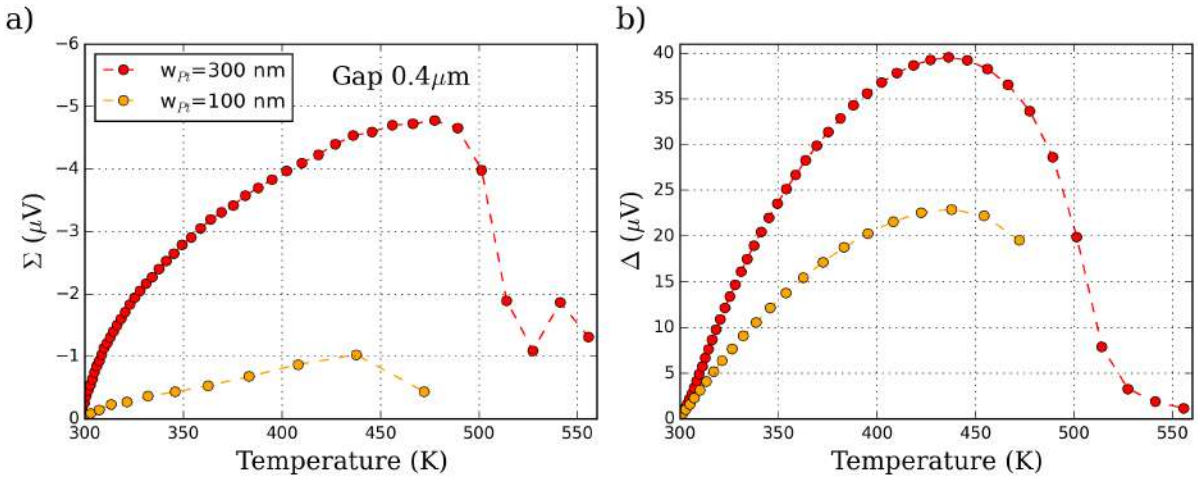

Figure 62: *Measured a) Σ and b) Δ signals for different Pt injector width for a gap of 0.4 μm. Using the fit in a), we have scaled the Δ signal according to the temperature elevation in the Pt injector.*

On the other side, the drop of the Σ signal seen in FIG.62.a does not scale exactly with the temperature. It means that the mechanism responsible for the drop of the SOT

signal is not only temperature dependent but could also result from the amplitude of the applied current intensity (current-induced magnetization switching [243], non-linear magnon scattering [4])

5.5 Conclusion

In this chapter, we investigated in more details the high power regime of the non-local magnon transport. The measurements show that the nonlinear spin conductance rise is systematically followed by a sudden drop of the total spin signal at large current/temperature near Curie temperature. By studying how this drop evolves with the distance between the two Pt strips, we point out that the origin of the Σ drop is located solely at the injector Pt strip. Low temperature experiments have revealed that the maximum spin conductance reached before the drop of the spin signal can be pushed toward higher current by decreasing the temperature. This sensitivity with the temperature is also found by varying the width of the Pt injector strip. From those experiments, it is undeniable that the third regime observed at high energy is mainly triggered by the temperature and prevents to reach large signals. The drop of Δ in our system could be attributed to the decrease of the magnetization saturation M_s with the temperature that is induced by Joule heating in the Pt injector that as a defined spatial distribution. The sign changes of the SSE observed in FIG.52.b might originate from the rising temperature distribution that tends to produce a positive magnon accumulation near the detector side. This interplay will be more detail in the next chapter. The drop of the Σ signal on the other hand is more complex. Even though the maximum spin conduction regime can be tuned by the temperature due to the magnetic properties of YIG, several parameters have to be taken into consideration. Through FMR measurements at low temperature, we have proven that the magnetic relaxation in YIG thin film is expected to increase at low temperature and is even more enhanced with a Pt overlayer that should rule the magnon transport with the decreasing temperature. To describe the magnon transport, we have used a model that takes into account thermal fluctuations. It suggests that the linear regime is also composed of subthermal fluctuations that present similar behavior with the current and the field than thermal magnon. We found that the experimental data strongly deviate from this model because the threshold current necessary to reach auto-oscillations is also influenced by the temperature rise. Due to this interplay, the nonlinear regime is found to be almost independent of the temperature of the cryostat. It implies that our estimation of I_{th} in our devices is distorted by the decrease of M_s with the current. It suggests that the subthermal magnon excitation in our system is strongly influenced by the temperature conditions. We also note that the magnon density excited by spin current does not benefit much from the low temperatures because of the large increase of the damping and M_s. This is an important statement in the quest of Bose-Einstein condensate that is mostly investigated in low temperature quantum systems.

Chapter 6

Influence of the thermal spatial distribution via an Al overlayer

As detailed in the last chapter, the magnon transport in YIG mediated by SOT is systematically attenuated at large applied current, which might be an issue for future spintronic devices using magnon information. In that matter, we have demonstrated that the temperature at the injector strip plays a net role since the current in which the spin signal drop can be enhanced by reducing the temperature of the system. However, a large number of parameters can vary at low temperatures such as Pt resistivity, magnon diffusion length, spin mixing conductance [15, 104] or even the damping [18]. So the real role of the temperature could not be distinguished. On the other hand the temperature asymmetry between the Pt injector and detector, due to the local Joule heating, is an issue regarding magnon transport. The large current density required to excite subthermal magnon population by SOT induces inevitably a large temperature gradient and a decrease of the spontaneous magnetization. It is thus important to reduce the amplitude of the temperature gradient induced by the injector strip.
In the following, we propose to cap our system with an Al layer to sink a part of the heat produced at the injector to moderate the temperature elevation in YIG. We will show that the spatial magnon distribution in YIG can be controlled by adding an Al capping layer on top of the YIG film. We systematically check the influence of the Al layer by measuring locally and non-locally the sign and amplitude of the spin signal recovered by ISHE in a Pt strip before and after putting the Al capping. We found that the magnon density can also be reliably tuned by changing the temperature profile. Moreover, we will demonstrate that the temperature plays a role regarding the non-local SOT signal in YIG.

6.1 Local measurement: Spin Seebeck and SMR

The fields of spin caloritronic is a promising branch of spintronics that relies on the interconversion of heat flow into a spin current. It has been largely demonstrated that this interplay is monitored by magnons. Since the first observation of the spin Seebeck [147], which translates the direct conversion of temperature gradient in a spin current, centered attention has been put toward Yttrium Iron Garnet (YIG) mainly for its insulating properties and thus its natural ability to carry spin waves within a large lifetime. The detection of spin current induced by temperature gradient can be realized via the inverse spin Hall effect (ISHE) that reliably converts a spin current into a charge current in heavy metals. This method as been extensively used in several reports to study the heat to spin conversion.
Recent work [221, 244, 245] addressed the non-local measurement of spin Seebeck in YIG|Pt system where a heat source is induced by the Joule heating in a first Pt strip while a non-local thermal spin signal is recovered by a second Pt strip deposited further away. The role of the thermal magnon diffusion has been largely put forward as the main transport mechanism. Near the heat source, a sign change of the thermal spin sign has been probed and has been attributed to the bulk nature of the spin Seebeck. But far away from the heat source, it is found that diffusive transport of thermal magnon rules the thermal spin signal since the temperature profile in YIG plays a poor role due to the small thermal mean free path of phonon in YIG at room temperature [246]. In this first part, we will investigate the influence of an Al capping layer on the non-local SSE signal.

We have studied the magnon accumulation profile on the 56 nm YIG film sample grow on a 500 μm GGG(111) substrate by liquid phase epitaxy (LPE).

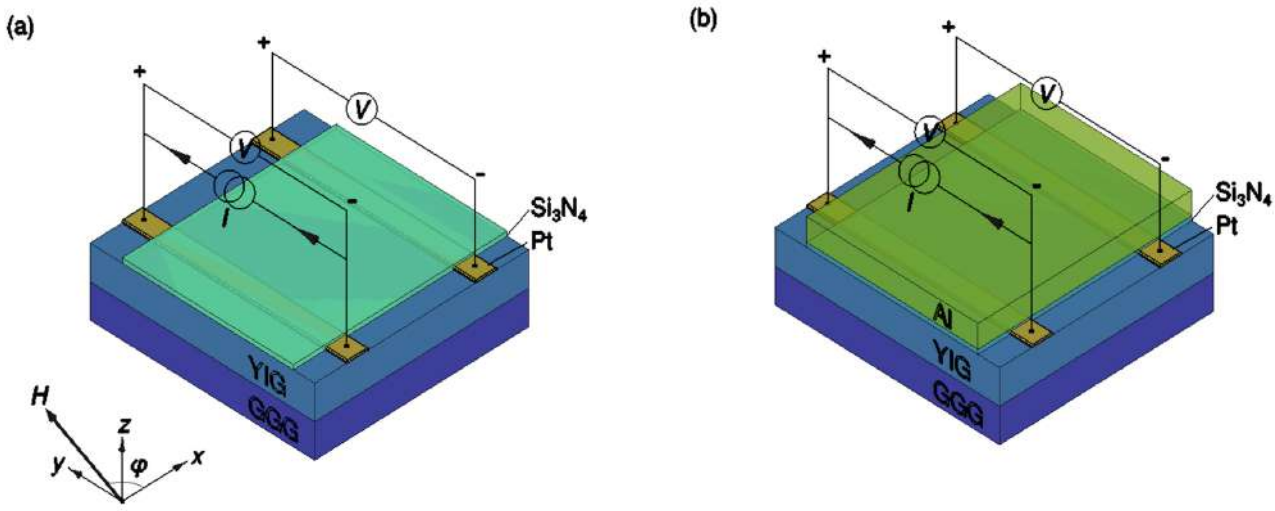

Figure 63: *a) Sketch of the local and non-local measurement of YIG|Pt|Si_3N_4 device. The Pt electrodes evaporated on the YIG film are electrically connected to measure the magnetoresistive behavior of YIG|Pt when an in-plane magnetic field B is rotating around around the z-axis in the (x,y) plane. The distance d between the two electrodes varies from 200 nm to 6 μm. b) Sketch of the YIG|Pt|Si_3N_4|Al structure. The thickness of the Al capping layer is 105 nm.*

The spin transport experiments are performed via Pt strip of width w=300 nm, length l =30 μm and thickness of 7 nm than have been evaporated directly on the top of the

YIG film. The sample is then covered with a 20 nm Si_3N_4 film to prevent Pt from oxidation. The sample is mounted into a magnet and magnetized via an external field $\mu_0 H_{\text{ext}}$ =2 kG rotating in-plane. The local magnon accumulation is probed by injecting a 10 ms pulse current [187] with a 6221 Keithley and measuring the voltage drop via a 2182A Keithley Nano-voltmeter in a single Pt strip as shown in FIG.63.a. We note that every Pt strip used in this study have been treated by local Joule heating (see section 2.3). The spatial profile of magnon can be recovered by non-local measurement where a second Pt strip is placed at variable distances (from 200 nm to 6 μm) from the injector strip. When the charge current is sent into the first Pt strip, a temperature gradient ∇T is induced by Joule heating. A thermal magnon accumulation is generated and can diffuse in the YIG. To investigate the influence of the thermal gradient in YIG to the thermal magnon distribution, a 105 nm thick Al layer has been deposited directly on the top of the YIG|Pt|Si_3N_4 structure and will act as a heat sink as display in FIG.63.b. In FIG.64 we have plotted the elevation of temperature in Pt strip as a function of the injected current. Due to the good insulating properties of Si_3N_4 layer [247, 248, 249], electrical shunt into Al pad are prevented. We have estimated the temperature ΔT in the Pt by measuring the relative change of resistivity using :

$$\rho(T) = \rho(T_0)(1 + \gamma \Delta T) \tag{6.1}$$

Where $\rho(T_0)$ =19.5$\mu\Omega$.cm is the Pt resistivity taken at room temperature T_0 and γ=478 K the thermal coefficient of the Pt that takes the form γ=$(1/\rho(T_0))(\Delta\rho/\Delta T)$. This coefficient has been carefully calculated in our devices by measuring the ratio $\Delta\rho/\Delta T$ within the range (100-300) K. The temperature in the YIG|Pt|Si_3N_4 system varied almost quadratically with the apply current owing to the Joule heating ($\propto I^2$).

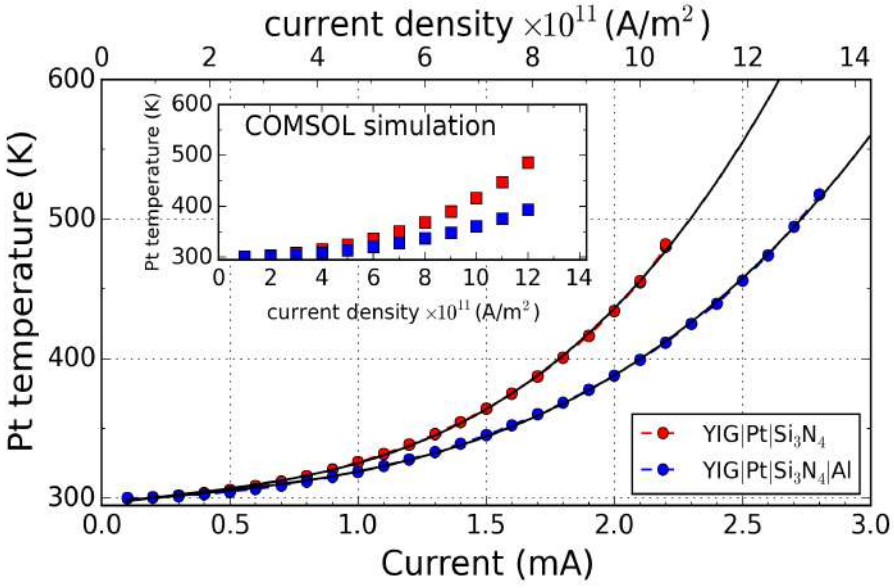

Figure 64: *Elevation of temperature in the Pt strip by Joule heating as a function of the injected current with (blue dot) and without Al capping (red dot) measured using relation* (6.1). *The back lines are polynomial fits. The insert is the elevation of Pt strip temperature calculated from COMSOL simulation for YIG|Pt and YIG|Pt|Si_3N_4|Al system.*

In the exact same Pt strip, we have measured again the elevation of temperature after depositing the Al capping layer. Since the resistivity of the Pt strip is found to be

similar after capping, we assume that the electrical and spin Hall properties of the Pt are not affected by the Al layer. Using a similar thermal coefficient γ, we have plotted as blue dots in FIG.64 the elevation of temperature in the YIG|Pt|Si_3N_4|Al system as a function of the apply current. We can see that the temperature elevation in the Pt at comparable current density is much lower with an Al capping. This result demonstrates that the Al is effectively able to sink a part of the heat from Pt. Additionally, we have performed finite element simulation using COMSOL to simulate the local temperature profile (see insert in FIG.64). We found that the average temperature of the Pt strip for an applied current of 2.0 mA is reduced to about 100 ° by adding an Al layer on the top of the strip. This matches perfectly with the experimental results in FIG.64. The simulation also revealed that this capping influences the thermal profile along the x-axis. Next, we have measured the local spin signal as the magnetic field is rotating in-plane. In FIG.65 we have displayed the local signal $V_{\varphi|I}$ probed in YIG|Pt|Si_3N_4 as a function of the angle φ between the external field H_0 and the x-axis. The measurement is performed for both polarity of the applied current and field $\pm I; \pm H$ and for an absolute current of 0.8 mA (320 K). To account for the Pt resistance and possible Seebeck signal, we have subtracted an offset signal $V_{//}$ that is measured when the magnetic field is aligned along the y-axis. We can see that the total spin signal $V_{\varphi|I}$-$V_{//}$ is quite asymmetric with the polarity of the current which can be ascribed to the simultaneous measurement of the spin Hall magnetoresistance and longitudinal spin Seebeck effect [104, 144, 62]. To make a clear distinction between those two effects, we have extracted local and non-local Σ and Δ in the same manner as in previous sections. FIG.65.b and FIG.65.c show the evolution of the extracted Σ and Δ signal as a function of the φ angle for different polarity of the current I.

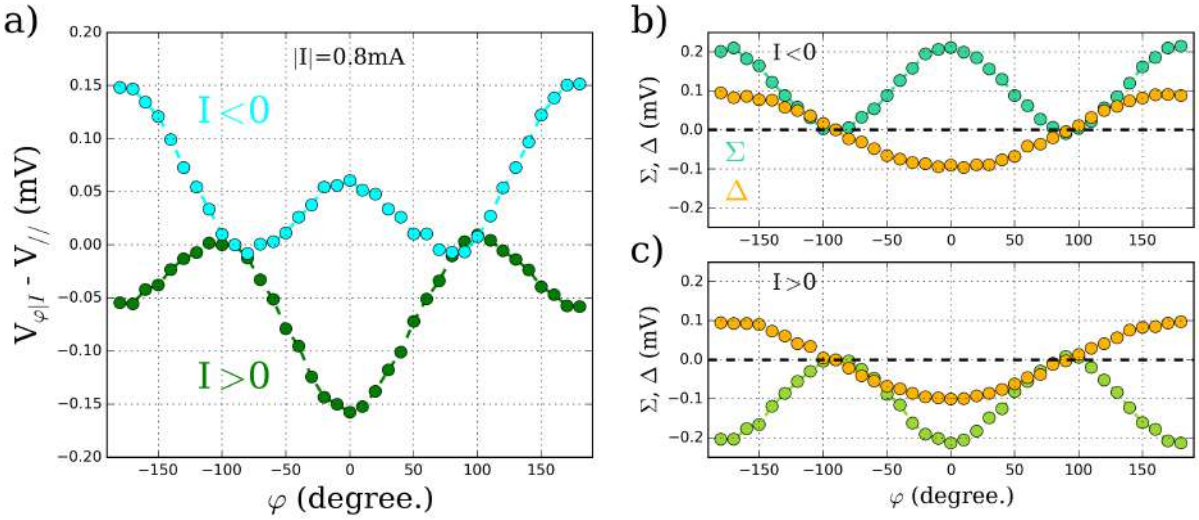

Figure 65: *a) Angular dependence of the local voltage measured in the Pt strip injector for an applied current of 0.8 mA and external magnetic field of 2 kG. From the raw signal $V_{\varphi|I}$ we have subtracted the voltage $V_{//}$ measured when the applied field is parallel to the Pt strip to separate the magnetoresistive effects from Pt resistance and Seebeck effect. In b) and c) we have decomposed the magnetoresistive signal into two components: Σ and Δ which are the even and odd contribution in respect to the field symmetry which allows us to disentangle the spin Seebeck effect $\Delta_{|I}$ from the spin Hall magnetoresistance $\Sigma_{|I}$.*

First, we can see that the Σ signal is antisymmetric with respect to the applied current polarity and evolves as a $\cos^2(\varphi)$. This behavior is expected for the spin Hall

magnetoresistance that corresponds to a change of the Pt resistivity according to the magnetization direction of YIG (even in field) and spin polarization direction at the YIG/Pt interface. Through the spin Hall magnetoresistance, we have also check that the spin transmission of the YIG/Pt interface remains constant after Al capping [221]. On the other hand, Δ displays a $\cos(\varphi)$ angular dependence and does not change sign as the polarity of the applied current I is switched from positive to negative and is coherent with a spin signal monitored by the spin Seebeck effect. Field dependence of the Δ signal (not shown) has not revealed any dependency of the thermal spin signal with the applied external field amplitude and saturation of the thermal signal is observed when M_s of YIG is reached. Thus any contribution of the anomalous Nernst effect [250, 251] can be disregarded. In the following, we will consider Σ and Δ signal as spin signal measured at φ =0.

6.2 Effect of the aluminum capping on the local and non-local spin Seebeck

FIG.66 shows the local and non-local spin Seebeck signal as a function of the applied current I in the Pt injector. We first focus on the local and non-local Δ in the YIG|Pt|Si_3N_4 system. One can see that the local signal is negative while the non-local Δ is positive. This observation is coherent with previous work [221, 244, 245] that reported a sign reversal of the transverse spin Seebeck measured via ISHE as the Pt probe is placed further away from the heat source. This effect has been ascribed to the spatial distribution of the thermal magnon population in YIG. As a current is inserted in the injector Pt strip, thermal magnon are induced by Joule heating underneath the heater strip and diffuses in the YIG film. The lack of magnon density due to the diffusion of thermal spin waves in YIG leads to a spatial depletion of magnon that can be characterized by a negative magnon accumulation and thus a negative local Δ signal. However, when the Pt probe is placed further away from the magnon depletion, thermal magnon accumulation due to the diffusion is recovered and gives rise to positive magnon accumulation and a positive non-local Δ signal.

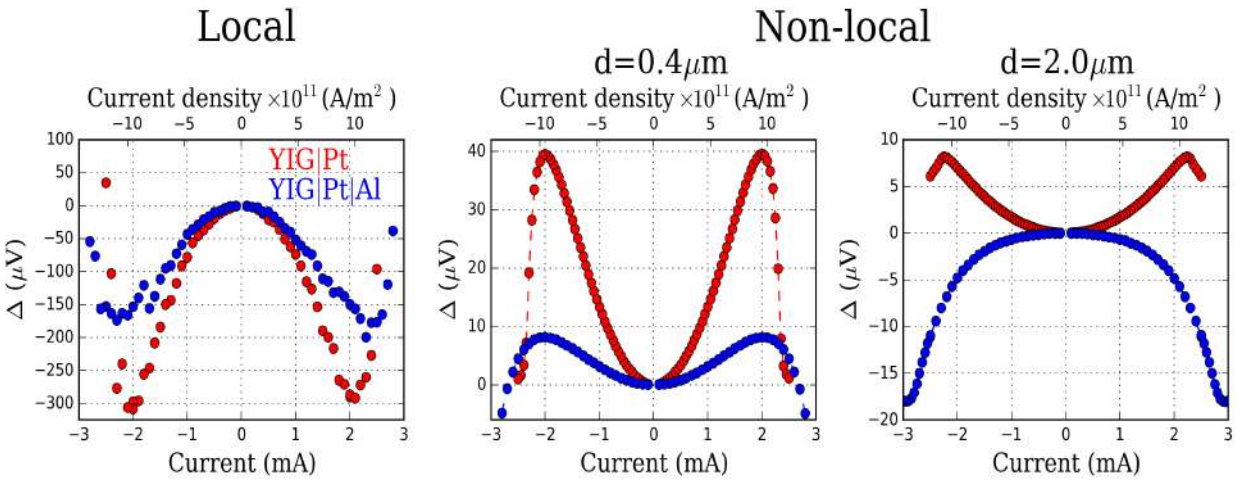

Figure 66: *Current dependence of the spin Seebeck effect Δ measured locally and non-locally on the same device before and after Al capping.*

It has been reported that the characteristic distance in which the spin Seebeck changes sign can be tuned by varying the thickness [221, 245] of the YIG or magnon diffusion length λ_m [244, 245] which essentially affects the magnon transport. After probing the spatial distribution of the thermal magnon in YIG|Pt|Si_3N_4, we have put on the same non-local devices Al capping layer and measured again the local and non-local spin Seebeck signal. It can be seen in FIG.66.a that the amplitude of the local Δ, is decreasing when the Al capping layer is put on top of the device. Moreover, for an applied current of 2.0 mA we see that Δ signal drop by a factor two from YIG|Pt|Si_3N_4 to YIG|Pt|Si_3N_4|Al system. This match perfectly with the estimation of Pt temperature in FIG.64 and COMSOL simulations. From this observation, we establish the direct sensitivity of the local Δ signal to the longitudinal temperature gradient at the YIG/Pt interface. Thus we can assert that the origin of the local Δ signal comes from a pure spin Seebeck effect. Furthermore, this ensures that a contribution of the recently discovered unidirectional spin Hall magnetoresistance [166] is not observed in our system and is in good agreement with the literature [252, 244]. Whereas the local magnon depletion is decreased due to the reduction of the thermal gradient, we found that Al capping strongly affects the spatial distribution of thermal magnons. It can be seen in FIG.66.b and FIG.66.c that the positive magnon accumulation is probed at 0.4 μm while a negative magnon accumulation is recovered much further away from the injection point at 2.0 μm. This thermal magnon distribution can be observed more in detail in FIG.67. While a single sign reversal of Δ is systematically observed for thin YIG|Pt systems, we observe a second sign reversal around 0.7 μm with Al capping and seems to confine the positive magnon accumulation in a defined region. We would like to empathize here that the Al capping does not change the transport properties of magnon in YIG but only the spatial temperature profile in YIG.

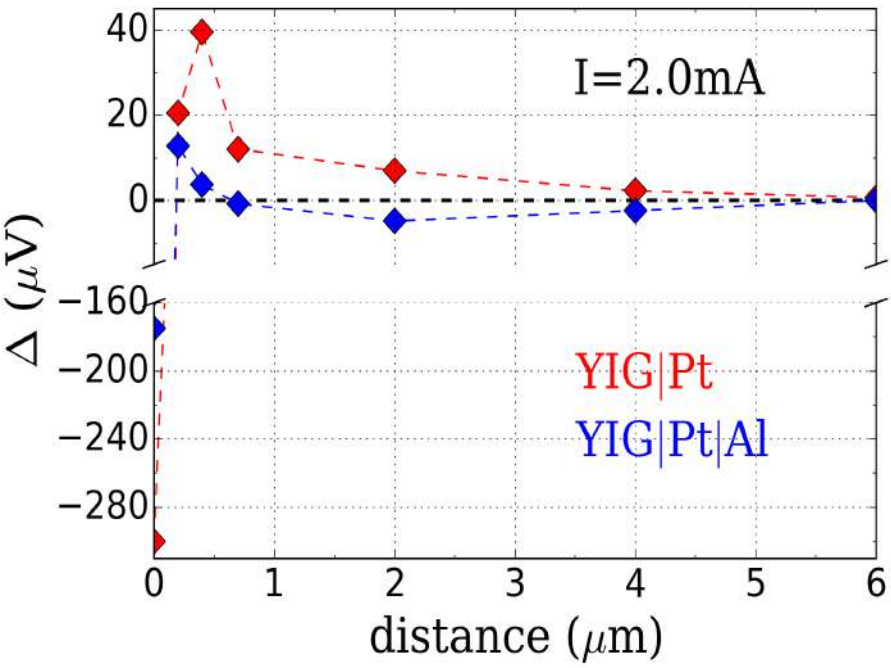

Figure 67: *Measured spin Seebeck signal Δ_I as a function of the distance from the injector with and without Al capping. Quite remarkably, the spin accumulation of the spin Seebeck signal is completely changed by adding an Al capping layer, which cannot be explained by a change of the longitudinal thermal gradient.*

6.3 Influence of the aluminum capping on the thermal magnon accumulation profile

Based on our experimental observation, we have modeled the magnon distribution profile in a YIG|Si_3N_4|Al layer via a collaboration with the group of Y.Tserkovnyak and is based on a paper under writing process. We only sketch the system in two dimensions (x,z) assuming that the magnon accumulation is homogeneously distributed along the y direction.
The spin current J_s injected to the Pt can be driven by both magnon chemical gradient μ_m and temperature gradient [253], which reads :

$$J_s(x) = -\sigma \frac{\partial \mu_m}{\partial z}(x) - S \frac{\partial T}{\partial z}(x), \tag{6.2}$$

where σ is the spin conductivity and S is the spin Seebeck coefficient. The temperature and its gradient are calculated using the finite element method, COMSOL. The measured Pt resistivity of 19.2×10^{-2} $\mu\Omega$m was used and all other parameters are summarized in Table 6.1.

	κ ($Wm^{-1}K^{-1}$)	t (nm)	w (μm)	l (μm)
GGG	7.0	0.5×10^6	1×10^3	1×10^3
YIG	8.8	56	1×10^3	1×10^3
Pt	71.6	7	0.3	30
Al	238	120	4	30

Table 6.1: *Material parameters used in simulation. t, w, and l are the thickness, width, and length.*

The limit conditions of the simulation has been set such that the bottom surface (GGG) is at room temperature while the boundaries are thermally isolated. The only heat source originate from the Joule heating of the Pt wire. The simulated temperature and temperature gradient profiles along the x direction are shown in FIG. 68.a and FIG. 68.b, respectively. We note that the temperature gradient of YIG|Pt|Si_3N_4|Al becomes larger than the one without Al capping at longer distances (blue in FIG. 68b) while the absolute temperature of YIG|Pt|Si_3N_4 is always higher than the other. For the chemical potential, we assume that the $\frac{\partial \mu_m}{\partial z}(x)$ has a simple exponential form [253] given by:

$$\frac{\partial \mu_m}{\partial z}(x) = \mu'_m(0) e^{-x/\lambda}, \tag{6.3}$$

where $\mu'_m(0) \equiv \frac{\partial \mu}{\partial z}|_{x=0}$ and λ is the thermal magnon diffusion length. The measured SSE (Δ) is proportional to the J_s, therefore it can be written

$$\Delta(x) \propto e^{-x/\lambda} + \frac{S}{\sigma \mu'_m(0)} \frac{\partial T}{\partial z}(x) \tag{6.4}$$

Now we fit our SSE data without the Al layer and obtain $\lambda = 1.1$ μm as shown in FIG. 68c. Then we use $\frac{S}{\sigma \mu'_m(0)}$ as a single fitting parameter to match the experimental data. We note that $\mu'_m(0)$ can differ for two cases while $\frac{S}{\sigma}$ should remain constant. The

best fit to the experimental results are shown in FIG 68.d, which yields $\frac{S}{\sigma\mu'_m(0)}$ to be -10 and -50 for YIG/Pt/Si_3N_4 and YIG|Pt|Si_3N_4|Al, respectively. We note that the $\mu'_m(0)$ decreases by a factor of 5 with the Al layer due to the decrease of temperature at the Pt injector strip.
From this model, it becomes clear that Al capping change the thermal magnon accumulation distribution.

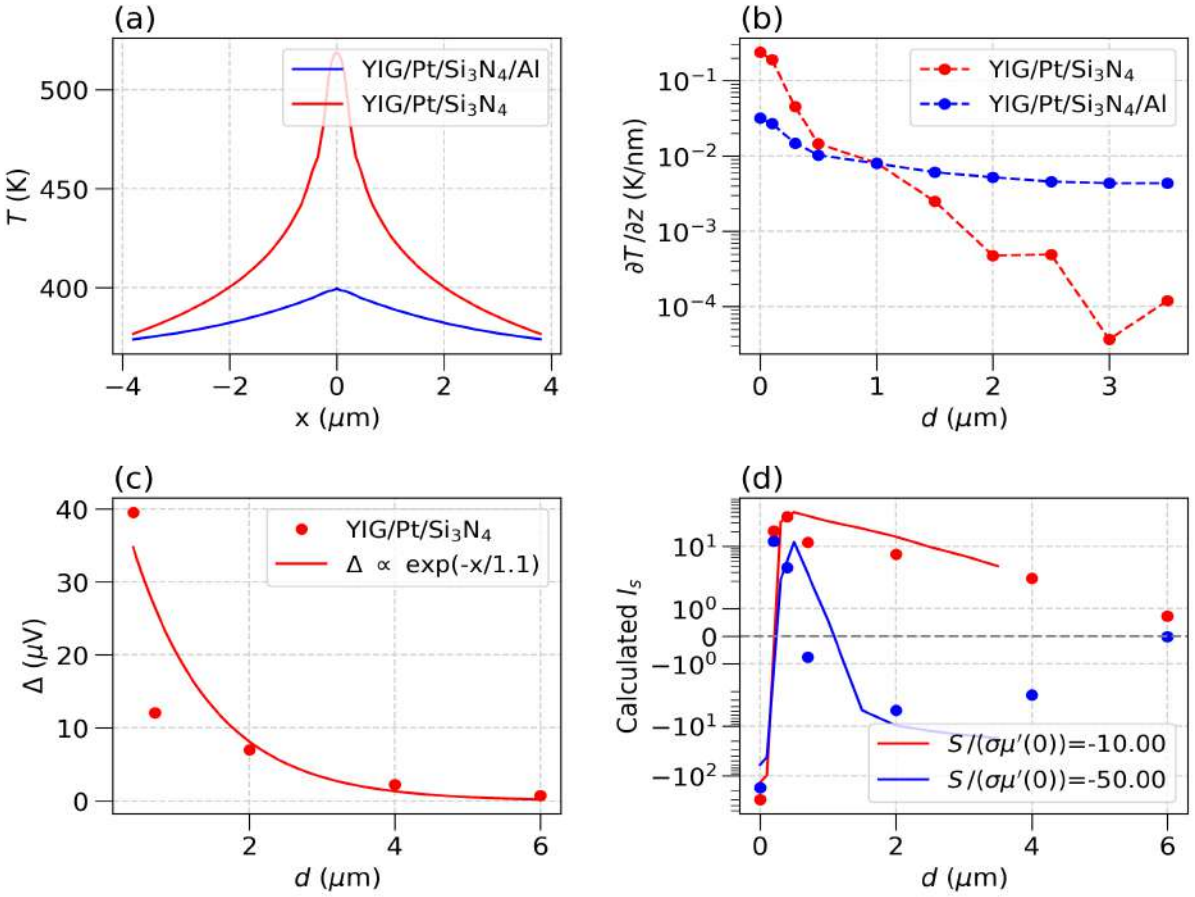

Figure 68: *a) Simulated lateral temperature profile at the interface between Pt and YIG at 2 mA. b) Simulated temperature gradient along the z direction as a function of distance between injector and detector. c) The measured* Δ *for the case without Al capping is compared with an exponential decay, which yields a decay length of 1.1* μm*. d) The measured spatial dependence of* Δ*'s are compared with simulations. The best fit to the data are shown with the corresponding parameters.*

In distance close to the heat source, the Al capping is able to take out part of the heat in Pt that results in a reduction of the thermal gradient. Because the thermal magnons are excited by the thermal flow underneath the Pt heater, the distance over the first sign change d_1 occurs is thus expected to decrease with the Al capping. This assumption could not be check because d_1 is in the order of the Pt width [221]. After the first sign change, a positive magnon chemical potential can be recovered due to the propagation of thermal magnon in YIG. The positive magnon accumulation starts to reach a maximum when the influence of the magnon depletion becomes null. Then the positive magnon accumulation decays exponentially with the distance due to the diffusive

transport of thermal magnon. This picture can be observed in the case of YIG|Pt|Si_3N_4 system. Nonetheless, by inserting the Al layer, we dramatically change the interplay between thermal profile in YIG and the thermal magnon propagation. For instance, we can see in the case of YIG|Pt|Si_3N_4|Al system, display as blue dots in FIG 68.d, that the maximum of positive magnon accumulation is reached in much less distance. This is because the thermal flow at the heat source is reduced due to the Al and decrease the radius of the magnon depletion. When the maximum of positive magnon accumulation is reached, we observe the diffusive character of thermal spin wave. But a second sign change happens at d_2 (see FIG 68.d) when a negative magnon accumulation starts to dominate again the Δ signal for distance larger than d_2 =0.7 μm. This phenomenon can be explained by the Al capping layer that induces an additional heat flow in the YIG much further away from the Pt injector. This heating generates thermal magnon due to the longitudinal spin Seebeck effect and thus a magnon depletion. Since the positive magnon accumulation is exponentially attenuated due to the diffusive transport, the negative magnon accumulation is overwhelming the thermal magnon transport at large distances and produces a negative Δ signal.

6.4 Effect of the aluminum capping to the local and non-local spin-orbit torque signals

We then present the evolution of the local and non-local Σ signal in FIG.69 as a function of the applied current. Let's first consider the local measurement of Σ that translate the spin Hall magnetoresistance. We observe that the sign of the local Σ signal is negative for positive current and reverses sign for negative current. This is in agreement with the expected behavior of the SMR in which the direction of the reflected spin current at the interface will depend on the spin polarization. One can also note that the SMR signal rises linearly with the amplitude of the current. This behavior cannot be totally attributed to a change of resistivity of the Pt strip with the temperature that would result in a quasi-quadratic increase due to Joule heating. This linearity is due to the increase of the spin current reflected at the interface which is reconverted as a charge current by ISHE. Using equation 2.6 we can extract a good spin mixing conductance in the order of $g_{\uparrow\downarrow}$ =2.4×10^{18}m^{-2}. For a pure YIG|Pt system, we observe a drop of the SMR signal for a current density of 8×10^{11} A/m^2. According to FIG.63, this corresponds to a temperature of 435 K. Unfortunately, we could not record the SMR of the exact same device after Al capping. Instead, we have taken another capped YIG|Pt devices that hold similar resistance and spin mixing conductance. It can be seen in FIG.69 that the local Σ of the YIG|Pt|Al system seems to match perfectly with the Σ of YIG|Pt in a low current region. However, the drop of the SMR appears for slightly lower current/temperature compare to the YIG|Pt system. This observation is in disagreement with the temperature dependence of the non-local signal which suggests that the drop appears at a precise local temperature of the Pt injector. Nonetheless, we can not make a definitive conclusion on those results considering the large noise at high current and possibly different physical properties of the YIG|Pt and YIG|Pt|Al sample measured (M_s, ρ_{Pt}, $\theta_{\mathrm{SHE}}^{\mathrm{Pt}}$).
Next, we turn on the current dependency of the non-local Σ signal. Contrary to the local Σ, the capped and uncapped non-local spin signals have been measured on the exact same devices. From this, we can really study the role of the temperature to the non-local Σ without changing the damping α, magnon diffusion length or spin mixing conductance of both YIG|Pt interfaces. The current dependence of the non-local Σ can be seen in FIG.69 for a gap of 0.4 μm and 2.0 μm. Quite remarkably, the linear regime amplitude of the

non-local Σ signal is decreased after Al capping. The difference does not simply match with the reduction of local Joule heating because of the temperature gradient induce in Al layer further away from the Pt injector as suggested by spin Seebeck signal. But we do observe a shift of the maximum conductance of the signal to higher current when Al capping is inserted in good agreement with low temperature measurement of non-local signal (section 5.2). The Σ signal drop until zero spin conductance is reached.

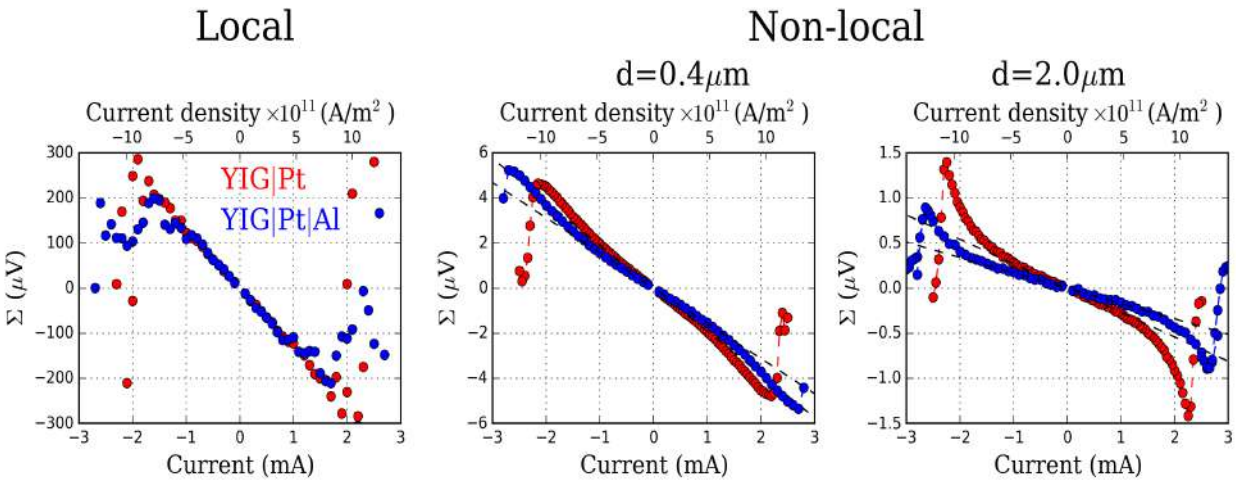

Figure 69: *Current dependence of the local and non-local Σ with (red dots) and without (blue dots) Al capping.*

The effect of the temperature on the non-local Σ and the subcritical crossover can be seen more clearly in FIG.70.a. We see that the drop does not depend on the current density. However, if we analyze more in detail the current in which the drop is observed, we notice that the corresponding temperature is identical for YIG|Pt and YIG|Pt|Al and is estimated to be around 485 K. This result is an important step to understand the origin of the drop of the spin signal because the low temperature measurement of Σ signal could not be totally conclusive due to the large enhancement of the damping. But from Al capping which only alters the local temperature produce by Joule heating, we can assert that the drop of the spin signal is solely triggered by the temperature. The other interesting fact revealed by this measurement is that the subcritical crossover is also tuned with Al capping. This blatant difference can be seen in FIG.70.b where we have plotted the inverse of the non-linear part of the non-local signal as a function of the apply current. Deviation of 25% of the spin signal from the linear conductance which is defined as the subcritical crossover I_c is crossed at 1.7 mA in the case of YIG/Pt while a current of 2.1 mA is necessary when Al capping is inserted on top of the structure and again lies in a similar temperature range (390-400 K). Although if we consider equation 1.87, the threshold current density is expected to decrease with saturation magnetization M_s of YIG. The increase of the crossover current density with Al capping implies that the reduction of M_s with the temperature elevation due to Joule heating plays a dominant role for subthermal magnon excitation. As more current density is applied in the Pt injector, the energy required to excite subthermal magnon is decreased due to the reduction of the magnetization saturation M_s (and probably a small reduction of the damping α). This causes the $\Sigma^{(t)}/\Sigma$ curve to diverge toward lower current due to the elevation of temperature. The divergence is less pronounced when a part of the temperature is absorbed by the Al that results in a lower decay of subcritical current I_c with the current I. We also note that the maximum of the inverse subthermal magnon density reached before

the drop of the signal is identical with or without Al capping and indicates again that this drop is triggered through the temperature gradient. The different currents where these maximum are reached result simply from the temperature difference in the YIG|Pt and YIG|Pt|Al systems. This measurement confirms that the excitation of subthermal magnon by SOT in our system is a thermally assisted process.

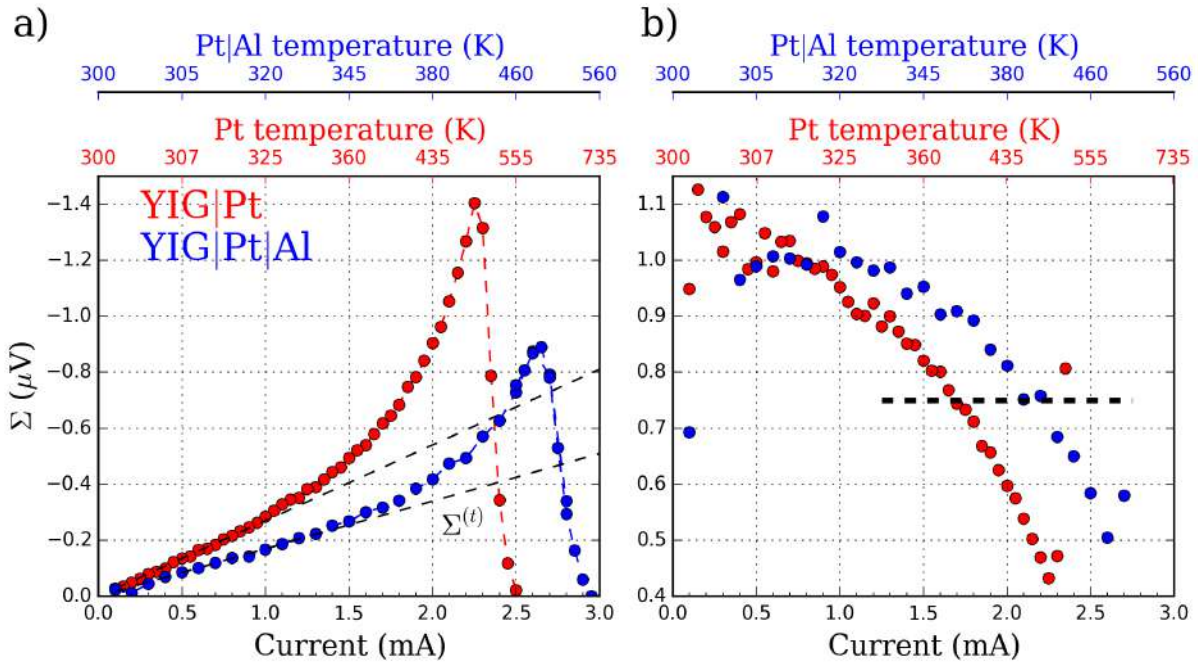

Figure 70: *a) Current dependence of the non-local Σ with and without Al capping for a gap of 2.0 μm. On the top axis, we inserted the corresponding temperature of the YIG|Pt and YIG|Pt|Al systems estimated from FIG.64. We have fitted in dash line the linear part of the Σ signal to extract the contribution of thermal magnon from the non-local signal. b) $\Sigma^{(t)}/\Sigma$ quantity as a function of the applied current which defines the inverse of the non-linear spin signal with current.*

Finally, we discuss the gap dependence of the Σ signal. From FIG.71.a we can see that the thermal magnon population in YIG|Pt|Si_3N_4, denoted as $\Sigma^{(t)}$, decay exponentially with the distance d between the two Pt electrode. We note that the 0.2 μm device presents a lower amplitude compared to the 0.4 μm and deviates from the diffusive regime. Most notably, with the Al capping we observe similar behavior at low gap where the thermal magnon population for 0.2 μm device is smaller than of the 0.4 μm device. From this observation, we can exclude the thermal magnon depletion to be the origin of this phenomenon. Indeed, if one would come back on the thermal magnon distribution in FIG.67, the depletion is expected to spatially decrease with Al capping due to the reduction of the thermal gradient. If $\Sigma^{(t)}$ would have been sensitive to the depletion, we would have seen higher thermal magnon signal at 0.2 μm than 0.4 μm in the case of YIG|Si_3N_4|Al system. We can possibly explain this to a low spin transmission of the 0.2 μm Pt injector device's (this hypothesis could not be verified). Nonetheless the diffusive like behavior of $\Sigma^{(t)}$ highlight the reproducibility of the spin transitivity of the other devices. Overall a reduction of the $\Sigma^{(t)}$ amplitude is observed when the Al capping is provided and agrees with the thermal nature of $\Sigma^{(t)}$ signal.
Next, we have extracted the maximum subthermal magnon density by subtracting the thermal magnon $\Sigma^{(t)}$ into the maximum non-local Σ conductance reached as can be seen

in FIG.71.b. The Al capping seems to also influence strongly the subthermal magnons density. This could possibly result from the increase of subcritical crossover current I_c with temperature and reduction of subcritical fluctuations. These results are not straightforward to explain and would require additional measurements and check to identify the spatial distribution of the subthermal magnons. Although this again shows that the temperature gradient affects the subthermal magnon transport.

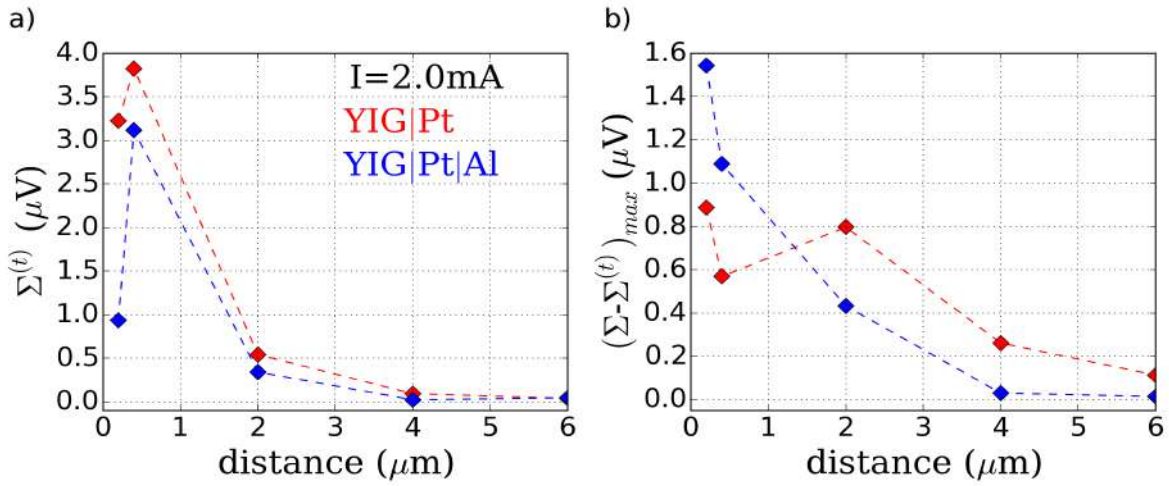

Figure 71: *Gap dependency of a) thermal magnon and b) Maximum subthermal magnon measured for an applied current of 2.0 mA without (red) and with (blue) Al capping.*

6.5 Conclusion

In this chapter, we have studied the influence of an Al capping layer on the spatial distribution of thermal and subthermal magnon in a thin YIG film. Through local and non-local magnon transport measurement we have seen that the Al layer is sinking a part of the thermal gradient produced by the Pt injector and changes the temperature across the YIG film. The interplay between magnon diffusion and temperature profile in YIG leads to a tuning of the thermal magnon spatial distribution. From this, we have demonstrated that inserting an Al capping layer allows a double sign change of the spin Seebeck signal with the distance from the Pt heater. This can be understood by the generation of an additional heat source provided by the Al layer. This secondary heat flow thus induces a propagative thermal magnon and a new magnon depletion center that is at the origin of negative spin Seebeck signal. This paradigm could be relevant for the field of spin caloritronic which aims to build spin logic via heat flow.
Decreasing locally the temperature gradient with an Al layer allowed us to distinguish the role of the temperature to the non-local SOT signal. We have seen that the subcritical crossover can be seen as a thermally assisted process where the reduction of the total magnetization saturation M_s of YIG plays a crucial role. Additionally, we have seen that the drop of the total spin signal is triggered by the high temperature in the Pt injector which is coherent with low temperature measurements. Nonetheless, the Al capping layer does not help very much in the matter of magnon transport at large applied torque. Indeed the signal drop can be pushed toward higher current density, but because of the thermally assisted character of the subthermal excitation, it is necessary to provide higher energy to excite non-linearity in YIG|Pt|Si_3N_4|Al rather than YIG|Pt|Si_3N_4. Due to the better thermalization of the YIG with Al, it is also not efficient for enhancing the subthermal

magnon density because the temperature conditions seem to be the dominant parameter due to the dependency of the subcritical crossover I_c with the current I (through M_s and α). Furthermore downgrading the temperature gradient seems to affect strongly the spatial distribution of SOT. We have observed that this capping layer is also able to tune the density of subthermal magnon that might result from different temperature conditions. More investigation needs to be done to puzzle out this result.

Chapter 7

Conclusion and Outlook

7.1 General conclusion

This thesis work focus on an investigation of the high energy spin transfer mechanisms in a magnetic insulator (Yttrium Iron Garnet), through the application of a static charge current in a strong spin-orbit metal adjacent layer (Pt). This interplay allows one to detect, generate and amplify propagative spin waves in ultra-thin YIG extended films via spin Hall effect and spin-orbit torque.

The second chapter aims is a characterization of thin YIG film for spin waves transport. Via ferromagnetic resonance measurements, we could have established the high quality of thin epitaxial YIG films which lies in their low magnetic losses. By inserting a Pt layer on the top of those films we could have probed the additional damping provided by the spin relaxation at the interface which is a direct proof of the interfacial spin-transfer on this system. Even though the spin pumping remains the main relaxation mechanism in thin YIG|Pt films, we have observed through a thickness d dependence that intrinsic additional damping is expected below 200 nm and follows a $1/d$ law suggesting a surface effect. The static magnetic characterization has confirmed the low saturation magnetization of those thin films and the Curie temperature (T_c =580 K) is found to be similar to bulk YIG. These results ensure the good compatibility of thin YIG for all electric spin transport experiments which has been details as well. Through symmetry consideration, we have demonstrated that the SOT signal can be separated from the thermal spin signal (spin Seebeck) by sorting the spin current according to their field symmetries. Via careful engineering of the YIG|Pt interface, we have experimentally demonstrated that the interfacial spin transmission can be improved via a local Joule heating without affecting directly the dynamic. This finding can be understood by the low energetic evaporation of the Pt layer onto the YIG where better coverage of the active surface contact can be performed by a local Joule heating.

In the third chapter, we reported the electrical properties of YIG thin film at high temperatures. We have demonstrated the large gap semi-conductor nature of YIG thin film due to large polaron conduction at high temperature provided by the p-type doping. The direct impact of the conductivity of YIG for large thermal fluctuation can be measured in a non-local geometry which has been used to measure pure spin signal in YIG. The contribution of electrical leakage in YIG regarded as a non-magnetic parasitic signal can be disentangled from the spin signal by systematically studying the sign and the angular dependence of the non-local voltage. Additionally, we investigated the non-local transport with an out-of-plane magnetization. While no magnon transfer is found owing to the geometry of the spin Hall effect, we do not observe any contribution of spin Nernst or anomalous magnetoresistance mediated by proximity effect in the measured thermal signal and can be attributed to a Righi-Leduc effect.

Throughout these characterizations, we could have unambiguously study spin waves

propagation in thin YIG excited by a large spin-orbit torque. We have highlighted a two-fluid transport in YIG whereas thermal magnons (THz) are preliminarily excited at low bias current while subthermal magnon (GHz) starts to rule the transport above an effective subcritical crossover current density of $J_c \approx 6 \times 10^{11}\mathrm{A/m^2}$. The high current regime can be attributed to the action of the damping like torque which partially compensates the damping of low-energy magnon. Due to nonlinear magnon scattering, the full compensation of the damping prevents the system to be driven into an auto-oscillation state and is instead thermalized toward the bottom of the spin waves spectrum. The spatial spectroscopy of the spin waves in YIG has shown that subthermal magnon reaches a typical propagation length that lies in $1.5\,\mu$m and a thermal magnon propagation length around $0.4\,\mu$m. Those results are compatible with the magnetostatic regime in the case of subthermal magnon, the exchange regime predicts a much smaller propagation length that the measured thermal magnon spatial spectroscopy. We have also demonstrated non-local spin wave transport in a magnetic insulator with large perpendicular magnetic anisotropy BiYIG which highlight an improved magnon propagation length compare to YIG. In this system, if the anisotropy field provided by the Bi-doped element compensates the demagnetized field, the uniform mode became free from the magnetization saturation and prevent a frequency redshift of the Kittel mode at large apply spin current. It enables a long propagation character of subthermal spin wave mode emitted by spin-orbit torque, due to an engineering of the spin wave spectrum, that has been confirmed by Brillouin light scattering spectroscopy [223]. All of those results are not compatible with a Bose-Einstein condensation or magnon supercurrent yet because of the strong nonlinear redistribution of the energy between the magnon modes in extended films.

Toward the application of large current density, we have seen that a third regime is reached whereas the total non-local magnon signal eventually drops. Various investigations (low temperature, gap dependence, influence of Pt width) have shown the dominant role of the temperature in the non-local magnon transport. A large increase in the YIG and YIG|Pt damping as been demonstrated due to a impurities relaxation and largely contribute to the increase of the subcritical threshold current at low temperature. However the application of large current in the Pt strip result to a consequent decrease of the magnetization saturation for large apply torque that tens to reduce the magnetic order and shift the subcritical (nonlinear) regime toward lower current. At high current density, the temperature is close to the Curie temperature which kills the emission and detection of spin waves in YIG. We should also expect a reduction of long wavelength magnon due to the destructive nonlinear linear dynamics. Unfortunately, the non-local magnon measurement cannot allow a clear establishment of this effect because of its insensibility with the detecting spin waves frequency. Although it has already been directly observed through μ-BLS [4] and spin pumping [92] and could possibly contribute to the drop of the SOT signal.

Finally, we attempted to reduce the strong thermal gradient in YIG|Pt by inserting a Al capping structure on the top of the nanostructures. We have seen that the large part of the thermal flow absorb by the metallic capping layer changes the lateral temperature profile in the YIG and is able to tune the magnon spatial distribution. This could be observed through the spin Seebeck effect were a double sign change occurs due to a secondary magnon depletion produced via the Al layer further away from the initial thermal spin injection. On the other hand, we observed that the Al capping overlayer play an role in the excitation of low-energy magnon via an increase of the crossover current due to a better thermalization of the YIG. The thermal and subthermal magnons transport is found to be strongly influenced by the temperature gradient in YIG as well.

7.2 Personal contribution

During my time as a PhD student, I had the opportunity to develop many abilities required to carry out this work. Through the close supervision of Laurent Vila, I realized the nanofabrication of all YIG|Pt and BiYIG|Pt devices presented in the manuscript using the PTA (Plateforme Technologique Amont) cleanroom facilities. It goes from the metal deposition on YIG films, etching process, SEM microscopy, chemical cleaning, lift-off and e-beam lithography.
I performed the electric and magnetic characterizations at low/high temperatures in a SQUID system. The nonlocal transports measured have been realized in a low-noise setup that I have mounted under the crucial help of Vladimir Naletov and the expert eye of Olivier Klein. I also contributed to automating the measurement, data acquisition and performed the analysis of all the results described in this thesis work.
So far several results presented in this manuscript have been published :

- The electrical properties of YIG thin films at high temperature and there impact on the nonlocal transport experiments, described in **Chapter 3**, is published in *Physical Review B* [163].
- Study of nonlinear spin conductance in YIG thin film driven by a large spin-orbit torque, presented in **Chapter 4**, is published in *Physical Review B* [187] as a rapid communication.

Other results are yet to be published :

- The study on the impact of a local Joule heating to the spin transmission of YIG|Pt interface, presented in **Chapter 2**, is under writing process.
- The spin transport at high energy in a magnetic insulator with strong perpendicular magnetic anisotropy BiYIG, partially described in **Chapter 4**, still need additional measurements and analysis to fully understand the drop of the SOT signal but should be published soon.
- The result on the double signs changes of the spin Seebeck effect in the YIG|Pt|Al system, described in **Chapter 6**, is under writing process.

Throughout our collaborators, I contributed in a publication as a co-author :

- Study of the temperature dependence of the magnetic properties of YIG ultrathin film grown by liquid phase epitaxy and the effect of a Pt overlayer, presented in **Chapter 5** and published in *IEEE Magnetic letters*. In this work, I performed the temperature dependence of magnetization of the YIG thin film and the e-beam evaporation of the Pt layer.

7.3 Outlook

Spin insulatronics is an emerging field. The fact that angular momentum can be generated and detected by an adjacent metal is of great interest. In magnetic insulators, the ultra-low dissipation facilitates brand new exciting possibilities for the exploration of novel and rich physical phenomena. The emergence of new materials or material combinations can empower future developments. Possible improvements in materials can open

novel avenues for spin transport. The material properties of magnetic insulators and their interfaces are essential. Here are some possible example of efforts and topic to be developed following this work.

In the bulk of magnetic insulators, reduced damping and control of anisotropies are important. Oxide materials offer a broad choice with numerous substitutions possible. Past efforts have mostly concentrated on spinels. The spinels are minerals that crystallize in the cubic form. Some candidates in the spinel ferrites are NiZnAl-ferrite ($\alpha = 3\ 10^{-3}$ in thin film form) and the magnesium aluminum ferrite $MgAl_{0.5}Fe_{1.5}O_4$ ($\alpha = 1.5\ 10^{-3}$ in 10 nm thick films) [2]. Recent developments in pulsed laser deposition techniques give access to a new class of epitaxial thin films with improved dynamic properties. Illustrative examples are manganite materials such as LSMO [254] with a reported low damping value. Among the oxide materials studied, apart from garnets, the other compounds that stand out are hexaferrites, of specific interest in the 80s. Of particular interest are the strontium hexaferrites [255], Ba-M hexaferrite [255], and zinc lithium ferrite [256], where the FMR linewidth can be as low as 30 MHz at 60 GHz in thin films, making them strong contenders for excellent spin conductors. While many experiments show that there can be a robust coupling between ferromagnetic/ferrimagnetic insulators and metals, there has been less exploration of antiferromagnetic insulators. Antiferromagnets comprise the majority of magnetically ordered materials. Antiferromagnetic insulators occur commonly among transition metal compounds, where the interaction between the magnetic atoms is indirect (super exchange), e.g., through oxygen ions as in hematite (Fe_2O_3), nickel oxide (NiO), cobalt oxide (CoO) or chromium oxides (Cr_2O_3). Fluorides like MnF_2 are also good potential candidates. In hematite, there is a demonstration of long-range spin transport across 80 micrometers [3]. With a higher level of purity, spins transport across micrometers is expected in the broader class of antiferromagnetic insulators. Pt couples to hematite as strong as on insulating ferrimagnets such as yttrium iron garnet [2]. For antiferromagnets, it would also be of interest to see how the spins at the two sublattices couple, possibly in different and unusual ways, to the spins in the metals depending on the crystal structures and interface directions. More precise insight into the electron-magnon coupling could enable a stronger and different control of the spin excitations in antiferromagnetic insulators.

The efficiency of the spin transfer into magnetic insulators from spin-orbit metals depends on the interfaces. The detection efficiency depends on the same parameters. Practical devices require both injection and detection of spins. The performance is, therefore, quadratic in the interface spin transparency, which is an essential factor. Measurements on yttrium-iron-garnet/platinum systems and yttrium iron garnet/gold systems [64, 65, 66, 67, 68, 69, 257] have established that the efficiency substantially varies with the preparation technique even for the same material combinations [170]. Better spin injections might also increase the efficiency of devices, possibly by the use of topological insulators [258, 61] or Rashba interfaces [60] in combination with magnetic insulators. Tuning of the extrinsic properties of the spin to charge conversion in spin-orbit metals via the implementation of impurities [178] could also be a promising way, even though a careful interface engineering is still lacking.

Spin-torque oscillators generate sustainable output ac signals from dc inputs [259, 108]. In ferromagnets, they utilize the spin-transfer or spin-orbit torque to evolve into a steady-state oscillation of the magnetization that in turn generates the output signal via magnetoresistance effects. The spin-transfer torque enhances or reduces the dissipation depending on the current direction. However, in dedicated geometries, its dependence on the precession cone angle can differ from that of the Gilbert damping. Therefore, for one current polarity, the spin-transfer torque compensates the Gilbert damping at an angle where steady-state oscillations take place. In ferromagnetic insulators, the reduced dissipation rate reflected in the smaller Gilbert damping constant can facilitate spin-torque

oscillators at lower applied currents. We can speculate that insulators might provide new ways to synchronize oscillators producing a desired larger output signal. It is also possible to envision spin-torque oscillators at much higher, THz, frequencies by using antiferromagnetic insulators [260, 261, 262].
Concerning spin waves transport mediated by spin-orbit interaction in a non-local geometry, several new possibilities can be envisaged. Ref.[263] reported the realization of a spin transistor by inserting a third "gate" electrode in between the magnon injector and detector where a DC current flows through an intermediate electrode. Depending on the current direction the magnon density in the YIG below is either enhanced or reduced, leading to a modulation of the magnon conductivity and the non-local signal by several percents. By making the YIG layer thinner and using higher DC currents, allowing a larger change in the magnon density, in this device geometry the observation of a magnon Bose-Einstein condensation was claimed [264]. Such interplay could be the aim of our future generation of devices based on ultra-thin YIG films. On the other hand, the temperature elevation induced by the large current injection in the YIG|Pt structures is a technological issue. It facilitates the emergence of the subcritical regime leading to the excitation of subthermal spin waves but disables long distance emission due to the frequency redshift. Thus more investigations need to be done to understand the magnon distribution in the spectrum at high temperatures. One could also think of taking advantage of the coupling of magnons with phonons. We have recently shown the long range dynamical coupling by phonons in vertical geometry [265], but this should also work in lateral device. Currently, there is an effort to understand the role of phonons in this non-local experiment [33, 266, 267, 268] near the 2nd crossing between the dispersion relation of phonons with magnons.

Appendix A

Brillouin Light Scattering

The Brillouin light scattering (BLS) spectroscopy is an optical method which mainly allow to measure the frequency and density of state of spin waves in a magnetic material. The principal of this technique lies in the inelastic scattering of spin waves with photons provided by monochromatic light. As described in equation A.1 and A.2 an incident photons with a wave vector k and frequency ν propagating in a magnetic medium will either create (Stokes) or annihilate (Anti-Stokes) a magnon due to scattering processes. The scattered photon will then loss/gain in energy and momentum due to conservative laws, and provide information on the frequency and intensity of detected spin waves.

$$h\nu_{\text{out}} = h\nu_{\text{in}} \mp h\nu_{\text{sw}} \tag{A.1}$$

$$hk_{\text{out}} = hk_{\text{in}} \mp hk_{\text{sw}} \tag{A.2}$$

BLS setup can be seen in FIG.72. The incident light is formed by solid-state laser beam with a typical wavelength of 532 nm. The primary light is spatially filtered by passing through a small diaphragm and is expended via a beam expander to reduce the laser spot focus. The light is then transmitted to a polarizer to improve the vectorial polarization ensuring better filtering of the inelastically scattered light. The resulting beam is thus reflected by a polarizing beam splitter and focus of the sample surface which is placed in a magnetic field. The sample itself is mounted into a piezoelectric stage to perform the translation in all three dimensions within a precision of 50 nm. To prevent any heating of the magnetic material by the focused beam, the laser power is set in the range 5-10 mW.

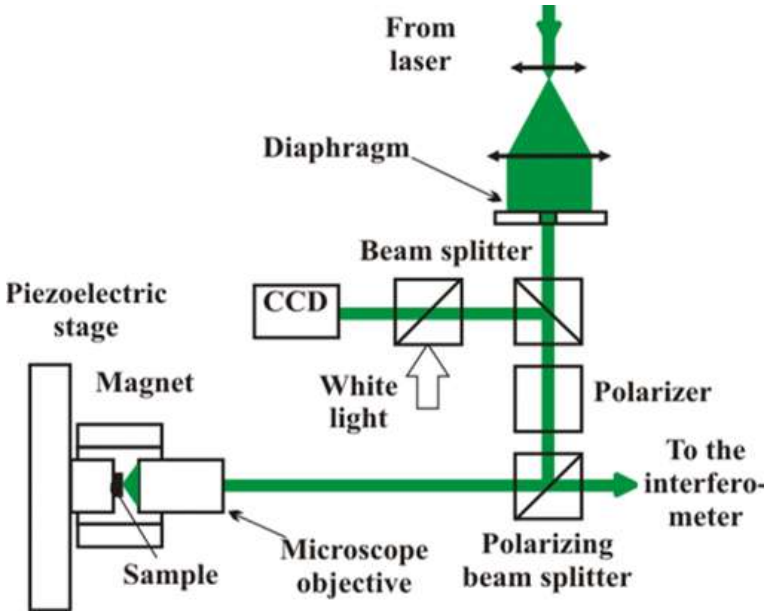

Figure 72: *Sketch of the setup for μ-BLS experiment taken from [269]*

The detection of the inelastically scattered light with spin waves is performed by a Fabry-Pérot interferometer. Analysis of the scattered light allows probing the spin waves energy. Since the laser wavelength is fixed, the wave length k_{in} of the emitted photon is fixed. To have a wave vector selectivity detection, the incident angle between the emitted light and sample surface is tune to control the momentum that is transferred from photon to magnon. This can be done experimentally by rotating the sample perpendicularly to the plane of the incident light. Thus the probed spin wave frequency is limited to :

$$k_{\text{sw}} = 2\frac{2\pi}{\lambda}\sin\varphi \tag{A.3}$$

where λ is the laser wavelength and φ the incidence angle. Taking into account the frequency of the laser, this gives a maximum accessible wave vector of k_{sw}=23.6 rad.μm^{-1}.

Appendix B

Nanofabrication

Most nanofabrication process on garnet thin films has been realised in the Platforme Technologique Amont in Grenoble. The fabrication of nanostructure on YIG films can be summarized as follow :

- First, the polymethyl methacrylate (PMMA) resist is deposited for patterning. An Aluminum film is evaporated on the surface in order to evacuate any charge from the resist. The PMMA resist is usually diluted in between 2-4% which allow to tune the resist thickness. The choice of the PMMA can be particularly critical in the case of nanowires because a thick resist have a higher chance to breakdown that would result in a inhomogeneous wire section. In that case, the deposition of a thinner PMMA resist revealed to be an efficient way to overcome this issue.
- Metal strips are defined with electronic lithography which allow a much better spatial resolution than optical lithography. It consists in exposing the resist to a focalised electron beam. The sample is mounted into a step motor control through a interferometer to ensure a precise location for writing the pattern on the resist. In this work we have set the intensity of the beam to 1 nA in the high speed mode while the exposure time (dose) modulated to take into account of the proximity effects between dense and more isolated parts of the design.
- For the development of the PMMA resist after lithography, the sample is emerged in a dilute $MIBK_{0.33}/IPA_{0.67}$ solution for 30 s.
- Before any metallic evaporation, we perform a soft in-situ Ar^+ etching within a acceleration voltage of 250 V in a controlled vacuum to clean the sample surface. Without breaking the vacuum the deposition of metals was made in an PLASSYS e-beam evaporator. The rate of material deposition is monitored via a quartz detector within the range 0.1-1 nm/s. The evaporation is realised with a define planar angle to prevent from shadowing effects.
- In order to make the different levels of patterning : micro-electrodes, Pt nanowires, electrical contacts, Al sink, some alignments marks are used. The detection conditions are tuned on the Ti|Au marks to target overlay alignment better than 20 nm (especially for the small gap samples). On each marks, the detection allows to define precisely the location of the pattern to be realized.
- Finally a lift-off is proceed to remove the resist that has not been exposed. This can be done by inserting the sample in acetone for long time to ensure dissolution to occur on the whole sample surface.

Bibliography

[1] Albert Fert. Nobel lecture: Origin, development, and future of spintronics. *Reviews of Modern Physics*, 80(4):1517, 2008.

[2] LJ Cornelissen, J Liu, RA Duine, J Ben Youssef, and BJ Van Wees. Long-distance transport of magnon spin information in a magnetic insulator at room temperature. *Nature Physics*, 11(12):1022, 2015.

[3] R Lebrun, A Ross, SA Bender, A Qaiumzadeh, L Baldrati, J Cramer, A Brataas, RA Duine, and M Kläui. Tunable long-distance spin transport in a crystalline antiferromagnetic iron oxide. *Nature*, 561(7722):222, 2018.

[4] VE Demidov, S Urazhdin, G De Loubens, O Klein, V Cros, A Anane, and SO Demokritov. Magnetization oscillations and waves driven by pure spin currents. *Physics Reports*, 673:1–31, 2017.

[5] BI Halperin and PC Hohenberg. Hydrodynamic theory of spin waves. *Physical Review*, 188(2):898, 1969.

[6] VV Kruglyak, SO Demokritov, and D Grundler. Magnonics. *Journal of Physics D: Applied Physics*, 43(26):264001, 2010.

[7] AV Chumak, VI Vasyuchka, AA Serga, and Burkard Hillebrands. Magnon spintronics. *Nature Physics*, 11(6):453, 2015.

[8] Y Kajiwara, K Harii, S Takahashi, Jun-ichiro Ohe, K Uchida, M Mizuguchi, H Umezawa, H Kawai, Kazuya Ando, K Takanashi, et al. Transmission of electrical signals by spin-wave interconversion in a magnetic insulator. *Nature*, 464(7286):262, 2010.

[9] Alexander G Gurevich and Gennadii A Melkov. *Magnetization oscillations and waves*. CRC press, 1996.

[10] Alvaro S Núnez, RA Duine, Paul Haney, and AH MacDonald. Theory of spin torques and giant magnetoresistance in antiferromagnetic metals. *Physical Review B*, 73(21):214426, 2006.

[11] RA Duine, PM Haney, AS Núñez, and AH MacDonald. Inelastic scattering in ferromagnetic and antiferromagnetic spin valves. *Physical Review B*, 75(1):014433, 2007.

[12] Peter Wadley, Bryn Howells, J Železnỳ, Carl Andrews, Victoria Hills, Richard P Campion, Vit Novák, K Olejník, F Maccherozzi, SS Dhesi, et al. Electrical switching of an antiferromagnet. *Science*, 351(6273):587–590, 2016.

[13] Christopher Marrows. Addressing an antiferromagnetic memory. *Science*, 351(6273):558–559, 2016.

[14] Christian Hahn, Gregoire De Loubens, Vladimir V Naletov, Jamal Ben Youssef, Olivier Klein, and Michel Viret. Conduction of spin currents through insulating antiferromagnetic oxides. *EPL (Europhysics Letters)*, 108(5):57005, 2014.

[15] Hailong Wang, Chunhui Du, P Chris Hammel, and Fengyuan Yang. Spin transport in antiferromagnetic insulators mediated by magnetic correlations. *Physical Review B*, 91(22):220410, 2015.

[16] Christian Hahn, Grégoire De Loubens, Olivier Klein, Michel Viret, Vladimir V Naletov, and J Ben Youssef. Comparative measurements of inverse spin hall effects and magnetoresistance in yig/pt and yig/ta. *Physical Review B*, 87(17):174417, 2013.

[17] Carsten Dubs, Oleksii Surzhenko, Ralf Linke, Andreas Danilewsky, Uwe Brückner, and Jan Dellith. Sub-micrometer yttrium iron garnet lpe films with low ferromagnetic resonance losses. *Journal of Physics D: Applied Physics*, 50(20):204005, 2017.

[18] Nathan Beaulieu, Nelly Kervarec, Nicolas Thiery, Olivier Klein, Vladimir Naletov, Hervé Hurdequint, Grégoire De Loubens, Jamal Ben Youssef, and Nicolas Vukadinovic. Temperature dependence of magnetic properties of a ultrathin yttrium-iron garnet film grown by liquid phase epitaxy: Effect of a pt overlayer. *IEEE Magnetics Letters*, 9:1–5, 2018.

[19] Yiyan Sun, Young-Yeal Song, Houchen Chang, Michael Kabatek, Michael Jantz, William Schneider, Mingzhong Wu, Helmut Schultheiss, and Axel Hoffmann. Growth and ferromagnetic resonance properties of nanometer-thick yttrium iron garnet films. *Applied Physics Letters*, 101(15):152405, 2012.

[20] O d'Allivy Kelly, A Anane, R Bernard, J Ben Youssef, C Hahn, A H Molpeceres, C Carrétéro, E Jacquet, C Deranlot, P Bortolotti, et al. Inverse spin hall effect in nanometer-thick yttrium iron garnet/pt system. *Applied Physics Letters*, 103(8):082408, 2013.

[21] MC Onbasli, A Kehlberger, DH Kim, G Jakob, M Kläui, AV Chumak, B Hillebrands, and CA Ross. Pulsed laser deposition of epitaxial yttrium iron garnet films with low gilbert damping and bulk-like magnetization. *Apl Materials*, 2(10):106102, 2014.

[22] Koichi Oyanagi, Saburo Takahashi, Ludo J Cornelissen, Juan Shan, Shunsuke Daimon, Takashi Kikkawa, Gerrit EW Bauer, Bart J van Wees, and Eiji Saitoh. Efficient spin transport in a paramagnetic insulator. *arXiv preprint arXiv:1811.11972*, 2018.

[23] Haiming Yu, O d'Allivy Kelly, V Cros, R Bernard, P Bortolotti, A Anane, F Brandl, F Heimbach, and D Grundler. Approaching soft x-ray wavelengths in nanomagnet-based microwave technology. *Nature communications*, 7:11255, 2016.

[24] M Collet, O Gladii, M Evelt, V Bessonov, L Soumah, P Bortolotti, SO Demokritov, Y Henry, V Cros, M Bailleul, et al. Spin-wave propagation in ultra-thin yig based waveguides. *Applied Physics Letters*, 110(9):092408, 2017.

[25] Etienne Du Trémolet de Lacheisserie. *Magnetostriction: theory and applications of magnetoelasticity*. CRC press, 1993.

[26] Glen A Slack. Crystallography and domain walls in antiferromagnetic nio crystals. *Journal of Applied Physics*, 31(9):1571–1582, 1960.

[27] Selma Greenwald and J Samuel Smart. Deformations in the crystal structures of anti-ferromagnetic compounds. *Nature*, 166(4221):523, 1950.

[28] L Dreher, M Weiler, M Pernpeintner, H Huebl, R Gross, MS Brandt, and STB Goennenwein. Surface acoustic wave driven ferromagnetic resonance in nickel thin films: Theory and experiment. *Physical Review B*, 86(13):134415, 2012.

[29] Ch Kittel. Interaction of spin waves and ultrasonic waves in ferromagnetic crystals. *Physical Review*, 110(4):836, 1958.

[30] J Holanda, DS Maior, A Azevedo, and SM Rezende. Detecting the phonon spin in magnon-phonon conversion experiments. *Nature Physics*, 14:500–506, 2018.

[31] Xufeng Zhang, Chang-Ling Zou, Liang Jiang, and Hong X Tang. Cavity magnomechanics. *Science advances*, 2(3):e1501286, 2016.

[32] H Matthews and RC LeCraw. Acoustic wave rotation by magnon-phonon interaction. *Physical Review Letters*, 8(10):397, 1962.

[33] Takashi Kikkawa, Ka Shen, Benedetta Flebus, Rembert A Duine, Ken-ichi Uchida, Zhiyong Qiu, Gerrit EW Bauer, and Eiji Saitoh. Magnon polarons in the spin seebeck effect. *Physical review letters*, 117(20):207203, 2016.

[34] Artem N Litvinenko, Alexandr V Sadovnikov, Vladimir V Tikhonov, and Sergey A Nikitov. Brillouin light scattering spectroscopy of magneto-acoustic resonances in a thin-film garnet resonator. *IEEE Magnetics Letters*, 6:1–4, 2015.

[35] Tadataka Watanabe, Shigeo Hara, Shin-Ichi Ikeda, and Keisuke Tomiyasu. Elastic instabilities in an antiferromagnetically ordered phase of the orbitally frustrated spinel geco 2 o 4. *Physical Review B*, 84(2):020409, 2011.

[36] VI Ozhogin and VL Preobrazhenskiĭ. Anharmonicity of mixed modes and giant acoustic nonlinearity of antiferromagnetics. *Soviet Physics Uspekhi*, 31(8):713, 1988.

[37] Yutaka Tabuchi, Seiichiro Ishino, Toyofumi Ishikawa, Rekishu Yamazaki, Koji Usami, and Yasunobu Nakamura. Hybridizing ferromagnetic magnons and microwave photons in the quantum limit. *Physical review letters*, 113(8):083603, 2014.

[38] J Jorzick, SO Demokritov, C Mathieu, B Hillebrands, B Bartenlian, C Chappert, F Rousseaux, and AN Slavin. Brillouin light scattering from quantized spin waves in micron-size magnetic wires. *Physical Review B*, 60(22):15194, 1999.

[39] A Osada, A Gloppe, R Hisatomi, A Noguchi, R Yamazaki, M Nomura, Y Nakamura, and K Usami. Brillouin light scattering by magnetic quasivortices in cavity optomagnonics. *Physical review letters*, 120(13):133602, 2018.

[40] Andrei Kirilyuk, Alexey V Kimel, and Theo Rasing. Ultrafast optical manipulation of magnetic order. *Reviews of Modern Physics*, 82(3):2731, 2010.

[41] Ji-Wan Kim, Mircea Vomir, and Jean-Yves Bigot. Ultrafast magnetoacoustics in nickel films. *Physical review letters*, 109(16):166601, 2012.

[42] Pascal Ruello, T Pezeril, S Avanesyan, Gwenaelle Vaudel, V Gusev, Ingrid C Infante, and Brahim Dkhil. Photoexcitation of gigahertz longitudinal and shear acoustic waves in bifeo3 multiferroic single crystal. *Applied Physics Letters*, 100(21):212906, 2012.

[43] Oleksandr Kovalenko, Thomas Pezeril, and Vasily V Temnov. New concept for magnetization switching by ultrafast acoustic pulses. *Physical review letters*, 110(26):266602, 2013.

[44] Gyung-Min Choi, Chul-Hyun Moon, Byoung-Chul Min, Kyung-Jin Lee, and David G Cahill. Thermal spin-transfer torque driven by the spin-dependent seebeck effect in metallic spin-valves. *Nature physics*, 11(7):576, 2015.

[45] JP Van der Ziel, PS Pershan, and LD Malmstrom. Optically-induced magnetization resulting from the inverse faraday effect. *Physical Review Letters*, 15(5):190, 1965.

[46] RV Mikhaylovskiy, TJ Huisman, AI Popov, AK Zvezdin, Th Rasing, RV Pisarev, and AV Kimel. Terahertz magnetization dynamics induced by femtosecond resonant pumping of dy 3+ subsystem in the multisublattice antiferromagnet dyfeo 3. *Physical Review B*, 92(9):094437, 2015.

[47] Takuya Satoh, Sung-Jin Cho, Ryugo Iida, Tsutomu Shimura, Kazuo Kuroda, Hiroaki Ueda, Yutaka Ueda, BA Ivanov, Franco Nori, and Manfred Fiebig. Spin oscillations in antiferromagnetic nio triggered by circularly polarized light. *Physical review letters*, 105(7):077402, 2010.

[48] NP Duong, Takuya Satoh, and M Fiebig. Ultrafast manipulation of antiferromagnetism of nio. *Physical review letters*, 93(11):117402, 2004.

[49] Andrea Rubano, Takuya Satoh, Alexey Kimel, Andrey Kirilyuk, Theo Rasing, and Manfred Fiebig. Influence of laser pulse shaping on the ultrafast dynamics in antiferromagnetic nio. *Physical Review B*, 82(17):174431, 2010.

[50] Tobias Kampfrath, Alexander Sell, Gregor Klatt, Alexej Pashkin, Sebastian Mährlein, Thomas Dekorsy, Martin Wolf, Manfred Fiebig, Alfred Leitenstorfer, and Rupert Huber. Coherent terahertz control of antiferromagnetic spin waves. *Nature Photonics*, 5(1):31, 2011.

[51] Wilma Eerenstein, ND Mathur, and James F Scott. Multiferroic and magnetoelectric materials. *nature*, 442(7104):759, 2006.

[52] Nicola A Hill. Why are there so few magnetic ferroelectrics?, 2000.

[53] Manfred Fiebig, Th Lottermoser, Dietmar Fröhlich, Andriy V Goltsev, and Roman V Pisarev. Observation of coupled magnetic and electric domains. *Nature*, 419(6909):818, 2002.

[54] N Hur, S Park, PA Sharma, JS Ahn, S Guha, and SW Cheong. Electric polarization reversal and memory in a multiferroic material induced by magnetic fields. *Nature*, 429(6990):392, 2004.

[55] AP Pyatakov and AK Zvezdin. Flexomagnetoelectric interaction in multiferroics. *The European Physical Journal B*, 71(3):419–427, 2009.

[56] P Rovillain, R De Sousa, YT Gallais, A Sacuto, MA Méasson, D Colson, A Forget, M Bibes, A Barthélémy, and M Cazayous. Electric-field control of spin waves at room temperature in multiferroic bifeo 3. *Nature materials*, 9(12):975, 2010.

[57] Andrei Pimenov, AA Mukhin, V Yu Ivanov, VD Travkin, AM Balbashov, and Alois Loidl. Possible evidence for electromagnons in multiferroic manganites. *Nature physics*, 2(2):97, 2006.

[58] Arne Brataas, Andrew D Kent, and Hideo Ohno. Current-induced torques in magnetic materials. *Nature materials*, 11(5):372, 2012.

[59] Jairo Sinova, Sergio O Valenzuela, J Wunderlich, CH Back, and T Jungwirth. Spin hall effects. *Reviews of Modern Physics*, 87(4):1213, 2015.

[60] JC Rojas Sánchez, Laurent Vila, G Desfonds, S Gambarelli, JP Attané, JM De Teresa, C Magén, and A Fert. Spin-to-charge conversion using rashba coupling at the interface between non-magnetic materials. *Nature communications*, 4:2944, 2013.

[61] AR Mellnik, JS Lee, A Richardella, JL Grab, PJ Mintun, Mark H Fischer, Abolhassan Vaezi, Aurelien Manchon, E-A Kim, N Samarth, et al. Spin-transfer torque generated by a topological insulator. *Nature*, 511(7510):449, 2014.

[62] H Nakayama, Matthias Althammer, Y-T Chen, K Uchida, Y Kajiwara, D Kikuchi, T Ohtani, Stephan Geprägs, M Opel, S Takahashi, et al. Spin hall magnetoresistance induced by a nonequilibrium proximity effect. *Physical review letters*, 110(20):206601, 2013.

[63] Aisha Aqeel, Nynke Vlietstra, Jeroen A Heuver, Gerrit EW Bauer, Beatriz Noheda, Bart J van Wees, and TTM Palstra. Spin-hall magnetoresistance and spin seebeck effect in spin-spiral and paramagnetic phases of multiferroic cocr 2 o 4 films. *Physical Review B*, 92(22):224410, 2015.

[64] Christian W Sandweg, Yosuke Kajiwara, Andrii V Chumak, Alexander A Serga, Vitaliy I Vasyuchka, Mattias Benjamin Jungfleisch, Eiji Saitoh, and Burkard Hillebrands. Spin pumping by parametrically excited exchange magnons. *Physical review letters*, 106(21):216601, 2011.

[65] CW Sandweg, Y Kajiwara, Kazuya Ando, E Saitoh, and B Hillebrands. Enhancement of the spin pumping efficiency by spin wave mode selection. *Applied Physics Letters*, 97(25):252504, 2010.

[66] LH Vilela-Leão, C Salvador, A Azevedo, and SM Rezende. Unidirectional anisotropy in the spin pumping voltage in yttrium iron garnet/platinum bilayers. *Applied Physics Letters*, 99(10):102505, 2011.

[67] SM Rezende, RL Rodríguez-Suárez, MM Soares, LH Vilela-Leão, D Ley Domínguez, and A Azevedo. Enhanced spin pumping damping in yttrium iron garnet/pt bilayers. *Applied Physics Letters*, 102(1):012402, 2013.

[68] A Azevedo, LH Vilela-Leão, RL Rodríguez-Suárez, AF Lacerda Santos, and SM Rezende. Spin pumping and anisotropic magnetoresistance voltages in magnetic bilayers: Theory and experiment. *Physical review B*, 83(14):144402, 2011.

[69] C Burrowes, B Heinrich, B Kardasz, EA Montoya, E Girt, Yiyan Sun, Young-Yeal Song, and Mingzhong Wu. Enhanced spin pumping at yttrium iron garnet/au interfaces. *Applied Physics Letters*, 100(9):092403, 2012.

[70] Hidekazu Kurebayashi, Oleksandr Dzyapko, Vladislav E Demidov, Dong Fang, Andrew J Ferguson, and Sergej O Demokritov. Controlled enhancement of spin-current emission by three-magnon splitting. *Nature materials*, 10(9):660, 2011.

[71] H Kurebayashi, O Dzyapko, VE Demidov, D Fang, AJ Ferguson, and SO Demokritov. Spin pumping by parametrically excited short-wavelength spin waves. *Applied Physics Letters*, 99(16):162502, 2011.

[72] Christian Hahn, Grégoire de Loubens, Michel Viret, Olivier Klein, VV Naletov, and J Ben Youssef. Detection of microwave spin pumping using the inverse spin hall effect. *Physical review letters*, 111(21):217204, 2013.

[73] André Kapelrud and Arne Brataas. Spin pumping and enhanced gilbert damping in thin magnetic insulator films. *Physical review letters*, 111(9):097602, 2013.

[74] Yaroslav Tserkovnyak, Arne Brataas, and Gerrit EW Bauer. Enhanced gilbert damping in thin ferromagnetic films. *Physical review letters*, 88(11):117601, 2002.

[75] Yaroslav Tserkovnyak, Arne Brataas, Gerrit EW Bauer, and Bertrand I Halperin. Nonlocal magnetization dynamics in ferromagnetic heterostructures. *Reviews of Modern Physics*, 77(4):1375, 2005.

[76] Arne Brataas, Yaroslav Tserkovnyak, Gerrit EW Bauer, and Bertrand I Halperin. Spin battery operated by ferromagnetic resonance. *Physical Review B*, 66(6):060404, 2002.

[77] Jiang Xiao, Gerrit EW Bauer, et al. Spin-wave excitation in magnetic insulators by spin-transfer torque. *Physical review letters*, 108(21):217204, 2012.

[78] Chunhui Du, Toeno Van der Sar, Tony X Zhou, Pramey Upadhyaya, Francesco Casola, Huiliang Zhang, Mehmet C Onbasli, Caroline A Ross, Ronald L Walsworth, Yaroslav Tserkovnyak, et al. Control and local measurement of the spin chemical potential in a magnetic insulator. *Science*, 357(6347):195–198, 2017.

[79] VE Demidov, S Urazhdin, B Divinskiy, VD Bessonov, AB Rinkevich, VV Ustinov, and SO Demokritov. Chemical potential of quasi-equilibrium magnon gas driven by pure spin current. *Nature communications*, 8(1):1579, 2017.

[80] A Hamadeh, O d'Allivy Kelly, C Hahn, H Meley, R Bernard, AH Molpeceres, VV Naletov, M Viret, A Anane, V Cros, et al. Full control of the spin-wave damping in a magnetic insulator using spin-orbit torque. *Physical review letters*, 113(19):197203, 2014.

[81] Vladislav E Demidov, Sergei Urazhdin, ERJ Edwards, Mark D Stiles, Robert D McMichael, and Sergej O Demokritov. Control of magnetic fluctuations by spin current. *Physical review letters*, 107(10):107204, 2011.

[82] Mark D Stiles and A Zangwill. Anatomy of spin-transfer torque. *Physical Review B*, 66(1):014407, 2002.

[83] Luc Berger. Emission of spin waves by a magnetic multilayer traversed by a current. *Physical Review B*, 54(13):9353, 1996.

[84] John C Slonczewski. Current-driven excitation of magnetic multilayers. *Journal of Magnetism and Magnetic Materials*, 159(1-2):L1–L7, 1996.

[85] M Haidar, P Dürrenfeld, M Ranjbar, M Balinsky, M Fazlali, M Dvornik, RK Dumas, Sergiy Khartsev, and Johan Åkerman. Controlling gilbert damping in a yig film using nonlocal spin currents. *Physical Review B*, 94(18):180409, 2016.

[86] Jiang Xiao, Gerrit EW Bauer, Ken-chi Uchida, Eiji Saitoh, Sadamichi Maekawa, et al. Theory of magnon-driven spin seebeck effect. *Physical Review B*, 81(21):214418, 2010.

[87] Silas Hoffman, Koji Sato, and Yaroslav Tserkovnyak. Landau-lifshitz theory of the longitudinal spin seebeck effect. *Physical Review B*, 88(6):064408, 2013.

[88] Scott A Bender, Rembert A Duine, and Yaroslav Tserkovnyak. Electronic pumping of quasiequilibrium bose-einstein-condensed magnons. *Physical review letters*, 108(24):246601, 2012.

[89] Scott A Bender, Rembert A Duine, Arne Brataas, and Yaroslav Tserkovnyak. Dynamic phase diagram of dc-pumped magnon condensates. *Physical Review B*, 90(9):094409, 2014.

[90] H Suhl. The theory of ferromagnetic resonance at high signal powers. *Journal of Physics and Chemistry of Solids*, 1(4):209–227, 1957.

[91] Victor S L'vov. *Wave turbulence under parametric excitation: applications to magnets*. Springer Science & Business Media, 2012.

[92] Martin Collet, Xavier De Milly, O d'Allivy Kelly, Vladimir V Naletov, Rozenn Bernard, Paolo Bortolotti, J Ben Youssef, VE Demidov, SO Demokritov, JL Prieto, et al. Generation of coherent spin-wave modes in yttrium iron garnet microdiscs by spin–orbit torque. *Nature communications*, 7:10377, 2016.

[93] VE Demidov, M Evelt, V Bessonov, SO Demokritov, JL Prieto, M Muñoz, J Ben Youssef, VV Naletov, G De Loubens, Olivier Klein, et al. Direct observation of dynamic modes excited in a magnetic insulator by pure spin current. *Scientific reports*, 6:32781, 2016.

[94] Mark Johnson and Robert H Silsbee. Interfacial charge-spin coupling: Injection and detection of spin magnetization in metals. *Physical Review Letters*, 55(17):1790, 1985.

[95] Xiaohua Lou, Christoph Adelmann, Scott A Crooker, Eric S Garlid, Jianjie Zhang, KS Madhukar Reddy, Soren D Flexner, Chris J Palmstrøm, and Paul A Crowell. Electrical detection of spin transport in lateral ferromagnet–semiconductor devices. *Nature Physics*, 3(3):197, 2007.

[96] Nikolaos Tombros, Csaba Jozsa, Mihaita Popinciuc, Harry T Jonkman, and Bart J Van Wees. Electronic spin transport and spin precession in single graphene layers at room temperature. *Nature*, 448(7153):571, 2007.

[97] Ludo J Cornelissen, Kevin JH Peters, Gerrit EW Bauer, RA Duine, and Bart J van Wees. Magnon spin transport driven by the magnon chemical potential in a magnetic insulator. *Physical Review B*, 94(1):014412, 2016.

[98] K Uchida, J Xiao, Hiroto Adachi, J-i Ohe, S Takahashi, J Ieda, T Ota, Y Kajiwara, H Umezawa, H Kawai, et al. Spin seebeck insulator. *Nature materials*, 9(11):894, 2010.

[99] Steven S-L Zhang and Shufeng Zhang. Magnon mediated electric current drag across a ferromagnetic insulator layer. *Physical review letters*, 109(9):096603, 2012.

[100] MB Jungfleisch, T An, Kazuya Ando, Y Kajiwara, K Uchida, VI Vasyuchka, AV Chumak, AA Serga, E Saitoh, and B Hillebrands. Heat-induced damping modification in yttrium iron garnet/platinum hetero-structures. *Applied Physics Letters*, 102(6):062417, 2013.

[101] Chris Safranski, Igor Barsukov, Han Kyu Lee, Tobias Schneider, AA Jara, Andrew Smith, Houchen Chang, Kilian Lenz, Juergen Lindner, Yaroslav Tserkovnyak, et al. Spin caloritronic nano-oscillator. *Nature communications*, 8(1):117, 2017.

[102] Kathrin Ganzhorn, Stefan Klingler, Tobias Wimmer, Stephan Geprägs, Rudolf Gross, Hans Huebl, and Sebastian TB Goennenwein. Magnon-based logic in a multi-terminal yig/pt nanostructure. *Applied Physics Letters*, 109(2):022405, 2016.

[103] Kumar Sourav Das, Jing Liu, Bart J van Wees, and Ivan J Vera-Marun. Efficient injection and detection of out-of-plane spins via the anomalous spin hall effect in permalloy nanowires. *Nano letters*, 18(9):5633–5639, 2018.

[104] Sebastian TB Goennenwein, Richard Schlitz, Matthias Pernpeintner, Kathrin Ganzhorn, Matthias Althammer, Rudolf Gross, and Hans Huebl. Non-local magnetoresistance in yig/pt nanostructures. *Applied Physics Letters*, 107(17):172405, 2015.

[105] AV Chumak, AA Serga, and B Hillebrands. Magnonic crystals for data processing. *Journal of Physics D: Applied Physics*, 50(24):244001, 2017.

[106] M Evelt, VE Demidov, V Bessonov, SO Demokritov, JL Prieto, M Muñoz, J Ben Youssef, VV Naletov, G De Loubens, Olivier Klein, et al. High-efficiency control of spin-wave propagation in ultra-thin yttrium iron garnet by the spin-orbit torque. *Applied Physics Letters*, 108(17):172406, 2016.

[107] Stephen Blundell. *Magnetism in condensed matter*. AAPT, 2003.

[108] Charles Kittel, Paul McEuen, and Paul McEuen. *Introduction to solid state physics*, volume 8. Wiley New York, 1976.

[109] Charles P Slichter. *Principles of magnetic resonance*, volume 1. Springer Science & Business Media, 2013.

[110] LR Walker. Magnetostatic modes in ferromagnetic resonance. *Physical Review*, 105(2):390, 1957.

[111] RF W Damon and JR Eshbach. Magnetostatic modes of a ferromagnet slab. *Journal of Physics and Chemistry of Solids*, 19(3-4):308–320, 1961.

[112] BA Kalinikos and AN Slavin. Theory of dipole-exchange spin wave spectrum for ferromagnetic films with mixed exchange boundary conditions. *Journal of Physics C: Solid State Physics*, 19(35):7013, 1986.

[113] Conyers Herring and Charles Kittel. On the theory of spin waves in ferromagnetic media. *Physical Review*, 81(5):869, 1951.

[114] Sung Yong An, Pavol Krivosik, Michael A Kraemer, Heidi M Olson, Alexey V Nazarov, and Carl E Patton. High power ferromagnetic resonance and spin wave instability processes in permalloy thin films. *Journal of applied physics*, 96(3):1572–1580, 2004.

[115] M Sparks, R Loudon, and Ch Kittel. Ferromagnetic relaxation. i. theory of the relaxation of the uniform precession and the degenerate spectrum in insulators at low temperatures. *Physical Review*, 122(3):791, 1961.

[116] Rodrigo Arias and DL Mills. Extrinsic contributions to the ferromagnetic resonance response of ultrathin films. *Physical review B*, 60(10):7395, 1999.

[117] T Kasuya and RC LeCraw. Relaxation mechanisms in ferromagnetic resonance. *Physical review letters*, 6(5):223, 1961.

[118] Walther Gerlach and Otto Stern. Der experimentelle nachweis der richtungsquantelung im magnetfeld. *Zeitschrift für Physik A Hadrons and Nuclei*, 9(1):349–352, 1922.

[119] Selman Hershfield and Hui Lin Zhao. Charge and spin transport through a metallic ferromagnetic-paramagnetic-ferromagnetic junction. *Physical Review B*, 56(6):3296, 1997.

[120] T Valet and A Fert. Theory of the perpendicular magnetoresistance in magnetic multilayers. *Physical Review B*, 48(10):7099, 1993.

[121] MI Dyakonov and VI Perel. Current-induced spin orientation of electrons in semiconductors. *Physics Letters A*, 35(6):459–460, 1971.

[122] Luqiao Liu, RA Buhrman, and DC Ralph. Review and analysis of measurements of the spin hall effect in platinum. *arXiv preprint arXiv:1111.3702*, 2011.

[123] MB Jungfleisch, AV Chumak, VI Vasyuchka, AA Serga, B Obry, H Schultheiss, PA Beck, AD Karenowska, E Saitoh, and B Hillebrands. Temporal evolution of inverse spin hall effect voltage in a magnetic insulator-nonmagnetic metal structure. *Applied Physics Letters*, 99(18):182512, 2011.

[124] J-C Rojas-Sánchez, N Reyren, P Laczkowski, W Savero, J-P Attané, C Deranlot, M Jamet, J-M George, Laurent Vila, and H Jaffrès. Spin pumping and inverse spin hall effect in platinum: the essential role of spin-memory loss at metallic interfaces. *Physical review letters*, 112(10):106602, 2014.

[125] Yaroslav Tserkovnyak, Arne Brataas, and Gerrit EW Bauer. Spin pumping and magnetization dynamics in metallic multilayers. *Physical Review B*, 66(22):224403, 2002.

[126] E Saitoh, M Ueda, H Miyajima, and G Tatara. Conversion of spin current into charge current at room temperature: Inverse spin-hall effect. *Applied physics letters*, 88(18):182509, 2006.

[127] Kazuya Ando, Saburo Takahashi, Junichi Ieda, Yosuke Kajiwara, Hiroyasu Nakayama, Tatsuro Yoshino, Kazuya Harii, Yasunori Fujikawa, M Matsuo, S Maekawa, et al. Inverse spin-hall effect induced by spin pumping in metallic system. *Journal of applied physics*, 109(10):103913, 2011.

[128] Steven S-L Zhang and Shufeng Zhang. Spin convertance at magnetic interfaces. *Physical Review B*, 86(21):214424, 2012.

[129] RH Liu, WL Lim, and S Urazhdin. Spectral characteristics of the microwave emission by the spin hall nano-oscillator. *Physical review letters*, 110(14):147601, 2013.

[130] Luqiao Liu, Chi-Feng Pai, DC Ralph, and RA Buhrman. Magnetic oscillations driven by the spin hall effect in 3-terminal magnetic tunnel junction devices. *Physical review letters*, 109(18):186602, 2012.

[131] Vladislav E Demidov, Sergei Urazhdin, Henning Ulrichs, Vasyl Tiberkevich, Andrei Slavin, Dietmar Baither, Guido Schmitz, and Sergej O Demokritov. Magnetic nano-oscillator driven by pure spin current. *Nature materials*, 11(12):1028, 2012.

[132] A Hamadeh, G De Loubens, VV Naletov, J Grollier, C Ulysse, V Cros, and O Klein. Autonomous and forced dynamics in a spin-transfer nano-oscillator: Quantitative magnetic-resonance force microscopy. *Physical Review B*, 85(14):140408, 2012.

[133] RA Duine, Arne Brataas, Scott A Bender, and Yaroslav Tserkovnyak. Spintronics and magnon bose-einstein condensation. *arXiv preprint arXiv:1505.01329*, 2015.

[134] Andreas Rückriegel and Peter Kopietz. Rayleigh-jeans condensation of pumped magnons in thin-film ferromagnets. *Physical review letters*, 115(15):157203, 2015.

[135] SO Demokritov, VE Demidov, O Dzyapko, GA Melkov, AA Serga, B Hillebrands, and AN Slavin. Bose–einstein condensation of quasi-equilibrium magnons at room temperature under pumping. *Nature*, 443(7110):430, 2006.

[136] Yu M Bunkov, Egor Mikhailovich Alakshin, RR Gazizulin, Aleksandr Vladimirovich Klochkov, Valerii Vasil'evich Kuzmin, TR Safin, and MS Tagirov. Discovery of the classical bose-einstein condensation of magnons in solid antiferromagnets. *JETP letters*, 94(1):68, 2011.

[137] Yu M Bunkov, EM Alakshin, RR Gazizulin, AV Klochkov, VV Kuzmin, VS L'vov, and MS Tagirov. High-t c spin superfluidity in antiferromagnets. *Physical review letters*, 108(17):177002, 2012.

[138] EB Sonin. Phase fixation, excitonic and spin superfluidity of electron-hole pairs and antiferromagnetic chromium. *Solid State Communications*, 25(4):253–255, 1978.

[139] EB Sonin. Spin currents and spin superfluidity. *Advances in Physics*, 59(3):181–255, 2010.

[140] So Takei and Yaroslav Tserkovnyak. Superfluid spin transport through easy-plane ferromagnetic insulators. *Physical review letters*, 112(22):227201, 2014.

[141] Hans Skarsvåg, Cecilia Holmqvist, and Arne Brataas. Spin superfluidity and long-range transport in thin-film ferromagnets. *Physical review letters*, 115(23):237201, 2015.

[142] Alireza Qaiumzadeh, Hans Skarsvåg, Cecilia Holmqvist, and Arne Brataas. Spin superfluidity in biaxial antiferromagnetic insulators. *Physical review letters*, 118(13):137201, 2017.

[143] Hiroyasu Nakayama, Kazuya Ando, Kazuya Harii, Tatsuro Yoshino, Ryo Takahashi, Yosuke Kajiwara, Ken-ichi Uchida, Yasunori Fujikawa, and Eiji Saitoh. Geometry dependence on inverse spin hall effect induced by spin pumping in ni 81 fe 19/pt films. *Physical Review B*, 85(14):144408, 2012.

[144] Yan-Ting Chen, Saburo Takahashi, Hiroyasu Nakayama, Matthias Althammer, Sebastian TB Goennenwein, Eiji Saitoh, and Gerrit EW Bauer. Theory of spin hall magnetoresistance. *Physical Review B*, 87(14):144411, 2013.

[145] Ssu-Yen Huang, X Fan, D Qu, YP Chen, WG Wang, J Wu, TY Chen, JQ Xiao, and CL Chien. Transport magnetic proximity effects in platinum. *Physical review letters*, 109(10):107204, 2012.

[146] Xiao Liang, Guoyi Shi, Longjiang Deng, Fei Huang, Jun Qin, Tingting Tang, Chuangtang Wang, Bo Peng, Cheng Song, and Lei Bi. Magnetic proximity effect and anomalous hall effect in pt/y 3 fe 5- x al x o 12 heterostructures. *Physical Review Applied*, 10(2):024051, 2018.

[147] Ken-ichi Uchida, Hiroto Adachi, Takeru Ota, Hiroyasu Nakayama, Sadamichi Maekawa, and Eiji Saitoh. Observation of longitudinal spin-seebeck effect in magnetic insulators. *Applied Physics Letters*, 97(17):172505, 2010.

[148] Vladimir Cherepanov, Igor Kolokolov, and Victor L'vov. The saga of yig: spectra, thermodynamics, interaction and relaxation of magnons in a complex magnet. *Physics reports*, 229(3):81–144, 1993.

[149] Houchen Chang, Peng Li, Wei Zhang, Tao Liu, Axel Hoffmann, Longjiang Deng, and Mingzhong Wu. Nanometer-thick yttrium iron garnet films with extremely low damping. *IEEE Magnetics Letters*, 5:1–4, 2014.

[150] Tao Liu, Houchen Chang, Vincent Vlaminck, Yiyan Sun, Michael Kabatek, Axel Hoffmann, Longjiang Deng, and Mingzhong Wu. Ferromagnetic resonance of sputtered yttrium iron garnet nanometer films. *Journal of Applied Physics*, 115(17):17A501, 2014.

[151] Adam Krysztofik, Luis Emerson Coy, Piotr Kuświk, Karol Załęski, Hubert Głowiński, and Janusz Dubowik. Ultra-low damping in lift-off structured yttrium iron garnet thin films. *Applied Physics Letters*, 111(19):192404, 2017.

[152] Brandon M Howe, Satoru Emori, Hyung-Min Jeon, Trevor M Oxholm, John G Jones, Krishnamurthy Mahalingam, Yan Zhuang, Nian X Sun, and Gail J Brown. Pseudomorphic yttrium iron garnet thin films with low damping and inhomogeneous linewidth broadening. *Ieee Magnetics Letters*, 6:1–4, 2015.

[153] Michael Schieber. Crystal growth of α-fe2o3 and gafeo3 by the flux method and segregation studies of fe3+ in ga2- x fe x o3 crystals. *Journal of Applied Physics*, 37(12):4588–4588, 1966.

[154] Yi-Heng Rao, Huai-Wu Zhang, Qing-Hui Yang, Dai-Nan Zhang, Li-Chuan Jin, Bo Ma, and Yu-Juan Wu. Liquid phase epitaxy magnetic garnet films and their applications. *Chinese Physics B*, 27(8):086701, 2018.

[155] Dao Thi Thuy Nguyet, Nguyen Phuc Duong, Takuya Satoh, Luong Ngoc Anh, and Than Duc Hien. Temperature-dependent magnetic properties of yttrium iron garnet nanoparticles prepared by citrate sol–gel. *Journal of Alloys and Compounds*, 541:18–22, 2012.

[156] A Mitra, O Cespedes, Q Ramasse, M Ali, S Marmion, M Ward, RMD Brydson, CJ Kinane, JFK Cooper, S Langridge, et al. Interfacial origin of the magnetisation suppression of thin film yttrium iron garnet. *Scientific reports*, 7(1):11774, 2017.

[157] H Wu, CH Wan, X Zhang, ZH Yuan, QT Zhang, JY Qin, HX Wei, XF Han, and Shufeng Zhang. Observation of magnon-mediated electric current drag at room temperature. *Physical Review B*, 93(6):060403, 2016.

[158] Junxue Li, Yadong Xu, Mohammed Aldosary, Chi Tang, Zhisheng Lin, Shufeng Zhang, Roger Lake, and Jing Shi. Observation of magnon-mediated current drag in pt/yttrium iron garnet/pt (ta) trilayers. *Nature communications*, 7:10858, 2016.

[159] AV Chumak, AA Serga, MB Jungfleisch, R Neb, DA Bozhko, VS Tiberkevich, and B Hillebrands. Direct detection of magnon spin transport by the inverse spin hall effect. *Applied Physics Letters*, 100(8):082405, 2012.

[160] P Pirro, T Brächer, AV Chumak, B Lägel, C Dubs, O Surzhenko, P Görnert, B Leven, and B Hillebrands. Spin-wave excitation and propagation in microstructured waveguides of yttrium iron garnet/pt bilayers. *Applied Physics Letters*, 104(1):012402, 2014.

[161] T Sebastian, Y Ohdaira, T Kubota, P Pirro, T Brächer, K Vogt, AA Serga, Hiroshi Naganuma, M Oogane, Y Ando, et al. Low-damping spin-wave propagation in a micro-structured co2mn0. 6fe0. 4si heusler waveguide. *Applied Physics Letters*, 100(11):112402, 2012.

[162] T Brächer, T Meyer, T Fischer, M Fabre, O Boulle, U Ebels, P Pirro, and G Gaudin. Excitation and detection of short-waved spin waves in ultrathin ta/cofeb/mgo-layer system suitable for spin-orbit-torque magnonics. *arXiv preprint arXiv:1701.01399*, 2017.

[163] N Thiery, VV Naletov, L Vila, A Marty, A Brenac, J-F Jacquot, G de Loubens, M Viret, A Anane, V Cros, et al. Electrical properties of epitaxial yttrium iron garnet ultrathin films at high temperatures. *Physical Review B*, 97(6):064422, 2018.

[164] Hyungyu Jin, Stephen R Boona, Zihao Yang, Roberto C Myers, and Joseph P Heremans. Effect of the magnon dispersion on the longitudinal spin seebeck effect in yttrium iron garnets. *Physical Review B*, 92(5):054436, 2015.

[165] Michael Schreier, Akashdeep Kamra, Mathias Weiler, Jiang Xiao, Gerrit EW Bauer, Rudolf Gross, and Sebastian TB Goennenwein. Magnon, phonon, and electron temperature profiles and the spin seebeck effect in magnetic insulator/normal metal hybrid structures. *Physical Review B*, 88(9):094410, 2013.

[166] Can Onur Avci, Kevin Garello, Abhijit Ghosh, Mihai Gabureac, Santos F Alvarado, and Pietro Gambardella. Unidirectional spin hall magnetoresistance in ferromagnet/normal metal bilayers. *Nature Physics*, 11(7):570, 2015.

[167] DD Sarma. Nature of dependence of spin-orbit splittings on atomic number. In *Proceedings of the Indian Academy of Sciences-Chemical Sciences*, volume 90, pages 19–26. Springer, 1981.

[168] Chunhui Du, Hailong Wang, Fengyuan Yang, and P Chris Hammel. Systematic variation of spin-orbit coupling with d-orbital filling: Large inverse spin hall effect in 3 d transition metals. *Physical Review B*, 90(14):140407, 2014.

[169] HL Wang, CH Du, Y Pu, R Adur, Peter Christopher Hammel, and FY Yang. Scaling of spin hall angle in 3d, 4d, and 5d metals from y 3 fe 5 o 12/metal spin pumping. *Physical review letters*, 112(19):197201, 2014.

[170] MB Jungfleisch, V Lauer, R Neb, AV Chumak, and B Hillebrands. Improvement of the yttrium iron garnet/platinum interface for spin pumping-based applications. *Applied Physics Letters*, 103(2):022411, 2013.

[171] Saül Vélez, Amilcar Bedoya-Pinto, Wenjing Yan, Luis E Hueso, and Fèlix Casanova. Competing effects at pt/yig interfaces: Spin hall magnetoresistance, magnon excitations, and magnetic frustration. *Physical Review B*, 94(17):174405, 2016.

[172] Duk Yong Choi and Su Jin Chung. Annealing behaviors of lattice misfit in yig and la-doped yig films grown on ggg substrates by lpe method. *Journal of crystal growth*, 191(4):754–759, 1998.

[173] Z Qiu, Kazuya Ando, K Uchida, Y Kajiwara, R Takahashi, H Nakayama, T An, Y Fujikawa, and E Saitoh. Spin mixing conductance at a well-controlled platinum/yttrium iron garnet interface. *Applied Physics Letters*, 103(9):092404, 2013.

[174] Sabine Pütter, Stephan Geprägs, Richard Schlitz, Matthias Althammer, Andreas Erb, Rudolf Gross, and Sebastian TB Goennenwein. Impact of the interface quality of pt/yig (111) hybrids on their spin hall magnetoresistance. *Applied Physics Letters*, 110(1):012403, 2017.

[175] B Gao, M Rudneva, KS McGarrity, Q Xu, F Prins, JM Thijssen, H Zandbergen, and HSJ Van der Zant. In situ transmission electron microscopy imaging of grain growth in a platinum nanobridge induced by electric current annealing. *Nanotechnology*, 22(20):205705, 2011.

[176] Vincent Castel, N Vlietstra, BJ Van Wees, and J Ben Youssef. Frequency and power dependence of spin-current emission by spin pumping in a thin-film yig/pt system. *Physical Review B*, 86(13):134419, 2012.

[177] ML Trouwborst, SJ Van Der Molen, and BJ Van Wees. The role of joule heating in the formation of nanogaps by electromigration. *Journal of Applied Physics*, 99(11):114316, 2006.

[178] P Laczkowski, Y Fu, H Yang, J-C Rojas-Sánchez, P Noel, VT Pham, G Zahnd, C Deranlot, S Collin, C Bouard, et al. Large enhancement of the spin hall effect in au by side-jump scattering on ta impurities. *Physical Review B*, 96(14):140405, 2017.

[179] Edurne Sagasta, Yasutomo Omori, Miren Isasa, Martin Gradhand, Luis E Hueso, Yasuhiro Niimi, YoshiChika Otani, and Fèlix Casanova. Tuning the spin hall effect of pt from the moderately dirty to the superclean regime. *Physical Review B*, 94(6):060412, 2016.

[180] Yuri K Fetisov, Carl E Patton, and Valeri T Synogach. Nonlinear ferromagnetic resonance and foldover in yttrium iron garnet thin films-inadequacy of the classical model. *IEEE transactions on magnetics*, 35(6):4511–4521, 1999.

[181] YS Gui, A Wirthmann, and C-M Hu. Foldover ferromagnetic resonance and damping in permalloy microstrips. *Physical Review B*, 80(18):184422, 2009.

[182] Matthias Althammer. Pure spin currents in magnetically ordered insulator/normal metal heterostructures. *Journal of Physics D: Applied Physics*, 51(31):313001, 2018.

[183] Kyeong-Dong Lee, Dong-Jun Kim, Hae Yeon Lee, Seung-Hyun Kim, Jong-Hyun Lee, Kyung-Min Lee, Jong-Ryul Jeong, Ki-Suk Lee, Hyon-Seok Song, Jeong-Woo Sohn, et al. Thermoelectric signal enhancement by reconciling the spin seebeck and anomalous nernst effects in ferromagnet/non-magnet multilayers. *Scientific reports*, 5:10249, 2015.

[184] M Haertinger, CH Back, J Lotze, M Weiler, S Geprägs, H Huebl, STB Goennenwein, and G Woltersdorf. Spin pumping in yig/pt bilayers as a function of layer thickness. *Physical Review B*, 92(5):054437, 2015.

[185] Evangelos Th Papaioannou, Philipp Fuhrmann, Matthias B Jungfleisch, Thomas Brächer, Philipp Pirro, Viktor Lauer, Jörg Lösch, and Burkard Hillebrands. Optimizing the spin-pumping induced inverse spin hall voltage by crystal growth in fe/pt bilayers. *Applied Physics Letters*, 103(16):162401, 2013.

[186] Devin Wesenberg, Tao Liu, Davor Balzar, Mingzhong Wu, and Barry L Zink. Long-distance spin transport in a disordered magnetic insulator. *Nature Physics*, 13(10):987, 2017.

[187] Nicolas Thiery, Antoine Draveny, Vladimir V Naletov, Laurent Vila, Jean-Philippe Attané, C Beigné, G de Loubens, M Viret, N Beaulieu, J Ben Youssef, et al. Nonlinear spin conductance of yttrium iron garnet thin films driven by large spin-orbit torque. *Physical Review B*, 97(6):060409, 2018.

[188] M Schneider, T Brächer, V Lauer, P Pirro, DA Bozhko, AA Serga, H Yu Musiienko-Shmarova, B Heinz, Q Wang, T Meyer, et al. Bose-einstein condensation of quasiparticles by rapid cooling. *arXiv preprint arXiv:1612.07305*, 2016.

[189] PK Larsen and R Metselaar. Electrical properties of yttrium iron garnet at high temperatures. *Physical Review B*, 14(6):2520, 1976.

[190] HB Lal, BK Verma, and Vijayee Ram Yadav. Electrical transport in heavy rare-earth iron garnets. *Journal of Materials Science*, 17(11):3317–3326, 1982.

[191] AN Petrov, GV Denisov, and VM Zhukovskii. Nature of electrotransport in yttrium-iron garnet. *Inorganic Materials*, 22(4):579–584, 1986.

[192] Lalitha Sirdeshmukh, K Krishna Kumar, S Bal Laxman, A Rama Krishna, and G Sathaiah. Dielectric properties and electrical conduction in yttrium iron garnet (yig). *Bulletin of Materials Science*, 21(3):219–226, 1998.

[193] KB Modi and PU Sharma. On the effect of shi irradiation on dielectric properties of y3+ x fe5- x o12 (x= 0.0–0.6) system. *Radiation Effects and Defects in Solids*, 169(8):723–739, 2014.

[194] M Sparks. Theory of surface-spin pinning in ferromagnetic resonance. *Physical Review Letters*, 22(21):1111, 1969.

[195] Z Fang, A Mitra, AL Westerman, M Ali, Chiara Ciccarelli, O Cespedes, BJ Hickey, and AJ Ferguson. Thickness dependence study of current-driven ferromagnetic resonance in y3fe5o12/heavy metal bilayers. *Applied Physics Letters*, 110(9):092403, 2017.

[196] Young-Min Kang, Sung-Hun Wee, Seong-Il Baik, Seong-Gi Min, Seong-Cho Yu, Seung-Hyun Moon, Young-Woon Kim, and Sang-Im Yoo. Magnetic properties of yig (y 3 fe 5 o 12) thin films prepared by the post annealing of amorphous films deposited by rf-magnetron sputtering. *Journal of applied physics*, 97(10):10A319, 2005.

[197] HL Wang, CH Du, Y Pu, R Adur, PC Hammel, and FY Yang. Large spin pumping from epitaxial y 3 fe 5 o 12 thin films to pt and w layers. *Physical Review B*, 88(10):100406, 2013.

[198] Christoph Hauser, Tim Richter, Nico Homonnay, Christian Eisenschmidt, Mohammad Qaid, Hakan Deniz, Dietrich Hesse, Maciej Sawicki, Stefan G Ebbinghaus, and Georg Schmidt. Yttrium iron garnet thin films with very low damping obtained by recrystallization of amorphous material. *Scientific reports*, 6:20827, 2016.

[199] O Philips'Gloeilampenfabrieken. A method of measuring specific resistivity and hall effect of discs of arbitrary shape. *Philips Res. Rep*, 13(1):1–9, 1958.

[200] PK Larsen and JM Robertson. Electrical and optical properties of thin films of pb2+-and si4+-doped yig produced by liquid phase epitaxy. *Journal of Applied Physics*, 45(7):2867–2873, 1974.

[201] LD Landau. Über die bewegung der elektronen in kristallgitter. *Phys. Z. Sowjetunion*, 3:644–645, 1933.

[202] Steven JF Byrnes. Basic theory and phenomenology of polarons. *Department of Physics, University of California at Berkeley, Berkeley, CA*, 94720, 2008.

[203] Douglas Natelson. *Nanostructures and nanotechnology*. Cambridge University Press, 2015.

[204] IG Lang and Yu A Firsov. Kinetic theory of semiconductors with low mobility. *Sov. Phys. JETP*, 16(5):1301, 1963.

[205] Jozef T Devreese. Polarons. *Encycl. Appl. Phys.*, 14(cond-mat/0004497):383–409, 1996.

[206] HG Reik and R Schirmer. Microscopic theory of reversible photomagnetic effects in yig (si). *Solid State Communications*, 10(12):1209–1212, 1972.

[207] IG Austin and N Fr Mott. Polarons in crystalline and non-crystalline materials. *Advances in physics*, 18(71):41–102, 1969.

[208] L Friedman and T Holstein. Studies of polaron motion: Part iii: The hall mobility of the small polaron. *Annals of Physics*, 21(3):494–549, 1963.

[209] David Carl Bullock and David Jacob Epstein. Negative resistance, conductive switching, and memory effect in silicon-doped yttrium-iron garnet crystals. *Applied Physics Letters*, 17(5):199–201, 1970.

[210] R Metselaar and PK Larsen. High-temperature electrical properties of yttrium iron garnet under varying oxygen pressures. *Solid State Communications*, 15(2):291–294, 1974.

[211] M Kokta and M Grasso. New substituted gallium garnets containing trivalent lanthanum on dodecahedral crystallographic sites. *Journal of Solid State Chemistry*, 8(4):357–359, 1973.

[212] S Geller, HJ Williams, GP Espinosa, and RC Sherwood. Ferrimagnetic garnets containing pentavalent antimony. *Journal of Applied Physics*, 35(3):542–547, 1964.

[213] Y Onose, T Ideue, H Katsura, Y Shiomi, N Nagaosa, and Y Tokura. Observation of the magnon hall effect. *Science*, 329(5989):297–299, 2010.

[214] Jing Liu, LJ Cornelissen, J Shan, Timo Kuschel, and BJ van Wees. Magnon planar hall effect and anisotropic magnetoresistance in a magnetic insulator. *Physical Review B*, 95(14):140402, 2017.

[215] Sibylle Meyer, Y-T Chen, Sebastian Wimmer, Matthias Althammer, T Wimmer, Richard Schlitz, S Geprägs, H Huebl, D Ködderitzsch, H Ebert, et al. Observation of the spin nernst effect. *Nature materials*, 16(10):977, 2017.

[216] B Madon, Do Ch Pham, J-E Wegrowe, D Lacour, M Hehn, V Polewczyk, A Anane, and V Cros. Anomalous and planar righi-leduc effects in ni 80 fe 20 ferromagnets. *Physical Review B*, 94(14):144423, 2016.

[217] Muhammad Syazwan Mustaffa, Nuraine Mariana Mohd Shahrani, et al. Sintering temperature effect on microstructure and magnetic evolution properties with nano- and micrometer grain size in ferrite polycrystals. *Sintering Technology: Method and Application*, page 45, 2018.

[218] Ludo J Cornelissen, J Shan, and BJ Van Wees. Temperature dependence of the magnon spin diffusion length and magnon spin conductivity in the magnetic insulator yttrium iron garnet. *Physical Review B*, 94(18):180402, 2016.

[219] LJ Cornelissen and BJ Van Wees. Magnetic field dependence of the magnon spin diffusion length in the magnetic insulator yttrium iron garnet. *Physical Review B*, 93(2):020403, 2016.

[220] Freeman J Dyson. General theory of spin-wave interactions. *Physical review*, 102(5):1217, 1956.

[221] Juan Shan, Ludo J Cornelissen, Nynke Vlietstra, Jamal Ben Youssef, Timo Kuschel, Rembert A Duine, and Bart J Van Wees. Influence of yttrium iron garnet thickness and heater opacity on the nonlocal transport of electrically and thermally excited magnons. *Physical Review B*, 94(17):174437, 2016.

[222] Lucile Soumah, Nathan Beaulieu, Lilia Qassym, Cécile Carrétéro, Eric Jacquet, Richard Lebourgeois, Jamal Ben Youssef, Paolo Bortolotti, Vincent Cros, and Abdelmadjid Anane. Ultra-low damping insulating magnetic thin films get perpendicular. *Nature communications*, 9(1):3355, 2018.

[223] M Evelt, L Soumah, AB Rinkevich, SO Demokritov, A Anane, V Cros, Jamal Ben Youssef, G De Loubens, O Klein, P Bortolotti, et al. Emission of coherent propagating magnons by insulator-based spin-orbit-torque oscillators. *Physical Review Applied*, 10(4):041002, 2018.

[224] VJ Fratello, SEG Slusky, CD Brandle, and MP Norelli. Growth-induced anisotropy in bismuth: Rare-earth iron garnets. *Journal of applied physics*, 60(7):2488–2497, 1986.

[225] Elena Popova, Andres Felipe Franco Galeano, Marwan Deb, Bénédicte Warot-Fonrose, Hamid Kachkachi, François Gendron, Frédéric Ott, Bruno Berini, and Niels Keller. Magnetic anisotropies in ultrathin bismuth iron garnet films. *Journal of Magnetism and Magnetic Materials*, 335:139–143, 2013.

[226] Mohammad Niyaifar and Hory Mohammadpour. Study on magnetic role of bi3+ ion by random cation distribution model in bi–yig system. *Journal of magnetism and Magnetic Materials*, 396:65–70, 2015.

[227] N Vlietstra, J Shan, Vincent Castel, BJ Van Wees, and J Ben Youssef. Spin-hall magnetoresistance in platinum on yttrium iron garnet: Dependence on platinum thickness and in-plane/out-of-plane magnetization. *Physical Review B*, 87(18):184421, 2013.

[228] Andrei Slavin and Vasil Tiberkevich. Nonlinear auto-oscillator theory of microwave generation by spin-polarized current. *IEEE Transactions on Magnetics*, 45(4):1875–1918, 2009.

[229] JF Dillon Jr. Ferrimagnetic resonance in yttrium iron garnet. *Physical Review*, 105(2):759, 1957.

[230] J Desvignes, D Mahasoro, and H Gall. Narrow fmr linewidth dependence on growth conditions in lpe yig films. *IEEE Transactions on Magnetics*, 23(5):3724–3726, 1987.

[231] P Hansen, K Witter, and W Tolksdorf. Magnetic and magneto-optic properties of lead-and bismuth-substituted yttrium iron garnet films. *Physical Review B*, 27(11):6608, 1983.

[232] Hiroshi Makino and Yasuharu Hidaka. Determination of magnetic anisotropy constants for bubble garnet epitaxial films using field orientation dependence in ferromagnetic resonances. *Materials Research Bulletin*, 16(8):957–966, 1981.

[233] Ei Shigematsu, Yuichiro Ando, Ryo Ohshima, Sergey Dushenko, Yukio Higuchi, Teruya Shinjo, Hans Jürgen von Bardeleben, and Masashi Shiraishi. Significant reduction in spin pumping efficiency in a platinum/yttrium iron garnet bilayer at low temperature. *Applied Physics Express*, 9(5):053002, 2016.

[234] CL Jermain, SV Aradhya, ND Reynolds, RA Buhrman, JT Brangham, MR Page, PC Hammel, FY Yang, and DC Ralph. Increased low-temperature damping in yttrium iron garnet thin films. *Physical Review B*, 95(17):174411, 2017.

[235] EG Spencer, RC LeCraw, and AM Clogston. Low-temperature line-width maximum in yttrium iron garnet. *Physical Review Letters*, 3(1):32, 1959.

[236] M Collet, R Mattana, J-B Moussy, K Ollefs, S Collin, C Deranlot, A Anane, V Cros, F Petroff, F Wilhelm, et al. Investigating magnetic proximity effects at ferrite/pt interfaces. *Applied Physics Letters*, 111(20):202401, 2017.

[237] Chi Tang, Qi Song, Cui-Zu Chang, Yadong Xu, Yuichi Ohnuma, Mamoru Matsuo, Yawen Liu, Wei Yuan, Yunyan Yao, Jagadeesh S Moodera, et al. Dirac surface state–modulated spin dynamics in a ferrimagnetic insulator at room temperature. *Science advances*, 4(6):eaas8660, 2018.

[238] Piotr Laczkowski, Henri Jaffrès, W Savero-Torres, J-C Rojas-Sánchez, Yu Fu, N Reyren, C Deranlot, Lucien Notin, Cyrille Beigné, J-P Attané, et al. Evaluation of spin diffusion length of auw alloys using spin absorption experiments in the limit of large spin-orbit interactions. *Physical Review B*, 92(21):214405, 2015.

[239] J Shan, LJ Cornelissen, J Liu, J Ben Youssef, L Liang, and BJ Van Wees. Criteria for accurate determination of the magnon relaxation length from the nonlocal spin seebeck effect. *Physical Review B*, 96(18):184427, 2017.

[240] Ken-ichi Uchida, Takashi Kikkawa, Asuka Miura, Junichiro Shiomi, and Eiji Saitoh. Quantitative temperature dependence of longitudinal spin seebeck effect at high temperatures. *Physical Review X*, 4(4):041023, 2014.

[241] Hiroto Adachi, Yutaka Yamamoto, and Masanori Ichioka. Spin seebeck effect in a simple ferromagnet near t c: a ginzburg–landau approach. *Journal of Physics D: Applied Physics*, 51(14):144001, 2018.

[242] John MD Coey. *Magnetism and magnetic materials*. Cambridge university press, 2010.

[243] Can Onur Avci, Andy Quindeau, Chi-Feng Pai, Maxwell Mann, Lucas Caretta, Astera S Tang, Mehmet C Onbasli, Caroline A Ross, and Geoffrey SD Beach. Current-induced switching in a magnetic insulator. *Nature materials*, 16(3):309, 2017.

[244] Kathrin Ganzhorn, Tobias Wimmer, Joel Cramer, Richard Schlitz, Stephan Geprägs, Gerhard Jakob, Rudolf Gross, Hans Huebl, Mathias Kläui, and Sebastian TB Goennenwein. Temperature dependence of the non-local spin seebeck effect in yig/pt nanostructures. *AIP Advances*, 7(8):085102, 2017.

[245] XJ Zhou, GY Shi, JH Han, QH Yang, YH Rao, HW Zhang, LL Lang, SM Zhou, F Pan, and C Song. Lateral transport properties of thermally excited magnons in yttrium iron garnet films. *Applied Physics Letters*, 110(6):062407, 2017.

[246] Stephen R Boona and Joseph P Heremans. Magnon thermal mean free path in yttrium iron garnet. *Physical Review B*, 90(6):064421, 2014.

[247] Hwan Soo Dow, Woo Sik Kim, and Jung Woo Lee. Thermal and electrical properties of silicon nitride substrates. *AIP Advances*, 7(9):095022, 2017.

[248] A Piccirillo and AL Gobbi. Physical-electrical properties of silicon nitride deposited by pecvd on iii–v semiconductors. *Journal of The Electrochemical Society*, 137(12):3910–3917, 1990.

[249] OA Lukianova, AN Khmara, SN Perevislov, DA Kolesnikov, and VV Krasilnikov. Electrical resistivity of silicon nitride produced by various methods. *Ceramics International*, 45(7):9497–9501, 2019.

[250] T Kikkawa, K Uchida, S Daimon, Y Shiomi, Hiroto Adachi, Z Qiu, D Hou, X-F Jin, S Maekawa, and E Saitoh. Separation of longitudinal spin seebeck effect from anomalous nernst effect: Determination of origin of transverse thermoelectric voltage in metal/insulator junctions. *Physical Review B*, 88(21):214403, 2013.

[251] T Kikkawa, K Uchida, Y Shiomi, Z Qiu, D Hou, D Tian, H Nakayama, X-F Jin, and E Saitoh. Longitudinal spin seebeck effect free from the proximity nernst effect. *Physical review letters*, 110(6):067207, 2013.

[252] Can Onur Avci, Kevin Garello, Johannes Mendil, Abhijit Ghosh, Nicolas Blasakis, Mihai Gabureac, Morgan Trassin, Manfred Fiebig, and Pietro Gambardella. Magnetoresistance of heavy and light metal/ferromagnet bilayers. *Applied Physics Letters*, 107(19):192405, 2015.

[253] Benedetta Flebus, SA Bender, Yaroslav Tserkovnyak, and RA Duine. Two-fluid theory for spin superfluidity in magnetic insulators. *Physical review letters*, 116(11):117201, 2016.

[254] Vegard Flovik, Ferran Macià, Sergi Lendínez, Joan Manel Hernàndez, Ingrid Hallsteinsen, Thomas Tybell, and Erik Wahlström. Thickness and temperature dependence of the magnetodynamic damping of pulsed laser deposited la0. 7sr0. 3mno3 on (111)-oriented srtio3. *Journal of Magnetism and Magnetic Materials*, 420:280–284, 2016.

[255] Young-Yeal Song, Sangita Kalarickal, and Carl E Patton. Optimized pulsed laser deposited barium ferrite thin films with narrow ferromagnetic resonance linewidths. *Journal of applied physics*, 94(8):5103–5110, 2003.

[256] Young-Yeal Song, Michael S Grinolds, Pavol Krivosik, and Carl E Patton. Pulsed laser-deposited single-crystal lizn-ferrite films with low microwave loss. *Journal of applied physics*, 97(10):103516, 2005.

[257] B Heinrich, C Burrowes, E Montoya, B Kardasz, E Girt, Young-Yeal Song, Yiyan Sun, and Mingzhong Wu. Spin pumping at the magnetic insulator (yig)/normal metal (au) interfaces. *Physical review letters*, 107(6):066604, 2011.

[258] YT Fanchiang, KHM Chen, CC Tseng, CC Chen, CK Cheng, SR Yang, CN Wu, SF Lee, M Hong, and J Kwo. Strongly exchange-coupled and surface-state-modulated magnetization dynamics in bi 2 se 3/yttrium iron garnet heterostructures. *Nature communications*, 9(1):223, 2018.

[259] TJ Silva and WH Rippard. Developments in nano-oscillators based upon spin-transfer point-contact devices. *Journal of Magnetism and Magnetic Materials*, 320(7):1260–1271, 2008.

[260] Ran Cheng, Di Xiao, and Arne Brataas. Terahertz antiferromagnetic spin hall nano-oscillator. *Physical Review Letters*, 116(20):207603, 2016.

[261] Roman Khymyn, Ivan Lisenkov, Vasyl Tiberkevich, Boris A Ivanov, and Andrei Slavin. Antiferromagnetic thz-frequency josephson-like oscillator driven by spin current. *Scientific reports*, 7:43705, 2017.

[262] OR Sulymenko, OV Prokopenko, VS Tiberkevich, AN Slavin, BA Ivanov, and RS Khymyn. Terahertz-frequency spin hall auto-oscillator based on a canted antiferromagnet. *Physical Review Applied*, 8(6):064007, 2017.

[263] LJ Cornelissen, J Liu, BJ Van Wees, and RA Duine. Spin-current-controlled modulation of the magnon spin conductance in a three-terminal magnon transistor. *Physical review letters*, 120(9):097702, 2018.

[264] Tobias Wimmer, Matthias Althammer, Lukas Liensberger, Nynke Vlietstra, Stephan Geprägs, Mathias Weiler, Rudolf Gross, and Hans Huebl. Spin transport in a charge current induced magnon bose-einstein condensate at room temperature. *arXiv preprint arXiv:1812.01334*, 2018.

[265] Kyongmo An, Artem N Litvinenko, Aufa A Fuad, Vladimir V Naletov, Laurent Vila, Ursula Ebels, Grégoire de Loubens, Hervé Hurdequint, Nathan Beaulieu, Jamal Ben Youssef, et al. Long range coupling of magnetic bi-layers by coherent phonons. *arXiv preprint arXiv:1905.12523*, 2019.

[266] LJ Cornelissen, K Oyanagi, T Kikkawa, Z Qiu, Timo Kuschel, GEW Bauer, BJ van Wees, and E Saitoh. Nonlocal magnon-polaron transport in yttrium iron garnet. *Physical Review B*, 96(10):104441, 2017.

[267] Simon Streib, Hedyeh Keshtgar, and Gerrit EW Bauer. Damping of magnetization dynamics by phonon pumping. *Physical review letters*, 121(2):027202, 2018.

[268] Simon Streib, Nicolas Vidal-Silva, Ka Shen, and Gerrit EW Bauer. Magnon-phonon interactions in magnetic insulators. *Physical Review B*, 99(18):184442, 2019.

[269] Sergej O Demokritov and Vladislav E Demidov. Micro-brillouin light scattering spectroscopy of magnetic nanostructures. *IEEE Transactions on Magnetics*, 44(1):6–12, 2007.